# ESRF HIGHLIGHTS 2008

A light for science

ESRF

# HIGHLIGHTS 2008

## CONTENTS



ESRF

European Synchrotron Radiation Facility

# Introduction

It was obvious at the outset that 2008 would be a decisive year for the ESRF, with a major impact on the future. In retrospect, the outcome has been positive in all aspects, blending continued scientific success with the beginning of a successful transition towards a bright future. The scientific highlights on the following pages testify to the breadth and quality of the scientific programme at the ESRF. Each result would merit a mention in this Introduction; we trust that every reader will find an example of outstanding research in a field that he or she is familiar with.

The numbers of proposals, experimental sessions, user visits and publications in peer-reviewed journals have hit new record highs. The figure of 2000 proposals was exceeded for the first time and the oversubscription on some beamlines emphasises the need to continue with the efforts to maintain and extend rapid throughput and efficient operation. Further details on user operations are included in the chapter on Facts and Figures. The beamlines for macromolecular crystallography continued to show the way, introducing remote access in 2008, unique in Europe; this earned the Bessy Innovation Award for the team who developed the necessary software. The ESRF's leadership in the field of beamline automation is a result of good cooperation, notably with the EMBL.

The world-class stability and reliability of the accelerators and X-ray source at the ESRF are an important factor for our capability to increase the scientific output year by year. In 2008, the 7/8 + 1 beam filling mode has become the new standard mode, meeting simultaneously the needs of two very different user communities. However, sixteen years after the first beams circulated in the storage ring, care has to be taken that old and/or obsolete technologies are replaced in due time. Even "simple" components can cause continued concern as their ageing leads to unpredictable phenomena or suppliers discontinue the delivery of spares. A major step forward in the process of continued replacement was the commissioning of the HQPS-2 in 2008, a next-generation system to ensure delivery of electric power even in the presence of spikes on the public power grid. HQPS-2 was gradually put into operation and its qualities have contributed to the result that statistically, 2008 has been the best year on record at the ESRF in terms of beam availability, mean time between failures, and the average duration of a failure.

The ESRF family has grown in 2008, with Slovakia being welcomed as the 19th member, establishing the Centralsync consortium with the Czech Republic and Hungary, thereby adding 1.05% of the Members' contributions to the ESRF budget. Earlier in the year, the Kurchatov Institute in Russia and the ESRF signed a Memorandum of Understanding to promote different areas of scientific collaboration.

In the area of office automation, the year 2008 was characterised by the transition to Windows Vista which required much preparation to ensure seamless integration with the various management information systems and, equally importantly, with scientific computing. Document archiving and data curation is also high on the agenda in scientific computing as data rates and data volumes continue to be the fastest-growing figures at the ESRF.

However, 2008 will truly be remembered as the year of the ESRF Upgrade Programme. The approval in principle, at the June meeting of the Council, and that of the budget for the first year of the Upgrade, at the November meeting, ensure the transition towards a bright future covering at least a decade. Much work was necessary to detail and hone the ESRF's proposals before an endorsement could be given by the Council. The work on the Upgrade Programme is documented in a separate section immediately following this introduction. Here, we would like to highlight the progress made with the definition of the building extensions, helped by a grant from the European Commission, within the Framework 7 Programme. This work has removed many uncertainties – both technical and financial – that would have impeded rapid progress with development of the first eight Upgrade beamlines.

More good news was the grant of 15 million Euros by French national and regional authorities (*Contrat de Projet Etat-Région*) to improve the infrastructure of the joint ILL/ESRF site over the next three years; this award will allow the construction of a new relocated site entrance, a visitor centre, and will make possible buildings for new partnerships with the ILL and other leading institutes. In addition, the ESRF will benefit from the ambitious plans for the surrounding area, since Grenoble has been selected to host a project within France's national Campus plan to aggressively modernise university infrastructure and governance.

The management of the ESRF has seen two new faces arriving in 2008, with Angelika E. Röhr taking over from Helmut Krech as Director of

Incoming and outgoing Directorate of the ESRF meeting at the eve of 2009. From left to right: Bill Stirling, Francesco Sette, Harald Reichert, Angelika Röhr, Pascal Elleaume, Serge Perez, who will take over from Sine Larsen as Director of Research in June 2009, Robert Feidenhans'l, Chairman of the ESRF Council, and Sine Larsen. Not included in the photo is Helmut Krech, Director of Administration until October *(Credit: C. Argoud)*.

Administration, and Harald Reichert as one of two Directors of Research. Pascal Elleaume was confirmed for another term as Director of the Accelerator and Source Division. To deal with the many new challenges of the Upgrade Programme, the Instrumentation Services and Development Division was created, regrouping activities formerly located in three other divisions. Together with the introduction of an ESRF-wide project management mechanism, this reorganisation shall ensure that the technical, financial and managerial challenges ahead are addressed in an adequate manner whilst at the same time continuing to deliver world-class science. Finally, the end of the year 2008 marked the end of Bill Stirling's eight-year term as ESRF Director General, and the handing over of the baton to Francesco Sette, who had been a Director of Research at the ESRF for the past seven years.

The ESRF is a highly visible European success story. Thirty publications per year in Nature and Science for both 2006 and 2007 do not remain unnoticed, nor do numerous invited talks at prestigious meetings like the 2008 IUCr Congress in Osaka (Japan). The celebration, on 26 November 2008, of the 20th anniversary of the signature of the intergovernmental convention establishing the ESRF was a good opportunity to gather the ESRF family from all over Europe and around the world to celebrate what has been achieved as a result of two decades of hard work.

We would like to use this opportunity to extend special thanks to our Member and Associate countries which, despite a difficult funding context, have given the green light for the Upgrade Programme. All of the colleagues whose support was so important for the acceptation of the Upgrade Programme, notably the members of the governing bodies of the ESRF - the Council, the AFC and the SAC - also deserve our thanks. We are also grateful to the thousands of users from the scientific fields covered by the 11 review committees, for their continued support and interest, and to the European Commission for the ESRFUP grant that funded part of the preparatory phase of the Upgrade Programme. Last but certainly not least, we wish to thank the staff of the ESRF who from behind the scenes make possible the remarkable scientific investigations carried out at the ESRF which the reader will discover on the following pages.

***P. Elleaume, R. Dimper, C. Habfast, H. Krech, S. Larsen, H. Reichert, M. Rodriguez Castellano, A.E. Röhr, F. Sette, P. Thiry and W.G. Stirling***

# Upgrade Programme

**2008 will be remembered as the year the Upgrade Programme turned from a vision into a project thanks to its approval in two steps: in June, an endorsement in principle followed in November by a green light in the form of a 10% increase to the budget for 2009 explicitly for the Upgrade.**

The path to approval deeply involved the Council, Science Advisory Committee (SAC) and User Communities without whom the positive decision would not have been possible. The staff and the management of the ESRF are grateful to the stakeholders and the funding agencies for having given a green light for the Upgrade Programme in a difficult international funding context.

The stage for the Upgrade Programme was set five years ago with the Long Term Strategy, a document looking to the future of the ESRF for the coming decade, which at the turn of 2003-04 received positive reactions from the Council and the subsequent User Meeting. This strategy document was followed up with the two-volume Purple Book (**Figure 1**), a detailed science and technological programme mapping out concrete ideas and proposals for new beamlines, infrastructure and techniques. At this time, the Upgrade was also included on the European Strategy Forum for Research Infrastructures (ESFRI) road map for large-scale European research infrastructures, showing the importance of a renewed ESRF for the European Research Area.

Since its publication in October 2007, the ideas of the Purple Book have been honed and elaborated in much detail. The effort and devotion of many ESRF staff resulted in a concrete plan for a Phase I of the Upgrade Programme in line with the funding capabilities of the ESRF Members and consolidated into national road maps for light source development.

This first of two phases will last seven years starting in 2009, and the overlapping phase will be submitted for consideration in due time to cover further developments until 2018. The budget envelope for Phase I includes 177 million Euros spread over seven years, of which 103 million Euros are additional funds with the remainder originating from the ESRF's regular investment budget. The lion's share of this will fund development of eight world-class beamlines unique in Europe, if not globally, housed in extensions to the current experimental hall (**Figure 2**). These new beamlines, targeted mostly at the exploitation of nano-focus beams, will be supported by new enabling technologies in areas like high precision optics and mechanics, detector and computing developments, and by improvements to the accelerator and X-ray source complex.

The detailed definition of these elements of the Upgrade Programme has seen major progress in 2008, preparing the ground for the hard work to come over the next few years. The inclusion of the Upgrade Programme into the ESFRI road map for future large-scale infrastructures opened the door to a 5 million Euros grant from the Framework 7 Programme (FP7) of the European Commission to catalyse preparatory work – without which the design studies could not have pushed ahead as quickly whilst full approval was being sought. Tasks as diverse as feasibility studies for high-field magnets, data archiving, beamline conceptual and technical design reports, improved software for user management, use of the GRID for light sources and architect designs

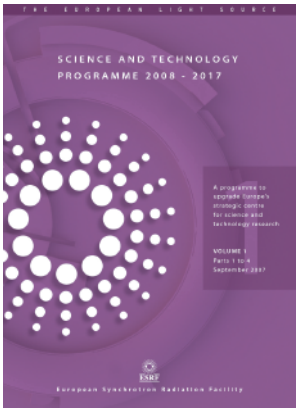


*Fig. 1:* The two volumes of the Purple Book outline the science cases and ideas for the future science and technology programme of the ESRF. The Purple Book can be downloaded in PDF form from the ESRF web site.

*Fig. 2:* Elements of the Upgrade Programme with the greatest part of funding being spent directly on new and improved beamlines and instrumentation. The area of the inner segments reflect the staff and recurrent costs, whilst the outer segment areas represent the capital investment costs.

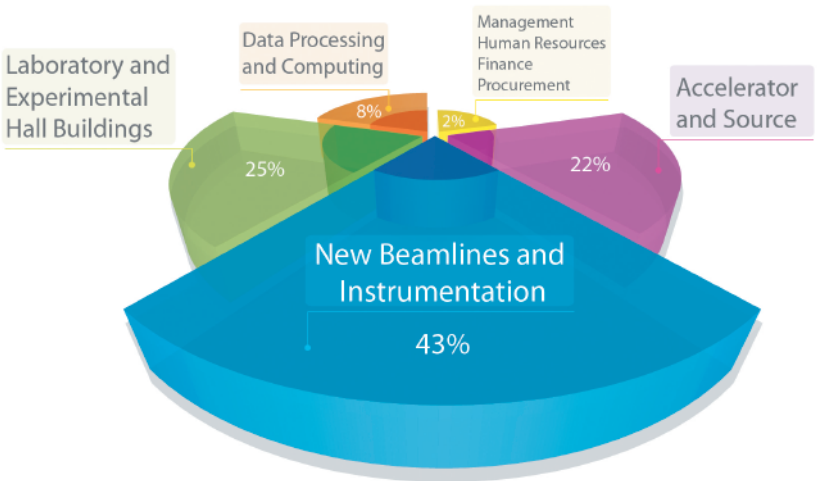

for the experimental hall extensions were all funded through this FP7 grant.

Buildings on their own rarely produce new science; the extensions to the existing experimental hall, necessary to house the long beamlines for nano-focussed beams, must be designed to minimum cost, whilst their civil engineering must interfere as little as possible with on-going user operations. It is important to maintain maximum access to the beamlines for the communities who rely on regular beam time. The detailed definition for the new buildings with the capacity to house up to fifteen long beamlines along with some support laboratories and office space, is therefore complex and time consuming, and these activities will continue well into 2009.

In spring 2008, an international architect competition was held, with the favourite design (**Figure 3**) now being updated with the latest scientific and budgetary requirements. Particular care and effort is being put into the design of the concrete slab to host the new beamlines as its vibrational stability is key to the beamlines meeting their design performance! Work included experiments like that of a

*Fig. 4:* Vibrating the floor of the ESRF (February, 2008).

*Fig. 3:* Artist's impression of the building extension design.

| | |
|---|---|
| UPBL1: | Local probe coherent diffraction imaging and nanobeam diffraction for characterisation of individual nanostructures |
| UPBL2: | High-energy beamline for buried interface structure and materials processing |
| UPBL3: | Nuclear resonance beamline for the study of nanoscale materials: the interplay of growth, structure, electric and magnetic properties as well as dynamics |
| UPBL4: | Beamline for imaging, fluorescence and spectroscopy at the nanoscale |
| UPBL5: | Beamline for parallel and coherent beam imaging |
| UPBL6: | High-energy resolution inelastic scattering in the hard X-ray range with micro- and nanofocus capabilities |
| UPBL7: | Soft X-rays for nanomagnetic and electronic spectroscopy |
| UPBL8: | Nano- and microbeam crystallography for structural and functional biology and soft matter |
| UPBL9: | (a) Sub-microradian angular resolution small-angle scattering for probing the structure and nonequilibrium dynamics of self-assembling soft matter and biological systems<br>(b) Structural dynamics of molecular assemblies |
| UPBL10: | Large-scale automated screening, selection and data collection for macromolecular crystallography |
| UPBL11: | Pushing the limits of energy-dispersive X-ray absorption spectroscopy towards the nano in spatial and temporal resolution |

*Table 1:* The eleven candidates for the Upgrade beamlines, honed from ideas in the Purple Book.

1.2 ton steel ball repeatedly being dropped on the ground in the centre of the ring to study how vibrations propagate across the site (**Figure 4**). Also, soil parameters were probed by test drillings at locations of future hall extensions. The coming year will be decisive as the designs for the buildings including the slabs will be finalised and the tendering of the contracts for construction will begin. The buildings are expected to be ready to move into starting from 2012.

Much care will also be devoted to the selection of the eight new Upgrade beamlines. In May 2008, the SAC endorsed the selection of eleven candidate beamlines from which the eight phase I beamlines will be chosen. The eleven candidates (**Table 1**) have in turn been distilled from the total of over forty proposals outlined in the Purple Book.

Brainstorming sessions with external experts and selected users were held, thanks to the FP7 grant, in the last

months of 2008 to hone the science cases and explore the technological limits of the 11 candidate beamlines leading towards detailed technical design reports. Further guidance on the new beamlines will be given by the SAC at the meeting in May 2009.

In parallel, a large-scale exercise to map out a floor plan for the entire ESRF beamline portfolio was undertaken in 2008, identifying the locations of the new beamlines, with clustering of beamlines linked by science or support facilities whenever beneficial and feasible. The result was endorsed by the SAC in November 2008 and is an important step to creating the overall plan for all ESRF beamlines at the end of Phase I of the Upgrade. Not only will eight new beamlines be developed, but the entire portfolio of beamlines must be maintained and refurbished where necessary, benefitting from the new technologies developed as part of the Upgrade.

Also in November 2008, the SAC gave the green light for three candidate beamlines to already start detailed design work, moving them from conceptual design into technical design report phase. At subsequent meetings, further beamlines will move to the design phase. This staggered approach adds flexibility to the Upgrade Programme and allows the ESRF to react rapidly should important new needs for synchrotron light arrive on the horizon.

As the accelerator and X-ray source are another key element of the ESRF's success, a particular effort will focus on maintaining both at the forefront. For example, several straight sections will be lengthened to increase their capacity and flexibility to host undulators, and the Klystron-based radio-frequency systems upgraded to semiconductor-based technology to improve reliability and prepare for a future increase in machine current. To this end, the development of a higher-mode-dampened prototype cavity began in 2008. Whereas 300 mA current in the storage ring remains an objective, implementation will ultimately also depend upon the cost of energy.

At the beamlines, the narrower nano-focus beams probing smaller samples will pose many technological challenges to the teams responsible for instrumentation, beam optics, sample preparation and sample manipulation. Also, tomorrow's detectors will feature larger arrays with higher sensitivity and better resolution, requiring in turn progress to be made in data storage and pre-processing as well as in easy-to-use data processing. Many of these new technologies will be developed in collaboration with other light sources in Europe. This is why some of the brainstorming sessions in 2008 addressed these areas and involved experts from other light sources, securing the route to cooperation on these developments which are both lengthy and very costly.

Partnerships are another element of the Upgrade Programme. The users of light sources are not as homogenous a community as other users of large research infrastructures. Although this is one of the reasons for the exciting and dynamic environment at synchrotron light sources, it also means that users increasingly come from institutes or research laboratories without much technological or scientific background in photon science.

The Partnership for Structural Biology (PSB) has shown us how to integrate these users: a partnership in close vicinity to the ESRF and the ILL beamlines. For the PSB, the partners include the EMBL Grenoble Outstation and the French *Institut de Biologie Structurale*. A laboratory was set up offering a mix of techniques, science, and technology open to partners both local and distant. As this concept has now proven useful in lowering the entry threshold for users to specialised photon and neutron techniques, soft condensed matter is the next candidate field for such a partnership, again to be shared with ILL, and a first proposal has received a very positive reaction from the ESRF governing bodies.

With our neighbouring sister institute, the ILL, also embarking on its own upgrade programme, ILL 20/20, it is important to recognise the need for general improvements of the site on which both are established. Together, the ESRF and ILL have a considerable impact upon the local economy and on the international visibility of Grenoble as a scientific metropole. French regional and local authorities confirmed in 2008 an investment of 15 million Euros spread over four years into partnership buildings on the site, a new site entrance building, improved roads and a restaurant extension, new stores and goods reception and a visitors' centre. In addition, Grenoble has been included into the national *Campus* programme which will, in the longer term, profoundly change the urban landscape in the neighbourhood of the ESRF through the addition of new laboratory and university buildings, housing and leisure facilities.

With the ESRF Upgrade, the ILL 20/20 programme, the investment in the site and the surrounding areas, the coming years will be an exciting time for the staff and the users of the ESRF as civil construction work and technology development will turn into new beamlines and facilities coming on-line. The new science these promise to deliver should keep the ESRF at the global forefront of light source development for more than a decade from now.

***E. Mitchell***
***and C. Habfast***

# High Resolution and Resonance Scattering

## Introduction

Traditionally the activities of the High Resolution and Resonance Scattering Group cover a wide scientific and methodological range from a better understanding of basic phenomena to applications and new developments. The main fields are investigations of electric and magnetic properties as well as structural dynamics, with an emphasis on extreme conditions such as high pressure, high and low temperature, external magnetic fields, and confined geometry. This section presents a broad set of examples and is structured according to basic phenomena, applications, and new developments.

A single photon can ionise only one electron of an atom, that is what we learn from the textbook. Double photoionisation with a single photon cannot occur directly but only by interaction of the electrons with each other within an atom. Such discoveries already date back a couple of years. Today, Huotari *et al.* present a systematic study of 3d transition metals in comparison with theory. Their study suggests that near threshold the excitation is a quasi-classical *knock-out* rather than a quantum-mechanical *shake-off* effect, and they found a universal scaling law for the double photoionisation energy evolution.

Hydrogen bonds are of paramount importance in many disciplines of natural sciences. Even in a chemically simple system such as water, and despite decades of intense research efforts, new insights are still being gained today. Tse *et al.* carried out X-ray Raman measurements on the solid and liquid phases of water in order to characterise the nature of the distinct pre-edge of the oxygen K-edge. Winkler *et al.* studied the dispersion of OH-stretching modes in diaspore (AlOOH), exploiting the unique possibility of inelastic X-ray scattering to study these high-energy excitations with a resolution of 6 meV.

The structures of some simple elements may change at high pressure becoming rather complex. Rb-IV (others include Na, Ka, Ba) belongs to the class of incommensurate host-guest systems, whose crystal structures have been studied in great detail. Loa *et al.* investigated the pressure dependence of the longitudinal acoustic phonon dispersion, and found that the guest lattice vibrations closely resemble a mono-atomic linear chain, indicating very weak coupling between the host and the guest structure.

Applications are going towards nanocrystalline material and catalysts. Stankov *et al.* were surprised that atomic vibrations in nanocrystalline grains are actually identical to those in the bulk even for extremely small grain sizes and that the anomalous dynamics of nanocrystalline material arises in fact from the atomic vibrations in the disordered interfaces.

Spectroscopic studies of catalytic reactions have received considerable public attention with the Noble Prize for Gerhard Ertl in 2007. The hard X-ray probe at the ESRF is ideally suited to the investigation of catalytic reactions on real catalysts under working conditions. This is crucial to advance the understanding of the chemistry. Two examples from ID26 are presented. The first concerns the oxidation of carbon monoxide that is relevant for the purification of feed gas for fuel cells and automotive exhaust gas. The second contribution presents the visualisation of a catalytic reaction in

space and in time by means of the ESRF FReLoN camera.

New developments continued to play an important role. The demand to access high-energy Mössbauer transitions is continuously growing. After last year's presentation of the nickel case, we continued to exploit this element utilising synchrotron radiation based perturbed angular correlation spectroscopy (SRPAC) **[1]**. In this issue antimony (37.1 keV) and the first tellurium (35.5 keV) results are presented. In the spotlight are skutterudites, a thermoelectric and ferromagnetic material, as well as phase change materials used in rewritable optical data storage.

Finally, Bosak *et al.* utilised thermal diffuse scattering (TDS) to visualise portions of the Fermi surface in three dimensions via intensity modulations which arise from Kohn anomalies in the phonon dispersion. The experiment on Zn was performed on the Swiss-Norwegian beamlines BM01, and gives a flavour of the great potential if an undulator based beamline and a state-of-the-art detector system could be utilised.

***R. Rüffer***

**Reference**
[1] I. Sergueev *et al.*, *PRB* **78**, 214436 (2008).

# Playing billiards with electrons: double photoionisation with a single photon

**Principal publication and authors**
S. Huotari (a), K. Hämäläinen (b), R. Diamant (c), R. Sharon (c), C.C. Kao (d), and M. Deutsch (c), *Phys. Rev. Lett.* **101**, 043001 (2008).
*(a) ESRF*
*(b) Division of Materials Physics, Department of Physics, University of Helsinki (Finland)*
*(c) Physics Department, Bar-Ilan University (Israel)*
*(d) National Synchrotron Light Source, Brookhaven National Laboratory (USA)*

A single photon can directly ionise only one electron of an atom. A simultaneous ejection of a second electron, *i.e.* double photoionisation, may occur only if the electrons within the atom interact with each other. If both electrons are ejected from the *K*-shell, a so-called hollow atom is formed, wherein the *K* shell is empty while higher shells are populated (**Figure 5**). Hollow atoms are of a great interest in many fields, ranging from atomic physics to surface science. When decaying by a $\underline{1s}^2 \rightarrow \underline{1s}^1\underline{2p}^1$ transition (underlining denotes hole states) they emit a $K^h\alpha_{1,2}$ hypersatellite photon **[1]**. Thus, double photoionisation and electron-electron interactions can be studied by high-resolution X-ray hypersatellite spectra measurements.

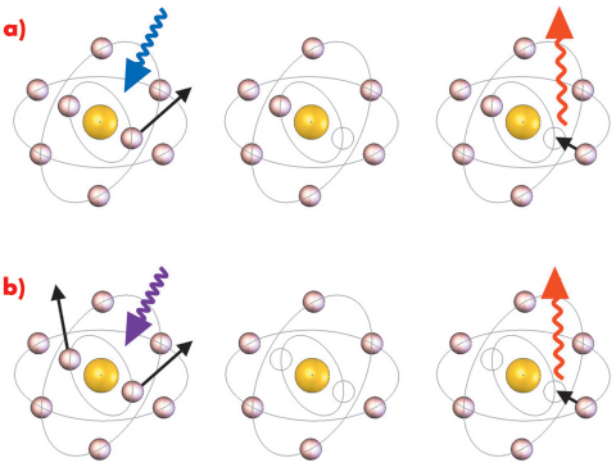


*Fig. 5:* Schematic representation of the processes for **a)** single photoionisation and **b)** double photoionisation, where wavy arrows denote photons, and straight arrows, electron motions. The final state of the hypersatellite emission process is left with a spectator hole, which is later filled by another electron creating conventional diagram X-ray emission lines.

Using beamlines **ID16** (ESRF) and X25 (NSLS, USA) we have studied double photoionisation near its energy threshold, $E_{th}$, in 3d transition metals, by high-energy-resolution hypersatellite spectroscopy. **Figure 6** compares the conventional Cu $K\alpha_{1,2}$ diagram spectrum of a $\underline{1s}^1 \rightarrow \underline{2p}^1$ transition with its hypersatellite counterpart. The $I(K\alpha_1)/I(K\alpha_2) = 2$ intensity ratio reflects the number ratio of the $L_{III}$ and $L_{II}$ electrons. For hypersatellites, the measured ratio is vastly different, being determined by selection rules rather than by the $L_{III}/L_{II}$ electron number ratio. The $K^h\alpha_1$ line requires flipping the shell-changing 2p electron's spin, which is forbidden in the *LS* coupling dominating low-*Z* atoms. In the range of *Z* studied here such flipping is partly allowed, and the $K^h\alpha_1$ line has a non-zero intensity.

**Figure 7** (inset) shows measured $R=I(K^h\alpha_{1,2})/I(K\alpha_{1,2})$ intensity ratios vs. ionising photon energy. This is the first systematic measurement of the near-threshold behaviour of *R* for a range of elements. The very long saturation range, ~70% of $E_{th}$, stands out immediately. $E_{th}$ and the saturation ranges and values in the inset differ

among the elements. Nevertheless, when scaled by the binding energies of the *indirectly*-ionised *K*-electrons and the saturation values (which, incidentally, are found to decrease as $\sim Z^{-1.6}$) an intriguing universal behaviour is revealed: all curves collapse onto a single curve (**Figure 7**).

How does the double photoionisation occur? For photons of energies $E >> E_{th}$, the ionised electron is ejected with a very high kinetic energy, changing abruptly the atomic potential acting on the other electrons. The secondary electron finds itself in an excited state, and has a finite probability of being ejected. This is the *shake-off* (SO) model, which, however, is invalid close to $E_{th}$, where the ionising photon's energy is just barely enough to overcome the binding energy of the electron. Of the other theoretical models only the *knock-out* (KO) model [2] agrees well (blue line in **Figure 7** and lines in the inset) with the measured universal evolution of *R* near threshold, where the ejected photoelectron is slow and stays longer within the bounds of the atom. In the KO model the double photoionisation proceeds by the directly-ionised electron knocking out the secondary one, as in billiards, on its way out. Moreover, the KO process turns out to be a quasi-classical, rather than a quantum, effect, in spite of its occurrence within the *sanctum sanctorum* of the quantum regime: the inner bounds of the atom.
Thus, double photoionisation seems to evolve from a quasi-classical KO billiards process near threshold to a fully quantum SO effect at high ionising photon energies.
In conclusion, we have determined double photoionisation probabilities by measuring the evolution of the hypersatellite spectrum from the threshold upwards for elements $23 \leq Z \leq 30$. We suggest that near the threshold the excitation is a quasi-classical KO effect rather than a quantum mechanical SO one, and demonstrate a universal scaling law for the double photoionisation energy evolution near threshold.

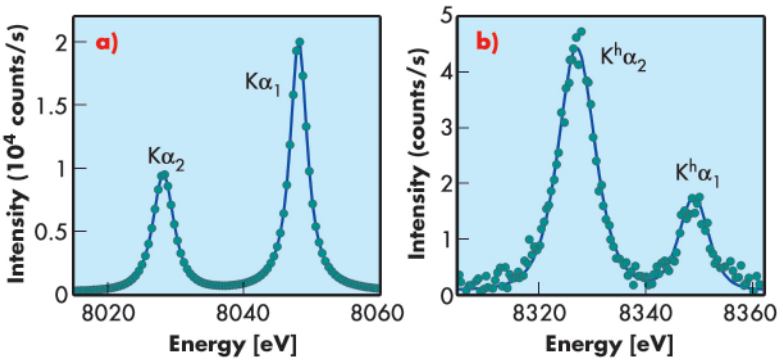


*Fig. 6:* **a)** The conventional Cu $K\alpha_{1,2}$ diagram spectrum. **b)** The hypersatellite Cu $K^h\alpha_{1,2}$ spectrum. Note the difference in the relative intensities of the two emission lines in the two spectra.

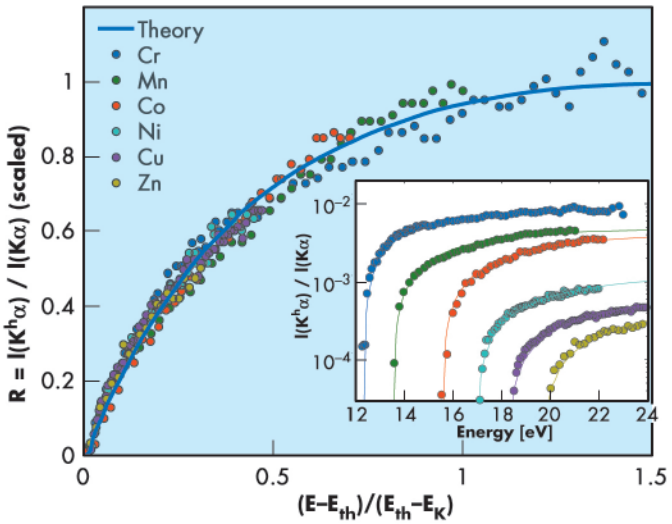


*Fig. 7:* Relative double photoionisation probability *R* for various elements as a function of the excess photon energy above threshold, $E\text{-}E_{th}$, scaled by the binding energy of the secondary ionised electron, $E_{th}\text{-}E_K$, where $E_K$ is the binding energy of the directly-ionised primary electron. The inset shows the raw cross-sections for each element. The solid curve is the (scaled) theoretical KO prediction [2].

**References**
[1] R. Diamant, S. Huotari, K. Hämäläinen, R. Sharon, C.C. Kao, and M. Deutsch, *Phys. Rev. Lett.* **91**, 193001 (2003).
[2] T. Schneider and J.M. Rost, *Phys. Rev. A* **67**, 062704 (2003).

## X-ray absorption of ordered and disordered ice

Despite extensive experimental and theoretical investigations over many decades, an unambiguous understanding of the structure and nature of the hydrogen bonding of water in disordered condensed phases remains an elusive goal [1]. The absorption spectrum of the core 1s oxygen (oxygen K-edge X-ray absorption XAS) is a sensitive atom-specific probe for the H-bond local environment around the absorbing

**Principal publication and authors**
J.S. Tse (a), D.M. Shaw (a), D.D. Klug (b), S. Patchkovskii (b), G. Vankó (c), G. Monaco (c), M. Krisch (c), *Phys. Rev. Lett.* **100**, 095502 (2008).
*(a) Physics and Engineering Physics, University of Saskatchewan, Saskatoon (Canada)*
*(b) Steacie Institute for Molecular Sciences, National Research Council of Canada, Ottawa (Canada)*
*(c) ESRF*

atom. From the comparison of oxygen 1s electronic excitations near the absorption threshold (pre-edge) with theoretical calculated spectrum of liquid water, it was postulated that there exists a large fraction of water molecules with broken hydrogen bonds **[2]**. This hypothesis challenges the conventional model of liquid water where each water molecule is approximately tetrahedrally coordinated to four neighbouring water molecules through hydrogen bonds (H-bond). The basic premise for this suggestion is the observation of a strong pre-edge absorption feature analogous to water adsorbed on surfaces with a broken H-bonding network.

To characterise the nature of the distinct pre-edge absorption, oxygen K-edge XAS of several ice polymorphs were studied using the method of X-ray Raman spectroscopy (XRS). Using X-ray radiation with energy much higher than the core ionisation, XRS measures energy losses due to electronic excitations in a method that is analogous to XAS. Thanks to the higher penetration depth of the X-ray, it is essentially a bulk technique and not affected by surface and saturation effects usually encountered in soft X-ray absorption. To ensure direct and unbiased comparison of different spectra, XRS measurements were made on several ice polymorphs under almost identical instrument resolution, energy calibration and sample environment. This was achieved by taking advantage of the well-characterised thermal induced *in situ* successive structural phase transformation of a high-density amorphous ice (HDA) to low density amorphous (LDA), to crystalline ice Ic and ice Ih and eventually to liquid water **[3]**. Oxygen K-edge XRS spectra were recorded at beamline **ID16**. It was imperative that the sample was at a well-defined temperature; therefore, experiments were carried out at 40 K with the sample bathed in cold flowing He gas. Radiation damage to the sample was minimised by shortening the collection time (less than 1 minute) and accumulating the spectra at multiple sites on the sample.

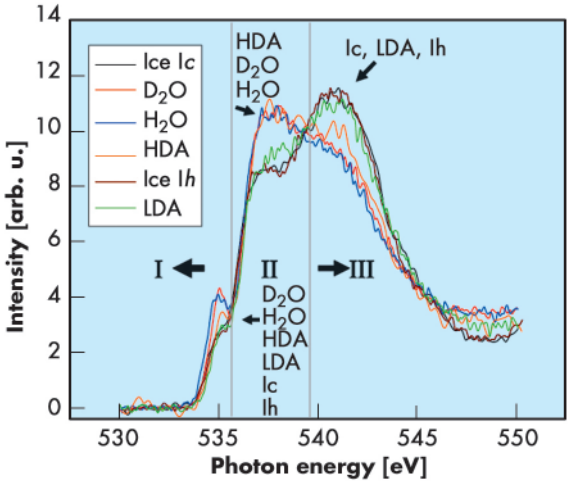


*Fig. 8:* X-ray Raman spectra for LDA, HDA, ice Ic, ice I*h*, $H_2O$, and $D_2O$ water. The spectra were normalised to equal area up to 550 eV. The XAS spectra can be divided into three regions: (I) pre-edge, (II) near-edge, and (III) post-edge. The order of the structures starting from the top peak in the pre-edge region is indicated in the lower central part of the figure. The structures that are in the highest peaks in regions II and III are indicated in each of these regions.

**Figure 8** compares the experimental XAS for the various forms of ice and water. In general, the oxygen K-XAS can be divided into three regions. A pre-edge region (I) starts from the absorption threshold at 533 to 536 eV. A near-edge region (II) from 537 to 539 eV, and a post-edge region (III) from 539 eV and beyond. All the ice samples show a pre-edge absorption at 535 eV. Moreover, the intensity of this peak decreases in the order from liquid water to HDA, and is almost the same for cubic ice I*c*, hexagonal ice I*h*, and LDA. In addition, an unusual trend is observed in regions II and III where the XAS can be divided into two distinct groups with similar absorption profiles. The first group consists of water and HDA ice (group A) and the second group consists of ice I*c*, ice I*h*, and LDA (group B). In the near-edge region (II) the intensities of group A are stronger than group B but the reverse is observed in the post-edge region (III). Comparison of the XAS profile for groups A and B suggests that the oscillator strengths of the excitations in the near-edge region for group B have been shifted into the post-edge region.

The experimental results show that core-hole excitations are localised and not strongly affected by the local environment. The observed XAS profiles can be correlated to the degree of the distortion of H-bond network of the ice polymorphs. In highly disordered ices, the intensity of the XAS is stronger near the oxygen-K

absorption edge. In contrast, for structurally more ordered ices, the XAS absorption intensity is distributed beyond the absorption edge. The difference in the absorption profile can be interpreted as an enhancement of Wannier over Frenkel excitations in an ordered crystal. The results further suggest important contributions from continuum electronic states which have been neglected in most theoretical calculations. Finally, the existence of the pre-edge feature is not a concise indicator of the magnitude of local disorder within the hydrogen bonded network.

**References**
[1] Thematic issue on Water, edited by L.R. Pratt, *Chem. Rev.* **102**, 2625 (2002).
[2] Ph. Wernet *et al.*, *Science* **304**, 995 (2004).
[3] C.A. Tulk *et al.*, *Science* **297**, 1320 (2002).

# Dispersion relation of an OH-stretching vibration from inelastic X-ray scattering

**Principal publication and authors**
B. Winkler (a), A. Friedrich (a), D.J. Wilson (a), E. Haussühl (a), M. Krisch (b), A. Bosak (b), K. Refson (c), V. Milman (d), *Physical Review Letters 101, 065501 (2008).*
*(a) Geowissenschaften, Goethe-Universität, Frankfurt a.M. (Germany)*
*(b) ESRF*
*(c) Rutherford-Appleton Laboratory, Didcot (UK)*
*(d) Accelrys, Cambridge (UK)*

Hydrogen bonds influence structure-property relations in a very large variety of compounds. Consequently, numerous experimental techniques are employed to study the detailed atomic arrangement and the dynamics of hydrogen bonds between *R*-O-H and O-*R*′ groups, where *R* and *R*′ represent parts of a structure, O-H represents a significantly covalent bond with a typical distance of *d*(OH) ~1 Å. The hydrogen bond exists between the hydrogen and the acceptor atom, with a typical distance of 1.5–1.72 Å. The dynamics of hydrogen bonds in crystals, melts, and glasses are routinely characterised using infrared or Raman spectroscopy. However, both infrared and Raman spectroscopy probe the hydrogen dynamics in the long wavelength limit and cannot provide information on the wave vector dependence of the stretching vibration. This is a significant limitation, as it prevents the elucidation of the coupling of the hydrogen dynamics to the remainder of the lattice dynamics. Due to a number of problems, such as limited flux at high energies, intrinsic limitation of the energy resolution and the large incoherent scattering cross section of hydrogen, coherent inelastic neutron scattering is not suitable for the study of the dispersion of high frequency OH stretching vibrations.

These limitations do not exist for inelastic X-ray scattering (IXS), and here we demonstrate that the dispersion relation of OH stretching frequencies can be determined by IXS. We performed experiments on diaspore, α-AlOOH, a model system to study hydrogen bonds of intermediate strength, as it has a comparatively small unit cell, simple chemistry, and is of intermediate (orthorhombic) symmetry. It has recently been studied by DFT calculations and by high-pressure single crystal X-ray diffraction up to 0.5 Mbar [1,2]. The hydrogen bond is slightly kinked, and the OH-stretching frequencies of the four symmetrically inequivalent modes at ambient pressure are centred at ~367 meV [2]. Density functional perturbation theory (DFPT)-based calculations using the CASTEP code revealed that for some wave vectors the OH-stretching vibration has an appreciable dispersion. Specifically, at reciprocal lattice points (0.5 0.5 0)

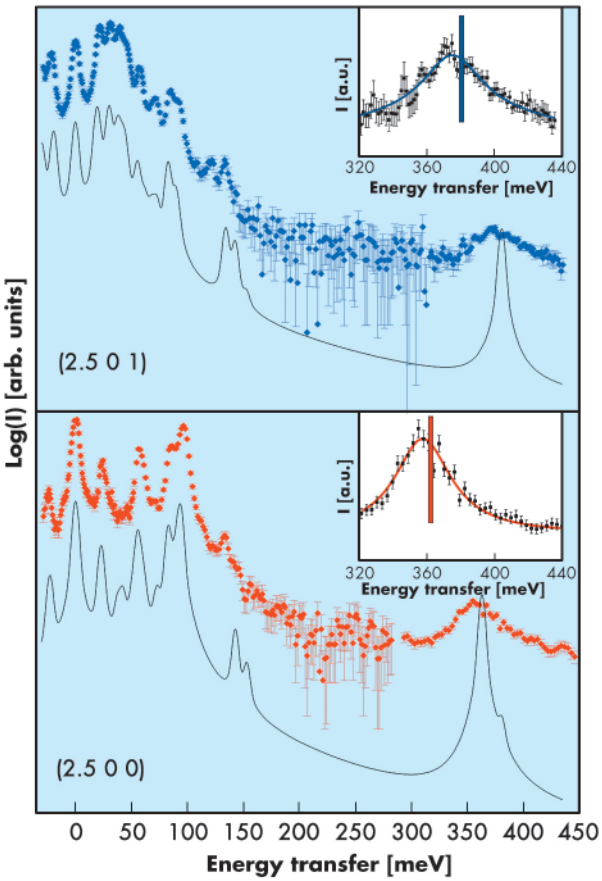


*Fig. 9:* Predicted (line, offset for clarity) and experimental (points) inelastic X-ray spectra of diaspore at (2.5 0 1) and (2.5 0 0), both corresponding to (0.5 0 0) in reduced lattice units. For these two configurations the IXS spectra are dominated by either one or the other doubly degenerate stretching mode. The insets show an enlargement of the high-energy part of the spectrum, and the vertical bars indicate the calculated mode energy.

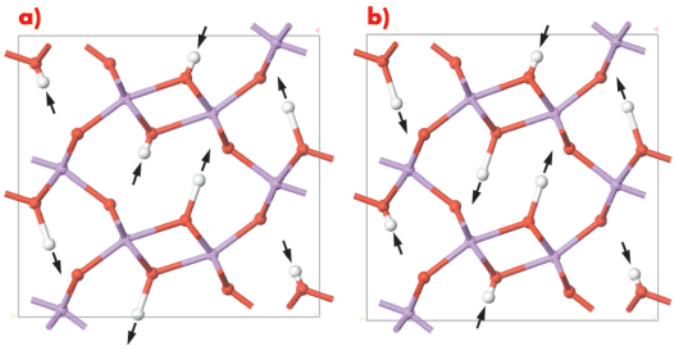


*Fig. 10:* Eigenvectors of the phonons at the Brillouin zone boundary at (0.5 0 0), showing that during the high frequency vibration (left) the hydrogen remain at a constant distance, while during the low frequency motion (right) the hydrogens move further apart. Purple red and white spheres represent Al, O and H atoms, respectively.

**References**
[1] A. Friedrich, D.J. Wilson, E. Haussühl, B. Winkler, W. Morgenroth, K. Refson, and V. Milman, *Phys. Chem. Miner.* **34**, 145 (2007).
[2] A. Friedrich, E. Haussühl, R. Boehler, W. Morgenroth, E.A. Juarez-Arellano, B. Winkler, *Am. Mineral.* **92**, 1640 (2007).

and (0.5 0 0), we predicted that there are two doubly degenerate vibrations with energies of approximately 360 and 378 meV, respectively, while at (0.5 0 0.5), all four stretching vibrations have energies of ~ 361 meV.

The experiment was carried out on the IXS beamline II (**ID28**). The instrument was operated using the silicon (8 8 8) configuration, which provides a total instrumental energy resolution of 6 meV full-width-half maximum. From a gem quality natural sample we have cut a 750 μm thick (001)-slice. The measurements were performed at ambient conditions. Counting times ranged from 60 to 2040 seconds per point. Optimal set-up parameters were determined prior to the experiment by computing theoretical spectra for a variety of wave vector transfers from the DFPT-based lattice dynamical calculations. **Figure 9** shows the excellent agreement between the predicted and experimentally determined spectra. Most notably, we find mode energies of 357 (1) meV and 374 (1) meV, in excellent agreement with calculation. Furthermore the dispersion of 17 meV as a function of q was confirmed by measurements for additional reciprocal lattice points.

An analysis of the eigenvectors (shown in **Figure 10**) revealed that for the high energy mode, the H-H distances remain constant during the vibration at about 2.42 Å, while for the antisymmetric low energy phonon, the hydrogens are further apart for most of the time. Hence, the H-H repulsion energy is lowered as the mode amplitude increases, lowering the potential and consequently the frequency of this mode.

The present experiment shows that dispersion relations at very high frequencies can be measured by IXS, thus offering new opportunities, for example, in the study of phase transformations which are governed by a change in the hydrogen bonding.

**Principal publication and authors**
I. Loa (a), L.F. Lundegaard (a), M.I. McMahon (a), S.R. Evans (a), A. Bossak (b), and M. Krisch (b), *Phys. Rev. Lett.* **99**, 035501 (2007).
*(a) The University of Edinburgh (UK)*
*(b) ESRF*

# Lattice dynamics of rubidium-IV, an incommensurate host-guest system

In recent years, a number of surprisingly complex crystal structures have been discovered in the elements at high pressures, in particular incommensurately modulated structures and incommensurate host-guest composite structures (see **[1]** for a review). The crystal structure of the high-pressure phase rubidium-IV shown in **Figure 11** belongs to the group of incommensurate host-guest structures that have also been observed in the elements Na, K, Ba, Sr, Sc, As, Sb, and Bi. The structure comprises a framework of rubidium host atoms with open channels that are occupied by linear chains of rubidium guest atoms, and the periodicities of the host and guest subsystems are incommensurate with each other (*i.e.*, they have a non-rational ratio). Although considerable progress has been made in determining the detailed crystal structures of the complex metallic phases at high pressure, little is known about their other physical properties, and the mechanisms that lead to their formation and stability are not yet fully understood.

We investigated the lattice dynamics in incommensurate composite Rb-IV by inelastic X-ray scattering (IXS) on beamline **ID28**. The focus was on the longitudinal-acoustic (LA) phonons along the direction of the incommensurate wavevector (parallel to the guest-atom chains). Calculations on simpler model systems predict these

phonons to reflect the incommensurability most clearly. Phase IV of Rb is stable at pressures of 16 to 20 GPa at room temperature, and a high-quality single crystal of Rb-IV was grown in a diamond anvil high pressure cell. In the IXS experiment, the incident radiation was monochromatised at a photon energy of 17.8 keV, and two grazing-incidence mirrors focussed the X-rays onto the sample with a focal size of 25 x 60 µm. The spectrum of the scattered radiation was analysed by a high-resolution silicon crystal analyser to yield an overall energy resolution of 3 meV.

**Figure 11** shows a typical IXS spectrum of Rb-IV along with its decomposition into the elastic line, the phonon excitation peaks and a constant background, which were obtained by least-squares fitting using the FIT28 software. From a series of IXS spectra collected for different momentum transfers $Q$, phonon dispersion curves were obtained as shown in **Figure 12a**. A central result of this study is the observation of *two* well-defined longitudinal-acoustic (LA)-type phonon branches along the chain direction. They are attributed to *separate* LA excitations in the host and the guest sublattices, which is a unique feature of an incommensurate composite crystal.

A series of dispersion curves was measured at different pressures, and from this the sound velocities of the host and guest excitations and their pressure dependences were determined (**Figure 12b**). While the absolute values of the sound velocities in the host and the guest are rather similar, their pressure dependences differ notably. A simple ball-and-spring model of Rb-IV with only one spring constant reproduces these observations semi-quantitatively. This suggests that the difference in the pressure dependences is determined largely by geometrical factors, *i.e.*, by the spatial arrangement of the atoms rather than differences in the chemical bonding in the two subsystems.

There is only very weak coupling between the incommensurate host and the guest in Rb-IV, which raises a rather interesting question. Can the 1D chains of guest atoms in Rb-IV be considered a manifestation of the "monatomic linear chain" treated in solid-state physics textbooks to introduce the concepts of crystal lattice dynamics? The pressure dependence of the interatomic spacing in the guest-atom chains was measured in earlier structural studies and enables the spring constant in the linear chain model to be determined, and also its pressure dependence. On this basis, the sound velocity in the linear chains and its pressure dependence were modelled as shown in **Figure 12b**. The results are in excellent agreement with the IXS data for the guest-atom chains in the composite Rb-IV structure, which can thus be regarded as a manifestation of the monatomic linear chain model with regard to the LA phonons.

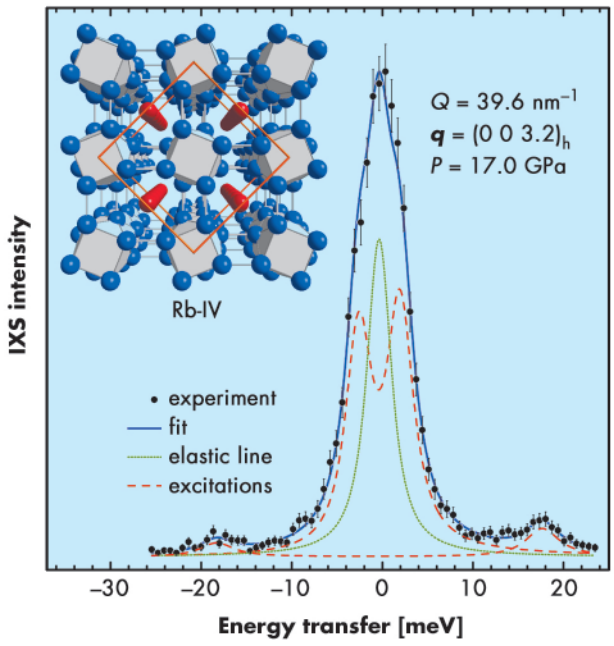


*Fig. 11:* Inelastic X-ray scattering spectrum of Rb-IV at 17.0 GPa, with the scattering vector $\boldsymbol{q} = (0\ 0\ 3.2)_h$ referring to the host lattice. The inset shows the composite crystal structure of Rb-IV with the rubidium host and guest atoms in blue and red, respectively.

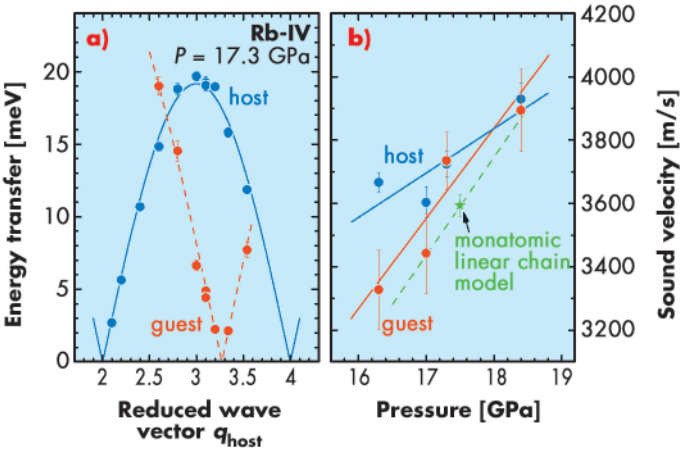


*Fig. 12:* **a)** Dispersion relations of longitudinal-acoustic phonons of the host and guest subsystem in Rb-IV. **b)** Pressure dependences of the host and guest LA sound velocities along the chain direction and results of the monatomic linear chain model. The dashed line indicates the pressure dependence obtained with the linear chain model.

**Reference**

[1] M.I. McMahon and R.J. Nelmes, *Chem. Soc. Rev.* **35**, 943 (2006).

# Vibrational properties of nanograins and interfaces in nanocrystalline materials

**Principal publication and authors**
S. Stankov (a), Y.Z. Yue (b,c), M. Miglierini (d), B. Sepiol (e), I. Sergueev (a), A.I. Chumakov (a), L. Hu (b,c), P. Svec (f), R. Rüffer (a), *Phys. Rev. Lett.* **100**, 235503 (2008).
*(a) ESRF*
*(b) Section of Chemistry, Aalborg University (Denmark)*
*(c) Shandong University, Jinan (China)*
*(d) Slovak University of Technology, Bratislava (Slovakia)*
*(e) University of Vienna (Austria)*
*(f) Slovak Academy of Sciences, Bratislava (Slovakia)*

**References**
[1] B. Fultz *et al.*, *Phys. Rev. Lett.* **79**, 937, (1997).
[2] U. Stuhr *et al.*, *Phys. Rev. Lett.* **81**, 1449 (1998).
[3] B. Roldan Cuenya *et al.*, *Phys. Rev. B* **76**, 195422 (2007).
[4] T. Slezak *et al.*, *Phys. Rev. Lett.* **99**, 066103 (2007).
[5] S. Stankov *et al.*, Phys. Rev. Lett. 99, 185501 (2007).
[6] A. Kara and T.S. Rahman, *Phys. Rev. Lett.* **81**, 1453 (1998).
[7] P.M. Derlet *et al.*, *Phys. Rev. Lett.* **87**, 205501 (2001).
[8] C. Hudon *et al.*, *Phys. Rev. B* **76**, 045409 (2007).

The dynamics of nanocrystalline materials has attracted a lot of scientific interest during the last decade due to the striking differences observed for their atomic vibrations relative to the bulk counterparts. These anomalies are the enhancement of their density of phonon states (DOS) at low and high energies and broadening of the phonon peaks [1]. In addition, the energy dependence of the low-energy part of their phonon DOS has been a source of long-standing debates. The experimental results are contradictory, reporting a linear dependence [2], a power law with n = 1.33 [3], and a quadratic (Debye-like) behaviour ([4, 5], and references therein). On the other hand, the theoretical calculations have also indicated that non-Debye dynamics could originate from the atoms located at the surfaces [6], at the grain boundaries [7], or in the porous areas [8] of the nanocrystalline materials. Therefore the thorough understanding of the atomic dynamics in these materials is of significant importance not only for fundamental physics, but also for tailoring of their beneficial properties like enhanced strength and hardness, and improved plasticity compared to the coarse-grained materials.

In order to investigate the vibrational dynamics of the nanograins and interfaces systematically, we studied a nanocrystalline $Fe_{90}Zr_7B_3$ alloy prepared by crystallisation of an amorphous precursor. A ribbon with composition $Fe_{90}Zr_7B_3$ enriched to 63% in $^{57}Fe$ was produced by the melt-spinning technique. Several nanocrystalline samples composed of α-Fe nanograins and homogeneous and porosity-free interfaces were prepared by annealing of the as-quenched ribbon in a vacuum of 1.6 x $10^{-6}$ mbar. The samples were characterised by X-ray diffraction (XRD), which did not show the presence of oxides or other crystalline phases. The average grain sizes were determined by Rietveld refinement of the XRD patterns and confirmed by transmission electron microscopy.
The high sensitivity of the Mössbauer spectroscopy to the local environment of the resonant nuclei ($^{57}Fe$) was employed to quantitatively determine the amount of iron located within the nanograins and the interfaces at various crystallisation stages. The partial, Fe-projected DOS was obtained from the nuclear inelastic scattering spectra measured with an energy resolution of 1.0 meV at beamline **ID18**. A simple model allowed separation of the DOS of the nanograins from that of the interfaces for a wide range of grain sizes and interface thicknesses. **Figure 13** shows that the phonon DOS of the nanograins does not depend on their size and remains close to that of the bulk even for 2 nm particles (**Figure 13a**). Furthermore, **Figure 14a** and **Figure 14b** show that the phonon DOS of the interfaces is entirely responsible for the observed anomalies exhibiting a shape typical for matter with a high degree of structural disorder. Reducing the interface thickness to the sub-nanometre range results in a dramatic transformation of the phonon DOS (**Figure 14c**). The excess of phonon states at low and

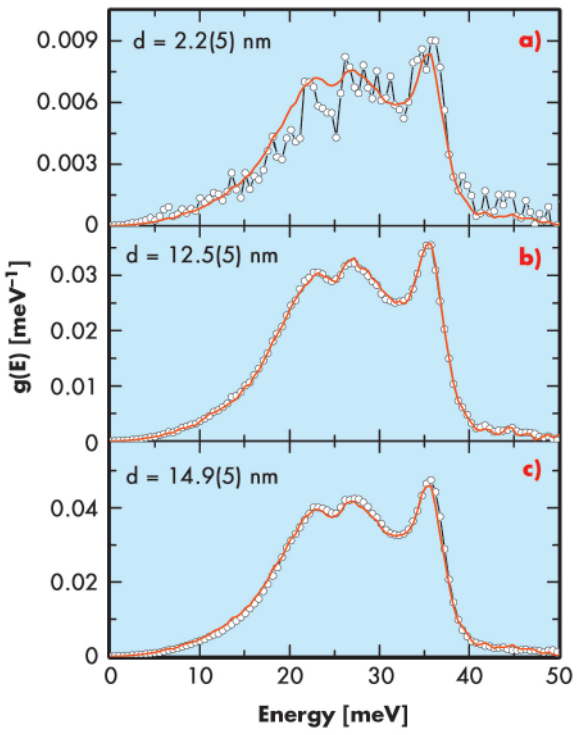


*Fig. 13:* The phonon DOS of α-Fe nanograins as a function of their size d.

high energies is suppressed significantly and characteristic peaks for the bulk Fe are observed. This suggests that in such thin interfaces (about 2 atomic layers thick) the atoms follow the vibrations of the neighbouring nanograins.

In summary, the anomalous dynamics of the bulk nanocrystalline materials originate from the disordered interfaces, while the phonon DOS of the nanograins is close to that of the bulk counterparts and size independent. The low-energy enhancement of the phonon states scales linearly to the atomic fraction of the interfaces and perfectly obeys the Debye law, thus excluding the presence of low dimensional effects. The deviation of the thermo-elastic properties (vibrational entropy, mean-square displacement, average force constants, specific heat) from the corresponding bulk values also follows a similar linear dependence.

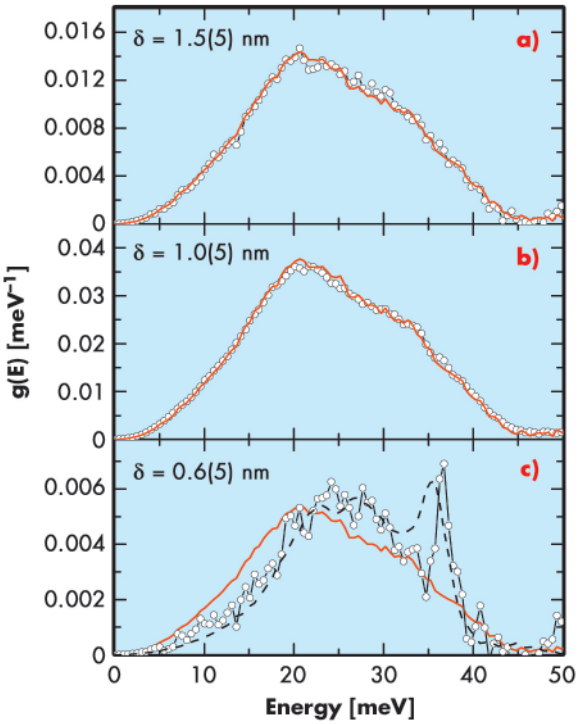


*Fig. 14:* The phonon DOS of α-Fe nanograin interfaces as a function of their thickness δ.

# Exploring the dynamic platinum structure during CO oxidation

The oxidation of carbon monoxide is one of the most intensively studied reactions in the field of catalysis because of its role in the purification of feed gas for fuel cells and automotive exhaust gas. Knowledge of the structure of the catalytically-active sites in these solid catalysts is essential to understand the functioning of solid catalysts and chemical processes. Despite the large effort in research in this field, fundamental questions about the active species and reaction mechanism remain disputed. Ertl and co-workers showed that on single crystals under low-pressure conditions, varying reconstruction of the platinum surface, which occurs after adsorption of carbon monoxide, leads to carbon monoxide-rich and oxygen-rich domains that have different reaction rates [1]. High-pressure experiments on single crystals however, suggested that oxidised platinum is the active phase [2]. In the work presented here, we have bridged both the pressure and materials gaps by determining the structure of a supported platinum catalyst during oxidation of carbon monoxide under real conditions. Bridging the pressure and materials gaps is essential to translate results from single crystal studies and understand catalytic processes under realistic conditions. This was achieved by combining *in situ*, time-resolved, and high-energy resolution fluorescence X-ray spectroscopy (HERFD XAS) [3,4] with kinetic measurements. HERFD yields sharper spectral features because the instrumental energy broadening is below the width due to the core-hole lifetime, which enables detection of considerably more spectral detail. HERFD XAS were collected at beamline **ID26** of ESRF and the time-resolved XAFS data was measured at the super XAS beamline of the Swiss Light Source.

Similar to results on single crystals [2,5], we observed a low- and a high-activity state of the catalyst (**Figure 15**). These two regimes were only observed at ratios of oxygen to carbon monoxide greater than stoichiometric. A sudden increase in activity to the high-activity regime was observed during heating. This so-called ignition occurred at lower temperature with increasing oxygen concentration. The HERFD spectra, which were obtained every two minutes, showed large

**Principal publication and authors**

J. Singh (a), E.M.C. Alayon (a), M. Tromp (b), O.V. Safonova (c), P. Glatzel (d), M. Nachtegaal (e), R. Frahm (f), J.A. van Bokhoven (a), *Angew. Chem. Int. Ed.* **47**, 9260 (2008).

(a) *Institute of Chemical and Bioengineering, ETH Zürich (Switzerland)*
*(b) School of Chemistry, University of Southampton (UK)*
*(c) Swiss Norwegian Beamlines (SNBL), ESRF, Grenoble (France)*
*(d) ESRF*
*(e) Paul Scherrer Institute, PSI, Villigen (Switzerland)*
*(f) Fachbereich C / Physik, University of Wuppertal (Germany)*

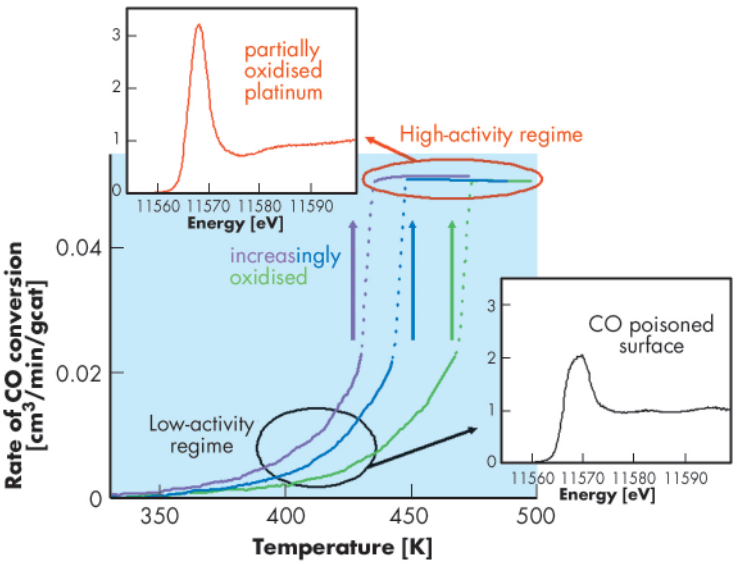


*Fig. 15:* Rate of oxidation of carbon monoxide over 2 wt% $Pt/Al_2O_3$ during heating (5 K/min) at oxygen to carbon monoxide ratios of 1 (green), 2 (blue), and 5 (pink). Pt $L_3$ edge HERFD XANES are shown in the low- and the high-activity regime.

changes between spectra taken below and above the ignition temperature. Below ignition, a whiteline of low intensity with a double feature was observed, which is characteristic of platinum particles with adsorbed carbon monoxide **[4]**. At temperatures above the ignition temperature, the spectra showed a strong increase in the intensity of the whiteline, while the edge energy shifted to lower energy. These features are characteristic of oxidised platinum **[4]**. The amount of oxidised platinum varied with conversion; at higher conversions, higher amounts of oxide were observed. This suggests that the high-activity regime is characterised by the presence of oxidic platinum, which is most likely present on the surface.

During the ignition, the spectra recorded with a time resolution of 0.5 seconds, using quick XANES measurements, showed increasing amounts of platinum oxide, which autocatalytically increased the conversion. This suggests that it is the formation of platinum oxide that enhances the catalytic rate. In contrast to single crystals under low pressures, which are covered by chemisorbed oxygen, nano-sized particles undergo oxidation.

This work showed that the catalyst is in a different structure in the low- and the high-activity regime: adsorbed carbon monoxide on platinum in the low-activity regime, that poisons the surface, and partially oxidic platinum in the high-activity regime as observed with *in situ* HERFD XAS and time-resolved XAFS. The rate-limiting step in the low-activity regime is desorption of carbon monoxide from the surface and subsequent dissociative adsorption of oxygen. In the high-activity regime, the catalyst surface is oxidised, because of low concentration of carbon monoxide at the catalyst surface. This surface shows a high rate of reaction. High temperature and a high oxygen concentration benefit the formation of the more active catalyst. High resolution XAS enabled the determination of the structure of supported nanoparticles in great detail and of loadings as low as 2 wt%. Because hard X-rays are involved in this experiment, structural information was obtained of the catalyst under real working conditions.

**References**
[1] G. Ertl, P.R. Norton, J. Ruestig, *Phys. Rev. Lett.* **49**, 177 (1982); G. Ertl, *Surf. Sci.*, **287-288**, 1 (1993).
[2] M.D. Ackermann *et al.*, *Phys. Rev. Lett.* **95**, 255505 (2005).
[3] P. Glatzel, U. Bergmann, *Coord. Chem. Rev.* **249**, 65 (2005).
[4] O.V. Safonova, M. Tromp, J.A. van Bokhoven, F.M.F. de Groot, J. Evans, P.Glatzel, *J. Phys. Chem. B* **110**, 16162 (2006).
[5] X. Su, P.S. Cremer, Y.R. Shen, G.A. Somorjai, *J. Am. Chem. Soc.* **119**, 3994 (1997).

**Principal publication and authors**
B. Kimmerle (a), J.-D. Grunwaldt (a,b), A. Baiker (a), P. Glatzel (c), P. Boye (d), S. Stephan (d) and C.G. Schroer (d), *J. Phys. Chem. C*, DOI:10.1021/jp810319v (2009).
*(a) Institute for Chemical and Bioengineering, Department of Chemistry and Applied Biosciences, ETH Zürich (Switzerland)*
*(b) Department of Chemical and Biochemical Engineering, Technical University of Denmark (Denmark)*
*(c) ESRF*
*(d) Institute of Structural Physics, TU Dresden (Germany)*

# Visualising the ignition of catalytic partial oxidation of methane

Catalytic reactions are present in many chemical processes. More than 90% of all chemical products have undergone at least one catalytic step. The development of new catalysts has often been triggered by the development of new techniques. Especially important is energy-related catalysis, to make catalysts more efficient and more stable and to substitute fossil fuels *e.g.* by biomass-related processes. One important reaction is the catalytic partial oxidation (CPO) of methane for the production of synthesis gas, which is catalysed by noble metals such as Pt, Rh and Ir. It can be regarded a key step in transformation of natural gas or biomass into liquid fuels such as methanol and higher alkanes **[1,2]**. Changes in chemical reactions like the CPO with time and/or in space are

often correlated to a change in state and structure of the catalyst [3]. To gain deeper insight, it is desirable to follow such structural changes in a spatiotemporal manner.

We studied the ignition of the catalytic partial oxidation of methane on a Pt-Rh/$Al_2O_3$ catalyst by spatially and time-resolved imaging of a catalytic reactor using a FReLoN (fast readout low noise) camera behind the microreactor [4]. The setup is shown in **Figure 16**.

The oxidation state of the noble metals is strongly dependent on the reaction conditions. Below the ignition temperature of the reaction towards CO and $H_2$, the catalyst is in an oxidised state, whereas above the ignition temperature, a reduction of the noble metals occurs. This can be followed by X-ray absorption spectroscopy (see *e.g.* ref. [3]). In particular, a strong change in X-ray absorption occurs at the whiteline of platinum (11568 eV). By tuning the energy of the incident X-rays to the maximum of the whiteline, a variation in X-ray absorption can uncover where the platinum constituent is reduced. In fact, by collecting X-ray transmission images of the microreactor with a frame rate of $4s^{-1}$, a strong structural change in X-ray absorption, and thus the structure of the catalyst, could be found during the ignition of the CPO of methane. Selected images at times $t_1$ (Pt is still in an oxidised state over the whole catalyst bed) and $t > t_1$ are depicted in **Figure 17**. Reddish and violet colours indicate a lower X-ray absorption and thus reduced Pt-species.

**Images 2a) to 2e)** were obtained by subtraction of the X-ray absorption image at time t from **Figure 17f)** below the ignition, which emphasises the difference in absorption and corrects for inhomogeneities in the sample. The full series taken of the ignition process was compiled into a movie and we observed that the front of reduced platinum species moves from the outlet towards the inlet of the reactor. The observed reduction of the noble metal occurred at the same time as the chemical reaction ignited (detected by on-line mass spectrometry). Note that the ignition starts at some specific single particles in the catalytic reactor (compare **Figures 17b** and **17c**).

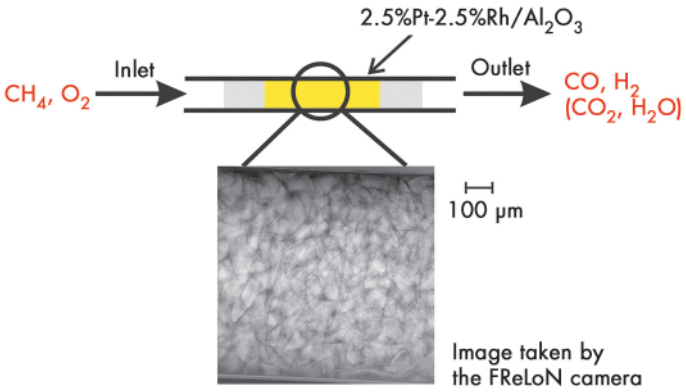


*Fig. 16:* Schematic figure of the catalytic microreactor for partial oxidation of methane to CO and $H_2$ on a 2.5wt%Pt-2.5wt%Rh/$Al_2O_3$ catalyst; a 1 mm x 1 mm snapshot taken with the FReLoN camera is depicted below.

The movement of the front from the outlet towards the inlet can be explained with a total oxidation - reforming mechanism. Below the ignition temperature methane is fully combusted to carbon dioxide and water over the whole length of the catalyst bed. Upon heating the reaction self-accelerates on some of the catalyst grains until all oxygen is consumed and then some new metallic species are formed. These new species promote the activation of methane and thus lead to the formation of hydrogen and carbon monoxide. Furthermore, the methane oxidation accelerates and the reduction propagates towards the inlet of the reactor, where the total oxidation of methane still occurs over oxidised noble metal particles.

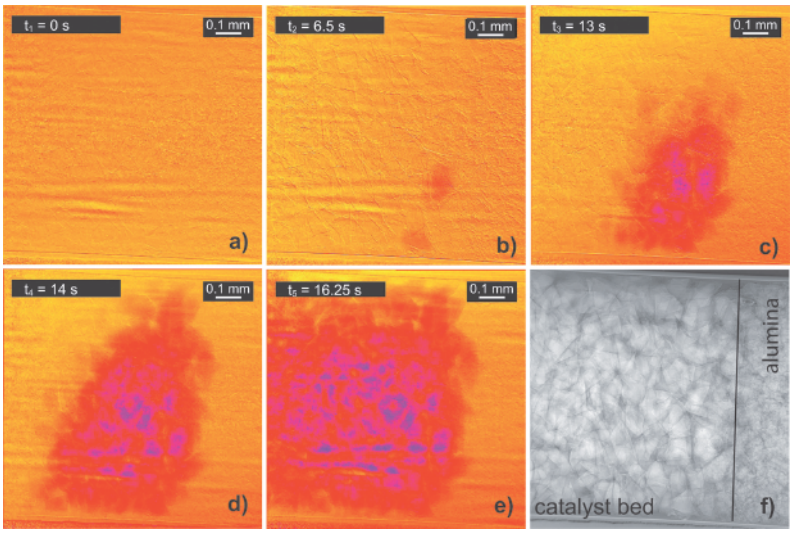


*Fig. 17:* **a)** to **e)**: Images recorded at the whiteline energy of Pt (Pt $L_3$-edge; 11586 eV) as a function of time with flow conditions as depicted in Figure 16: reddish colour indicates the formation of reduced Pt-species; **f)** X-ray absorption image recorded below the CPO ignition temperature, showing that the images were taken at the end of the catalyst bed composed of Pt-Rh/$Al_2O_3$ on the left and only inert alumina material on the right.

In conclusion, by using high resolution transmission X-ray imaging we could determine the structure of a catalyst not only *in situ* but also in a spatiotemporally resolved manner. Thereby, important insight into the first stages of the ignition reaction could be gained. This allows an understanding of the ignition/extinction of catalytic reactions, reaction mechanisms and also chemical oscillations in more detail.

**References**
[1] D.A. Hickman, and L.D. Schmidt, *Science* **259**, 343 (1993).
[2] J.-D. Grunwaldt, L. Basini, B.S. Clausen, *J. Catal.* **200**, 321 (2001).
[3] J.-D. Grunwaldt, S. Hannemann, C.G.Schroer, A. Baiker, *J. Phys. Chem. B* **110**, 8674 (2006).
[4] J.-D. Grunwaldt, B. Kimmerle, A. Baiker, P. Boye, C.G. Schroer, P. Glatzel, C. Borca, F. Beckmann, *Catal. Today*, on-line, doi: 10.1016/j.cattod.2008.11.002.

# Nuclear resonant spectroscopy on $^{121}$Sb and $^{125}$Te

**Principal publication and authors**
H.-C. Wille (a,b), R. P. Hermann (c,d), I. Sergueev (b), O. Leupold (a), P. van der Linden (b), B.C. Sales (e), F. Grandjean (d), G.J. Long (f), R. Rüffer (b), and Yu.V. Shvyd'ko (g), *Phys. Rev. B* **76**, 140301(R) (2007); H.-C. Wille *et al.*, *Phys. Rev. B* (submitted).
*(a) Hamburger Synchrotronstrahlungslabor (Germany)*
*(b) ESRF*
*(c) Institut für Festkörperforschung, Forschungszentrum Jülich (Germany)*
*(d) Department of Physics B5, Université de Liège (Belgium)*
*(e) Solid State Division, Oak Ridge National Laboratory (USA)*
*(f) Department of Chemistry, University of Missouri-Rolla (USA)*
*(g) Advanced Photon Source, Argonne National Laboratory, Illinois (USA)*

Nuclear forward (NFS) and nuclear inelastic scattering (NIS) have developed rapidly during the last ten years and have been expanded to many isotopes beyond $^{57}$Fe. NIS is a powerful tool for the study of lattice dynamics. It complements other techniques like inelastic neutron scattering: the vibrational density of states (VDOS) can be derived directly from the measured inelastic spectrum and the technique is element specific. However, only materials comprising a Mössbauer isotope can be studied. Fortunately, many interesting materials with Mössbauer isotopes are *en vogue*, with even some materials consisting only of 'Mössbauer elements'.

High-resolution monochromators are essential for the NIS technique. To resolve phonon spectra, the monochromator has to filter out a meV spectral bandwidth from the broad X-ray spectrum of synchrotron radiation. For X-ray energies lower than 30 keV, multi-bounce high-resolution monochromators based on silicon crystals have been developed very successfully, but above 30 keV their implementation can only be achieved with a major loss in reflectivity **[1]**. Our studies on $^{121}$Sb and $^{125}$Te became possible by utilising a sapphire Bragg backscattering high resolution monochromator, an alternative to silicon, and more efficient in the range from 30 keV to 60 keV, because sapphire offers sufficient angular acceptance, (sub-)meV resolution and high reflectivity **[2]**. Sapphire also provides a large choice of Bragg back-reflections, matching the fixed nuclear transition energies at certain temperatures. The $^{121}$Sb resonance at 37.1298 keV could be studied with the (15 13 -28 14) reflection at a sapphire temperature $T_0$ = 146.54 K and the $^{125}$Te resonance at 35.4931 keV could be studied with the (20 6 -26 2) reflection at $T_0$ = 206.22 K. Because the energy varies by ~100 meV per K, a temperature stabilisation in the mK regime is used. The Bragg angle is kept constant at 89.9 degrees and the energy of the reflected photons is changed by a controlled change of the crystal temperature.

An interesting compound built from 'Mössbauer elements' is the $EuFe_4Sb_{12}$ skutterudite, a thermoelectric and ferromagnetic material, where our recent NIS studies on Sb have completed the full element specific VDOS study of all three constituents. **Figure 18** shows the VDOS of Sb in

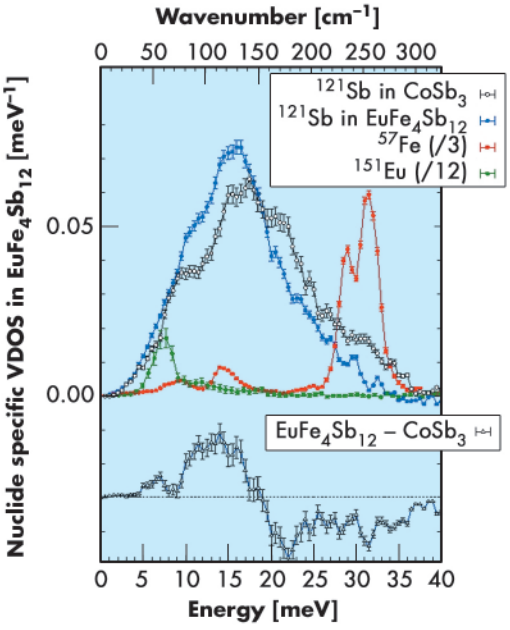


*Fig. 18:* The element specific vibrational density of states (VDOS) of Sb, Eu and Fe (weighted by elemental content per formula unit) in $EuFe_4Sb_{12}$ and of Sb in $CoSb_3$. The difference of the Sb VDOS in the filled and unfilled skutterudites has a maximum at the local mode of the rattler (Eu), which indicates rattler-cage hybridisation.

$EuFe_4Sb_{12}$ and $CoSb_3$ and the VDOS of Eu and Fe in $EuFe_4Sb_{12}$. For comparison the difference in the Sb VDOS is shown. The peak in the difference at the same energy as the peak in the Eu VDOS gives evidence for a coupling of the cage (Sb) and the rattler (Eu) in skutterudites. This hybridisation is needed to obtain a low thermal conductivity, which in combination with a high electric conductivity and a large Seebeck coefficient results in a large thermoelectric figure of merit.

Other examples of pure 'Mössbauer' compounds are phase change materials used in rewritable optical data storage that have the formula $Ge_xSb_yTe_z$. In a first experiment, shown here, we demonstrated the applicability of NFS and NIS on the $^{125}$Te isotope, using the sapphire monochromator. **Figure 19a** shows the NFS time spectrum of $^{125}$Te metal. The $^{125}$Te transition has only 1.48 ns half-life, which makes this transition the nuclear transition with the shortest lifetime ever studied by NFS and NIS. Fast detector electronics allowed counting to start only 2 ns after the exciting synchrotron radiation bunch, considerably earlier than for standard NFS timing experiments. The extracted quadrupole splitting in Te metal is 7.85 mm/s in good agreement with 7.77 mm/s obtained by classical Mössbauer spectroscopy, corresponding to 2.97 times the natural linewidth $\Gamma_0 = 0.313$ μeV. The possibility for carrying out NIS measurement was demonstrated with a sample of $Sb_2{}^{125}Te_3$. The count rate of forward (NFS) and inelastic (NIS) scattering with respect to the incoming photon energy is shown in **Figure 19b**. The NFS signal represents the instrumental resolution of the HRM, 2.6 meV. The NIS signal yields the phonon spectrum of the material. The experiments were carried out at the beamline **ID22N**.

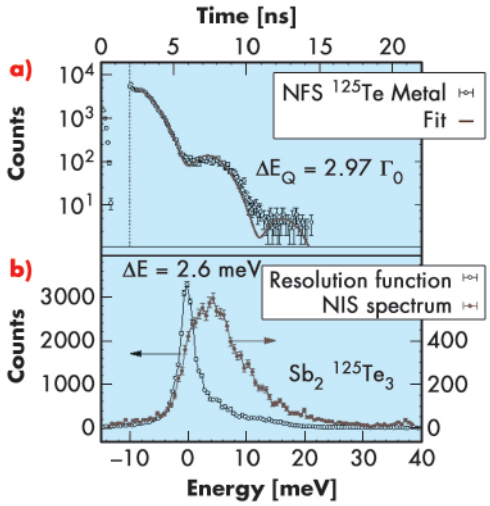


*Fig. 19:* **a)** the NFS time spectrum of Te metal (black) and the theoretical curve (brown); **b)** the NFS (black) and NIS (brown) energy spectra of $Sb_2Te_3$. The instrumental function (NFS) shows a resolution of 2.6 meV.

**References**

[1] S. Tsutsui, Y. Yoda and H. Kobayashi, *J. Phys. Soc. Jpn.* **76**, 065003 (2007).

[2] Yu.V. Shvyd'ko and E. Gerdau, *Hyp. Int.* **123/124**, 741 (1999).

## 3D-imaging of the Fermi surface by thermal diffuse scattering

The Fermi surface is one of the most important theoretical concepts in solid state physics. It is the surface in electron momentum space of a metal that separates occupied and empty electronic states. Indeed, the shape of the Fermi surface controls the electric, magnetic and thermal properties of materials. The most commonly used experimental techniques for the determination of the Fermi surface are the oscillation of transport properties in a magnetic field (*i.e.* the de Haas-van Alphen effect and the Shubnikov-de Haas effect) and angle-resolved photoemission spectroscopy (ARPES). Two-photon positron annihilation and Compton scattering are more indirect methods of probing the nature of the Fermi surface.

Interestingly, one of the earliest techniques proposed to study the Fermi surface was to look for the abrupt variations in the dispersions of phonons **[1]**. These so-called Kohn anomalies arise from changes in the charge screening by the conduction electrons when the phonon wave vector $q$ exceeds the spanning across the Fermi surface $k = 2k_F$. Here, we exploit the fact that the phonon dispersions of a material give rise to thermal diffuse scattering (TDS) of X-rays that reflect the dispersion anomalies in characteristic intensity variations of the TDS. Using only a standard X-ray diffraction set-up and an area detector, we show that portions of the zinc Fermi surface can be visualised in three dimensions.

**Principal publication and authors**

A. Bosak (a), M. Hoesch (a), M. Krisch (a), D. Chernyshov (b), P. Pattison (b), B. Winkler (c), V. Milman (d), K. Refson (e), D. Farber (f,g), D. Antonangeli (h), submitted to *Phys. Rev. B.*

*(a) ESRF*

*(b) Swiss-Norvegian Beam Lines, Grenoble (France)*

*(c) Geowissenschaften, Goethe-Universität, Frankfurt a.M. (Germany)*

*(d) Accelrys, Cambridge (UK)*

*(e) Rutherford-Appleton Laboratory, Chilton, Oxfordshire (UK)*

*(f) Lawrence Livermore National Laboratory, Livermore (USA)*

*(g) University of California, Santa Cruz (USA)*

*(h) Institut de Minéralogie et de Physique des Milieux Condensés, UMR CNRS 7590, Institut de Physique du Globe de Paris, Université Paris 6 et 7 (France)*

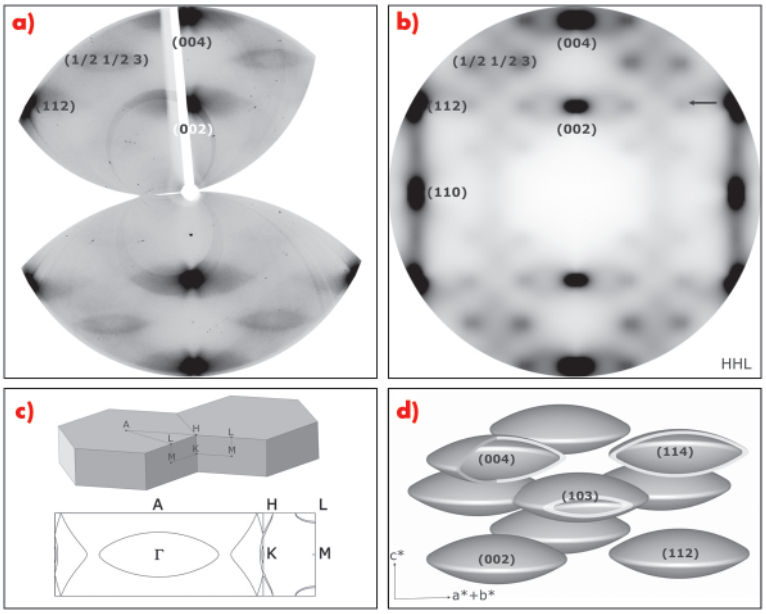


*Fig. 20:* **a)** (HHL) plane reconstruction of the experimental X-ray scattering data; **b)** model TDS pattern derived from *ab initio* phonon calculations (CASTEP); **c)** zinc Brillouin zone and (HHL) Fermi surface section as obtained from *ab initio* electron band structure calculations (Wien2k); **d)** scheme of the assembly of lens-like Kohn surfaces centred around strong Bragg spots and their dissection by HHL planes. Experimental features not obeying the symmetry operations are experimental artifacts due to the non-linear image plate response and diffraction from the nickel filter.

The experiment was performed on the Swiss-Norwegian Beam Lines (SNBL) **BM01** in transmission geometry at λ = 0.722 Å using a MAR345 image plate. A high-quality, 30-µm-thick, zinc single crystal (MaTecK GmbH) was mounted on a rotation stage with its <110> direction a few degrees off the rotation axis. Diffuse scattering patterns were recorded with an increment of 1° over an angular range of +/- 60°. A 15-µm-thick nickel foil was used to reduce the fluorescence signal from zinc. Three-dimensional maps were reconstructed, using the CrysAlis software (Oxford Diffraction). **Figure 20a** shows the reconstructed diffuse scattering in the HHL plane. Two types of lens-like objects of different size are clearly visible. Larger lenses, *i.e.* centred around (0 0 2*n*) Bragg spots have the strongest intensity in the centre, whereas the smaller lens-like objects, *i.e.* centred around (1/2 1/2 3) appear hollow. We assign features in the intensity variation maps of the TDS to Kohn anomalies and thus to portions of the Fermi surface. To further support our interpretation, we performed *ab initio* calculations of the Fermi surface and the TDS patterns, using the Wien2k [2] and CASTEP [3] algorithms.
As **Figure 20c** reveals, the large lens-like objects correspond to the inner part of the Fermi surface around the Γ point. The shape of the inner part of the Fermi surface makes the corresponding surface of dispersion anomaly locations (Kohn surface) just its homothetic transformation with a scaling factor 2 ($q = 2k_F$). The hollow lens-like objects of smaller size are, in fact, just sections of the large "lenses" (see **Figure 20d**). Additional support is given by the modelling of the TDS intensity (see **Figure 20b**). While the exact shape and sharpness of Kohn anomalies are not reproduced with the CASTEP calculation, the overall resemblance in terms of contrast and intensity distribution is very convincing.

Our proof-of-principle demonstration underlines the great potential of TDS in the study of lattice dynamics and electron-phonon coupling. We have shown that the 3D-shape of the Kohn surface can be reconstructed within the timescale of hours using standard X-ray diffraction equipment. It is important to emphasise that, by using an insertion device synchrotron beamline and energy-selective area detectors, the data quality and data collection efficiency could be further increased by some orders of magnitude.

**References**
[1] W. Kohn, *Phys. Rev. Lett.* **2**, 393 (1959).
[2] P. Blaha, K. Schwarz, G.K.H. Madsen, D. Kvasnicka, J. Luitz, *Wien2k, An Augmented Plane Wave + Local Orbitals Program for Calculating Crystal Properties* (Karlheinz Schwarz, Techn. Universität Wien, Austria), 2001.
[3] S.J. Clark, M.D. Segall, C.J. Pickard, *et al., Zeitschrift für Kristallographie* **220**, 567 (2005).

# Materials Science

## Introduction

The properties of materials depend on the way the constituent atoms combine with each other, for example to form molecules, the aggregation of molecules and atoms into crystalline or disordered solids, liquids or glasses, and the microstructural arrangement of the grains of a material to make up the bulk. Synchrotron X-ray radiation provides some of the most powerful tools to study these structures and thereby gain an understanding of why materials behave as they do, and how properties can be tailored and improved for specific applications. Many experiments at the ESRF and CRG beamlines fall into the broad category of materials science, exploiting the techniques of diffraction, scattering or imaging. Choosing just a few examples from such a broad expanse of work is difficult. The accounts presented in this chapter are only the very tip of the iceberg as far as materials research at the ESRF is concerned.

Synchrotron radiation can be used to study the evolution of structure in systems. The first example involves the dissociation of an organometallic molecule induced by a flash of laser light, where the various dissociation products are identified, and the pathways by which these revert to the starting structure are followed on the timescale of nanoseconds, thus enabling fundamental chemical processes of bond breaking and making to be studied in detail. On a more human timescale, experiments have revealed the recrystallisation and growth of nanoparticles of palladium on exposure to hydrogen gas, with implications perhaps for future solid hydrogen-storage systems, and of grain growth in an aluminium-based alloy on annealing. The mechanical properties of polymers depend intimately on the conditions of temperature and flow under which they are formed and processed. *In situ* studies of the crystallisation of high-density polyethylene give new insights into how morphology and structure can be linked to the thermo-mechanical history of the sample.

The interactions between liquids and surfaces can have profound effects on the properties of a system: everyone knows that wet sand makes a better sandcastle, and understanding how is of great importance for more serious issues concerning landslides, or for the processing of powdered substances in the food and pharmaceutical industries. Micro-tomographic imaging was used to visualise the intricate networks of liquid that form between small glass spheres (a model system) with different liquid contents. In another study, high energy X-ray reflectivity probed the interaction between a sapphire surface and liquids composed of bulky charged ions (so called ionic liquids, with potential applications including solvents for advanced chemical syntheses), revealing the extent to which the ions order or disorder with varying chemical composition and temperature.

The chemical elements, which might be expected to be the simplest of systems, continue to surprise at temperatures or pressures away from those of everyday life. Thus seven distinct phases for sodium were discovered within a narrow pressure and temperature range close to 118 GPa, some of extraordinary structural complexity. Sulphur at low temperatures and high pressures is found to undergo a number of structural changes, including a change from a high density to low-density amorphous phase, or at higher pressures to an incommensurately modulated structure via a charge density wave instability. For iron at high temperatures and pressures, X-ray emission spectroscopy, a local probe of the 3*d*

spin magnetic moment, demonstrates the collapse of the short-range magnetic state under these conditions.

The final examples in the chapter involve crystal structure analysis via high-resolution-powder or single-crystal techniques, giving insight into the electronic behaviour and superconductivity in hole-doped $Nd_{1-x}Sr_xFeAsO$; the solution of the crystal structure of novel organometallic complexes of copper with peptides, which reveals a pleasing network of hydrogen bonds; and metal-organic framework materials containing rare-earth ions that combine high thermal stability and other multifunctional properties (magnetism, luminescence, microporosity, hydrophobicity). The combination of a luminescent $Ln^{3+}$ centre and the chosen ligands results in materials that can sense ethanol in air even in the presence of water.

Preparations are underway for the experiments that will yield the articles of future editions of the ESRF highlights. Ideas and plans for improved experimental approaches are always being sought, and, with the start of the ESRF Upgrade Programme, two beamlines relevant to this chapter are under consideration. The first is for high-energy diffraction using a microfocussed beam for penetrating through or into samples with high spatial resolution, and the second is a fully-dedicated beamline for pump-probe time-resolved diffraction. These would each greatly enhance the ESRF's capabilities in these exciting areas.

***A. Fitch***

---

**Principal publication and authors**
Q. Kong (b), J.H. Lee (a), A. Plech (c), M. Wulff (b), H. Ihee (a), M.H.J. Koch (d), *Angew. Chem. Int. Ed.* **47**, 5550 (2008).
*(a) Center for Time-Resolved Diffraction, Department of Chemistry, KAIST, Daejeon (Republic of Korea)*
*(b) ESRF*
*(c) Fachbereich Physik der Universität Konstanz (Germany)*
*(d) EMBL, Hamburg Outstation (Germany)*

# Ultrafast X-ray solution scattering reveals a new reaction intermediate in the photolysis of $Ru_3(CO)_{12}$

The triangular metal carbonyl cluster $Ru_3(CO)_{12}$ is one of the simplest thermally-stable metal carbonyls. The complex is used in controlled photoactivated synthesis where specific bonds in the complex are broken upon irradiation at different wavelengths. As the mechanism leading to the cleavage of metal-metal bonds is of great theoretical and practical interest, the photolysis of $Ru_3(CO)_{12}$ has been extensively studied by spectroscopy in solid matrices and in solution. Structural characterisation of the intermediates has, however, been very difficult. Recent ultrafast infrared spectroscopy measurements have shown that when solutions of $Ru_3(CO)_{12}$ in non-coordinating solvents like cyclohexane are excited with either an ultraviolet (266 nm) or a visible (400 nm) optical pulse, competing reactions yield two transient intermediates containing bridging carbonyls, $Ru_3(CO)_{11}(\mu\text{-CO})$ (Intermediate 1) for the metal-metal cleavage reaction channel and $Ru_3(CO)_{10}(\mu\text{-CO})$ (Intermediate 2) for the CO loss reaction channel, respectively [1]. Infrared spectroscopy specifically monitors the time course of the concentration of these two intermediates via the characteristic absorption bands of their bridging carbonyls. This leaves the possibility that other intermediates could go unnoticed, especially those containing only terminal carbonyls with absorption bands overlapping those of the parent molecule.

In contrast to infrared spectroscopy, the signal from time-resolved X-ray or electron scattering contains contributions from all interatomic distances in the volume probed by the incident beam. In principle, this makes it possible to detect all transient intermediates [2]. Except for the simplest cases, however, there is no unique solution to recover the three-dimensional structural information

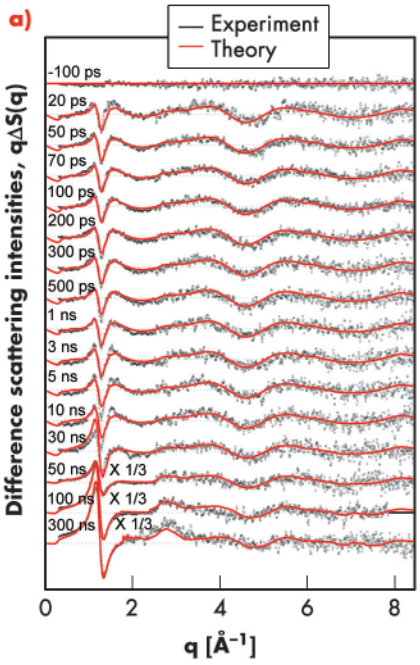


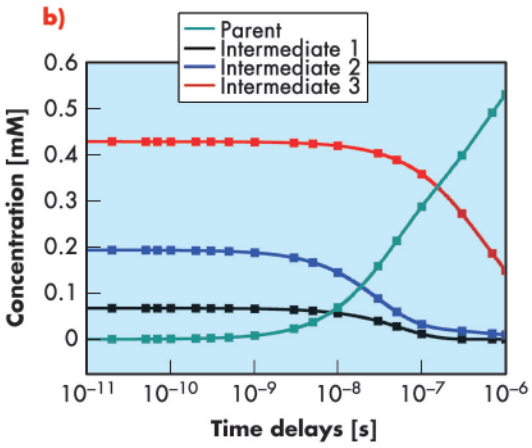


*Fig. 21:* **a)** Time-resolved difference scattering intensities $q\Delta S(q,t)$ as a function of time delays after photolysis of $Ru_3(CO)_{12}$ in cyclohexane. The black dots correspond to the experimental data and the red curves to the theoretical least-squares fits. **b)** Concentration changes of the relevant chemical species during the photoreaction as a function of time.

from scattering data and this inverse problem can only be solved by modelling based on theoretical calculations. This approach was used to study the photodissociation of $Ru_3(CO)_{12}$ dissolved in cyclohexane in a pump-probe experiment performed on beamline **ID09B**. Visible (390 nm) laser pulses (2 ps) were used for excitation and 100 picosecond X-ray pulses for probing the transient intermediates. In these experiments the sample flows through a nozzle which produces a thin layer of liquid. The pump-probe sequence is repeated with different time delays between pump and probe at a frequency of 986.3 Hz and the scattered signal is accumulated on a MarCCD detector. The difference X-ray scattering intensities ($q\Delta S(q,t)$) illustrating the structural changes due to the laser excitation are shown in **Figure 21a** as a function of different time delays.

Initial attempts at fitting the curves with only the known intermediates 1 and 2 failed to give satisfactory results and suggested the presence of a third intermediate. By modelling the measured difference scattering intensities $\Delta S(q,t)$ using the structures of 16 putative intermediates calculated by density functional theory (DFT), modelled in solution with molecular dynamics (MD) simulations, the concentration of each of the intermediates could be determined (**Figure 21b**). The results show that

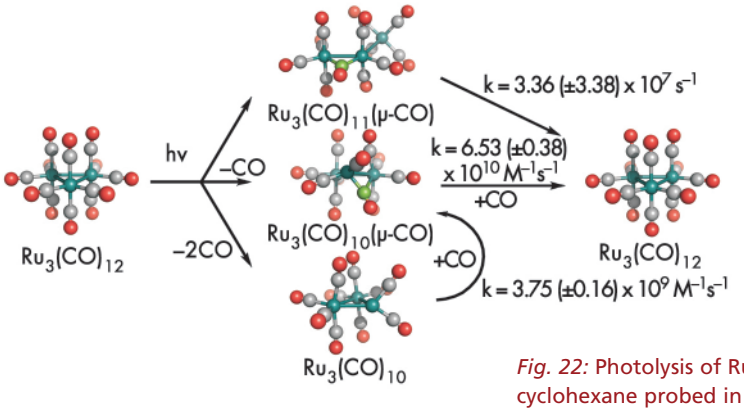


*Fig. 22:* Photolysis of $Ru_3(CO)_{12}$ in cyclohexane probed in solution by time-resolved X-ray scattering. Beside the two known intermediates, $Ru_3(CO)_{11}(\mu\text{-CO})$ and $Ru_3(CO)_{10}(\mu\text{-CO})$, the hitherto undetected major intermediate $Ru_3(CO)_{10}$ was found.

three intermediates, $Ru_3(CO)_{11}(\mu\text{-CO})$, $Ru_3(CO)_{10}(\mu\text{-CO})$ with bridged CO and $Ru_3(CO)_{10}$ with terminal CO only, are formed at the onset of the reaction from the initial molecule $Ru_3(CO)_{12}$, indicating the rupture of Ru-C and Ru-Ru bonds in $Ru_3(CO)_{12}$ by the optical excitation. The new intermediate $Ru_3(CO)_{10}$ with only terminal CO dominates at all time delays. It recombines non-geminately with one CO ligand to $Ru_3(CO)_{10}(\mu\text{-CO})$ which eventually decays into the starting molecule $Ru_3(CO)_{12}$ by non-geminate recombination with another CO. $Ru_3(CO)_{11}(\mu\text{-CO})$ relaxes rapidly to the parent molecule $Ru_3(CO)_{12}$ through geminate recombination.

These results strikingly illustrate the complementary nature of ultrafast X-ray scattering and ultrafast spectroscopy. Indeed, a good fit to the experimental X-ray scattering data could only be obtained if intermediate 3, which does not contain any bridging

**References**
[1] E.A. Glascoe, M.F. Kling, J.E. Shanoski and C.B. Harris, *Organomet.* **25**, 775 (2006).
[2] Q.Y. Kong, M. Wulff, J.H. Lee, S. Bratos and H. Ihee, *J. Am. Chem. Soc.* **129**, 13584 (2007).

carbonyl and is thus invisible in infrared spectroscopy, is included in the refinement. It would have been very difficult using X-ray scattering alone to establish the existence of the minor intermediate $Ru_3(CO)_{11}(\mu\text{-}CO)$ because its contribution to the overall scattering curve is much smaller than that of $Ru_3(CO)_{10}$. As its existence has been unequivocally established by spectroscopy it is entirely justified to include it in the fit to the X-ray data. Together these techniques clearly indicate the existence of at least three intermediates with very different molecular structures (**Figure 22**).

**Principal publication and authors**
M. Di Vece (a), D. Grandjean (a), M.J. Van Bael (a), C.P. Romero (a), X. Wang (a), S. Decoster (b), A. Vantomme (b) and P. Lievens (a), *Phys. Rev. Lett.* **100**, 236105 (2008).
*(a) Laboratorium voor Vaste-Stoffysica en Magnetisme & INPAC - Institute for Nanoscale Physics and Chemistry, K.U. Leuven (Belgium)*
*(b) Instituut voor Kern- en Stralingsfysica & INPAC - Institute for Nanoscale Physics and Chemistry, K.U. Leuven (Belgium)*

# Hydrogen-induced Ostwald ripening

The main aim in hydrogen storage research is to obtain high hydrogen concentrations in a material that possesses suitable transport properties under ambient conditions. A promising way to favourably alter the material's properties is by reducing its size to the extent that surface and quantum effects begin to play a major role. The investigation of nanocluster metal hydrides may therefore reveal novel properties. Palladium is one of the most widely studied metals with respect to hydrogen absorption. At elevated temperatures palladium nanoclusters change size due to Ostwald ripening: the larger clusters capture mobile atoms at the expense of smaller clusters **[1]**. As hydrogen in a metal can decrease the strength of the host metal bonding, this raises the question of how an ensemble of palladium nanoclusters will interact during and after hydrogenation. A morphological or structural change of the nanocluster ensemble may affect the hydrogenation properties as compared to a single cluster.

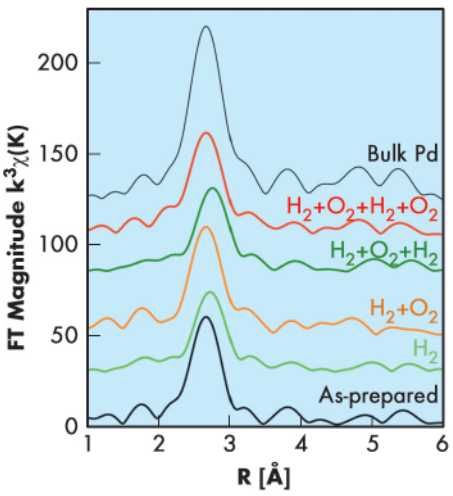


*Fig. 23:* Phase-corrected Fourier transforms of the $k^3$-weighted Pd nanocluster EXAFS as a function of the atomic distance (R).

We investigated the effect of hydrogen exposure on a palladium cluster assembled film produced with a dual-target dual-laser vaporisation source with three different techniques: extended X-ray absorption fine structure (EXAFS), X-ray diffraction (XRD) and scanning-tunnelling microscopy (STM). These three complementary methods were used to determine the size changes of the palladium nanoclusters upon exposure to hydrogen and oxygen. The average grain size was derived both from the coordination number around palladium atoms obtained from EXAFS (**Figure 23**) and the width of the XRD Bragg peaks, whereas the (lateral) diameter of the nanoclusters at the sample surface was measured directly by STM. X-ray absorption data (**Figure 23**) collected at the DUBBLE beamline (**BM26A**) yielded additional parameters such as inter-atomic distances, degree of disorder and electronic information through the shift of the absorption edge; these support the observation of size changes. Upon hydrogenation, the increase in the nanocluster size measured with XRD, EXAFS, and STM is 22%, 38%, and 37%, respectively. This increase is much larger than the increase of about 8.1% in the Pd phase unit cell volume corresponding to the hydride formation. The cluster growth is due to an atomic reorganisation by three-dimensional Ostwald ripening, in which the larger clusters take up mobile atoms at the expense of smaller clusters **[1]**. For most materials, spontaneous Ostwald ripening is an extremely slow process at room temperature. However, the presence of a hydrogen atom in the metal reduces the binding energy, thus increasing the probability of

detachment of palladium atoms as shown schematically in **Figure 24**. This process can be qualitatively understood in terms of the difference between the sublimation energy of palladium metal and palladium hydride. The sublimation energy of palladium decreases with increasing hydrogen concentration and is about 50% lower at a H/Pd ratio of 0.3 **[2]**. The effect of hydrogen on the palladium cluster sublimation has the same result as if the temperature of the clusters was doubled. Since our experiment was performed at room temperature, a doubled temperature would correspond to approximately 600 K (327°C), a temperature at which Ostwald ripening would occur. Thus the observed cluster size increase is attributed to Ostwald ripening induced by exposure to hydrogen: the absorbed hydrogen decreases the sublimation energy of palladium, which stimulates the detachment of atoms from the clusters at room temperature.

To conclude, the morphological and structural changes occurring in an ensemble of palladium nanoclusters have been studied after several hydrogenation cycles with EXAFS, XRD, and STM. Initial hydrogenation increased the cluster size, a result that is attributed to hydrogen-induced Ostwald ripening. This phenomenon originates from the higher mobility of palladium atoms resulting from the low sublimation energy of palladium hydride as compared to that of the palladium metal. The universality of this phenomenon makes it important for the application of future nanostructured hydrogen storage materials.

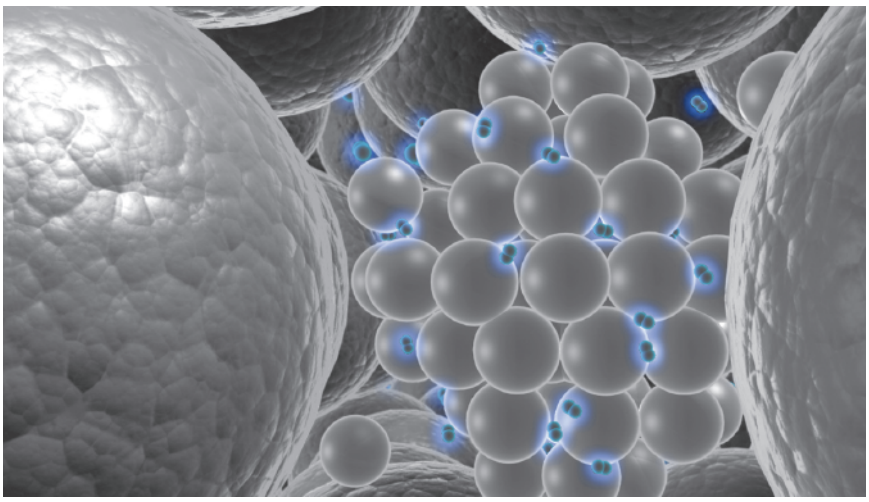

*Fig. 24:* A schematic impression of the palladium cluster building blocks. The palladium atoms become free to move due to the interstitial hydrogen.

**References**
[1] W. Ostwald, *Z. Phys. Chem. (Leipzig)* **34**, 495 (1900).
[2] N.V. Piskunov *et al.*, *J. Eng. Phys. Thermophys.* **74**, 1217 (2001).

## Direct observation of 3D grain growth in Al-0.1%Mn

Metals and alloys are typically polycrystalline and are processed by plastic deformation and annealing. During annealing the so-called grain growth process may occur, whereby some of the grains in the polycrystalline ensemble grow at the expense of others, resulting in a coarsening of the microstructure. This has important implications for the properties of the material; widely known applications are transformer steels and devices for power current based on $T_c$ superconductor compounds. Grain growth has been studied extensively for decades both experimentally - mostly by optical microscopy - and theoretically, leading to the proposition of a range of grain growth models.

Here we present a 3D mapping study of an Al-0.1%Mn alloy using the three-dimensional X-ray diffraction (3DXRD) microscope situated at the material science beamline **ID11**. As a function of the treatments, the average grain volume increases from $2.9 \times 10^5$ μm$^3$ to $4.2 \times 10^6$ μm$^3$ and the number of grains within the illuminated part of the sample reduces from 483 to 32, see **Figure 25**. The volume distribution of the initial grains is shown in **Figure 26a**. Marked in red are the 27 grains that remained after annealing. As expected these are predominantly the larger grains. Notably three grains smaller than the median size were also observed to grow. As illustrated in **Figure 26b** the texture of both the initial and the final distributions are

**Principal publication and authors**
S. Schmidt (a), U.L. Olsen (a), H.F. Poulsen (a), H.O. Sørensen (a), E.M. Lauridsen (a), L. Margulies (a,b), C. Maurice (c) and D. Juul Jensen (a), *Scripta Mater.* **59**, 491 (2008).
*(a) Center for Fundamental Research: Metal Structures in Four Dimensions, Risø National Laboratory at the Technical University of Denmark, Roskilde (Denmark)*
*(b) ESRF*
*(c) Materials centre, Ecole des Mines, Saint Etienne (France)*

close to random. Hence, within the statistics of the study, no apparent correlation is found between orientation and the probability of growth. To our knowledge, for the first time a bulk sample has been completely characterised before and after a set of annealing treatments.

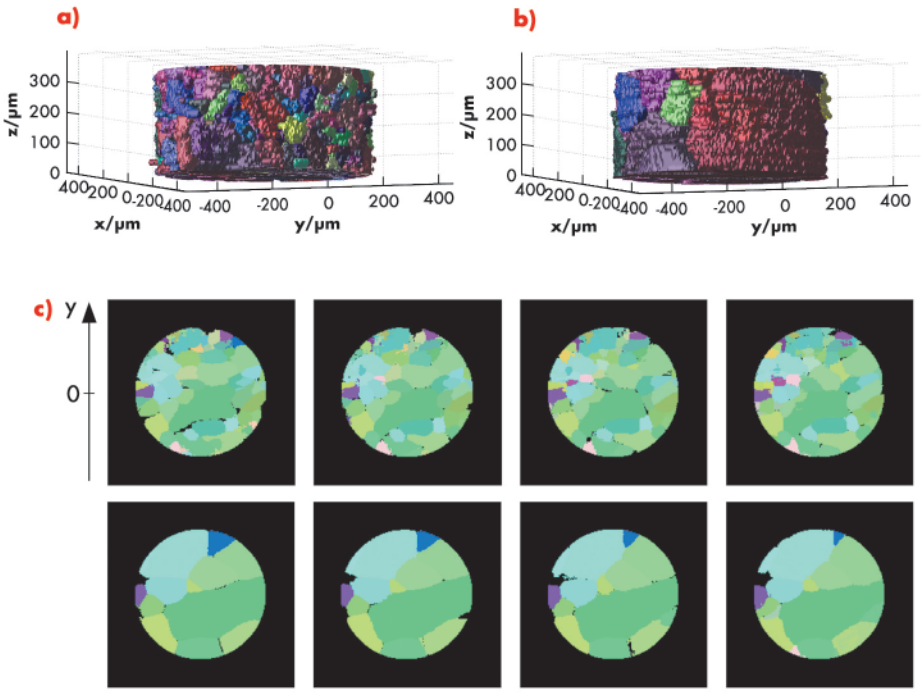


*Fig. 25:* **a)** 3D grain map after first annealing for an Al-0.1%Mn alloy. **b)** the same volume is shown after the final annealing. **c)** the four layers in the middle of the volume are shown after the first annealing, top row, and final annealing, bottom row, respectively. The interlayer spacing is 10 µm. Colours symbolise crystallographic orientation. Black denote vacancies; internal vacancies being an artefact of the program. The pixel size in the maps is 5 µm x 5 µm.

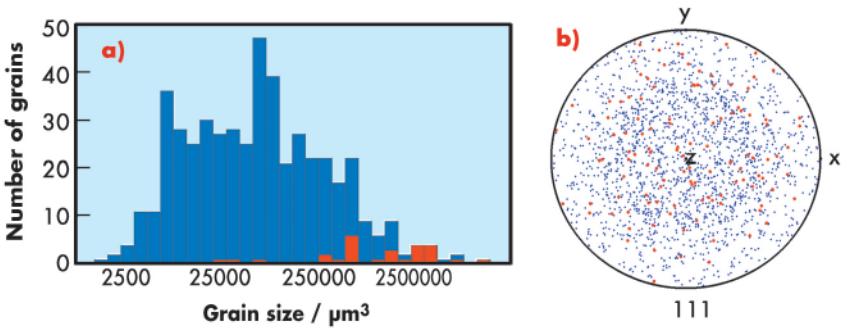


*Fig. 26:* Characteristics of grains. **a)** Grain volume distribution before annealing. Red colour: the sub-set of grains remaining after the annealing; blue colour: all other grains. **b)** (111)-polefigure with respect to sample reference system (x,y,z). Same colour scheme as for a).

**Authors**
L. Balzano (a), G.W.M. Peters (a), S. Rastogi (b), G. Portale (c), L. Fernandez-Ballester (c) and W. Bras (c).
*(a) Eindhoven University of Technology (The Netherlands)*
*(b) Loughborough University (UK)*
*(c) BM26, ESRF*

## Crystallisation and dissolution of flow-induced precursors

Easy processability of polymeric materials is a parameter that is of crucial importance to promote their use in an increasing number of both high-tech as well as commodity applications. Production of polymeric materials often involves shaping the product from the melt by applying flow at high temperatures (thermo-mechanical history). The flow rate and temperature can strongly influence the final properties of the material. For semi-crystalline polymers, the link between this thermo-mechanical history and the properties is reflected in the crystalline structure and morphology.

The crystallisation of these entangled, *i.e.* spaghetti like, macromolecules poses intriguing problems from a fundamental scientific viewpoint but

obviously has implications for applied material technology as well.

It is well established that when a strong flow is applied to a polymer melt, the molecules orient and stretch with the flow. When the temperature is sufficiently low, orientation and stretch of the molecules can be frozen-in with the onset of crystallisation (**Figure 27**). Anisotropic (fibrillar) crystals are formed and, in the next stage, overgrown by disk-like lamellae. This crystalline morphology is called shish-kebab because of the analogy with the Mediterranean meat dish. The origin of this morphology is currently a topic of discussion. It is well accepted that the initial stages of the process are very important and synchrotron scattering techniques, based on SAXS and WAXD, have proven indispensible for these studies. Experiments from our group at the Technische Universiteit Eindhoven, performed at the Dutch Belgian beamline **BM26,** as well as **ID11** and **ID02**, permitted an understanding of the very early stages of shish-kebab formation **[1-4]**. Our findings point to the existence, prior to nucleation, of flow-induced precursors (FIPs) consisting of non-crystalline nano bundles of stretched molecules. The key discovery is that these FIPs can be formed at temperatures higher than the material's melting point and represent the 'memory' that the material has of its thermo-mechanical history. *In situ* observation of FIPs in melts of mixtures of high density polyethylene (HDPE), with different molecular weights, at 142°C, highlighted their fibrillar morphology and their dynamics as a function of the size. Large FIPs can crystallise (become nuclei) and grow into shish-kebabs whereas small FIPs dissolve in the melt. The presence of a critical size for nucleation is in agreement with the classical theory of nucleation. However, the same theory does not consider the formation of non-crystalline (and long lasting) structures prior to nucleation. Our experiments are, therefore, a bridge between the classical theory and new views on (flow induced) nucleation of macromolecules.

The dissolution of small FIPs, for which the development stops in the very early stages, occurs on the same timescale as the diffusion (reptation) of the longest molecules of the melt. This suggests that dissolution of these small FIPs is strongly correlated with the reptation of the longest molecules along the precursor backbone (**Figure 28**), *i.e.* the early FIPs are rich with the longest chains.

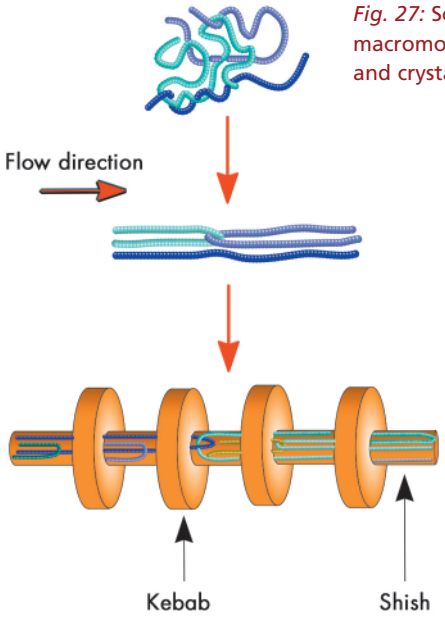


*Fig. 27:* Schematic representation of coiled macromolecules that can be stretched with flow and crystallise into highly-anisotropic shish-kebabs.

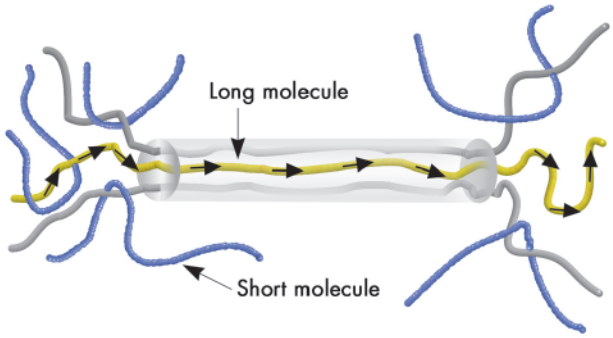


*Fig. 28:* Hypothetical structure of a flow-induced precursors (FIP). This is a bundle made of the longest molecules of the melt that are stretched with the application of flow.

To summarise, in crystallisation of entangled macromolecules like polymers, morphology and structure depend on the whole thermo-mechanical history **[3,4]**. The memory of gradients of flow applied even at high temperatures is stored into FIPs **[2]**. In the very early stages of crystallisation, FIPs can direct the process towards the formation of highly anisotropic crystals with shish-kebab type morphology. The clarification of the basic mechanisms for structure formation during processing of macromolecules helps the exploitation of the properties of existing materials and could lead, eventually, to the benefit of materials with properties tailored to the application.

**References**

[1] L. Balzano, N. Kukalyekar, S. Rastogi, G.W.M. Peters, J.C. Chadwick, *Physical Review Letters* **100**, 048302 (2008).

[2] L. Balzano, *Flow induced crystallization of polyolefins*. PhD thesis, Eindhoven University of Technology (2008).

[3] L. Balzano, S. Rastogi, G.W.M. Peters, *Macromolecules* **41**, 399 (2008).

[4] L. Balzano, G.Portale, S. Rastogi, G.W.M. Peters, *Macromolecules* **41**, 5350 (2008).

**Principal publications and authors**
M. Scheel (a), R. Seemann (a,b), M. Brinkmann (a), M. DiMichiel (c), A. Sheppard (d), B. Breidenbach (e), S. Herminghaus (a), *Nature Materials*, **7**, 189 (2008); *J. Phys.: Cond. Mat.* **20**, 494236 (2008).
*(a) Max Planck Institute for Dynamics and Self-Organization, Göttingen (Germany)*
*(b) Experimental Physics, Saarland University, Saarbrücken (Germany)*
*(c) ESRF*
*(d) Department of Applied Mathematics, Australian National University Canberra (Australia)*
*(e) Theoretical Physics Institute, University Erlangen-Nürnberg, Erlangen (Germany)*

# Morphological clues to wet granular pile stability

When dry sand is mixed with water, it acquires a visco-plastic texture, stiff enough for sculpting sand castles. The well-known experience at the beach that the mechanical properties of this material do not depend critically on the liquid content is of great potential importance for understanding wet granular systems in general, such as encountered in land slides, or in the pharmaceutical or food industry. The insignificance of the water content is particularly unexpected if one considers the enormous geometric complexity of the liquid structures which form inside the granular pile, and change dramatically with the liquid content.

The geometrical structure of the liquid was analysed by means of X-ray microtomography. Owing to the high temporal resolution available at beamline **ID15A**, inherent ageing problems in the samples could be circumvented and high quality data of highly absorbing static and dynamic samples were obtained. **Figure 29a** shows an image of a three-dimensional liquid cluster formed in a pile of glass spheres. It turned out that most of the space between the spheres is not filled with liquid, but with air. This can be seen more clearly in **Figure 29b**, where the smallest liquid morphologies are presented. For liquid contents $W < 0.02$ only capillary bridges can be found in a wet pile. These morphologies are the building blocks for all larger morphologies, *i.e.* liquid clusters emerging for $W > 0.02$ are built from capillary bridges (cb), trimers (tr), or filled tetrahedron gaps "glued together" at their edges. The surface to volume ratio of those extended liquid morphologies was found to be about constant for all observed liquid contents.

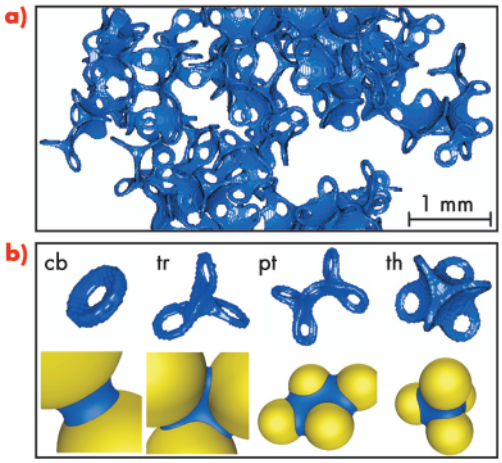


*Fig. 29:* **a)** X-ray microtomography of a liquid cluster in a dense pile of glass beads of 0.8 mm diameter at a liquid content of $W \approx 0.11$. $W$ is defined with respect to the entire sample volume. **b)** Smallest liquid morphologies emerging in wet piles of glass beads. *Top row:* as found by X-ray tomography, *bottom row:* as calculated numerically. For $W < 0.02$ only capillary bridges (cb) can be found. For larger liquid contents the capillary bridges might merge to form trimers (tr), pentamers (pt), etc. At low liquid content, filled tetrahedron gaps (th) can also be found.

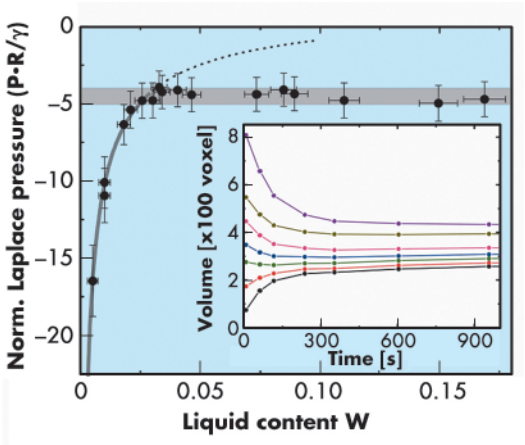


*Fig. 30:* The Laplace pressure within the liquid clusters, as a function of the liquid content of the sample. The grey bar indicates the universal pressure value calculated from the sample parameters (surface tension and size of spheres), its width corresponds to the uncertainty in the wetting angle. The inset shows the equilibration of individual liquid clusters after preparation.

A closer analysis shows that the internal geometry of these intertwined structures of liquid, air, and the grains can be well characterised by a few parameters. In particular, it can be predicted from the packing geometry that the Laplace pressure within equilibrated liquid clusters acquires a universal value for liquid contents, above $W \sim 0.02$. It should only depend upon the surface tension of the liquid, its wetting angle, and the typical size and shape of the grains. That this is in fact the case is shown in **Figure 30**, where the Laplace pressure, which could be inferred from the tomographic data, is shown as a function of the liquid content. Over almost the full range of data, it stays at the grey bar, which represents the universal value for the Laplace pressure as derived from the sample parameters. The liquid morphologies equilibrate after a typical time delay of 5 minutes for the beads used in our experiment, as displayed in the *inset* of **Figure 30**. Liquid morphologies with a smaller Laplace pressure will grow at the cost of liquid morphologies with larger Laplace pressure. In equilibrium any liquid morphology in the sample

will have the same Laplace pressure (see the grey bar in **Figure 30**).

This result entails a constant material stiffness over the full range of data, even for small liquid content where the Laplace pressure deviates from the grey bar. In this regime, the wetted area varies as well, but in such a way that the resulting cohesion forces remain constant down to the lowest contents investigated. As a result, the cohesion strength of a wet granular pile is largely independent of liquid content over the full range investigated. We could furthermore present evidence that this general behaviour is also valid for non-spherical granules, like real sand grains.

# Molecular layering of fluorinated ionic liquids at a charged sapphire (0001) surface

Room temperature ionic liquids (RTILs) are comprised of molecular ions. They are interesting materials from a physical point of view as they allow us to modify the interactions between the molecular ions as well the interaction with other materials by simply modifying the individual ionic molecules chemically **[1]**. To date several thousand ionic liquids have been synthesised and many of them are available from commercial sources.

Room temperature ionic liquids are also very promising candidates for a variety of new technological applications, such as solvents in green chemistry, catalysis, batteries, and fuel and solar cells. Although crucial for understanding their properties in applications, very little is known about the structural arrangement of the anions and cations at solid interfaces. In order to access these interfaces, high energy X-ray reflectivity (E = 72.5 keV) at the instrument HEMD, for high-energy microdiffraction, at beamline **ID15A** has been employed, which is an ideal tool to reach deeply buried interfaces within bulk samples. The measured X-ray reflectivity could then be used to extract information on the laterally-averaged electron-density profile at the RTIL/$Al_2O_3$ interface.

Systematic studies of the interfacial structure as a function of composition and temperature were performed with several RTILs at an $Al_2O_3$ (0001) surface. By choosing different combinations of anions and cations, it was possible to tune the ion-ion and ion-substrate interaction. By changing the temperature, the ratio between entropy and interfacial energy could be varied, driving the system closer to a disordered liquid or interfacial ordering, respectively. **Figure 31** shows the normalised high energy reflectivity for three different RTILs containing the same anion $[fap]^-$. All three measurements show distinct features in the normalised reflectivity which could be attributed to pronounced molecular layering at the RTIL/$Al_2O_3$ interface. The measurements are perfectly

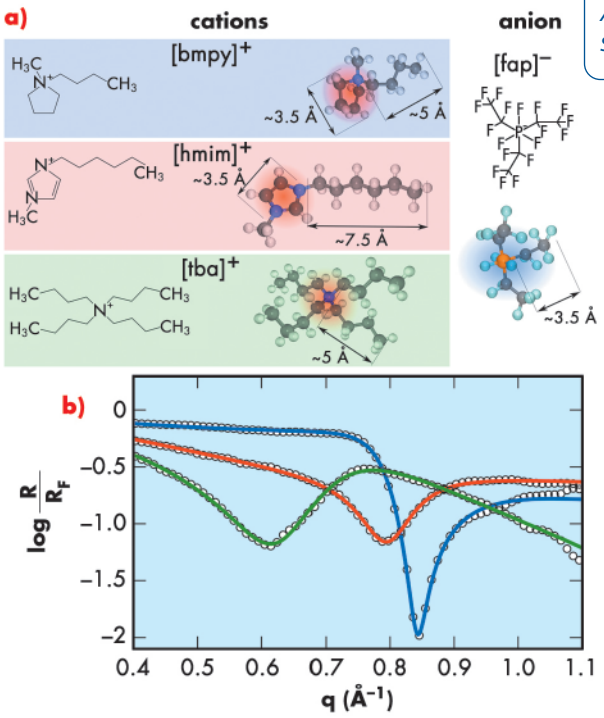


*Fig. 31:* **a)** Sketch of the molecular ions: three different cations have been combined with the $[fap]^-$ anion. **b)** Normalised high energy X-ray reflectivities of the three different RTILs in contact with a $Al_2O_3$ (0001) surface. The lines are best fits using a modified distorted crystal model ($[fap]^-[bmpy]^+$: blue line, $[fap]^-[hmim]^+$: red line, $[fap]^-[tba]^+$: green line).

**Principal publication and authors**

M. Mezger (a), H. Schröder (a), H. Reichert (a), S. Schramm (a), J.S. Okasinski (a), S. Schöder (a,b), V. Honkimäki (b), M. Deutsch (c), B.M. Ocko (d), J. Ralston (e), M. Rohwerder (f), M. Stratmann (f), H. Dosch (a,g), *Science* **322**, 424 (2008).

*(a) Max-Planck-Institut für Metallforschung, Stuttgart (Germany)*
*(b) ESRF*
*(c) Physics Department, Bar-Ilan University, Ramat-Gan (Israel)*
*(d) Condensed Matter Physics and Materials Science Department, Brookhaven National Laboratory, Upton (USA)*
*(e) Ian Wark Research Institute, University of South Australia, Mawson Lakes (Australia)*
*(f) Max-Planck-Institut für Eisenforschung, Düsseldorf (Germany)*
*(g) Institut für Theoretische und Angewandte Physik, Universität Stuttgart (Germany)*

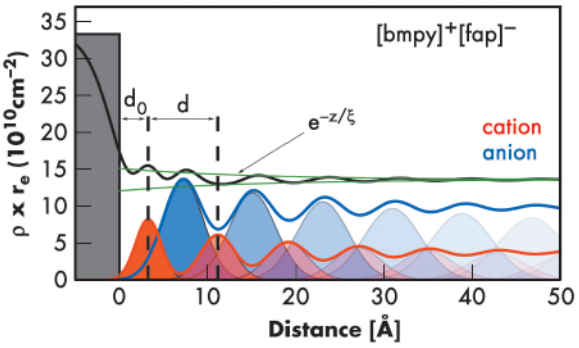


*Fig. 32:* Electron density profile of the interface $[fap]^-[bmpy]^+/Al_2O_3$ at T = –15°C: cation (red), anion (blue) and total (black) electron densities. Red and blue lines indicate cation and anion Gaussian distributions contributing to the respective partial electron density profiles (solid lines); black line, total electron density profile; grey bar, electron density of the sapphire substrate without roughness.

reproduced by a modified distorted crystal model. **Figure 32** shows an example, the reconstructed density of the interface $[fap]^-[bmpy]^+/Al_2O_3(0001)$. The first layer at the interface is comprised of cations, which may seem counterintuitive at first sight, followed by a second layer of anions, thus ensuring charge neutrality. Additional measurements employing a Kelvin probe confirmed that the substrate is negatively charged, thereby explaining the formation of a purely cationic layer directly at the interface.
The molecular layering decays exponentially with a decay length of approximately two molecular double layers. Similar results have been found for the other two interfaces $[fap]^-[hmim]^+/Al_2O_3$ and $[fap]^-[tba]^+/Al_2O_3$.

Dilute aqueous electrolytes containing water-screened weakly-interacting ions have been successfully described by mean field theories of charge double layers. This description neglects, however, correlations between ions. In contrast, the interaction between the oppositely-charged RTIL ions is very strong because no other molecule is available for screening. The ions are, therefore, strongly correlated. Such correlations also lead to other apparently counterintuitive phenomena like charge inversion and attraction between like-charged objects. Our findings are corroborated by recent molecular dynamics simulations of (simpler) RTILs in slit pores with Lennard-Jones potentials for the dispersion interactions of the molecules as well as for the wall-molecule interaction, where a clear separation of the anions and cations into distinct layers was also observed **[2]**. Information on the structure of such interfaces should help us to develop a deeper understanding of their properties, such as their transport properties, for future applications.

**References**
[1] P. Wasserscheid, T. Welton, *Ionic liquids in Synthesis* (Wiley-VCH, Weinheim Germany, 2007).
[2] C. Pinilla, *et al., J. Phys. Chem. B* **111**, 4877 (2007).

# Super-soft element 11

**Principal publication and authors**
E. Gregoryanz (a), L. Lundegaard (a), M. McMahon (a), C. Guillaume (a), R. Nelmes (a), M. Mezouar (b), Structural Diversity of Sodium, *Science* **320**, 1054 (2008).
*(a) Centre for Science at Extreme Conditions and School of Physics, University of Edinburgh (UK)*
*(b) ESRF*

The melting temperature of sodium is unique, being lower at very high pressures than at ambient pressure. In a recent experiment at beamline **ID27**, this unique feature of sodium was explorated in order to conduct the highest-pressure single-crystal structure refinements ever made. This has revealed that the low melting temperature of elemental sodium is associated with a number of extremely complex new crystal structures.
The complex phase diagram of this "simple" metal above 100 GPa suggests extraordinary states in both the liquid and solid phases at extreme conditions and has implications for other "simple" metals.

For decades, a combination of fundamental and applied physics has been utilised to synthesise new materials having intriguing and potentially useful properties such as super-hardness or superconductivity. When materials are compressed, their bulk and shear moduli and their strength (all measures of how compressible and therefore how hard materials are) as well as their melting temperatures all typically increase. For example, at a pressure of 55 GPa, the strength of elemental argon exceeds that of hardened steel under ambient conditions **[1]**, while its melting temperature above 130 GPa is expected to exceed that of iron.
The two lightest elements – hydrogen and helium – have extremely high compressibility, and helium, owing to its chemical inertness, is commonly used as a pressure transmitting medium to create hydrostatic pressures in high-pressure experiments.

At pressures up to 25 GPa, the melting temperatures of hydrogen and helium are the lowest of all elements and lie below 500 K. However, their melting temperatures continue to increase monotonically with pressure, reaching ~1000 K at 100 GPa, while their strength at these pressures is such that they do not create even quasi-hydrostatic conditions.

Recently, it has been shown that although the melting temperature of sodium metal initially behaves "normally" and increases from 370 K at ambient pressure to ~1000 K at 30 GPa, it then decreases rapidly and drops to just above room temperature at pressures of 118 GPa, before increasing again [2]. The melting temperature at 118 GPa is thus lower than at ambient pressure – behaviour that is unique amongst all known materials. The low melting temperature of sodium at 118 GPa means it is the only known "super-soft" system which can be used as a truly hydrostatic medium at pressures above 100 GPa. High-pressure single-crystal diffraction experiments were carried out using the high intensity and micro-focused X-ray beam available at beamline ID27. The minimum in the melting curve of sodium at 118 GPa was shown to be associated with a large number of extremely complex crystal structures (Figure 33). Indeed, one of these structures contains more than 500 atoms in the unit cell.

The low melting temperature of sodium at 118 GPa means that it is relatively easy to melt the sample *in situ* and the proximity of the melting curve ensures hydrostatic conditions. It was therefore possible to grow high quality single crystals at such high pressures by slow cooling from the liquid phase. A typical single-crystal diffraction image collected under these extreme conditions is presented in Figure 34. The number of different phases found in the vicinity of the melting minimum was surprising, seven in total. Very small changes in pressure and/or temperature resulted in transitions between the different structural forms. Several of the structures were extremely complex – more so than anything else previously observed for any element, even at ambient conditions.

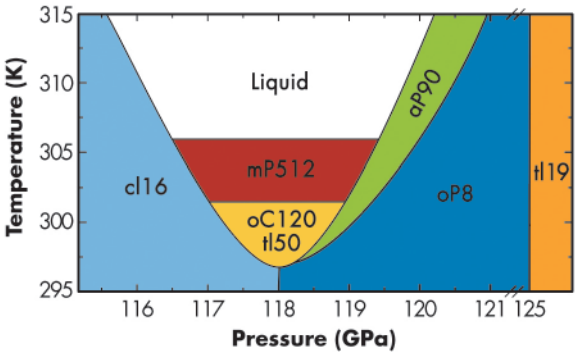


*Fig. 33:* Observed phases of sodium in the vicinity of the minimum of the melting curve.

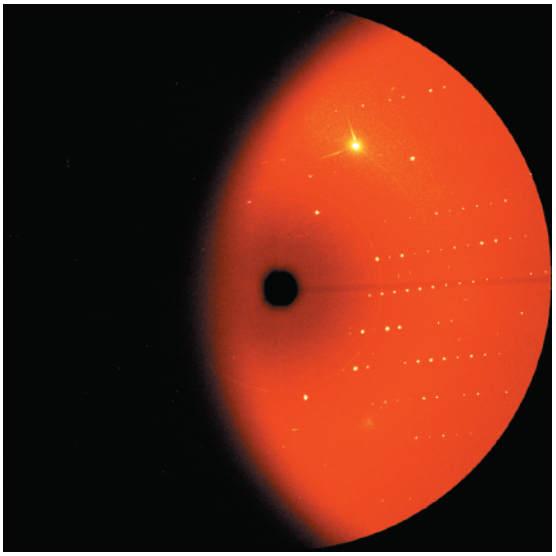

*Fig. 34:* Composite diffraction image showing representative data from the primitive trigonal phase with 90 atoms in the unit cell.

Using single-crystal methods, which have been developed as a three-year long term project at the ESRF, it has been possible to determine the lattice parameters of all seven phases and, so far, to refine the atomic positions in three of them – reaching the highest ever pressure for which the full single-crystal structure refinement has been carried out. The composite diffraction image in Figure 34 shows representative data from a primitive trigonal structure with 90 atoms in the unit cell.

Early theoretical calculations on hydrogen have suggested that at extreme compressions it might have a liquid ground state with very unusual properties and a family of the related anisotropic structures associated with its liquid state [3]. The results on sodium show something very similar being realised in nature, giving hope that the theoretically-predicted bizarre states of hydrogen do indeed exist even though they are currently unreachable in experimental studies.

**References**

[1] H. Mao *et al., J. of Physics-Condensed Matt.* **18**, S963 (2006).

[2] E. Gregoryanz *et al., Phys. Rev. Lett.* **94**, 185502 (2005).

[3] E. Brovman, Yu. Kagan, A. Kholas, *Soviet Physics JETP* **34**, 1300 (1972); *Soviet Physics JETP* **35**, 783 (1972).

# Polyamorphic transition, charge-density waves and superconductivity in sulphur

**Principal publications and authors**
C. Sanloup (a), E. Gregoryanz (b), O. Degtyareva (b), and M. Hanfland (c), *Phys. Rev. Lett.* **100**, 075701 (2008);
O. Degtyareva (b), M.V. Magnitskaya (d), J. Kohanoff (e) G. Profeta (f) S. Scandolo (g) M. Hanfland (c), M. I. McMahon (b) and E. Gregoryanz (b), *Phys. Rev. Lett.* **99**, 155505 (2007).
*(a) School of Geosciences and Centre for Science at Extreme Conditions, University of Edinburgh (UK)*
*(b) SUPA, School of Physics and Centre for Science at Extreme Conditions, University of Edinburgh (UK)*
*(c) ESRF*
*(d) Institute for High Pressure Physics, Russian Academy of Sciences, Troitsk (Russia)*
*(e) Atomistic Simulation Centre, Queen's University Belfast (UK)*
*(f) CNISM-Dipartimento di Fisica, Universita` degli Studi di L'Aquila (Italy)*
*(g) The Abdus Salam International Centre for Theoretical Physics (ICTP) and INFM/CNR "Democritos" National Simulation Centre, Trieste (Italy)*

Elemental sulphur, a yellow insulating mineral, is composed of crown-like 8-member ring molecules that form a complex crystal structure. Compression has a dramatic effect on these molecules: they break apart forming various chain and ring structures on pressure increase [1] changing colour to red at around 8 GPa. By compressing sulphur at low temperatures, where the phase transitions are kinetically inhibited, we find that the ambient pressure phase of sulphur with $S_8$ molecules persists in a metastable form to much higher pressures becoming amorphous above 40 GPa. Sulphur becomes metallic and superconducting above 90 GPa with $T_c$ = 10 K [2] forming an incommensurately modulated crystal structure at 300 K [3]. By studying the crystal structure of metallic sulphur at low temperatures close to the superconducting transition, we find a charge-density wave (CDW) instability, responsible for the structural modulation, to be in competition with the superconducting state.

Using high-pressure X-ray powder diffraction techniques on beamline ID09A with a liquid He cryostat, we compressed the S-I phase of sulphur at low temperatures observing a transition to an amorphous state (a-S) at pressures above 40 GPa. A change in the diffraction pattern of a-S is seen at 65 GPa and 80 K (Figure 35a), signalling a transformation from one amorphous form to another. Diffraction-based direct density measurements give a 7% density discontinuity (Figure 35b) corresponding to a transition from a low-density amorphous (LDA) to a high-density amorphous (HDA) form. The similarities between the densities and local structures of LDA and HDA sulphur with those of phases S-III (square chains) and S-IV (incommensurately modulated) are striking, suggesting a nanocrystalline nature instead of truly amorphous form of a-S. Further compression of the high-density a-S resulted in its recrystallisation into phase S-IV at 99 GPa and 40 K.

We observed sharp modulation reflections in the S-IV phase, characteristic of a long-range ordered CDW, and traced their positions and intensities as a function of pressure and temperature. From Rietveld refinement of diffraction patterns (Figure 36a) at each *P-T* point we obtained the amplitude of the atomic displacements due to modulation in the *P* range from 100 to 165 GPa and *T* range from 300 down to 15 K, close to the superconducting transition temperature (Figure 36b). The amplitude of the structural modulation (Figure 36a, inset) decreases with pressure increase, which correlates with the gradual increase in $T_c$ from 10 to 14 K [2]. The modulation disappears at 153 GPa, signalling the suppression of the CDW, leading to the enhancement of $T_c$ from 14 to 17 K at this pressure.

In conclusion, we have shown that sulphur exhibits a pressure-induced amorphisation at low temperatures and pressures above 40 GPa, with a further transition from a low-density to a high-density amorphous form at 65 GPa. Present work has extended the

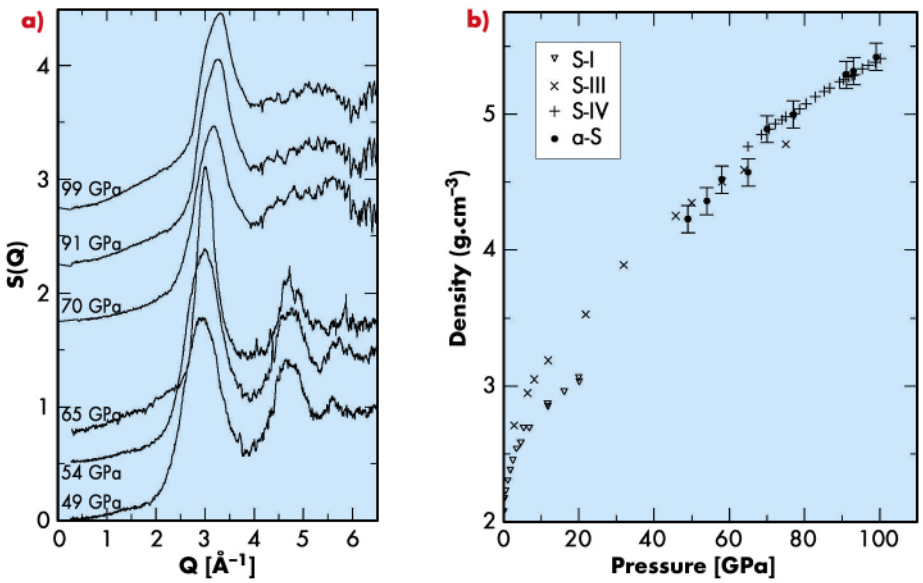


*Fig. 35:* **a)** Structure factors of low-density amorphous form of sulphur (49 and 54 GPa and 175 K, 65 GPa and 80 K) and high-density amorphous form of sulphur (70, 91 and 99 GPa and 40 K). **b)** Pressure dependence of density of a-S compared to crystalline phases.

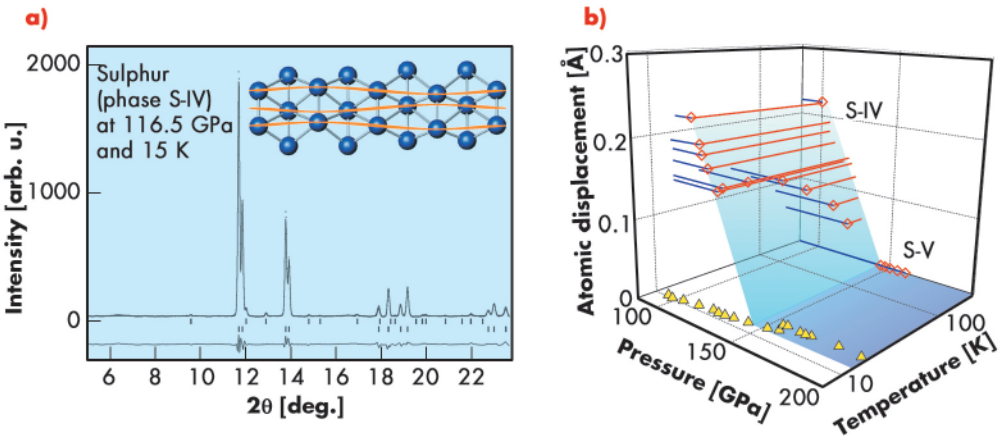


*Fig. 36:* **a)** X-ray diffraction profile of S-IV and a Rietveld refinement on the basis of the incommensurately modulated structure. The inset shows the crystal structure of S-IV. **b)** Observed maximum atomic displacement in S-IV and S-V as a function of pressure and temperature, shown as open diamond symbols. Triangles show $T_c$ from Ref. **[2]**.

pressure range of the direct density measurements of amorphous materials in the diamond anvil cells by a factor of 100. At a higher pressure of 100 GPa, sulphur crystallises into an incommensurately modulated structure, which is formed because of a CDW instability. Sulphur now represents a unique example of an elemental metal undergoing a CDW transition within a superconducting state, and joins a large group of complex materials showing an enhancement of $T_c$ upon pressure-induced suppression of a CDW.

**References**
[1] O. Degtyareva *et al., J. Chem. Phys.* **126**, 084503 (2007).
[2] E. Gregoryanz *et al., Phys. Rev. B* **65**, 064504 (2002).
[3] C. Hejny *et al., Phys. Rev. B* **71**, 020101(R) (2005).

# Short range magnetic collapse of iron under high pressure at high temperatures

**Principal publication and authors**
J.-P. Rueff (a,b), M. Mezouar (c) and M. Acet (d), *Phys. Rev. B.* **78**, 100405(R) (2008).
*(a) Synchrotron SOLEIL, Gif sur Yvette (France)*
*(b) Laboratoire Chimie Physique - Matière et Rayonnement, CNRS - UPMC, Paris (France)*
*(c) ESRF*
*(d) Experimentalphysik, Universität Duisburg-Essen, Duisburg (Germany)*

Knowledge of iron's phase diagram under high-pressure (HP) and high-temperature (HT) conditions is not only of importance for geophysics but also as a model system for the theoretical understanding of 3*d* electronic properties. High-pressure magnetism in particular is believed to play a crucial role in the stability of iron's structural phases and elastic properties. Theoretical improvements beyond the local-density approximation now make it possible to derive the correct magnetic ground state at ambient conditions. However, puzzling results recently observed under extreme conditions have perturbed the situation anew. Superconductivity was found in Fe along with ferromagnetism at low temperature and high pressure **[1]** and hints of antiferromagnetic (AF) coupling in ε-Fe, the supposedly nonmagnetic hcp HP phase. Even more poorly understood is the γ-Fe fcc phase stabilised at high temperature and high pressure. First-principles calculations favour a noncollinear magnetism in the form of spin spiral density waves **[2]** but results in the γ phase are extremely scarce because of the HP/HT experimental constraints. Here, we demonstrate the collapse of the short-range iron magnetic state in the HP/HT phases by X-ray emission spectroscopy (XES), a local probe of the 3*d* spin magnetic moment.

The spin sensitivity of XES arises from the core-hole/3*d* exchange interaction in the final state which splits the emission spectrum into a main peak and satellite. We focus on the Kβ emission line which shows the highest sensitivity to the spin state in a transition metal. The spectra were measured at beamline **ID27** at 33 keV, simultaneously to X-ray diffraction, using the Si(531) analyser from **ID16**. The sample was loaded in a diamond-anvil cell together with $Al_2O_3$ powder both for thermal isolation and pressure-transmitting medium. HP/HT conditions were achieved *in situ* by a double-sided laser heating technique where an intense laser beam heats the sample inside the pressure cell. **Figure 37** shows the evolution of the Kβ emission spectra under high pressure at 300 K and 1400 K.

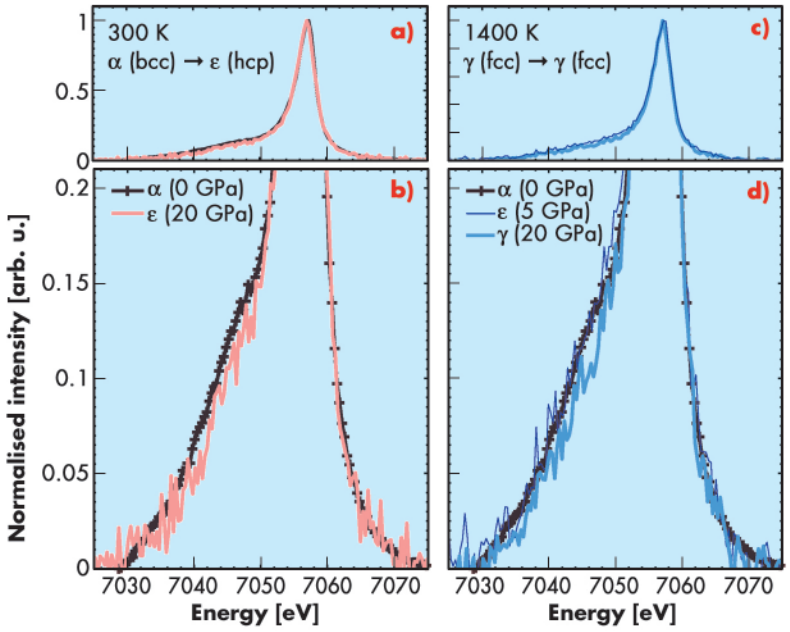


*Fig. 37:* Kβ emission spectra of iron under high pressure and temperature in the α, ε and γ phases: **(a,c)** full scale; **(b,d)** expanded intensity scale.

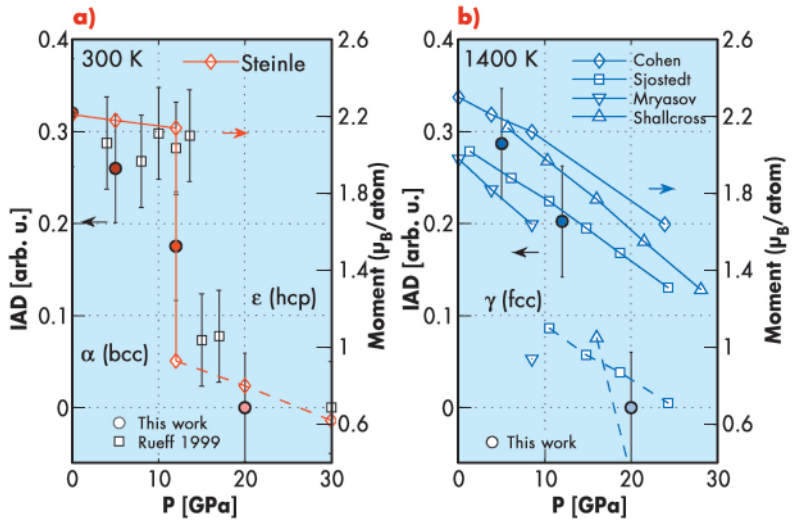


*Fig. 38:* Iron spin magnetic moment derived from the XES spectra (left scale, circles) and calculated (right scale, lines).

In iron metal, the satellite is notably weaker than that in other iron compounds. Nevertheless, we clearly notice a decrease in the satellite intensity at high pressure which suggests a change in the iron spin state.

The magnetic information contained in the XES spectra can be extracted by means of integrated absolute difference (IAD), a quantity that is linearly related to the 3*d* spin moment. **Figure 38** shows the pressure dependence of the spin state from the IAD analysis. At 300 K, the results bear out the magnetic collapse when iron enters the HP ε phase, as already known from XES and Mössbauer spectroscopy. Additionally, we observe non vanishing magnetism above the transition that decays at higher P. This agrees with recent theoretical model suggesting that the magnetic moment is not completely suppressed in ε-Fe but instead remains up to a fairly large pressure in presence of AF coupling. This is in contrast to the high-spin (HS) to low-spin (LS) transition usually evoked at the α-ε structural change. The behaviour in γ-Fe at 1400 K is remarkably similar to that at 300 K, suggesting that the mechanism of the magnetic transition in the γ phase primarily involves a HS to LS transition, besides the occurrence of a spin spiral density wave. Comparing our results to the theoretical magnetic moment of iron computed in the spin spiral density wave model, we find a fair agreement at low pressure, while at high pressure a better match is found when considering the low *q* limit of the spin spiral density wave structure. The latter corresponds to a magnetic state with saturated ferromagnetism and a clearly defined HS-to-LS transition.

XES therefore appears as a powerful probe of the 3*d* magnetic properties under extreme conditions. In iron, the results show hints of non-vanishing magnetism in the ε-phase under pressure in agreement with predictions of non-collinear magnetism while in the γ phase, we observe a LS collinear structure at HP/HT. This substantially minimises the role of spin spiral density waves in the magnetic change at extreme conditions in the γ phase.

**References**
[1] K. Shimizu *et al., Nature London* **412**, 316 (2001).
[2] S. Shallcross *et al., Phys. Rev. B* **73**, 104443 (2006).

# Hole-doping-induced superconductivity in NdFeAsO

**Principal publication and authors**

K. Kasperkiewicz (a), J.W.G. Bos (a), A.N. Fitch (b), K. Prassides (c), S. Margadonna (a), *Chem. Commun.* DOI:10.1039/B815830D (2009).

*(a) Department of Chemistry, University of Edinburgh (UK)*
*(b) ESRF*
*(c) Department of Chemistry, University of Durham (UK)*

Superconductivity at the surprisingly high temperature of 55 K has been recently reported in fluorine-doped rare-earth iron oxyarsenides, $REFeAsO_{1-x}F_x$ (RE = rare earth) [1]. The magnitude of $T_c$ and the apparent similarities with the high-$T_c$ cuprates – layered conducting FeAs slabs and proximity to antiferromagnetic and structural instabilities – have made these systems an intensely studied research field. REFeAsO possesses a tetragonal crystal structure comprising layers of edge-sharing $FeAs_4$ tetrahedra interleaved with REO layers. On cooling, a structural phase transition to orthorhombic crystal symmetry, accompanied by the development of long range antiferromagnetic order occurs. The magnetic instability is suppressed upon fluorine-doping before the onset of superconductivity, while orthorhombic symmetry survives well within the superconducting dome [2]. The mechanism of superconductivity in these materials is still under debate. Inelastic X-ray measurements on $NdFeAsO_{1-x}F_x$ on ID28 have shown that electron-phonon coupling could play a role in determining the superconducting state properties [3]. The family of Fe-based superconductors has now further expanded to include, among others, the binary $FeSe_{1-x}$ phases [4].

While electron-doping in $REFeAsO_{1-x}F_x$ has been intensively studied, very little is known about the structural and electronic properties of hole-doped phases (*e.g.* partial replacement of the RE ion by alkaline earths). Confirming the existence of superconducting phases upon hole doping, probing how $T_c$ varies with composition, and revealing the influence of doping on the structural and magnetic transitions are of fundamental importance for the understanding of the pairing mechanism.

Recently, we have investigated the new family of hole-doped systems, $Nd_{1-x}Sr_xFeAsO$ (x= 0.05, 0.1, 0.2). Inspection of the room temperature diffraction profiles collected at beamline ID31 reveals the tetragonal unit cell (*P4/nmm*) established before for REFeAsO (Figure 39). Rietveld analysis shows that the *a*-axis increases monotonically with *x* as expected considering the larger ionic radius of $Sr^{2+}$, while the *c*-axis initially contracts at small *x* before undergoing a considerable expansion at $x > 0.1$. The *c*-axis dimensions are influenced by the geometry of the $AsFe_4$ pyramidal units with the Fe-As-Fe angle, $\theta$, first increasing for $0 < x < 0.1$ and then decreasing for $x > 0.1$ (Figure 39). The electronic structure of the REFeAsO systems depends on small changes in the geometry of the $AsFe_4$ pyramidal units which controls both the Fe near- and next-near-neighbour exchange interactions and the width of the electronic conduction band. The sudden increase in the compression of the $AsFe_4$ pyramidal units coupled

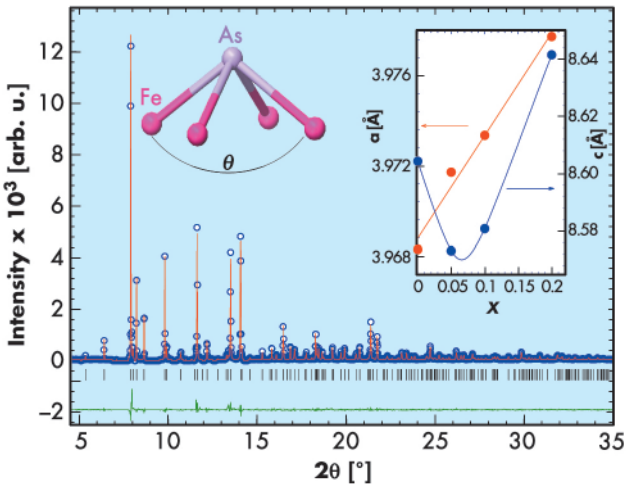


*Fig. 39:* Synchrotron X-ray (λ = 0.40301 Å) powder diffraction profile of $Nd_{0.8}Sr_{0.2}FeAsO$ at room temperature. Inset: evolution of the room temperature tetragonal lattice constants as a function of $Sr^{2+}$ doping and schematic diagram of the $AsFe_4$ pyramidal unit.

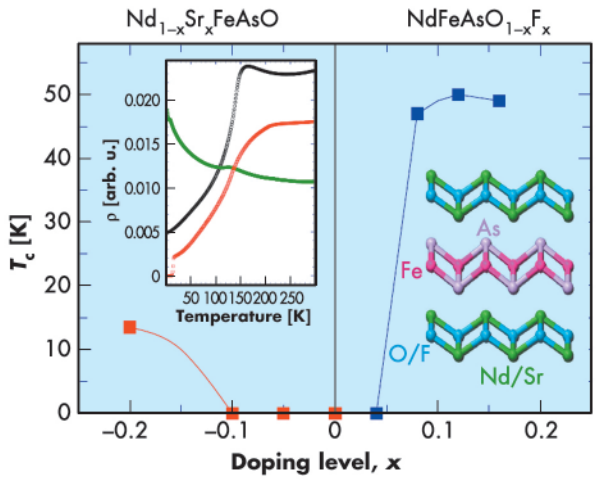


*Fig. 40:* Electronic phase diagram of electron/hole doped NdFeAsO. Blue (red) squares mark the superconducting transition temperatures for electron (hole) doping. Inset: schematic diagram of the tetragonal structure of $Sr^{2+}$ and $F^-$ doped NdFeAsO and temperature dependence of the resistivity for $Nd_{1-x}Sr_xFeAsO$ [$x = 0$ (black), $x = 0.05$ (green), $x = 0.2$ (red)].

with the larger lattice dimensions for the $x$ = 0.2 composition may lead to a much smaller bandwidth and changes the electronic behaviour as compared to that at small $x$. Low temperature diffraction profiles of all compositions showed the presence of a structural phase transition from tetragonal to orthorhombic (space group *Cmma*) in analogy with the undoped and electron-doped REFeAsO systems. However, increasing the $Sr^{2+}$ content does not suppress the structural transition which occurs at almost the same temperature for all compositions.

In agreement with the diffraction experiments, resistivity (ρ) measurements show considerable differences with increasing $x$. While the parent compound displays the typical behaviour of REFeAsO systems, the resistivity curve for x = 0.05 reveals a drastic change with ρ increasing on cooling. It thus appears that at low $x$, the electron charge carriers in NdFeAsO are initially depleted pushing the system through a transition from bad metal to semiconductor. Further hole doping increases the amount of hole-type carriers, and metallic conductivity is restored. Indeed, the x = 0.2 system shows metallic-type behaviour with ρ decreasing with temperature and a superconducting transition occurs at $T_c$ =13.5 K (**Figure 40**).

Our experimental observations show that hole-doping of NdFeAsO via partial replacement of $Nd^{3+}$ by $Sr^{2+}$ is a successful route to induce superconductivity. However, the structural and electronic response with doping is different from and non-symmetric to that in the electron-doped side of the phase diagram (**Figure 40**). For NdFeAsO, higher levels of hole doping are necessary to observe a similar phenomenology to the electron-doped systems as an increased number of carriers is necessary to overcome the initial semiconducting behaviour.

**References**
[1] Y. Kamihara, T. Watanabe, M Hirano and H. Hosono, *JACS* **130**, 3296 (2008).
[2] S. Margadonna, Y. Takabayashi, M.T. McDonald, M. Brunelli, G. Wu, R.H. Liu, X.H. Chen and K. Prassides, *Phys. Rev. B* **79**, 014503 (2009).
[3] M. Le Tacon, M. Krisch, A. Bosak, J.-W.G. Bos, and S. Margadonna, *Phys. Rev. B* **78**, 140505 (2008).
[4] S. Margadonna, Y. Takabayashi, M.T. McDonald, K. Kasperkiewicz, Y. Mizuguchi, Y. Takano, A.N. Fitch, E. Suard and K. Prassides, *Chem. Commun.*, 5607 (2008).

# Metal-peptide frameworks

**Principal publication and authors**
A. Mantion (a), L. Massüger (b), P. Rabu (c), C. Palivan (a), L.B. McCusker (b), A. Taubert (a,d), *J. Am. Chem. Soc.*, **130**, 2517 (2008).
*(a) Department of Chemistry, University of Basel (Switzerland)*
*(b) Laboratory of Crystallography, ETH Zurich (Switzerland)*
*(c) IPCMS, UMR 7504 CNRS - Université Louis Pasteur (Strasbourg)*
*(d) Institute of Chemistry, University of Potsdam (Germany)*

Like zeolites, the class of materials known as metal organic frameworks (MOFs) are both porous and crystalline. However, while a zeolite framework is purely inorganic and is restricted to tetrahedral building units, the MOF coordination polymers are inorganic/organic hybrids and the possibilities for varying the nature of the metal centres and of the organic linkers to induce specific characteristics in the resulting material are innumerable. Interestingly, the possibility of using peptides as connectors has not been reported, although they offer a rich structural diversity and are intrinsically chiral. To explore their potential as linkers in the fabrication of chiral metal peptide frameworks (MPFs), a series of syntheses using $Cu^{2+}$ and $Ca^{2+}$ as metal centres and oligovalines as linkers was performed. The combination of $Cu^{2+}$ and the Z-(L-Val)$_2$-L-Glu(OH)-OH oligopeptide (**Figure 41**) produced the polycrystalline material "MPF-9".

*Fig. 41:* The Z-(L-Val)$_2$-L-Glu(OH)-OH oligopeptide.

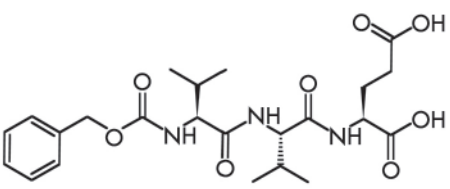


Powder diffraction methods had to be used for structure solution because there were no single crystals of the product. To this end, high-resolution powder diffraction data were collected using the diffractometer on **BM01B** (Swiss-Norwegian Beamline). The pattern could be indexed with a monoclinic unit cell ($a$ = 19.2610 Å, $b$ = 4.8885 Å, $c$ = 30.5096 Å, $\beta$ = 92.524°) and the systematic absences were consistent with the space groups $C2$, $C2/m$ or $Cm$. As a non-centrosymmetric structure was expected, $C2$ was assumed for structure analysis.

The data proved to be of only modest resolution in reciprocal space ($d_{min}$ of ≈ 1.4 Å), but considerable chemical information about the peptide structure and the Cu coordination geometry was known, so a direct-space approach to structure solution was attempted. For this purpose, the direct-space global-optimisation algorithms implemented in the computer program FOX **[1]** were

used. A simplified structural model with limited conformational degrees of freedom was used as input, and the model with the best fit to the data was then taken as a starting point for structure completion and Rietveld refinement. For the latter, the complete pattern was used, and bond distance and angle restraints were included to keep the model chemically sensible during the course of the refinement. The profile fit for the final model ($R_F$ = 0.103, $R_{wp}$ = 0.266, $R_{exp}$ = 0.217) is shown in **Figure 42**.

The $Cu^{2+}$ ions in the structure are each coordinated to two oxygen atoms of the peptide carboxylate groups and to two ammonia molecules in a distorted square planar geometry (**Figure 43**). One of the coordinated $NH_3$ molecules forms a hydrogen bond with the L-glutamic acid residue of the neighbouring complex along the [001] direction, while the other forms hydrogen bonds with two water molecules, which form a helical hydrogen bonding network along the [010] direction. The peptide ligands themselves also form hydrogen bonds to one another along the [010] direction to create a $\beta$-sheet-like structure. This extended hydrogen-bonding network accounts for the insolubility of MPF-9$^-$ in both water and organic solvents, and the concomitant difficulty in growing single crystals.

The structure is, within the limits of the method, very well defined. It is also consistent with the results of the elemental analysis, TGA, EPR and magnetic measurements.

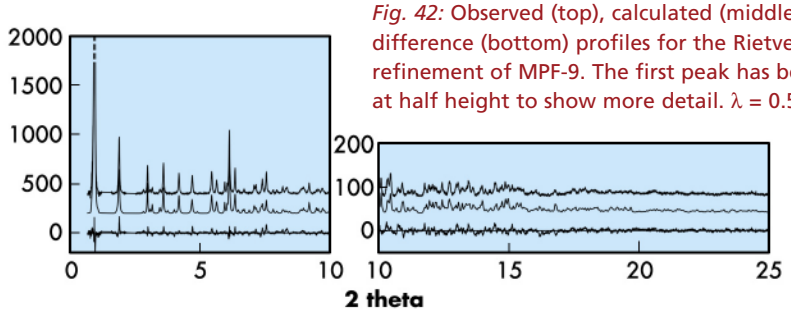


*Fig. 42:* Observed (top), calculated (middle) and difference (bottom) profiles for the Rietveld refinement of MPF-9. The first peak has been cut at half height to show more detail. λ = 0.50007 Å.

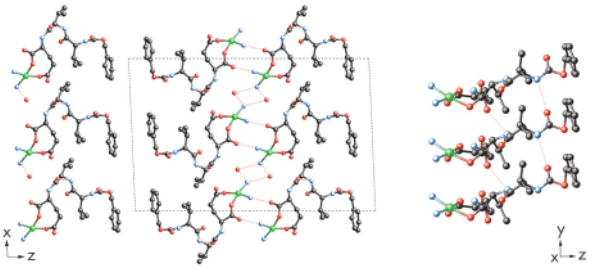

*Fig. 43:* Projections of the structure of MPF-9 along [010] (left) and along [110] (right) showing the H-bonding network.

It can be described in terms of two 2-dimensional substructures. The first of these consists of a double layer of copper ions in the *ab* plane, in which the two layers are diagonally displaced with respect to one another, and the second is that of the peptide with the long axis of the molecule oriented roughly along [001]. In addition to the hydrogen bonding network along the [010] direction, the phenyl groups of neighbouring peptides along [001] form columns along [010] and are oriented to allow π-π interactions.

Although MPF-9 does not have an extended 3-dimensional Cu-peptide network, magnetic interactions were found to occur between magnetic centres; the structure does have some porosity and the peptide has been shown to be a viable ligand meriting further investigation.

**Reference**
[1] V.R. Favre-Nicolin, R. Cerny, *J. Appl. Crystallogr.* **35**, 734-743 (2002).

## Metal-organic nanoporous structures as photoluminescent chemical sensors

The field of multifunctional materials has seen rapid progress with the discovery of structures which combine a set of well-defined properties for specific applications within the same crystal. Properties such as nanoporosity, luminescence, and magnetism are required for sensors, lasers, nonlinear optics, displays, and electroluminescent devices.

Lanthanide-based porous metal-organic frameworks (Ln-MOFs) can possess some of these properties and are therefore excellent candidates for such multifunctional materials for sensors. However, the pore sizes of most known Ln-MOF materials are too small to allow the diffusion of molecules of interest, precluding their use in photoluminescence sensors.

**Principal publication and authors**
B.V. Harbuzaru (a), A. Corma (a), F. Rey (a), P. Atienzar (a), J.L. Jordá (a), H. García (a), D. Ananias (b), L.D. Carlos (b), J. Rocha (b), *Angewandte Chemie International Edition*, **47**, 1080 (2008).
*(a) Instituto de Tecnología Química, (UPV-CSIC), Valencia (Spain)*
*(b) Departments of Chemistry and Physics, CICECO, University of Aveiro (Portugal)*

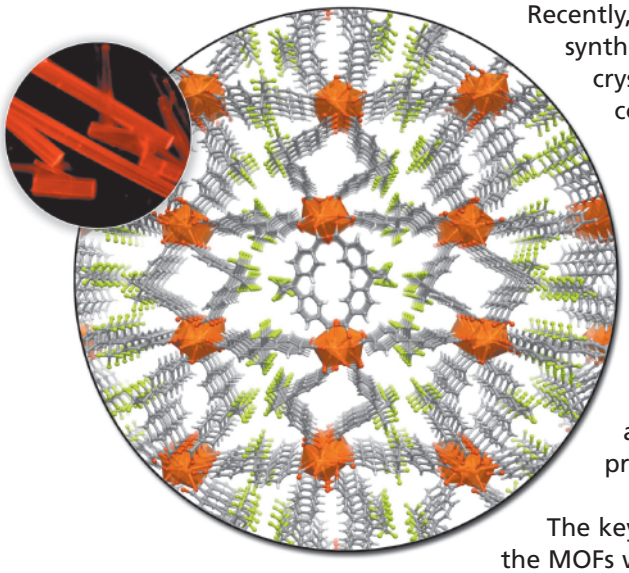

*Fig. 44:* Crystal structure of ITQMOF-2 (C grey, F yellow: H white, O red, Eu orange). Upper-left inset: $Eu^{3+}$-containing ITQMOF-2 crystals under UV light.

Recently, we designed and synthesised two novel crystalline MOFs containing rare-earth cations that combine microporous structure, hydrophobicity, high adsorption capacity, high thermal resistance, anisotropic photoluminescence and magnetic properties.

The key design element of the MOFs was the inclusion of the organic spacer, 4,4′-(hexafluoroisopropylidene)-bis(benzoic acid) (HFIPBB). This molecule has high hydrophobicity because of the presence of aromatic rings and $-CF_3$ groups, an antenna effect from its aromatic groups, strong interaction with the metal centre through the carboxylic groups, and two coordination centres that are required for the microporous 3D structure. The chosen metal atoms were any single lanthanide (except radioactive promethium), or mixtures of them. Two new materials, named "ITQMOF-1" and "ITQMOF-2", were obtained with similar composition but different crystal structures.

The structure of ITQMOF-1 could not be solved due to severe twinning, although it has been recently described by another Spanish group [1]; the structure of ITQMOF-2 was solved using single crystal data collected at the beamline **BM16** (**Figure 44**).

Both materials are insoluble in water and in common organic solvents, and have excellent thermal stability; powder XRD of samples heated *in situ* reveals that ITQMOF-1 is stable in air at temperatures above 400°C, and decomposes at *ca.* 450°C.

To demonstrate the potential applications of these materials in sensor devices, $Eu^{3+}$-containing ITQMOF-1 was used for detecting the presence of ethanol in air. This was done by monitoring the emission at 619 nm under alternating streams of air saturated with ethanol and ethanol-free air. In the presence of ethanol, we observed a rapid decrease of the emission intensity, which recovers rapidly when the material is exposed to clean air. This behaviour may be explained by considering that ethanol coordinates the $Ln^{3+}$ ions, quenching the photoemission through coupling with the vibrational states of the O-H oscillators. The addition of water to both streams did not modify these results, confirming the interest of the hydrophobic properties of the materials for measuring ethanol in a water-containing air stream.

Importantly, it is possible to obtain materials with different emission colours and magnetic properties by carefully selecting the $Ln^{3+}$ ions. For example, $Tb^{3+}$-ITQMOF-1 presents a ferromagnetic interaction between the metal ions and a strong green emission in UV light, while $Eu^{3+}$-ITQMOF-2 exhibits a red colour in UV light (**Figure 44**, inset) with paramagnetic interactions. Moreover, the (5% $Eu^{3+}$ - 95% $Gd^{3+}$)-ITQMOF-1 sample shows an antiferromagnetic interaction between the $Gd^{3+}$ ions, and a red colour in UV light due to the $Eu^{3+}$ ions. Remarkably, this material presents both a $^5D_0$ quantum efficiency q = 0.83 (to our knowledge, the largest reported for solid-state $Eu^{3+}$ compounds with organic ligands) and the largest value of absolute emission quantum yield ($\eta$ = 0.48, excitation wavelength of 290 nm) reported for $Eu^{3+}$-based MOFs. Furthermore, this emission is highly anisotropic, depending on the orientation of the crystals relative to the incident beam and the detector.

In conclusion, we show that a judicious choice of the ligand (HFIPBB) allowed the design of novel lanthanide-based metal-organic frameworks with high thermal stability and interesting multifunctional properties (magnetism, luminescence, microporosity and hydrophobicity). The combination of photoluminescent $Ln^{3+}$ centres and HFIPBB resulted in materials which efficiently sense ethanol, even in the presence of water and under ambient conditions. Current studies are now focused on exploring the combination of optical and magnetic properties for sensor applications and data storage.

**Reference**
[1] F. Gándara, A. de Andrés, B. Gómez-Lor, E. Gutiérrez-Puebla, M. Iglesias, M.A. Monge, D.M. Proserpio, N. Snejko, *Crystal Growth & Design*, **8**, 378 (2008).

# Soft Condensed Matter

## Introduction

Soft Matter studies seek to unravel the link between a material's microstructure and dynamics, and its macroscopic properties. This chapter presents a broad set of examples from the morphology of synthetic polymer fibres to structural dynamics of biomolecules in bulk and at interfaces. These studies involve a diverse class of systems from supercooled liquids to highly self-assembled biological complexes. This diversity is one of the particular strengths of the activities at the Soft Condensed Matter Group beamlines, articulating significant overlap with other disciplines such as materials science, biology, and surface science.

The past year saw many important scientific and technical developments. It has been a very hectic year with preparation for the ESRF Upgrade Programme and joint review of all four beamlines in the Soft Condensed Matter Group (ID02, ID10A, ID10B, and ID13) in spring 2008. The outcome of this review was very positive, without exception. The review panels recognised the outstanding technical status and scientific accomplishments of these beamlines. The review panels also approved the upgrade proposals for the beamlines.

The highlights selected for this chapter represent only a sub-set of the many interesting scientific results and technical developments over the year. A large fraction of the articles illustrate the unique feature of scattering techniques in terms of the combined access to the relevant length and time scales not readily feasible by other techniques. Studies of dynamic processes especially at interfaces are receiving increased attention.

The first two articles deal with adsorption of biomolecules at curved and planar interfaces. In the first article, the adsorption of proteins onto tethered polyelectrolyte brushes was probed in real time by SAXS, which revealed the sub-diffusive motions of proteins in the grafted polyelectrolyte layer. The second article presents the structural details of the adsorbed monolayer of DNA on a solid substrate with a soft functionalised organic layer, elucidating their two-dimensional order by X-ray reflectivity. This is followed by a study of low frequency viscoelastic behaviour of a supercooled liquid near the glass transition probed by XPCS at grazing incidence which demonstrated striking similarities in the temperature dependence of viscosity and elasticity. The fourth article reports diffuse scattering and reflectivity investigations of the formation and self-organisation of gold nanoparticles at liquid-liquid and air-water interfaces illustrating an unexpected clustering of particles.

Soft Condensed Matter Group beamlines are involved in a variety of technical developments. The first article in this category demonstrates that hard X-ray holographic diffraction imaging is an excellent technique for determining electron density profiles of nanostructures. With the availability of higher coherent flux, this technique offers the possibility of imaging fast dynamic processes. In conventional fibre diffraction experiments, the fibre axis is perpendicular to the X-ray beam. With special specimen preparation, the possibility of passing the microbeam along the fibre axis has been demonstrated, which then reveals fine details of skin-core morphology without requiring elaborate modelling. Manipulating micrometre-size objects in solution within a microbeam is a challenging task. In the subsequent article, the effectiveness of laser traps

for manipulating large multilamellar liposomes in a microdiffraction experiment has been illustrated.

The final two articles present structural dynamics of proteins when they perform their biological functions. In the first article, the quaternary transition of human haemoglobin from ligand bound relaxed state to unbound tense state and back to the relaxed state was studied by nanosecond pump-probe techniques at beamline ID09B. In the last article, the molecular mechanism of muscle braking action under rapid stretch was revealed by X-ray interference combined with high-resolution muscle mechanics.

The joint review process of the beamlines also set the momentum for the Partnership for Soft Condensed Matter (PSCM) together with the ILL. The ESRF Science Advisory Committee supported the establishment of the PSCM on a step-by-step basis, initially as a support laboratory for ancillary equipments. As a first step, the support laboratories within the SCM group are becoming better streamlined. The scientific scope and content for the partnership is being refined. Further discussion with the User Community is foreseen in the near future.

***T. Narayanan***

# Directed motion of proteins along tethered polyelectrolytes

**Principal publication and authors**
K. Henzler (a), S. Rosenfeldt (a), A. Wittemann (a), L. Harnau (b), S. Finet (c), T. Narayanan (c), and M. Ballauff (a), *Phys. Rev. Lett.* **100**, 158301 (2008).
*(a) Physikalische Chemie I, University of Bayreuth (Germany)*
*(b) MPI Stuttgart and ITAP, University of Stuttgart (Germany)*
*(c) ESRF*

The adsorption and immobilisation of proteins from aqueous solutions onto solid surfaces is a topic of considerable interest in both soft matter and biochemical research [1]. Many biologically important processes are interfacial in nature and very often, charged and uncharged polymers attached to surfaces are used to tune the interaction with the proteins. Various biotechnological processes require immobilisation of enzymes with full retention of their biological activity. Reversible adsorption of proteins onto charged surfaces is used in protein purification by ion exchange chromatography and in many natural processes such as cell adhesion. Nevertheless, unspecific adsorption of proteins must be suppressed in many practical applications in order to prevent foreign body reactions to materials from a host. Little is known about the kinetics of protein adsorption and the self-organisation of biomolecules with tethered polymer chains at a molecular level.

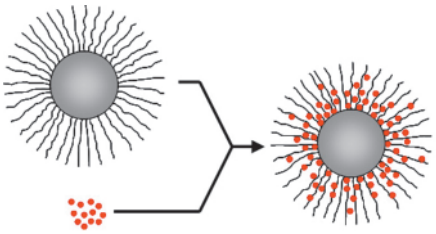

*Fig. 45:* Sketch of the uptake of proteins (red spheres) by spherical brushes consisting of a solid core (grey sphere) and grafted polyelectrolyte chains (wavy lines).

Here we report on the first study of the motion of proteins (bovine serum albumin, BSA) in a layer of tethered polyacrylic acid chains on colloidal polystyrene particles (**Figure 45**) using time-resolved small-angle X-ray scattering (TR-SAXS) combined with stopped-flow rapid mixing at beamline **ID02**. The pH value of the aqueous solution was kept well above the isoelectric point of the charged proteins and the ionic strength in the solution was adjusted to 7 mM to ensure full uptake of proteins by the spherical polyelectolyte brushes (SPB). The driving force is the counterion release mechanism, *i.e.*, the exchange of confined counterions with charged proteins. **Figure 46a** displays the typical evolution of the scattering intensity, $I(q)$, as a function of time, $t$. The gradual uptake of protein can be followed directly from the shift of the side maxima to smaller scattering vectors q with increasing time (see the dotted vertical line). The continuous lines indicate the calculated intensities using the radial electron density profile of SPB loaded with BSA and the screened Coulomb interaction between the SPB obtained from a reference interaction site integral equation theory. The TR-SAXS data revealed that the uptake of the

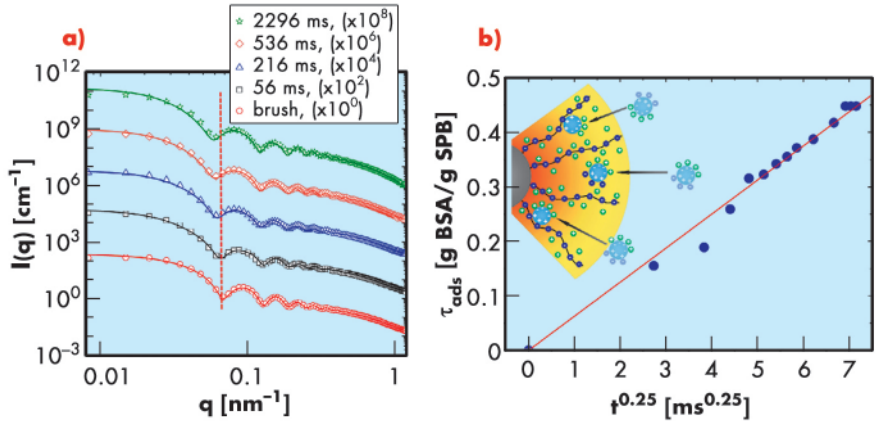


*Fig. 46:* **a)** TR-SAXS intensities, *I(q)*, as a function of time, *t*. For clarity, successive upper curves have been shifted by a factor 100 (as indicated in the legend). The continuous lines represent the model. **b)** The time dependence of the amount of adsorbed protein obtained from the radial electron density profiles derived from the fits in (a). The inset illustrates the directed motion of proteins through the brush layer.

proteins into the brush layer is relatively fast and the final state is reached within 3 seconds. However, the time needed by a single protein molecule to diffuse freely through the tethered layer is less than a millisecond. This means that the motion of the proteins in the brush layer has been slowed significantly. From the radial electron density profiles, the total amount of adsorbed protein per SPB ($\tau_{ads}$) at a given time can be derived. **Figure 46b** depicts that $\tau_{ads}$ increases with time as $t^{1/4}$. For unhindered diffusive motion of proteins, the mean-square-displacement is expected to increase with time as $t^{1/2}$. The observed sub-diffusive behaviour is due to a balance of frictional and external forces acting on the proteins as shown schematically in the inset of **Figure 46b**.

In summary, we have demonstrated that protein adsorption can be monitored directly with high temporal and spatial resolution on surface-modified colloidal spheres using TR-SAXS. The uptake of charged proteins by spherical polyelectrolyte brushes follows a sub-diffusive behaviour. A similar directed motion of proteins and other biomolecules through biological membranes could play a pivotal role in their self-assembly.

**Reference**
[1] *Proteins at Solid-Liquid Interfaces*, P. Dejardin (Ed), Springer (2006).

## DNA adsorption at liquid/solid interfaces studied by X-ray reflectivity

DNA interactions with surfaces can be repulsive, leading to confinement or depletion, or attractive. A repulsive interaction exists between negatively charged phosphates of DNA and phospholipids of membranes and contributes to enclose the genetic material within the cell. Depletion forces also confine DNA within viral capsids. Repulsive interactions are a common requirement in micro- and nanofluidics. Attractive interactions lead to adsorption. Chemisorption is at the core of solid-phase synthesis of polynucleotides. Physisorption is also of wide technological interest and biological relevance. In hybridisation techniques such as Southern blots, northern blots, or biochips, nucleic acids are immobilised on surfaces, either through chemisorption or physisorption. Chromatographic techniques rely on a reversible immobilisation of DNA. It is thus of great importance to understand the details of DNA interactions with interfaces, liquid/solid, liquid/liquid **[1]** or vapor/liquid **[2]**.

Few experimental techniques can be employed to study the conformation of biological macromolecules on a molecular length-scale. Atomic force microscopy, for example, can be carried out within a liquid solution and has yielded impressive atomic-resolution images of strongly adsorbed double-stranded DNA molecules on a solid substrate. Here we performed X-ray reflectivity studies at the aqueous buffer/solid substrate interface to detect the adsorption of a

**Principal publications and authors**
C. Douarche (a,b,c), R. Cortès (a), S.J. Roser (d), J.-L. Sikorav (e) and A. Braslau (f), *J. Phys. Chem. B* **112**, 13676–13679 (2008);
C. Douarche (a,b), R. Cortès (a), C. Henry de Villeneuve (a), S.J. Roser (c), and A. Braslau (e), *J. Chem. Phys.* **128**, 225108 (2008).
*(a) Physique de la Matière Condensée, École Polytechnique, CNRS, Palaiseau (France)*
*(b) Institut de Recherche Interdisciplinaire, Villeneuve d'Ascq (France)*
*(c) Service de Biologie Intégrative et de Génétique Moléculaire, CEA/Saclay, Gif-sur-Yvette (France)*
*(d) Department of Chemistry, University of Bath (UK)*
*(e) Institut de Physique Théorique, CNRS URA 2306, CEA/Saclay, Gif-sur-Yvette (France)*
*(f) Service de Physique de l'État Condensé, CNRS URA 2464, CEA/Saclay, Gif-sur-Yvette (France)*

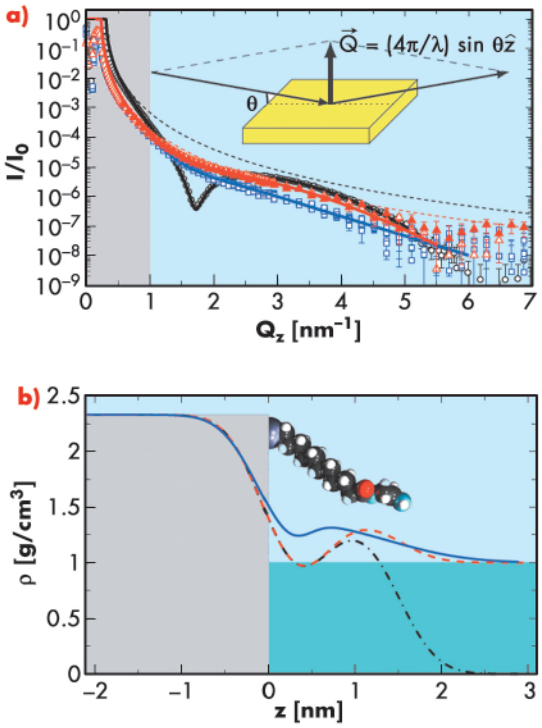


*Fig. 47:* Synchrotron X-ray reflectivity **a)** measurements and **b)** density profile model.

monomolecular layer of DNA molecules onto (and into) a soft, organic functionalisation layer, positively charged, covalently grafted on an oxide-free, atomically flat, single-crystal silicon wafer. Experiments were carried-out on beamline **ID10B** using 22.2 keV X-rays to traverse a 30 mm water path-length. The originality of the method was to characterise the grafted substrates at two different density contrasts (**Figure 47**): measured first under air, then under buffer solution, and then to analyse the data conjointly, as is often the practice for neutron scattering. This severely constrained the model parameters yielding a simple, robust measurement of the soft structure. Thus, the very subtle change observed *in situ* upon adsorption of the somewhat disordered monomolecular layer of DNA could be reliably interpreted in terms of adsorbed mass and therefore quantified. The high density of this layer then implies that the thin layer of monodisperse DNA double-stranded chains must exhibit some 2D nematic ordering (**Figure 48**), although this is not observable directly in the experiment.

This interpretation of the results goes against common beliefs about strong adsorption of macromolecules. This adsorption can be irreversible, yet the molecules still retain some mobility (rolling or sliding) to allow rearrangements and compaction through annealing. Even strongly adsorbed on a solid surface, DNA molecules remain accessible to molecular interactions with enzymes, for example, as can be shown through some elegant biochemical experiments **[3]**. The tethering of single molecules extending into the free solution is therefore not strictly necessary for biotechnological applications and this opens possibilities for the conception of new hybridisation biochips, in particular, with aims of taking advantage of electrical coupling with the oxide-free semiconductor substrates. Enhanced efficiency of the hybridisation reaction can also be gained through a reduction of dimensionality **[4]** on adsorption of the reactants to a surface.

**References**

[1] A. Goldar and J.-L. Sikorav, *Eur. Phys. J. E* **14**, 211 (2004).

[2] C. Douarche, J.-L. Sikorav, and A. Goldar, *Biophys. J.* **94**, 134 (2008).

[3] D. Rhodes and A. Klug, *Nature (London)* **286**, 573 (1980).

[4] G. Adam and M. Delbrück, Reduction of Dimensionality in Biological Diffusion Processes. In *Structural Chemistry and Molecular Biology*; A. Rich and N. Davidson, Eds.; W. H. Freeman and Company: San Francisco, 198 (1968).

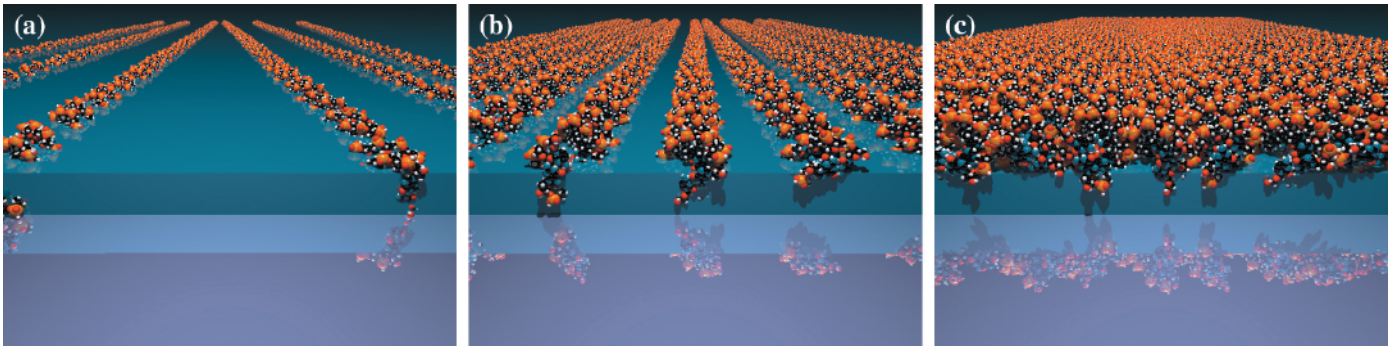


*Fig. 48:* Molecular models of the organisation of the adsorbed DNA layer **a)** full embedding, **b)** intermediate and **c)** full coverage.

# Elastic behaviour of a supercooled liquid

**Principal publication and authors**
Y. Chushkin, C. Caronna, and A. Madsen, *Europhys. Lett.* **83**, 36001 (2008).
*ESRF*

It is well known that liquids flow readily but at the same time they exhibit elastic response under an instantaneous deformation. Such behaviour can be described by the Maxwell-Debye (MD) viscoelastic model: After a sudden shear, the stress decays exponentially to zero with a relaxation time given by $\tau_{MD} = \eta/G(\infty)$, where $\eta$ is the dynamic viscosity and $G(\infty)$ is the instantaneous shear modulus [1]. Thus, on timescales much shorter than $\tau_{MD}$ the system responds elastically - like a solid - while the usual fluid behaviour is retrieved on longer timescales. The MD picture is also useful in describing the transition from a supercooled viscous liquid to a glass. For a glass-forming liquid in the supercooled state the viscosity increases strongly as the temperature decreases. Hence, $\tau_{MD}$ increases several orders of magnitude and finally exceeds 100–1000 s at the glass transition temperature ($T_g$) resulting in predominantly solid-like response, except on very long timescales.

Contrary to the MD picture, a different and intriguing solid-like behaviour was reported in the low-frequency regime for a variety of simple liquids and polymer melts. For instance, an elastic plateau in the storage modulus, the real part of the shear modulus $G(\omega)$, was detected by rheometry [2]. Soft, solid-like behaviour can be modelled by the Voigt-Kelvin (VK) approach where the materials display elastic response to applied stresses at low frequencies, but start flowing at higher frequencies and/or stresses. Such behaviour is often observed in complex fluids, *e.g.* gels, emulsions, and foams. Typically, these fluids consist of two or more separate phases and hence their structural organisation differs from that of simple liquids and polymer melts.

To study the response of a supercooled liquid close to $T_g$, we used grazing incidence X-ray photon correlation spectroscopy (XPCS) [3] from the surface. Liquid surfaces undergo continuous fluctuations due to the presence of thermally-excited capillary waves and their dynamics is governed by the surface tension and by bulk properties like the viscosity and the shear modulus. Grazing incidence XPCS was performed to probe the surface dynamics of the fragile glassformer polypropylene glycol with a molecular weight of 4 kDa (PPG 4000, $T_g$ ~ 200 K). The measured dispersion relations (**Figure 49**) of the surface fluctuation were extracted by fitting the intensity correlation functions (inset, **Figure 49**) at various temperatures and momentum transfers (q). Obviously, the dispersion curves are not crossing the origin so they deviate from predictions of both the classical capillary wave theory and the MD model. The data can only be modelled if elements from the VK model are employed accounting for the presence of low-frequency elasticity. A novel model combining

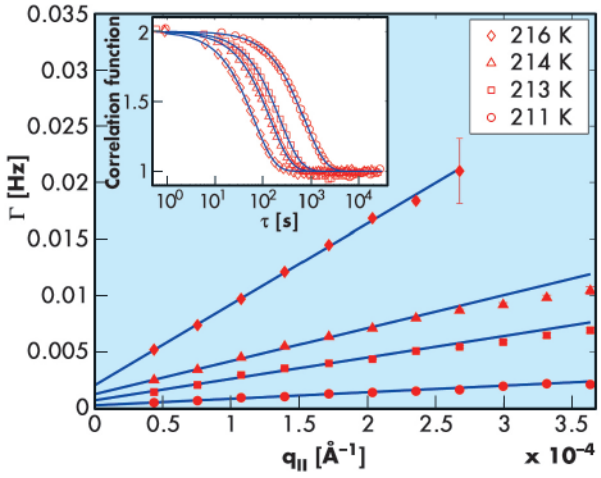


*Fig. 49:* Low-temperature dispersion curves. The lines are fits with the model. The inset displays normalised correlation functions (symbols) and fits (lines) at $q_{\parallel} = 7.55 \times 10^{-5}$ Å$^{-1}$.

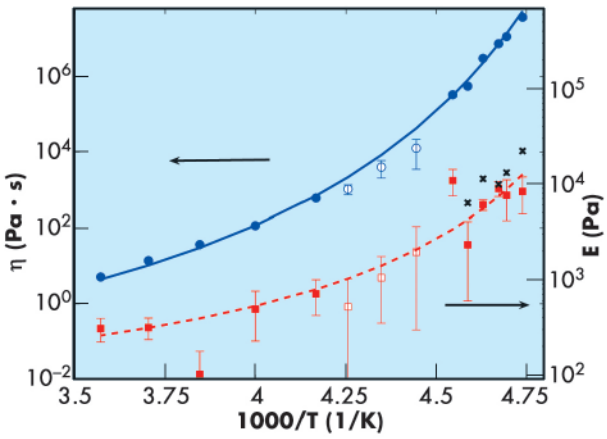


*Fig. 50:* The circles show the temperature dependence of the viscosity ($\eta$) and a fit with the VTF model is indicated (solid blue line). The red squares show the elasticity (E) extracted from XPCS and the black crosses indicate E deduced from static scattering data. The dashed red line is a guide for the eye following the VTF behaviour.

MD and VK viscoelasticity was developed and hence the viscosity and elasticity could be extracted as a function of temperature (**Figure 50**). As expected, the viscosity follows the Vogel-Tamman-Fulcher (VTF) expression and surprisingly the elasticity exhibits similar behaviour (**Figure 50**). This suggests a connection between low-frequency elasticity and dynamical heterogeneity with density fluctuations in the supercooled state that appear frozen at the time scale of the experiment.

**References**
[1] J.D. Ferry, *Viscoelastic Properties of Polymers* (Wiley & Sons. Inc. 1980).
[2] H. Mendil, P. Baroni and L. Noirez, *Eur. Phys. J. E* **19**, 77 (2006).
[3] G. Grübel, A. Madsen, A. Robert, X-ray Photon Correlation Spectroscopy *in Soft Matter Characterization, Eds. R. Borsali and R. Pecora*, pp 953-996. Springer (2008).

# Formation and ordering of gold nanoparticles at toluene-water and air-water interfaces

**Principal publications and authors**
M.K. Sanyal (a,b), V.V. Agrawal (b), M.K. Bera (a,c), K.P. Kalyanikutty (b), J. Daillant (d), C. Blot (d), S. Kubowicz (d), O. Konovalov (e), C.N.R. Rao (b), *J. Phys. Chem. C* **112**, 1739 (2008); M.K. Bera (a,c), M.K. Sanyal (a), S. Pal (a), J. Daillant (d), A. Datta (a), G.U. Kulkarni (b), D. Luzet (d), O. Konovalov (e), *Europhys. Lett.* **78**, 56003 (2007).
*(a) Saha Institute of Nuclear Physics (India)*
*(b) Jawaharlal Nehru Centre for Advanced Scientific Research (India)*
*(c) S.N. Bose National Centre for Basic Sciences (India)*
*(d) LIONS, CEA (France)*
*(e) ESRF*

Gold nanoparticles with sizes around 2 nm and below are being studied extensively because they exhibit novel electronic, magnetic, optical and catalytic properties. We are investigating the formation of Au-55 types of gold nanoparticles through a reduction reaction at a liquid-liquid interface. Diffuse X-ray scattering and reflectivity techniques **[1]** allow us to monitor the formation of gold nanoparticles at liquid-liquid interface. These techniques also provide information regarding the out-of-plane and in-plane structure of the gold nanoparticles at liquid surface and liquid-liquid interface.

*In situ* X-ray scattering measurements were carried out at beamline **ID10B** during the formation of gold nanoparticles at a toluene-water interface. The reduction reaction **[2]** uses an organic precursor of gold kept in the toluene layer and a reducing agent kept in the slightly alkaline water layer. As the reaction occurs through the creation of fingers from one liquid to another, the size (1 nm diameter) of the nanoparticles remain monodisperse. The reflectivity data collected as the reaction progresses are shown in **Figure 51a** and **Figure 51b** with the extracted electron density profiles across the interface. The peaks in the diffuse data shown in **Figure 51d** and the electron density profiles obtained from reflectivity clearly show the formation of a 1.2 nm nanoparticles core with a 1 nm organic shell which reorganize amongst themselves to give 13 member clusters with nanoparticle-nanoparticle separation, $d_2$ ~ 3 nm (**Figure 51c**), and cluster-cluster separation, $d_1$ ~ 18 nm (**Figure 51e**). Formation of organic layers at toluene-water interface could be monitored by measuring interfacial tension that reduces by an order of magnitude through diffuse scattering arising from capillary waves. This *in situ* high-energy (required to go through the upper liquid) X-ray

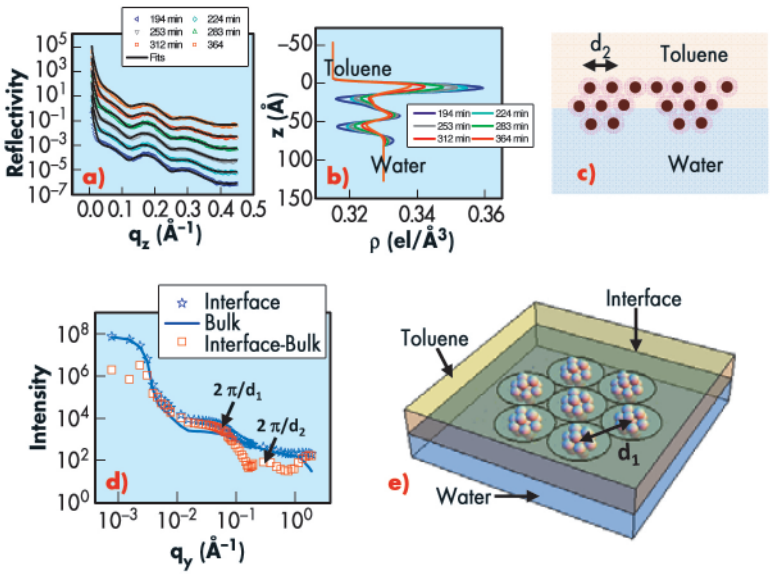


*Fig. 51:* **a)** X-ray reflectivity data and **b)** the electron density profile obtained by fitting. **c)** Cross-sectional view of the interface showing the three layers of nanoparticles. **d)** GID data and **e)** 3D view of the 13 member cluster-model.

scattering technique developed here will provide us with unique information regarding asymmetric interfacial reactions important not only for formation of tiny nanoparticles but also for several biological reaction mechanism. The published result is one of the most viewed papers in American Chemical Society journals.

We are also investigating methods to improve the packing density of nanoparticles on substrates by transferring a Langmuir monolayer from a water surface. Hydrophobic thiol-capped gold nanoparticles were spread on a water surface and the ordering of these particles was studied by X-ray scattering techniques as a function of in-plane pressure and temperature. The primary purpose of this study is to understand the structure and morphology of a monolayer of thiol-capped 2 nm gold nanoparticles on a water surface over the large reversible region of isotherm (1–15 mN/m) and to develop a method to improve coverage of these nanoparticles in deposited monolayer films. **Figure 52** shows ($q_{||}$-$q_z$) contour plots of the grazing incidence diffraction (GID) data collected from the monolayer at different surface pressures and temperatures. **Figure 52 (a,b,c)** show the bending of Bragg-rod at $q_z$ = 0.19 Å$^{-1}$ with higher surface pressure (13 mN/m). The rod straightens after decompression (1 mN/m) at 10°C. The Bragg-rod is also straightened (**Figure 52 (d,e)**) by annealing the monolayer at 44°C. The detailed analysis of the data shows that a monolayer of gold nanoparticles exhibits reversible buckling under a compression-decompression cycle and can be annealed thermally. We annealed a monolayer film at 13 mN/m from 16°C to 33°C and found that the annealed monolayer provides much more compact structures in the transferred films on a substrate. Atomic force microscopy measurements of these deposited films are shown in **Figure 52 (f,g)**.

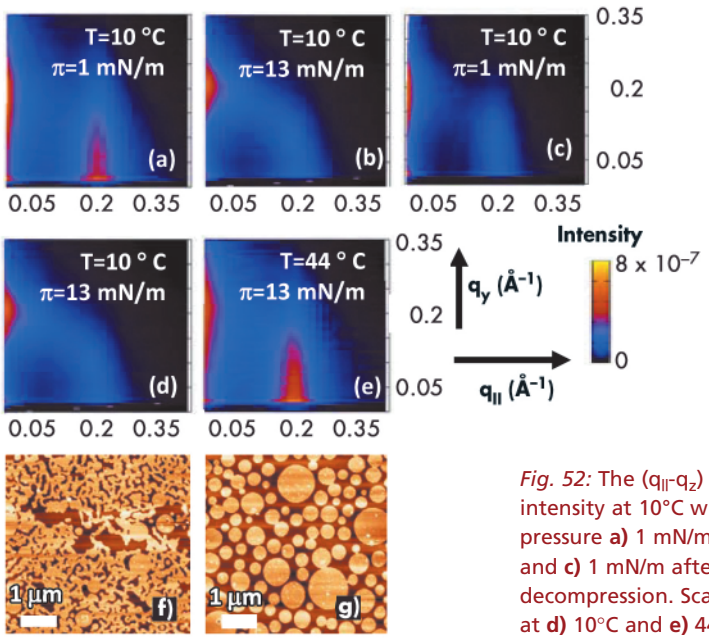


*Fig. 52:* The ($q_{||}$-$q_z$) contour plots of intensity at 10°C with surface pressure **a)** 1 mN/m, **b)** 13 mN/m and **c)** 1 mN/m after decompression. Scattered intensity at **d)** 10°C and **e)** 44°C w th 13 mN/m. AFM images of films deposited with 13 mN/m at **f)** 16°C and **g)** 33°C.

**References**
[1] M.K. Sanyal, S.K. Sinha, K.G. Huang, B.M. Ocko, *Phys. Rev. Lett.* **66**, 628 (1991).
[2] C.N.R. Rao, G.U. Kulkarni, P.J. Thomas, V.V. Agrawal, P. Saravanan, *J. Phys. Chem. B* **107**, 7391 (2003).

# Holographic diffraction imaging with hard X-rays

Nanoscience needs the ability to characterise the structure of objects on the nanoscale. For several reasons, hard X-rays are very attractive for this purpose: a wavelength in the order of ≈ 1 Å allows excellent spatial resolution; the high penetration into matter permits the study of thick samples or even buried structures in an easy-to-realise experimental setup; and with the upcoming hard X-ray free-electron lasers, the achievable time resolution will reach the femtosecond (fs) regime. Here, we demonstrate how coherent hard X-rays can be used for a determination of the absolute electron density of a lithographically tailored gold nanostructure (the letter P) from a single diffraction experiment, yielding both the shape and the height of the sample. We combine Fourier transform holography **[1]**, which – by a single Fourier transform – gives an unambiguous image of the sample structure, with iterative phase retrieval procedures **[2]** that enable us

**Principal publication and authors**
L.-M. Stadler (a), C. Gutt (a), T. Autenrieth (a), O. Leupold (a), S. Rehbein (b), Y. Chushkin (c), G. Grübel (a), *Phys. Rev. Lett.* **100**, 245503 (2008).
*(a) HASYLAB at DESY, Hamburg (Germany)*
*(b) BESSY, Berlin (Germany)*
*(c) ESRF*

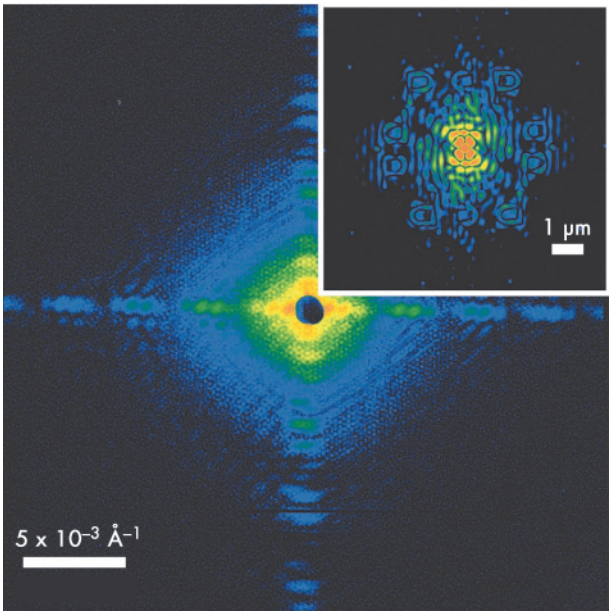


*Fig. 53:* Recorded hologram of a gold nanostructure – the capital letter P – surrounded by 5 reference scatterers. The inset shows the central part of the modulus of the Fourier transform of the recorded diffraction intensities, imaging the object and its rotated copy 5 times each. Both images are shown on a logarithmic pseudocolour scale.

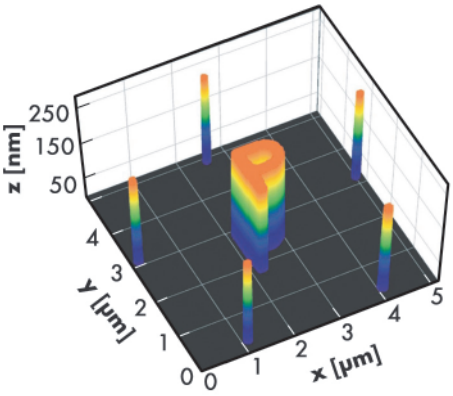


*Fig. 54:* Visualisation of the object geometry (letter plus reference dots) as determined from the electron density profile.

to push the spatial resolution toward the diffraction limit, which is determined by the maximum photon momentum transfer.

In Fourier transform holography, phase retrieval becomes particularly simple since, in a typical setup, the object and a spatially nearby reference are coherently illuminated. A single Fourier transform of the recorded hologram yields the convolution of the object and reference amplitudes, where the spatial resolution achievable is comparable to the reference source size **[1]**. In the present case 5 gold dots with about 175 nm diameter were placed on a circle of 2.5 µm radius around the gold nanostructure, each acting as reference source in the scattering process.

The corresponding hologram, which is shown in **Figure 53**, was recorded at beamline **ID10C** using coherent 8 keV photons. A single Fourier transform of the measured intensities gives the spatial autocorrelation of the overall object, including the cross-correlation between the object and the dots, which yields the object shape directly and its complex conjugate (a 180°-rotated copy) for each dot, as can be seen in the inset of **Figure 53**. The individual images are averaged to improve the statistics and the result – already comprising a qualitative image of the object – is fed into further iterative phase retrieval algorithms that are commonly used in coherent diffraction imaging **[2]**. Carrying out such phase retrieval runs yielded an image of the sample's electron density projected along the beam direction with ≈ 25 nm resolution. Knowing that the sample under investigation was made of gold and exploiting the fact that the scattering process can be described as Thomson scattering, it is straight forward to derive a mean sample height, which would be the correct height if the sample were flat. Actually, in the present case we can tell how well the assumption of a flat sample topography is, since this information is encoded in the phases of the hologram's Fourier transform. For our sample, a homogeneous height is confirmed with the actual value of ≈ 235 nm, as illustrated in **Figure 54**.

In conclusion, we have shown that hard X-ray holographic diffraction imaging is an excellent technique for determining electron density profiles on the nanoscale. A combination of the Fourier transform holography result and iterative phase retrieval methods made it possible to push the spatial resolution toward the diffraction limit. By virtue of this concept, we determined the absolute electron density and derived both shape and height of a lithographic gold nanostructure. This approach with coherent hard X-rays is ideally suited for applications in materials science, where samples can be thick, may consist of buried structures, or have to be measured under extreme conditions such as high pressure. Finally, we envision experiments of similar type to be carried out at future hard X-ray free-electron laser sources, where diffraction patterns can be collected within a single shot at the time scale of ≈ 10 fs, opening fascinating possibilities for imaging fast dynamic processes.

**References**
[1] S. Eisebitt, J. Lüning, W.F. Schlotter, M. Lörgen, O. Hellwig, W. Eberhardt, J. Stöhr, *Nature (London)* **432**, 885 (2004).
[2] H.N. Chapman, A. Barty, S. Marchesini, A. Noy, S.P. Hau-Riege, C. Cui, M.R. Howells, R. Rosen, H. He, J.C.H. Spence *et al., J. Opt. Soc. Am. A* **23**, 1179 (2006).

# On-axis microstructural studies of high-performance polymeric fibres

**Principal publications and authors**

R.J. Davies, M. Burghammer, C. Riekel, *Macromol.*, **40**, 5038 (2007); R.J. Davies, M. Burghammer, C. Riekel, *J. Appl. Crysta.*, **41**, 563 (2008); R.J. Davies, C. Koenig, M. Burghammer, C. Riekel, *Appl. Phys. Let.*, **92**, 101903 (2008).

*ESRF*

Microfocus X-ray diffraction ($\mu$XRD) is one of the few techniques that can probe the microstructures within individual polymeric fibres. Until recently, most $\mu$XRD studies of single fibres were performed in the standard fibre diffraction geometry. In this geometry, with the fibre perpendicular to the incoming beam, skin-core variations can be investigated based upon the changes observed between diffraction patterns collected at different positions across the fibre diameter. This approach is somewhat limited by the lack of information concerning the origin of scattering elements along the X-ray beam path. This makes it necessary to employ modelling in order to reconstruct skin-core morphologies in detail. Not only does this require a simplification of fibre structure, it risks the introduction of model bias.

A novel approach to skin-core microstructural studies has been demonstrated recently at the **ID13** microfocus beamline. By adopting an on-axis $\mu$XRD geometry, skin-core microstructural variations can be imaged directly from within single fibres exhibiting preferred orientation, and without the need for complex modelling. The technique involves carefully aligning a short section of fibre to the beam axis and then collecting diffraction patterns over a two-dimensional area (**Figure 55**). From the resulting diffraction data it is possible to reconstruct an image of the fibre cross-section based upon different microstructural parameters. For example, point-to-point variations in rotational disorder can be visualised directly between the fibre skin and core whilst the nature of radial crystallographic texture can be studied in detail.

On-axis $\mu$XRD experiments on single as-spun poly(*p*-phenylene benzobisoxazole) (PBO) fibres reveal a microstructure consisting of a relatively disordered skin and core, separated by an intermediate region which exhibits a lower degree of rotational disorder (**Figure 56a**). The width of the fibre skin appears to vary with position around the fibre circumference whilst the core region is slightly offset from the geometric centre of the fibre. This general skin-core morphology can be explained in terms of differences in coagulation rate and local variations in chain mobility during fibre formation. Structural asymmetry, meanwhile, suggests a heterogeneous coagulation environment.

High performance fibres, like many other materials, have hierarchical microstructures. It is therefore also necessary to consider structural features which may exist over larger length scales when investigating skin-core morphologies, such as those accessible to small-angle X-ray scattering (SAXS). On-axis SAXS experiments on single poly(*p*-phenylene terephthalamide) (PpTA) fibres reveal variations in SAXS

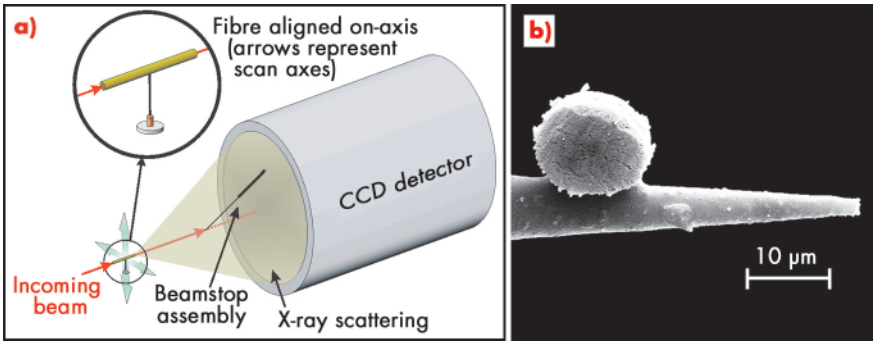


*Fig. 55:* **a)** Schematic of on-axis $\mu$XRD geometry and **b)** Scanning Electron Micrograph of a PpTA fibre section mounted on a glass capillary and viewed on-axis (prepared using a pulsed UV laser cutter).

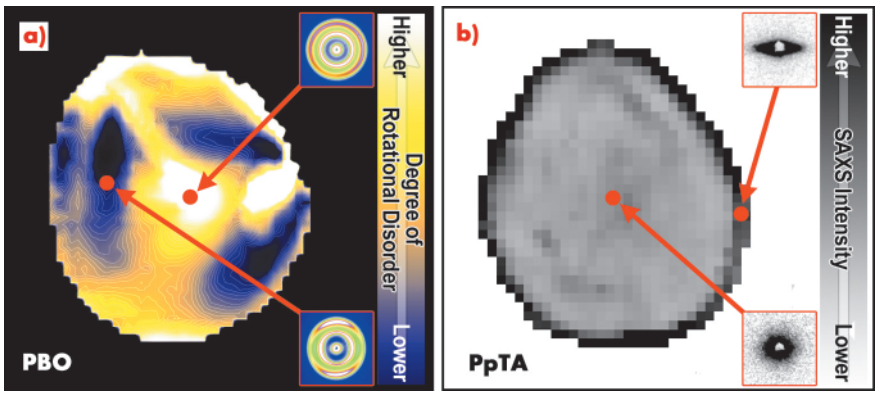


*Fig. 56:* **a)** Skin-core variations in rotational disorder for PBO fibre and **b)** variation of SAXS intensity over PpTA fibre cross-section. Individual diffraction patterns are shown inset.

between the fibre skin and core (**Figure 56b**), and differences between fibres having different processing histories. Following fibre spinning, the skin region contains elongated structures aligned parallel with the fibre's edge whilst the remainder of the fibre exhibits an isotropic SAXS pattern indicative of randomly oriented or cylindrical scattering elements. Following heat treatment, SAXS is reduced in all but the very core of the fibre. This suggests that, like coagulation, structural modification due to the heat treatment process may also occur heterogeneously.

Aside from skin-core microstructural variations, the on-axis $\mu$XRD geometry also allows radial crystallographic texture to be investigated in detail. Both PBO and PpTA fibres are found to exhibit this type of preferred orientation over their entire cross-sections. A model has been developed which allows azimuthal scattering profiles to be calculated for specific hk0 reflections under an on-axis geometry. By minimising the model against diffraction data, the nature of radial crystallographic texture can be probed. The results reveal that, for as-spun PBO, the $a^*$ unit cell axis is offset from the fibre radial direction by 23°. This angle corresponds to an almost radial arrangement of the highly planar PBO molecules. This suggests that solvent outflow during coagulation is at the origin of the radial crystallographic texture. In an edge-on arrangement, the PBO chains have the lowest drag coefficient.

Adopting an on-axis $\mu$XRD geometry has revealed many new microstructural features for high performance fibres whilst allowing previously known features to be examined in greater detail or confirmed from model predictions. The interest in characterising such microstructures is considerable. Not only are they thought to influence fibre mechanical properties, they can also dictate the interfacial performance of composite materials. If these complex structure-property relationships can be elucidated, it could provide a cost-effective way to tailor fibre properties during manufacture whilst opening the door to producing the super-fibres of tomorrow.

**Authors**
D. Cojoc (a), H. Amenitsch (b), C. Riekel (c), E. Ferrari (a), M. Rappolt (b), M. Burghammer (c), S. Santucci (a), G. Grenci (a), B. Sartori (b), B. Marmiroli (b).
*(a) TASC National Laboratory, Trieste (Italy)*
*(b) Institute of Biophysics and Nanosystems Research, Austrian Academy of Sciences, Graz (Austria)*
*(c) ESRF*

# X-ray microdiffraction of microsamples manipulated in fluidic environment without mechanical contact

Sample manipulation is one of the critical issues in synchrotron radiation microbeam experiments and in particular for experiments in special environments such as microfluidic cells. A common requirement is to position and move the sample in front of the beam. This is usually accomplished by fixing the sample on a support (*e.g.* capillary tip, grid), which is then moved precisely into the beam (**Figure 57a**). Consequently, this limits the degrees of freedom for sample orientation and manipulation and does not allow interactions between two independent objects to be studied in terms of mutual orientation, mutual growth

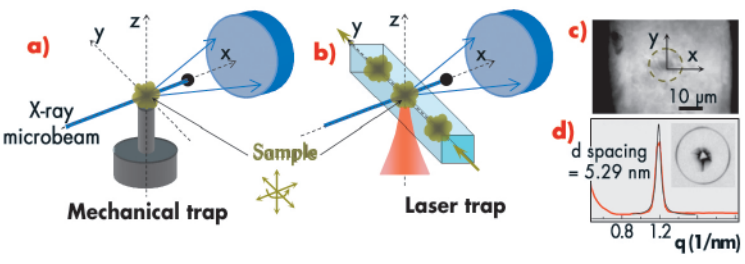


*Fig. 57:* Sample manipulation in X-ray microdiffraction experiments: **a)** Mechanical contact/trap and **b)** Laser trap without mechanical contact. **c)** Microscope image of a cluster of liposomes trapped optically (dash line) inside a capillary (the walls of the capillary are seen in black on the lateral sides), scale bar 10 µm. **d)** Plot of the azimuthally integrated intensity (red) and the Lorentz function (black) fitted to experimental data for the diffraction pattern (inset) at one position of the X-ray beam on an optically trapped POPE cluster.

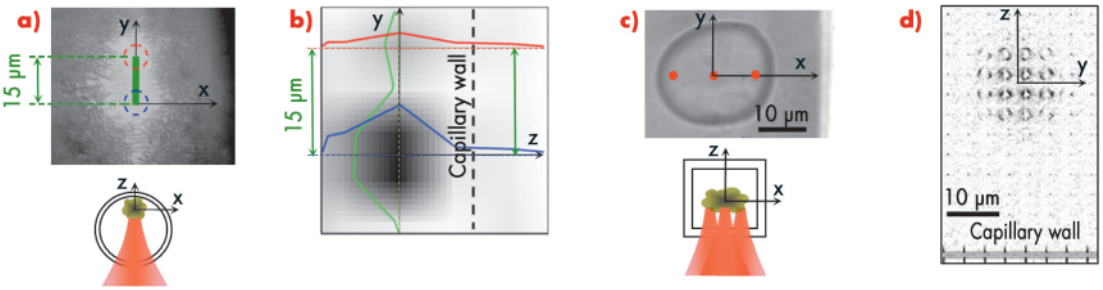


*Fig. 58:* Two clusters of liposomes trapped at separate positions, indicated by red and blue lines: **a)** microscope image of the traps (infrared laser) and **b)** X-ray scanning diffraction image (azimuthaly integrated intensities, mesh 3 µm x 5 µm) from the two clusters, with the corresponding intensity profiles. **c)** Microscope image of a large starch granule trapped with three laser traps (red spots) and **d)** scanning diffraction image (diffraction patterns) of the starch ({001}-9 nm).

(single cell study, real time crystal growth) [1].

One solution, laser tweezers have emerged as a powerful tool to manipulate a large variety of microparticles immersed in fluids [2]. We have now built a laser tweezer setup based on a custom inverted microscope and an infrared laser to trap, manipulate and aggregate micrometre-scale liposome particles inside a 100 micrometre glass capillary [3]. The micro-focused synchrotron radiation and laser beams are aligned to intersect each other, allowing the X-ray diffraction signal to be associated with the micrometre-sized region of interest inside the capillary (**Figure 57b**). This setup has been demonstrated at the **ID13** microfocus beamline by trapping about 50 multilamelar palmitoyl-oleoyl-phosphatidylethanolamine (POPE) liposome clusters of about 10 µm diameter (**Figure 57c**) and performing a scanning diffraction experiment with a 1 µm beam at about 13 keV. The azimuthally integrated intensity of the diffraction pattern obtained from the liposome cluster at one position of the X-ray beam is shown in **Figure 57d**. Multiple laser traps can be created using diffractive optical elements implemented on a spatial light modulator [4]. This allows manipulation of small separated clusters of liposomes and their fixation within the optical path of the X-ray beam. Using two traps, two different clusters could be brought into contact and, consequently, a reaction between them could be induced. The proof of concept is illustrated by **Figure 58**. Multiple traps can be also used to trap and manipulate larger particles such as starch granules, as shown in **Figure 58c**. We have improved the initial laser tweezers setup, allowing 2D optical trapping in a cylindrical capillary (**Figure 58a**), to a setup with full 3D optical trapping in a 80 µm squared capillary (**Figure 58c**). This enables positioning and orienting the sample in any point of the capillary [5]. The scanning diffraction image taken from a 20 x 24 µm starch granule is illustrated in **Figure 58d** together with refraction from the wall of the capillary thus demonstrating the trapping capability far away from the capillary wall.

The results presented here have given a first insight into this fascinating new field - to look to single supra-molecular assemblies with micrometre- and submicrometre-sized X-ray beams, which will find multiple applications in third- and in particular future fourth-generation synchrotron radiation sources.

**References**

[1] C. Riekel *et al., Curr. Opin. Struct. Biol.* **63** 556 (2005).
[2] D.G. Grier, *Nature* **424** 810 (2003).
[3] H. Amenitsch *et al., AIP Conf. Proc.* **879** 1287 (2006).
[4] D. Cojoc *et al., Appl.Phys. Lett.* **91** 234107 (2007).
[5] D. Cojoc *et al. Nat. Meth.* submitted (2008).

**Principal publication and authors**
M. Cammarata (a,b), M. Levantino (c), F. Schotte (d), P.A. Anfinrud (d), F. Ewald (a), J. Choi (e), A. Cupane (c), M. Wulff (a), H. Ihee (e), *Nature Methods* **5**, 881 (2008).
*(a) ESRF*
*(b) Centre for Molecular Movies, Niels Bohr Institute, University of Copenhagen (Denmark)*
*(c) Department of Physical and Astronomical Sciences, University of Palermo (Italy)*
*(d) Laboratory of Chemical Physics, National Institute of Diabetes and Digestive and Kidney Diseases, National Institutes of Health, Bethesda (USA)*
*(e) Center for Time-Resolved Diffraction, Department of Chemistry (BK21), Korea Advanced Institute of Science and Technology, Daejeon (Republic of Korea)*

# Probing protein structural changes in solution

Proteins are sequences of aminoacids that fold in 3D structures to accomplish their biological functions. Several studies have shown that protein conformational changes often play a crucial role in function regulation. So far, direct structural information on molecular motions has been obtained only in the crystal state by time-resolved protein crystallography [1]. However, protein crystals, while allowing model-free atomic resolution reconstruction, may induce stress/strain in the protein and hinder biologically-important structural changes. For proteins in solution, only indirect information has been obtained so far through time-resolved optical spectroscopy [2], thus highlighting the need of more direct, time-resolved, structural probes. In the last decade, protein solution scattering has undergone tremendous improvements in instrumentation and understanding of the experimental data, thus opening the possibility of studying protein structures in solution although at somewhat limited resolution of 5-10 angstroms [3].

We have therefore attempted to combine the exceptional time resolution achievable at ID09B (down to 100 ps) with the structural sensitivity already demonstrated for protein solution scattering.

We demonstrate this approach by using it to monitor the structural changes of different proteins after photodissociation of the ligand. The basic idea of the experiment is as follows: X-ray pulses are selected from the storage ring using a synchronised ultra-fast mechanical shutter (Figure 59). Synchronised laser pulses are produced by the laser system available at ID09B, where different pulse lengths and laser wavelength can be used. The laser/X-ray pulse pairs (suitably shifted by a time delay that can be varied electronically with an accuracy of ~ 10 ps) are sent to the sample to excite and probe the structure respectively. Typically, for a given time delay, the sample has to be exposed to about 1000 single laser/X-ray pulses to make efficient use of the CCD dynamic range.

For reciprocal vector ($q = 4\pi / \lambda \sin(\theta/2)$) in the range 0.05 to 2 Ang$^{-1}$ protein structural features gives rise to modulations of the scattering pattern that are fingerprints of the protein structure thus giving a direct structural probe. Since the light-induced differences are relatively small (< 5%), the data are usuallypresented as laseron-laseroff difference scattering patterns.

To test this new experimental approach we studied human haemoglobin because it offers a well-known example of structurally tuned biological function. Haemoglobin is made of four subunits each of them able to reversibly bind small molecules such as oxygen or carbon monoxide; it performs its biological task efficiently (oxygen delivery) thanks to the equilibrium between two conformations (called "R" and "T") having a dramatically different ligand affinity. Because of its fundamental biological importance, the transition between the R and T conformations (called "quaternary transition") has attracted the interest of many researchers over the last decades.

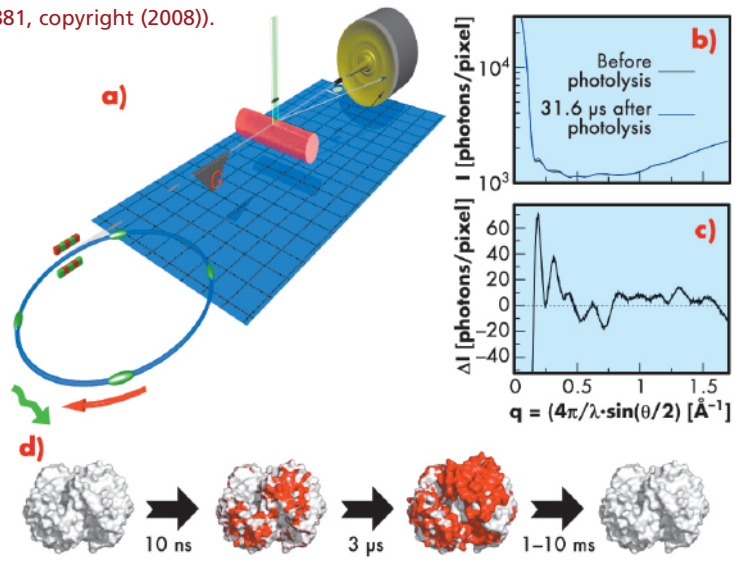


*Fig. 59:* Schematic of the TR-WAXS experimental technique (Adapted by permission from Macmillan Publishers Ltd: Nature Methods M. Cammarata *et al.*, *Nature Methods* **5**, 881, copyright (2008)).

In our experiment, a short laser pulse was able to break the protein-ligand bonds thus triggering protein structural relaxation from the initial ligand bound (R) structure to the unbound (T) structure; ligand rebinding from the solution eventually restores the initial condition.

Thanks to the high photon flux available at **ID09B**, we were able to provide a direct observation of the R –> T transition and to measure unambiguously the "waiting time" before the quaternary transition takes place. We found a time scale of about 2 μs challenging the previous assignment obtained with absorption spectroscopy **[4]** but in agreement with more recent time-resolved Raman data **[2]**. The main results are shown in **Figure 60**. The difference scattering patterns (laser at a given time delay – laser off) show a clear evolution of the signal that can be interpreted as the transition from an intermediate structure to the unbound equilibrium structure. The fact that the 3 μs and the 10 μs curves are very similar immediately suggests a time scale for the transition of a few microseconds.

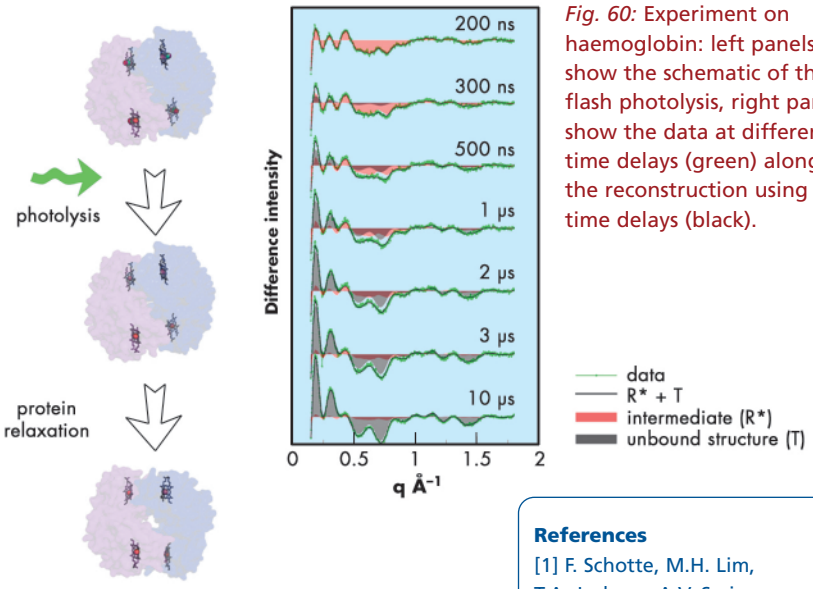


*Fig. 60:* Experiment on haemoglobin: left panels show the schematic of the flash photolysis, right panels show the data at different time delays (green) along with the reconstruction using two time delays (black).

This study shows that time resolved scattering can be a valuable experimental technique to gain insight into protein structures and their changes. Different excitation mechanisms like pH jump or T-jump could also be used and preliminary tests are being carried out.

**References**

[1] F. Schotte, M.H. Lim, T.A. Jackson, A.V. Smirnov, J. Soman, J.S. Olson, G.N. Phillips, M. Wulff, P.A. Anfinrud, *Science* **300**, 1944 (2003).

[2] G. Balakrishnan, M.A. Case, A. Pevsner, X.Z.C. Tengroth, G.L. McLendon, T.G. Spiro, *J. Mol. Biol.* **340**, 843 (2004).

[3] D.I. Svergun and M.H. Koch, *Rep. Prog. Phys.* **66**, 1735 (2003).

[4] J. Hofrichter, J.H. Sommer, E.R. Henry, W.A. Eaton, *Proc. Natl. Acad. Sci. USA* **80**, 2235 (1983).

# The molecular basis of the braking action of muscle studied by X-ray interference

**Principal publication and authors**

E. Brunello (a), M. Reconditi (a), R. Elangovan (a), M. Linari (a), Y.-B. Sun (b), T. Narayanan (c), P. Panine (c), G. Piazzesi (a), M. Irving (b) and V. Lombardi (a), *Proc. Natl. Acad. Sci. USA* **104**, 20114-119 (2007).

*(a) Università degli Studi di Firenze (Italy)*

*(b) King's College London (UK)*

*(c) ESRF*

We normally think of muscles as the motors that drive the movements of the body, but they can also act as brakes to resist an external force. An everyday example of this is the action of the muscles in the front of the legs to resist the force of gravity while walking down stairs. A more dramatic example would be deceleration of the body on landing after a jump (**Figure 61**), when the brakes must be applied in a small fraction of a second. This rapid braking response to an external force is an intrinsic property of isolated skeletal muscle cells. Our recent results at beamline **ID02** have revealed its molecular basis for the first time.

Skeletal muscle cells are packed with parallel arrays of two kinds of filaments, composed of the proteins myosin and actin respectively. Myosin is the motor protein; biochemically driven changes in the shape of part of the myosin molecule, called its motor domain, drive muscle contraction. The actin filaments form the molecular tracks for these myosin motors; when a muscle contracts the myosin motors pull the actin filaments along the

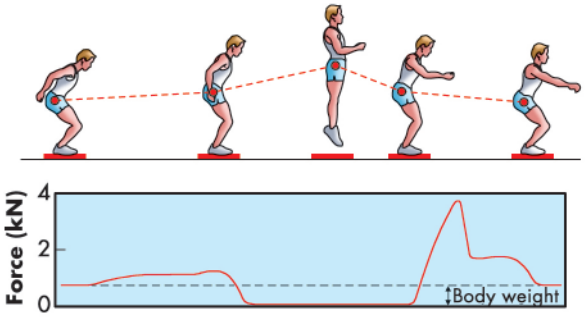


*Fig. 61:* The leg extensors decelerate the body after a jump (adapted from Cerretelli, Fisiologia dell'Esercizio, SEU, 2001).

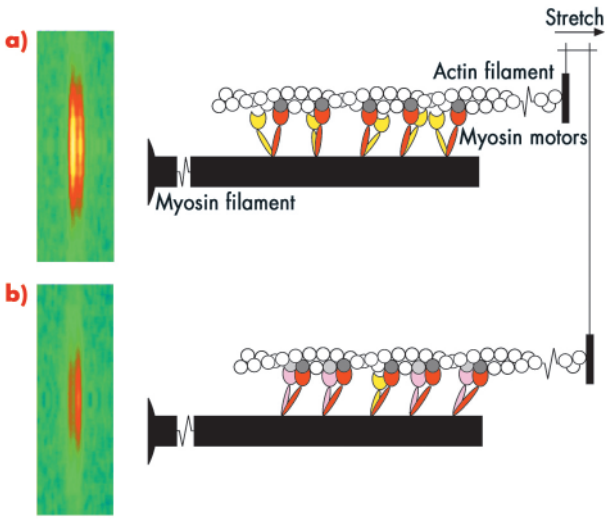


*Fig. 62:* Molecular basis of muscle braking; the M3 X-ray reflection and the conformation of the myosin motors before **a)**, and after being stretched **b)**.

myosin filaments. The filaments have an almost crystalline structure; motor domains are spaced at regular intervals along the myosin filaments, and this regular structure produces a measurable diffraction pattern when an isolated muscle fibre is illuminated by a narrow beam of X-rays. One of the X-ray reflections, called the M3, has two closely spaced peaks, **Figure 62** (left); this fine structure is an interference effect related to the bipolar structure of the myosin filament: each myosin filament actually contains two arrays of myosin molecules. This X-ray interference effect has proved to be a powerful technique to reveal molecular mechanisms in muscle contraction because it can measure the movements of the myosin motors along the filaments with angstrom resolution in an intact single muscle cell.

Measurements of these X-ray interference signals with sub-millisecond time resolution were previously used to investigate the molecular basis of force generation and active shortening in the myosin motor **[1-3]**. We have now used the technique to determine the mechanism of the braking response of muscle to a rapid stretching movement. The results showed that the response of a muscle to being stretched is fundamentally different to that during force generation or active shortening. An important clue to the mechanism came from high resolution mechanical measurements, which showed that the stiffness of the muscle fibre increases in less than a millisecond after being stretched quickly. The integrated mechanical/structural mechanism was revealed by combining the mechanical and X-ray interference results, and taking into account the fact that each myosin molecule has two motor domains. Before being stretched (**Figure 62a**), one of the motor domains (red) of each myosin molecule is attached to an actin monomer (dark grey), but its partner motor (yellow) is detached. When the muscle is stretched (**Figure 62b**), some of the partner motors (pink) attach to the neighbouring actin monomer (light grey) and resist being stretched, with the first motor acting as the strain sensor. This model can explain quantitatively the increase in stiffness and the changes in both interference peaks of the M3 X-ray reflection. It also provides an answer to the longstanding question: 'why does each myosin molecule in muscle have two motor domains?' When muscle is working as a motor to generate force and active movement, each myosin uses only one of its two motor domains. The partner domain is held in reserve, to act almost instantaneously as a brake when its attachment is promoted by strain in the first motor domain. In this way muscle resists an external stretching movement while minimising the stress on an individual motor.

**References**
[1] G. Piazzesi *et al. Nature* **415**, 659-662 (2002)
[2] M. Reconditi *et al. Nature* **428**, 578-581 (2004)
[3] G. Piazzesi *et al. Cell* **131**, 784-795 (2007)

# Structural Biology

## Introduction

Macromolecular crystallography has continued to evolve at the ESRF. The investment made in automation and beamline reliability is bearing fruit in a number of interesting ways. It is now clear that, in many cases, the complexity of the biological systems under study can only be fully revealed by combining extensive initial sample evaluation with detailed examination of the most promising crystals on the beamline best suited to the experiment. Obtaining the maximum information from a crystal also requires optimisation of the data collection procedure. Only by employing more complex experimental strategies can we hope to obtain a successful outcome to large numbers of experiments.

The improved operational reliability of the macromolecular crystallography (MX) beamlines has enabled a recent change to the way they can be accessed. Remote access was introduced during 2008 and allows complete instrument control from the user's home laboratory. This mode of access has already proven popular, currently accounting for more than 20% of all macromolecular crystallography experiments, a figure we expect to see rising. However, the advent of remote access has revealed a number of areas where further instrument development would be useful. It has also emphasised the need for the ESRF to adapt staffing levels and staff profiles in order to fully support such access to the beamlines.

The results presented in this chapter reveal the extent to which access to a broad portfolio of beamlines and synchrotron techniques is important for achieving success. We observe that both microfocus X-ray beams and tunability of the X-ray source are critical. In this latter context, the CRG beamlines BM14, BM16 and BM30A also play an important role, providing excellent services for their respective communities. The increased study of macromolecular complexes has led to a resurgence of interest in small-angle X-ray scattering from protein solutions. To provide much needed extra capacity ID14-3 has been converted to a SAXS beamline in a collaboration with the EMBL; it will provide rapid access for experiments in this area. The first such experiments were carried out on the beamline in 2008 and we look forward to a productive year in 2009.

Some of the fruits of the research undertaken in 2008 on the ESRF MX beamlines are reported in this chapter. We concentrate only on biological structures obtained and the insights that these give. Methodology contributing to this success is reported in the chapter on

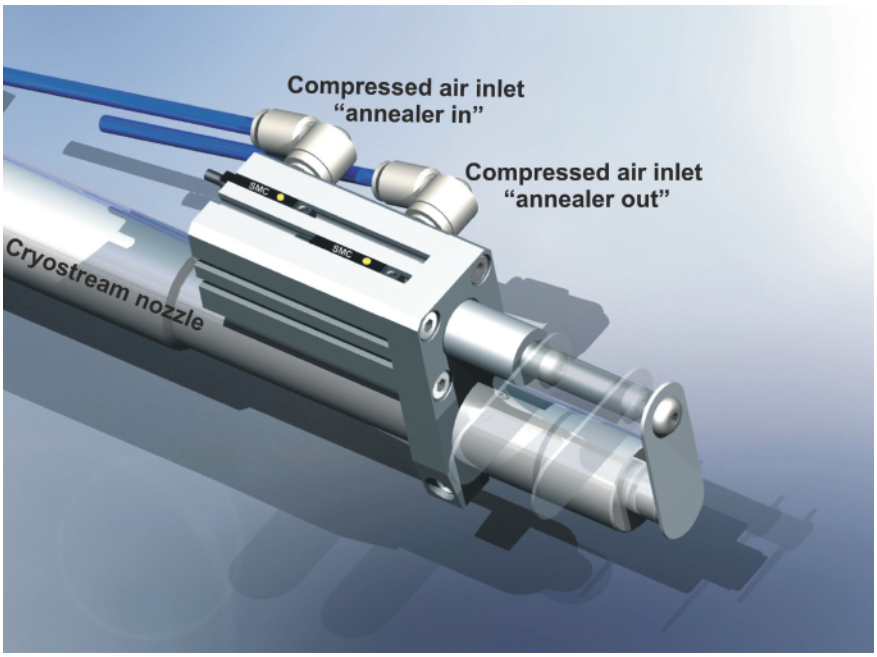


*Fig. 63:* Cryogenic cooling is used to prolong the life-time of crystals in an X-ray beam. However, in some cases flash-cooling degrades crystal quality if conditions are not ideal. Annealing or tempering of samples adversely affected by cryocooling can often improve diffraction quality and is now considered a standard technique in macromolecular crystallography. A small, inexpensive automatically-operated annealing device is installed on all ESRF macromolecular crystallography beamlines that allows annealing of samples either from the beamline or by users accessing the beamline remotely. For details see: T. Giraud *et al., J. Appl. Cryst.* **42**, 125-128 (2009).

Methods and Instrumentation (p. 120), and in **Figure 63**, which presents a new annealing device available on the beamlines.

The current degree of automation available on the MX beamlines is due to the consistent hard work of the ESRF BLISS, SciSoft, and MX Groups in partnership with the EMBL Grenoble outstation. Their efforts were recognised by the annual BESSY innovation award. Work on renewing the MX suite of beamlines will continue through 2009 with the development of detailed plans for new beamlines and modes of access. We look forward to the help and input of our User community in the continuation of these projects.

***G. Leonard***
***and S. McSweeney***

# An open and shut case

**Principal publication and authors**
W. Wang (a), S.S. Black (b), M.D. Edwards (b), S. Miller (b), E.L. Morrison (b), W. Bartlett (b), C. Dong (a), J.H. Naismith (a) and I.R. Booth (b), *Science* **321**, 1179 (2008).
*(a) Centre for Biomolecular Sciences, University of St. Andrews (UK)*
*(b) School of Medical Sciences, University of Aberdeen (UK)*

Bacteria are survivors and cope with dramatic changes in environment during their life cycle. One such stress is osmotic shock, in moving from a salty environment (such as biological fluids) to a salt-free environment (water), whereby bacteria experience pressures up to 14 atm. The pressure is felt as a swelling of the cytoplasm (turgor pressure), and, unless relieved, the consequence is rupture of the membrane. However, bacteria are able to release this pressure build up using the mechanosensitive channels, MscS and MscL.

The breakthrough in the structural understanding of mechanosensitive channels came from the work of the Rees lab **[1]**. This 3.95 Å structure showed that MscS is a heptamer with each monomer consisting of three transmembrane helices at the N-terminus and a large cytoplasmic domain. The heptamer is arranged symmetrically around a 7-fold symmetry axis normal to the membrane. One of the transmembrane helices (TM3) is split into two TM3a and TM3b. Two rings of leucine side chains on TM3a point into the central channel. This provides a "vapour lock" and, in essence, these side chains prevent any ions or proteins from travelling from the cytoplasm into the periplasm. Under pressure this lock must be opened, however the mechanism by which this is accomplished remained obscure.

The route to structural insight came from identifying mutants which were more likely to be open from electrophysiology studies.

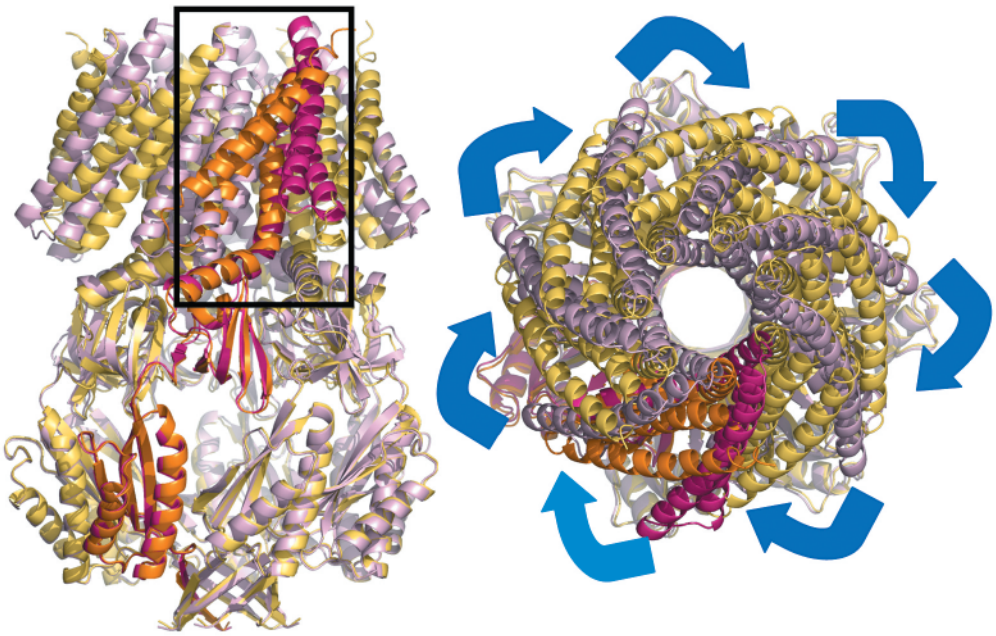

*Fig. 64:* The open structure of MscS is shown in orange (A subunit) and yellow (subunits B-G). The closed structure is shown in red (A subunit) and pink (subunits B-G). TM1 and TM2 have rotated around the seven-fold axis.

Thus we set out to study the crystal structures of different mutants of MscS to see whether any showed an altered state. The project would have been impossible without the ESRF facilities, membrane protein crystals do not diffract well and we screened many hundreds of crystals from several mutants before finally arriving at a 3.45 Å structure for the A106V mutant. This mutation appears to destabilise the previously observed closed form but does not appear to stabilise the open form. Compared to the native structure, the mutant MscS shows dramatic changes in the position and orientation of transmembrane helices, most notably TM1 and TM2. These two helices have moved around 1/7 of a revolution and increased their tilt with respect to the membrane (**Figure 64**). As a result of this dramatic movement, TM3a pivots at G113 in such a way that it become parallel to the membrane normal. It is also "pulled" out of the central pore.

The movement of TM3a results in a iris like motion of the leucine side chains which create an open pore. Thus a picture emerges of TM1 and TM2 acting as the pressure sensor which in turn operates the valve on TM3a. The structural data of course are only a model for the situation inside the cell. The structural model for the opening and closing of MscS predicts a number of key side chain interactions. These hypotheses were tested by site directed mutagenesis and gave strong support to the structural model.

The significance of our work lies in understanding the physiology of pathogens; the opening and closing of channels is an important topic in biology. The second significant finding is that carefully chosen site directed mutants may provide an important route to the observation of conformational states of membrane proteins.

**Reference**
[1] R.B. Bass, P. Strop, M. Barclay, D.C. Rees, *Science* **298**, 1582 (2002).

## Structural basis of Dcp2 recognition and activation by Dcp1

**Principal publication and authors**
M. She (a), C.J. Decker (b), D.I. Svergun (c), A. Round (c), N. Chen (a), D. Muhlrad (b), R. Parker (b), H. Song (a), *Mol. Cell* 29, 337 (2008).
*(a) Laboratory of Macromolecular Structure, Institute of Molecular and Cell Biology (Singapore)*
*(b) Department of Molecular and Cellular Biology and Howard Hughes Medical Institute, University of Arizona (USA)*
*(c) Hamburg Outstation, EMBL (Germany)*

RNA degradation plays an important role in the control of gene expression and in the elimination of aberrant mRNAs. Decapping is a critical step since it promotes the bulk of mRNA turnover and functions in specialised pathways such as nonsense-mediated decay (NMD), adenine/uridine-rich element (ARE)-mediated decay, and the turnover of some mRNAs promoted by miRNAs **[1]**.

Removal of the 5′ cap structure is catalysed by the decapping complex consisting of at least two subunits: Dcp1p and Dcp2p. Dcp1p is a small protein containing an EVH1 domain, which is generally a protein-protein interaction module. The catalytic subunit, Dcp2p, recognises capped mRNA substrates and cleaves the pyrophosphate bond of the $m^7$GpppN cap, releasing $m^7$GDP as product. Dcp2p belongs to the nudix hydrolyase family, which contain the nudix signature nudix motif. The crystal structure of Dcp2p from *S. pombe* reveals that a conserved N-terminal region forms a two-lobed structure with an α-helical domain preceding the nudix domain **[2]**. That Dcp2p prefers longer RNA substrates suggests the presence of spatially separated RNA-binding and catalytic sites on the nudix domain, but the nature and site of the RNA binding domain of Dcp2p has not yet been determined. Additionally, despite the conservation of Dcp1p and its requirement for decapping, how Dcp1p interacts with and activates Dcp2p remains elusive.

We determined the crystal structure of Dcp1p in complex with a truncated *S. pombe* Dcp2p (Dcp2n) using data collected on beamline **ID29**. The structure reveals both open and closed forms of the Dcp1p/Dcp2n complex (**Figure 65**). In the closed complex, a compact structure is formed with both Dcp1p and the N-terminal α-helical domain of Dcp2n being in close proximity to the nudix domain of the latter. In the open form, the α-helical

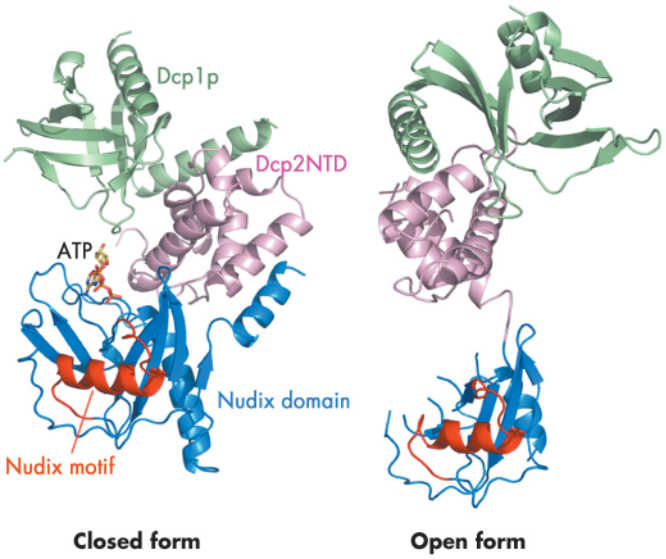


*Fig. 65:* Ribbon diagrams of the Dcp1p-Dcp2n complex in the closed and open conformations. Dcp1p is shown in green, the N-terminal domain (NTD) of Dcp2n in pink, the nudix domain of Dcp2n in blue and its nudix motif in red. In the closed confor mation, the ATP molecule we observe in the active site is shown in a stick representation.

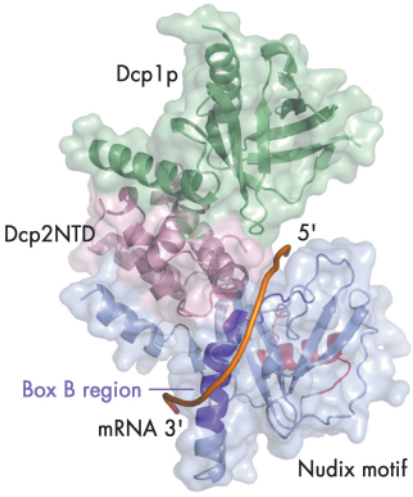


*Fig. 66:* A model illustrating the putative RNA binding channel in the closed form of the Dcp1p-Dcp2n complex. A 12-mer poly(A) mRNA is shown in a tube representation and the Box B region of Dcp2n is coloured in dark purple.

and nudix domains of Dcp2n do not interact and are separated by a flexible linker, making the whole molecule resemble a dumb-bell. Small-angle X-ray scattering (SAXS) analysis confirmed that the two forms of the Dcp1p/Dcp2n complex also exist in solution and that formation of the closed complex is influenced by ligand binding. Interestingly, we observed that ATP is bound to the catalytic centre (**Figure 65**), and that ATP, di-nucleotide (pAA) and the cap analogue $m^7$GpppA enhance the formation of the closed complex and inhibit decapping. Mutational analysis in the flexible linker region indicated that the closed complex we observe is, or closely resembles, the catalytically more active form, suggesting that a conformational change between open and closed complexes might control decapping. We have also identified a region involved in RNA binding which is located some distance from the active site (**Figure 66**).

Our structural analyses coupled with biochemical data suggest a possible mechanism by which Dcp2p recognises its substrate. The substrate is bound in a channel on the surface of Dcp2p with the cap structure in the active site (**Figure 66**). The main body of the RNA then wraps across the nudix domain and follows the channel along the Box B helix. This model provides a possible structural explanation for the preference of decapping enzymes for longer RNA substrates: RNA would need to be at least 12 residues long to bind in both the active site and the Box-B region on Dcp2p.

Our analyses suggest that Dcp1p stimulates the activity of Dcp2p by stabilising the closed complex, which is promoted by the presence of substrate in the active site. Finally our structure also reveals that the Dcp1/Dcp2 interface is not fully conserved, explaining why the Dcp1-Dcp2 interaction in higher eukaryotes requires an additional factor.

**References**

[1] J. Coller, and R. Parker, *Annu Rev Biochem* **73**, 861 (2004).

[2] M. She, C.J. Decker, N. Chen, S. Tumati, R. Parker, and H. Song, (2006). *Nat Struct Mol Biol* **13**, 63 (2006).

# Structural biochemistry of a bacterial checkpoint protein

**Principal publication and authors**

G. Witte (a,b), S. Hartung (a,b), K. Büttner (b,c) and K.-P. Hopfner (a,b), *Mol. Cell* **30**, 167-178 (2008).

*(a) Munich-Centre for Advanced Photonics, Munich (Germany)*

*(b) Center for Integrated Protein Science at the Gene Center, Munich (Germany)*

*(c) Present address: Max-Planck-Institute for Biochemistry, Martinsried (Germany)*

Maintaining genome integrity is one of the most important processes for the sustainment of life and the prevention of cytotoxic or cancerogenic DNA aberrations. Cells possess various DNA repair pathways as well as DNA damage checkpoint control mechanisms, to ensure that cell cycle progressions occur only with intact chromosomes. In humans, inactivated DNA repair pathways and damage checkpoint controls lead to genetic instability, cancer and ageing syndromes. DisA (DNA integrity scanning A) was recently identified as a checkpoint protein in *Bacillus subtilis* **[1]**. It appears to co-localise with sites of DNA double-strand breaks, delaying

the cell from entering the sporulation phase. Intriguingly, DisA appears to exist in a single, large complex inside *B. subtilis* that scans the chromosome for DNA damage. To reveal the molecular and structural mechanism of DisA we used a combination of high-resolution X-ray crystallography, small-angle X-ray scattering (SAXS) and biochemical and biophysical analysis.

We determined the crystal structure of the *Thermotoga maritima* DisA homolog (TmaDisA) to 2.1 Å resolution, using multiple-wavelength anomalous dispersion data collected at beamline **ID29**. According to analytic ultracentrifugation, DisA forms a large octamer with a molecular weight of ~360 kDa. We verified the likely octamer observed in the crystal lattice using SAXS. A protomer of TmaDisA can be divided into 3 domains (**Figure 67**): an N-terminal globular domain (domain of unknown function, DUF147), a central helical domain and a C-terminal HhH domain. In the octamer eight DUF147 domains form the core of the complex, while the HhH domains form two peripheral tetrameric putative DNA binding platforms.

What is the function of DUF147? Surprisingly, at each of the four interfaces between opposing DUF147 domains we found additional electron density for new types of cyclic dinucleotides. We identified these ligands as cyclic diadenosine monophosphates and have shown that DUF147 of DisA is in fact a diadenylate cyclase. It uses pairs of ATP molecules bound to opposing DUF147 domains for the cyclisation reaction. Thus we suggested renaming the N-terminal domain DUF147 to "DAC-domain" (for diadenylate cyclase). The finding of novel diadenylate cyclase activity and c-di-AMP as product of an enzymatic reaction is quite intriguing, considering the well known and important role of its cousin c-di-GMP as a second messenger in various bacterial processes, including biofilm formation **[2]**. Possibly, c-di-AMP also acts as messenger, *e.g.* to coordinate DNA repair and sporulation, or more generally cell division since DisA is also found in non sporulating bacteria.

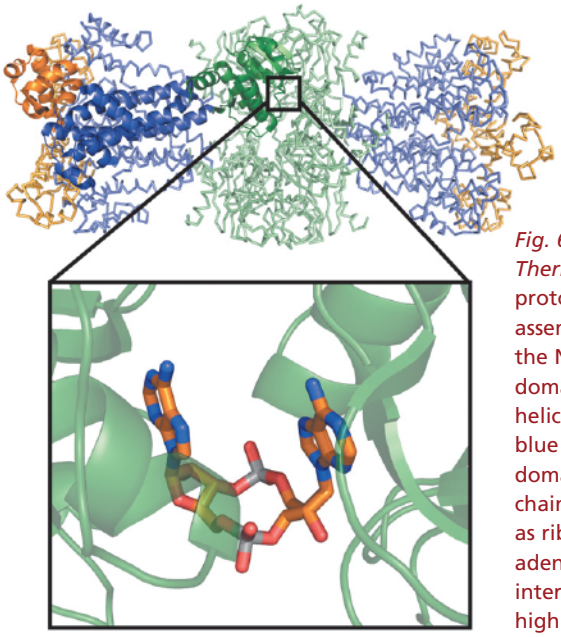

*Fig. 67:* Overall structure of *Thermotoga maritima* DisA. One protomer of the octameric assembly is shown in cartoon style: the N-terminal DAC (DUF147)-domain is shown in green, the helical central spine domain in blue and the C-terminal HhH domain in orange. The other chains in the octamer are shown as ribbons. The binding of cyclic-di-adenosine monophosphate at the interface of two DAC-domains is highlighted.

How is di-adenylate cyclase linked to DNA damage scanning? The presence of four HhH-motifs at both ends of the DisA octamer suggests that DisA may not recognise DNA double-strand breaks, but rather its repair intermediates, *e.g.* Holliday junctions. Gel-electrophoretic mobility shift assays showed that DisA preferentially binds to DNA strands resembling such recombination intermediates but not to plain ssDNA or dsDNA. Consistently, branched DNA substrates, but not plain ssDNA or dsDNA, strongly inhibited the DAC-activity. The structural arrangement of the octamer is ideally suited to allosterically regulate di-adenylate cyclase activity by binding of branched DNA to the HhH-domains array via conformational changes transmitted by the helical middle domain (**Figure 68**).

Our results suggest that DisA may detect sites of unfinished DNA double

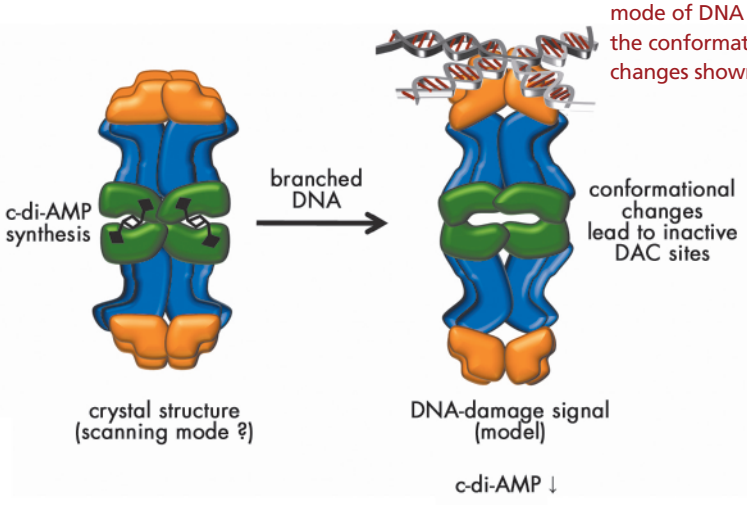


*Fig. 68:* Model for the mechanism of action of DisA in checkpoint control. In the absence of chromosomal damage (scanning mode), DisA synthesises c-di-AMP. Recognition of branched nucleic acids such as stalled replication forks or recombination intermediates might inhibit c-di-AMP synthesis thus signalling the presence of unsegregatable chromosomes. Several aspects of the model are speculative, such as the precise mode of DNA binding and the conformational changes shown.

strand break repair, recombination intermediates or stalled replication forks - all of which should not occur during sporulation or cell division. DisA may signal the presence of such structures via c-di-AMP (or lack of c-di-AMP) although the precise role of c-di-AMP needs to be addressed in future studies. Intriguingly, DUF147 is present in many other bacteria as well as in archaea, arguing for the existence of other c-di-AMP associated processes.

**References**
[1] M. Bejerano-Sagie *et al., Cell* **125**, 679 (2006).
[2] U. Römling and D. Amikam, *Curr Opin Microbiol.* **9**, 218 (2006).

**Acknowledgements**
This work was supported by grants from the German Research Council (SFB 684) and the European Union (IP DNA Repair) to K.-P.H.

# Pilus assembly across the bacterial outer membrane

**Principal publication and authors**
H. Remaut (a), C. Tang (c), N.S. Henderson (d), J.S. Pinkner (e), T. Wang (c), S.J. Hultgren (e), D.G. Thanassi (d), G. Waksman (a), and H. Li (c), *Cell* **133**, 640 (2008).
*(a) Institute of Structural and Molecular Biology, Birkbeck College/UCL London (UK)*
*(c) Biology Department, BNL, NY (USA)*
*(d) CID, Stony Brook University, NY (USA)*
*(e) DMM, Washington University School of Medicine, MO (USA)*

The chaperone-usher (CU) pathway is a translocation system used to assemble adhesive multi-subunit fibres on the outer surface of gram-negative bacteria. CU pili are formed by the non-covalent polymerisation of several hundreds or thousands of pilus subunits which consist of an incomplete immunoglobulin (Ig)-like fold lacking the C-terminal β-strand. In the periplasm, a cognate chaperone assists in pilus subunit folding by donating a β-strand to complement the truncated Ig-like fold of the pilus subunit, a process termed donor-strand complementation (**Figure 69**, A*) **[1]**. Chaperone:subunit complexes are then recruited to a pilus assembly platform in the outer membrane (OM) called the "usher". The usher catalyses ordered subunit polymerisation and mediates translocation of the nascent pilus to the cell surface. Polymerisation of pilus subunits occurs through an intermolecular fold complementation mechanism involving the first 10-20 residues (termed "N-terminal extension" or Nte) of the pilus subunit next in assembly. The Nte of a newly recruited subunit inserts in the groove (left by the missing strand) of the subunit previously assembled, competing off the chaperone still associated with that subunit (**Figure 69**, B*) **[2]**. This so-called "donor-strand exchange" process, in which the chaperone donor-strand is exchanged for an incoming subunit's Nte, occurs in the absence of an electrochemical gradient or an hydrolysable energy source. How subunit polymerisation and fibre translocation across the membrane are orchestrated by the usher remains poorly understood, largely due to the lack of high resolution structural information on the assembly platform.

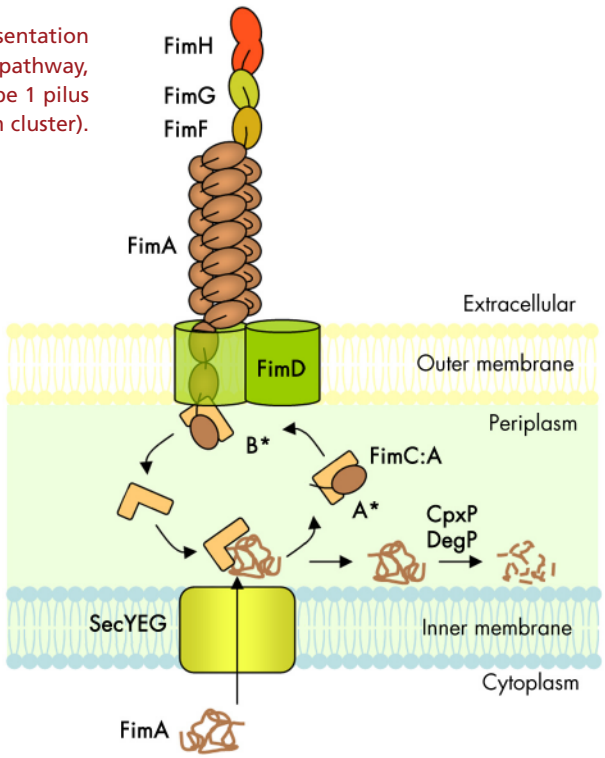


*Fig. 69:* Schematic representation of the CU biosynthetic pathway, labelled according the type 1 pilus system (Fim cluster).

Using data collected at the beamlines **ID29** and **ID23-1**, we determined the crystal structure of the detergent-solubilised translocation domain of the P pilus usher PapC to 3.2 Å resolution. Ushers are ~800 residue proteins comprising a central β-barrel domain flanked by periplasmic soluble domains of ~125 and ~170 residues at the N- and C-termini respectively. The N-terminal domain forms the

recruitment site for chaperone:subunit complexes. The function of the C-terminal domain is unknown, though some indications point to a possible role in an early activation event.
The crystal structure reveals the usher translocation pore comprises a 24-stranded β-barrel that gives rise to a channel with inner diameter of ~ 45 by 25 Å, compatible with the translocation of folded pilus subunits (**Figure 70**).
In its non-activated form, however, this pore is occluded by a folded plug domain that is inserted into the loop between strands 6 and 7. In addition, a β-hairpin formed by adjacent strands curves back out of the barrel wall, into the pore lumen and contacts the base of the plug domain. Most likely usher activation necessitates a conformational change in these two elements, resulting in opening of the pore. The crystals of the PapC translocation domain also exhibit a dimerisation interface along the flat surface of the kidney-shaped β-barrel, very similar to the twinned pore observed by electron microscopy of 2D crystals of lipid-reconstituted full-length PapC.

In combination with the single particle cryo-electron microscopy imaging of the type 1 pilus usher (FimD) bound to a translocating three-subunit assembly intermediate (**Figure 70**), this structure provides, for the first time, a molecular snapshot of a twinned pore translocation machinery responsible for CU pilus assembly at the bacterial outer membrane. Unexpectedly, only a single pore is used for organelle secretion. The combined structures suggest a model in which both usher protomers are required for subunit polymerisation through a mechanism of alternating chaperone:subunit complex recruitment. At each step of the incorporation cycle, the N-terminal domain of one of the two pores is engaged in binding the chaperone:subunit complex at the base of the growing fibre, whilst the N-terminal domain of the opposing pore forms the docking site for a newly incoming chaperone:subunit complex. During donor-strand exchange, the chaperone at the now penultimate site in the fibre is released, thereby liberating that usher's N-terminal domain for a new recruitment step. In this way, alternations in chaperone:subunit recruitment at either usher N-terminus allow the step-wise incorporation of new pilus subunits, with the growing fibre translocating through the activated channel in the twinned pore complex.

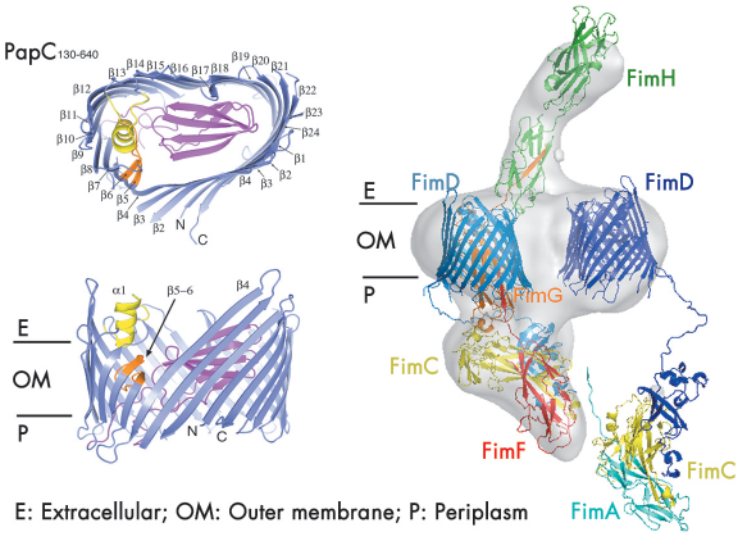


*Fig. 70:* (Left) Side and top views of the PapC translocation channel. (Right) Model of the type 1 pilus assembly intermediate ($FimD_2$:FimC:FimF:FimG:FimH) docked into the reconstructed electron density obtained with single particle cryo-EM. A newly incoming chaperone:subunit complex (FimC:FimA) is modelled in, bound to the N-terminal domain of the second usher (FimD).

**References**
[1] F.G. Sauer, K. Fütterer, J.S. Pinkner, K.W. Dodson, S.J. Hultgren and G.Waksman *Science* **285**, 1058 (1999).
[2] H. Remaut, R.J. Rose, T.J. Hannan, S.J. Hultgren, S.E. Radford, A.E. Ashcroft, and G. Waksman, *Molecular Cell* **22**, 831 (2006).

## Structural insights into the DegP protease-chaperone

Most proteins acquire a precisely-defined 3D-structure to fulfill their cellular functions. However, this molecular architecture is highly susceptible to various stress conditions such as heat-shock. The resultant misfolding not only impairs protein functionality but also generates molecular aggregates that are extremely toxic for the cell. To survive stress conditions, all organisms employ sophisticated protein-quality-control (PQC) systems in which dedicated chaperones and proteases collaborate closely with each other to reduce the amount of misfolded, aggregation-prone protein species produced.

The heat-shock protein DegP, a member of the HtrA family of proteases, is an essential PQC factor in the cellular envelope of Gram-positive

**Principal publication and authors**
T. Krojer (a), J. Sawa (a), E. Schäfer (b), H.R. Saibil (b), M. Ehrmann (c) and T. Clausen (a), *Nature* **453**, 885 (2008).
*(a) Research Institute for Molecular Pathology - IMP, Vienna (Austria)*
*(b) Crystallography Department and Institute of Structural Molecular Biology, Birkbeck College, London (UK)*
*(c) Centre for Medical Biotechnology, FB Biology and Geography, University Duisburg-Essen, Essen (Germany)*

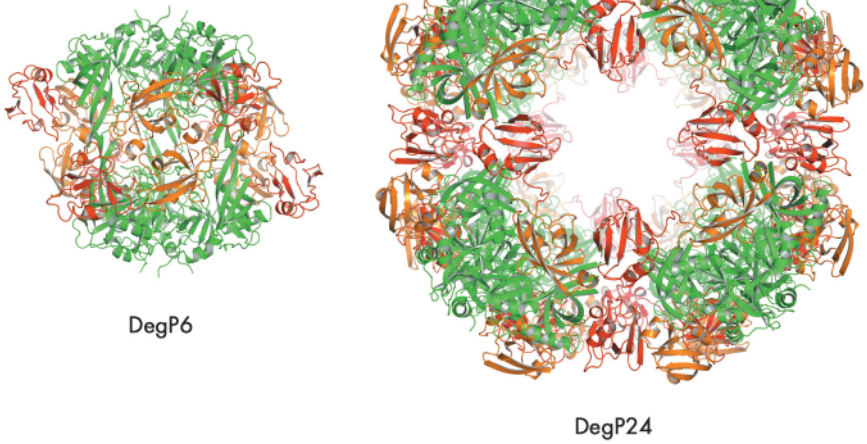


*Fig. 71:* Comparison of DegP6 and DegP24. The colour code is the same for the two molecules: protease domains (green), PDZ1 (orange), PDZ2 (red).

bacteria [1] and exhibits strikingly different properties to those of the functionally-related protease complexes found in the cytosol: (i) Since the periplasm is devoid of nucleotides, DegP has to function without ATP. (ii) DegP can reversibly switch between protease and chaperone functions in a temperature- and substrate-dependent manner [2]. This switch in activity allows an immediate response to environmental changes that are sensed more directly in the periplasm than in the cytosol due to the porous character of the outer membrane. (iii) DegP acts exclusively on misfolded proteins and does not depend on co-factor adaptor or regulatory proteins. The autonomy of DegP is based on an intricate multi-domain organisation comprising a chymotrypsin-like protease domain linked to two C-terminal PDZ domains that contain different binding sites for substrate proteins, allosteric effectors and even cellular membranes.

In the absence of stress conditions, DegP exists as a hexamer (DegP6), a structure that we determined in 2002 using data collected at the ESRF [3]. DegP6 was present in a proteolytically inactive state, in which the loop LA played a central role in stabilising the hexamer as well as in inhibiting the proteolytic activity of an adjacent protomer. Recent data revealed that DegP6 acts as a substrate trap that assembles, upon substrate binding, into the functionally active particles DegP12 and DegP24. Notably, the size of the transformed complexes, 12 or 24mer, depends on the mass and concentration of substrate. Moreover, we could also show that complex formation is transient with DegP recycling into the hexameric state after substrates are chopped up. In contrast to complexes with unfolded model substrates, complexes with co-purified outer membrane proteins (OMPs) were remarkably stable. Interestingly, DegP selectively stabilised folded OMP protomers, whereas unfolded membrane proteins were immediately degraded. The role of DegP in safeguarding OMP precursors through the periplasm was confirmed by the phenotype of a *degP* deletion strain, where OMP targeting to the outer membrane was significantly impaired.

We were able to crystallise the DegP24/OMP(SeMet) complex and performed single anomalous dispersion (SAD) experiments at beamlines **ID14-4** and **ID23-1**. In the resulting structure (**Figure 71**), eight DegP trimers are located at the vertices of a cube yielding a particle with 432 symmetry. Most importantly, oligomer assembly is correlated with the removal of the inhibitory loop LA from the active site yielding a fully functional DegP protease. Unfortunately, we could not observe the bound OMPs in our structure, most likely due to positional and chemical heterogeneity. However, cryo electron microscopy (carried out by E. Schäfer and H. Saibil, Birkbeck College, London) of the DegP12/OMP complex revealed that OMPs are bound - presumably in a folded state - in the inner cavity of DegP thus confirming our biochemical data.

Taken together, our work has revealed a novel regulatory mechanism for proteases that is based on substrate-induced oligomer assembly and has provided molecular insight into the antagonistic protease and chaperone activities of DegP. While encapsulation of folded OMP protomers is protective and might allow safe transit through the periplasm, misfolded proteins are eliminated in the proteolytic folding chamber.

**References**
[1] B. Lipinska, O. Fayet, L. Baird and C. Georgopoulos, *Journal of Bacteriology* **171**, 1574 (1989).
[2] C. Spiess, A. Beil and M. Ehrmann, *Cell* **97**, 339 (1999).
[3] T. Krojer, M. Garrido-Franco, R. Huber, M. Ehrmann and T. Clausen, *Nature* **416**, 455 (2002).

# Structure-function analysis of a bacterial tyrosine kinase involved in capsule assembly

**Principal publication and authors**
V. Olivares-Illana (a), P. Meyer (a), E. Bechet (b), V. Gueguen-Chaignon (a), D. Soulat (b), S. Lazereg-Riquier (c), I. Mijakovic (d), J. Deutscher (e), A. Cozzone (b), O. Laprévote (c), S. Morera (a), C. Grangeasse (b) and S. Nessler (a), *PLoS Biol.* **6**, e143 (2008).
*(a) LEBS, CNRS UPR 3082, Gif sur Yvette (France)*
*(b) IBCP, UMR 5086 CNRS, Université de Lyon (France)*
*(c) ICSN, CNRS UPR 2301, Gif sur Yvette (France)*
*(d) Center for Microbial Biotechnology, DTU, Lyngby (Denmark)*
*(e) LMGM, AgroParisTech, CNRS, INRA, Thiverval-Grignon (France)*

In bacteria, some polysaccharides co-polymerases involved in capsule synthesis have been identified as protein-kinases belonging to a new family of tyrosine-kinases and called BY-kinases. They show no sequence similarity with eukaryotic protein-kinases. BY-kinases contain Walker A and B nucleotide-binding motifs characteristic of the so-called P-loop proteins. They undergo autophosphorylation on a C-terminal tyrosine cluster and further phosphorylate endogenous protein substrates. In proteobacteria, BY-kinases are transmembrane proteins containing a periplasmic domain and a cytoplasmic catalytic domain. In firmicutes, BY-kinases are encoded by two adjacent genes and split in two polypeptides, which correspond each to one of these two domains.

In this work, we focused on the BY-kinase CapA/CapB of *Staphylococcus aureus*, a pathogen responsible for a diverse spectrum of animal and human diseases that predominates among clinical isolates. The interaction between the cytoplasmic protein-kinase CapB and the C-terminal juxtamembrane fragment of the membrane protein CapA (CapA-Ct) is required to promote CapB activity. Here we present the crystal structures of the chimerical protein CapA-Ct/CapB (CapAB) and of its inactive P-loop mutant CapAB(K55M).

Non-denaturing electrophoresis and mass spectrometry analysis demonstrated that the purified CapAB protein is autophosphorylated. It crystallised in 20% PEG 1000 and high-resolution diffraction data (1.8 Å) were collected at beamline **ID23-2**. The CapAB structure was solved by molecular replacement using the P-loop ATPase MinD as starting model. It is monomeric, with CapB harbouring the typical α/β-fold of P-loop proteins. The phosphorylated C-terminal tyrosine cluster of CapB is disordered. CapA-Ct forms α-helix followed by a β-strand that completes the central β-sheet of CapB. CapA-Ct is involved in nucleotide binding via its penultimate residue Phe221a, which participates in a stacking interaction with the purine ring of the ADP molecule found close to the P-loop of CapB (**Figure 72**).

This explains the stimulatory effect of CapA-Ct on the kinase activity of CapB.

The structure of the inactive P-loop mutant CapAB(K55M) was solved at beamline **ID29**. It presents a subunit fold highly similar to that of the CapAB with an rmsd of 0.67 Å over 241 aligned residues. The major difference concerns its quaternary structure. Surprisingly, the unphosphorylated protein forms a ring-shaped octamer (**Figure 73**) with

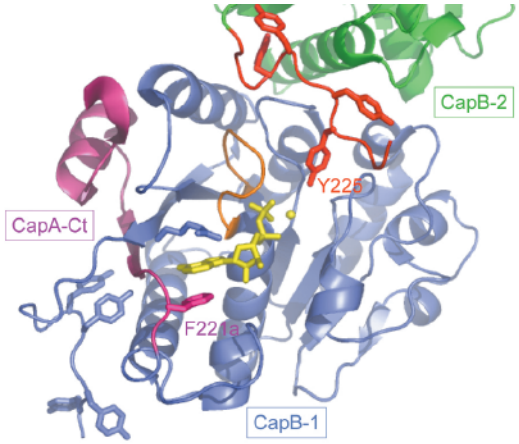


*Fig. 72:* A view of the active site of the *S. aureus* BY-kinase mutant CapAB(K55M). The P-loop of the blue CapB-1 is shown in orange with bound ADP-Mg in yellow. The CapA-Ct activator domain is shown in magenta. F221a involved in nucleotide binding is highlighted as are the phosphorylatable Y225 from the C-terminal tyrosine cluster (red) of a neighbouring CapB-2 subunit (green).

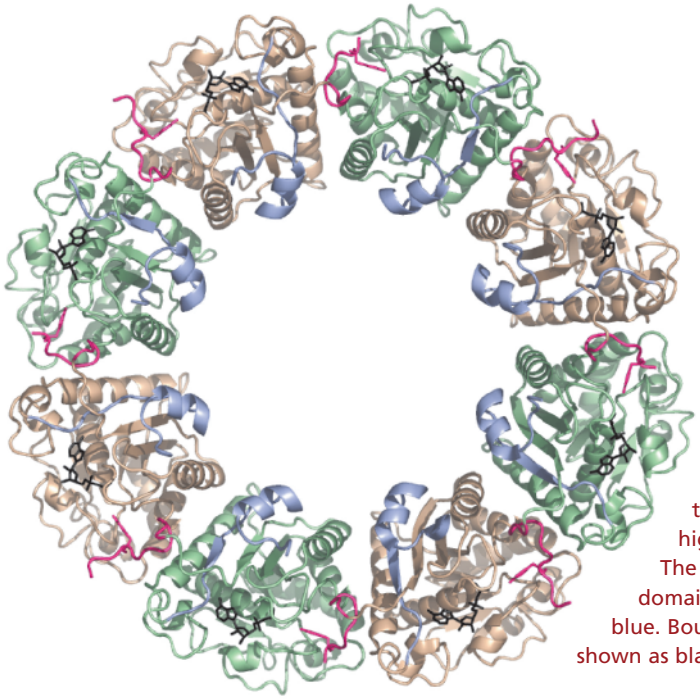

*Fig. 73:* Ring-shaped octamer of the *S. aureus* BY-kinase mutant CapAB(K55M). CapB subunits are alternatively colored green and beige with the C-terminal tyrosine clusters highlighted in pink. The CapA-Ct activator domains are shown in blue. Bound nucleotides are shown as black sticks.

the C-terminal tyrosine cluster from each molecule inserted into the active site of a neighbouring one (**Figure 72**). The last tyrosine residue in the cluster, Tyr225, points towards the phosphate tail of the bound ADP and interacts with the catalytic Asp79 that is in a position to deprotonate the Tyr225 hydroxyl group, a prerequisite for its phosphorylation.

In the octamer, the buried surface areas between neighbouring CapAB subunits (more than 2000 $A^2$) are typical of those required for biological interactions. Moreover, when a comparison is made with the other BY-kinase sequences, the absolute conservation of the residues involved in monomer-monomer interactions clearly demonstrates that the octamer is physiologically important.
Our structural analysis clearly shows that BY-kinase autophosphorylation proceeds via an intermolecular mechanism. Our data further suggest that the cytoplasmic kinase domains dissociate from each other upon phosphorylation, inducing conformational changes transmitted to the other components of the capsule synthesis machinery via the associated transmembrane activation domain.
In this model, cyclic phosphorylation/dephosphorylation of the BY-kinase seems to be intimately correlated to its polysaccharide co-polymerase activity.

This work represents the basis for structure-based drug design projects aiming at blocking bacterial capsule production. In *S. aureus*, but also in other bacterial pathogens, capsular polysaccharides are considered as major virulence factors. Considering the idiosyncratic nature of BY-kinases, which are not present in eukaryotic organisms, these enzymes represent promising targets for the design of drugs with limited side effects on host cells.

**Principal publication and authors**
D. Hatherley, S.C. Graham, J. Turner, K. Harlos, D.I. Stuart, A.N. Barclay, *Mol. Cell* **31**, 266 (2008).
*University of Oxford (UK)*

## SIRP structures explain paired-receptor specificity

The complex immune system of vertebrates must be tightly controlled in order to respond to pathogenic challenge without inducing unnecessary side effects. While soluble markers such as cytokines enable immune cells to localise to the site of infection, specific protein:protein interactions formed between cells fine-tune the immunological response.

The signal-regulatory proteins (SIRPs) are a family of cell-surface proteins expressed primarily on myeloid cells comprising three members: SIRPα, SIRPβ and SIRPγ **[1]**. While the extracellular regions of all three are very similar, the intracellular regions of these proteins are not alike and they convey very different signals to cells. SIRPα recognises CD47, a protein expressed on the surface of most cells that acts as a molecular 'marker of self', and formation of this CD47/SIRPα interaction *inhibits* engulfment of cells by macrophages. SIRPβ, on the other hand, does not recognise CD47 and interaction of SIRPβ with its (unknown) extracellular ligand *stimulates* macrophage engulfment. While SIRPγ recognises CD47 with lower affinity than SIRPα, it is expressed on the surface of T-cells rather than macrophages and is thought to have no direct signalling function. The SIRPs thus typify the class of membrane protein families called "paired receptors", which comprise several proteins with similar extracellular regions but radically different transmembrane/cytoplasmic regions with distinct (activating, inhibitory or neutral) signalling potentials.

The extracellular regions of SIRPs comprise three immunoglobulin (Ig) domains in a linear array. We had previously determined the structure of the first (amino-terminal) Ig domain of SIRPα **[2]**. Using site directed mutagenesis we showed that the interaction with CD47 was mediated by the N-terminal (apical) loops of SIRPα, more closely resembling how antibodies

recognise antigens rather than general Ig-domain mediated cell:cell contacts.

To determine the precise mechanism by which SIRPα recognises its ligand, we solved the structure of the N-terminal SIRPα domain in complex with the sole extracellular Ig domain of CD47 in two crystal forms by molecular replacement using data collected at **BM14** and **ID23-2**. **Figure 74** shows the CD47/SIRPα interface, which is unlike those seen for other moderate-affinity Ig domain mediated cell-surface interactions as it is highly convoluted, well fitting, and extensive, with a mutual involvement of loops from the amino-terminal ends of both SIRPα and CD47.

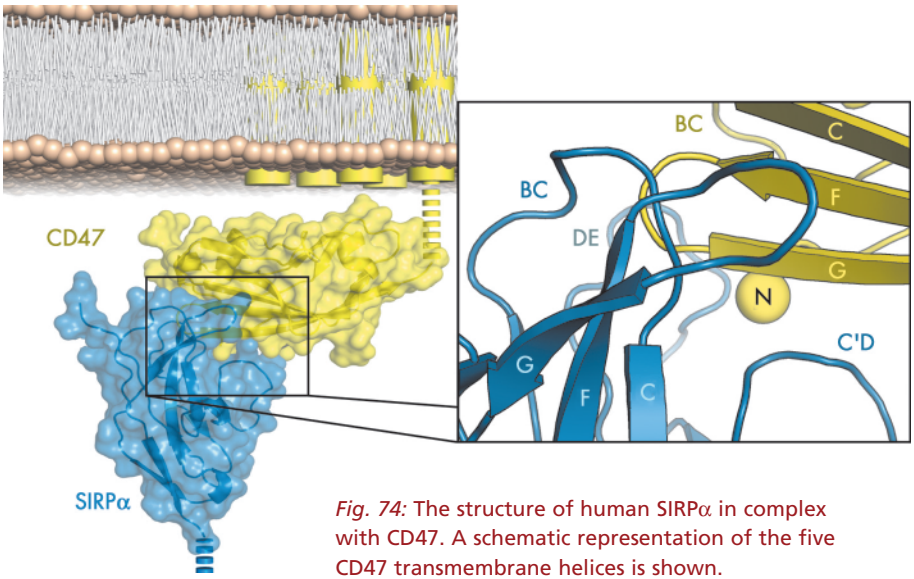


*Fig. 74:* The structure of human SIRPα in complex with CD47. A schematic representation of the five CD47 transmembrane helices is shown.

In contrast to SIRPα, SIRPβ and SIRPγ bind CD47 weakly or not at all, despite sharing > 90% sequence identity with SIRPα. We solved structures of the N-terminal domains of SIRPγ and two isoforms of SIRPβ by molecular replacement using data collected at **BM14**. These structures demonstrate the exquisite selectivity of the SIRP interaction interface. Overall, the structures of SIRPs α, β and γ are very similar (**Figure 75**). However, for both isoforms of SIRPβ specific amino acid differences with respect to SIRPα could be identified which result in the inability of SIRPβ to bind CD47. Further, by introducing a single amino acid mutation in the sequence of one isoform of SIRPβ we were able to confer the ability to bind CD47 with an affinity approaching that of SIRPα.

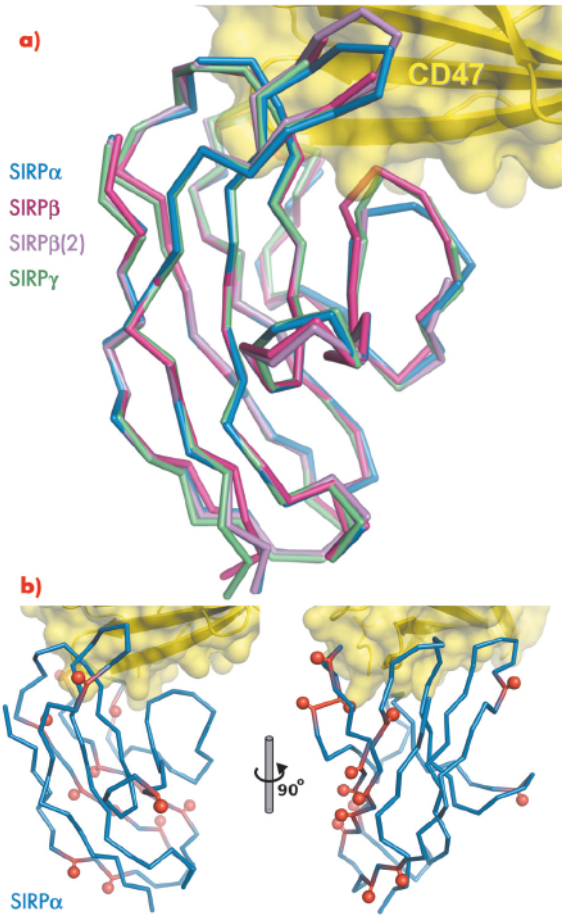


*Fig. 75:* **a)** Superposition of SIRPβ and SIRPγ on the CD47/SIRPα complex shows that the SIRPs have very similar structures. However, only SIRPα binds CD47 with high affinity. **b)** Sites of SIRPα amino acid polymorphism (red spheres) partition away from the CD47/SIRPα interaction interface.

The N-terminal ligand-binding domain of SIRPα has much higher sequence variability than most other cell-surface receptors. Mapping this sequence variability onto the structure of the CD47/SIRPα complex shows that most SIRPα polymorphisms reside away from the interaction interface (**Figure 75**), implying that the sequence variability does not modulate the strength of the CD47 interaction. We propose that the driving force for this sequence variability might be to avoid recognition of SIRPα by pathogens, which would exploit the ability of SIRPα to down-regulate macrophage activity. An extension of the idea that SIRPα might be a target for pathogens is that SIRPβ may have evolved to mimic the extracellular regions of SIRPα, its similar structure but opposite (activating) signalling activity serving to frustrate attempts by pathogens to exploit the inhibitory potential of SIRPα.

The structure of SIRPα in complex with CD47, together with the structures of SIRPβ and SIRPγ in isolation, has shown us in molecular detail how this paired receptor binds its ligand and how

**References**
[1] A.N. Barclay, M.H. Brown, *Nat. Rev. Immunol.* **6**, 457 (2006).
[2] D. Hatherley, K. Harlos, D.C. Dunlop, D.I. Stuart, A.N. Barclay, *J. Biol. Chem.* **282**, 14567 (2007).

subtle amino acid variations in the ligand-binding regions account for the exquisite ligand selectivity of the SIRP family. The partitioning of SIRPα polymorphisms away from the CD47 interaction interface suggests that pathogenic challenge may drive SIRPα polymorphism. Pathogen pressure on the inhibitory receptor provides a plausible *raison d'être* for the existence of paired receptors, with their similar extracellular structures but opposing signalling potentials.

# Atomic structure of a molecular switch for blood coagulation and fibrinolysis

**Principal publication and authors**
L. Sanglas (a), Z. Valnickova (b), J.L. Arolas (c), I. Pallarés (a), T. Guevara (c), M. Solà (a), T. Kristensen (b), J.J. Enghild (b), F.X. Aviles (a) and F.X. Gomis-Rüth (c). *Mol. Cell* **31**, 598 (2008).
*(a) Institut de Biotecnologia i de Biomedicina and Departament de Bioquímica i Biologia Molecular, Universitat Autònoma de Barcelona, Bellaterra (Spain)*
*(b) Center for Insoluble Protein Structures at the Department of Molecular Biology, University of Århus (Denmark)*
*(c) Department of Structural Biology at the Molecular Biology Institute of Barcelona, CSIC (Spain).*

After blood-vessel injury, hemostasis induces fibrin clot formation to prevent blood loss and trigger vessel repair. This clot must be removed after tissue repair to restore blood flow. These two processes are tightly regulated by the coagulation and fibrinolytic cascades because imbalance may lead to thrombosis, heart attack and stroke, or to bleeding as in hemophilia [1]. Hemostasis is modulated by thrombin-activatable fibrinolysis inhibitor (TAFI). It attenuates fibrinolysis by removing surface-exposed C-terminal lysine residues from the fibrin clot. TAFI is the zymogen of a B-type zinc-dependent metallocarboxypeptidase of the funnelin tribe of proteases [2,3] and it is the only funnelin found in human plasma. During coagulation, TAFI is processed by thrombin/thrombomodulin to TAFIa through removal of its pro-domain. In contrast to pancreatic funnelins, both TAFI and TAFIa uniquely display carboxypeptidase activity against larger substrates. However, while TAFIa has a half-life of less than ten minutes, TAFI is stable in circulation [4,5].

We obtained a stable form of TAFIa *in vitro* employing purified bovine TAFI, which was activated in the presence of a proteinaceous inhibitor, TCI, from the tick. This produced a stable enzyme-inhibitor complex.

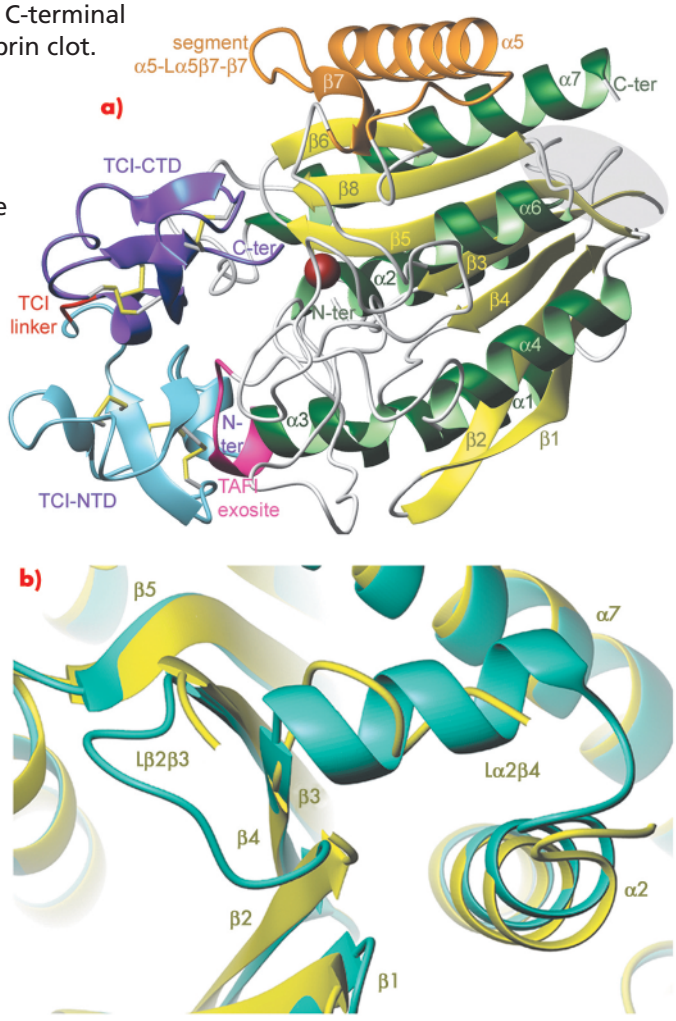


*Fig. 76:* Structure of the TAFIa/TCI complex. **a)** Richardson plot of the complex showing TAFIa in standard orientation. The region of the proposed fibrinolysis switch is shown over gray background. TCI is coloured as follows: N-terminal domain (light blue), linker (red), C-terminal domain (purple). **b)** Close-up view of (a) after a vertical rotation of ~90° showing the proposed fibrinolysis switch region of TAFIa (yellow) superimposed with the equivalent region of human pancreatic CPB1, which is taken as a highly-stable reference (green).

We were able to solve the crystal structure to high resolution using synchrotron radiation at beamline **ID23-2**. These studies revealed that TAFIa conforms to the α/β-hydrolase fold of funnelins and that it displays two unique flexible loops on the molecular surface, which account for structural instability and susceptibility to proteolysis (**Figure 76**). In addition, point mutations reported to enhance protein stability *in vivo* are mainly located in the first loop and in another surface region, which is a potential heparin-binding site. The protein inhibitor contacts both the TAFIa active site and an exosite, thus contributing to high inhibitory efficiency.

**References**

[1] M.B. Boffa, M.E. Nesheim and M.L. Koschinsky, *Curr. Drug Targets Cardiovasc. Haematol. Disord.* **1**, 59 (2001).
[2] J.L. Arolas, J. Vendrell, F.X. Avilés and L.D. Fricker, *Curr. Pharm. Des.* **13**, 349 (2007).
[3] F.X. Gomis-Rüth, *Crit. Rev. Biochem. Mol. Biol.* **43**, 319 (2008).
[4] M.B. Boffa, W. Wang, L. Bajzar and M.E. Nesheim, *J. Biol. Chem.* **273**, 2127 (1998).
[5] Z. Valnickova, I.B. Thogersen, J. Potempa and J.J. Enghild, *J. Biol. Chem.* **282**, 3066 (2007).

# Assembly and channel-opening in a bacterial drug efflux machine

**Principal publication and authors**

V.N. Bavro (a), Z. Pietras (a), N. Furnham (a), L. Pérez-Cano(b), J. Fernández-Recio (b), X. Yuan Pei (a), R. Misra (c) and B. Luisi (a), *Mol. Cell.* **30**, 114 (2008).

*(a) Department of Biochemistry, University of Cambridge (UK)*
*(b) Barcelona Supercomputing Center (Spain)*
*(c) Arizona State University, Tempe (USA)*

Resistance to drugs remains a major obstacle in the treatment of infections caused by pathogenic bacteria. One drug resistance mechanism originates from the activity of transmembrane transporters that displace a broad range of antibiotics and other toxic compounds from the bacterium. In the case of Gram-negative bacteria, the toxic compound may need to be displaced across both the inner- and outer-membranes and the interstitial periplasm in order to be properly expelled from the cell. A special class of three-component efflux pumps accomplishes this task. Typically, these pumps are composed of an inner membrane protein, an outer membrane protein, and a protein that traverses the periplasm to link the two membrane proteins.

A well studied representative of the family of multi-drug efflux pumps is the *Escherichia coli* AcrB/AcrA/TolC assembly. Crystal structures are available for each of the three components of the tripartite assembly **[1, 2 and references cited therein]**, but the structure of the ternary assembly is presently unknown. Accumulating structural and functional data provides a rough idea of the architecture of the pump, and **Figure 77** summarises these in a speculative model for the entire assembly based on docking the crystal structures of the individual components. The trimeric AcrB is the inner membrane component, and it powers the efflux pump using the energy from proton electrochemical gradients. The trimeric TolC is the outer membrane protein, which is shaped like a cylinder with a hollow interior. One end of the cylinder is open to the extracellular medium while the other tapers towards its periplasmic end, where it is maintained in a closed state by salt bridges and van der Waals contacts between the adjacent subunits. It seems clear that transport

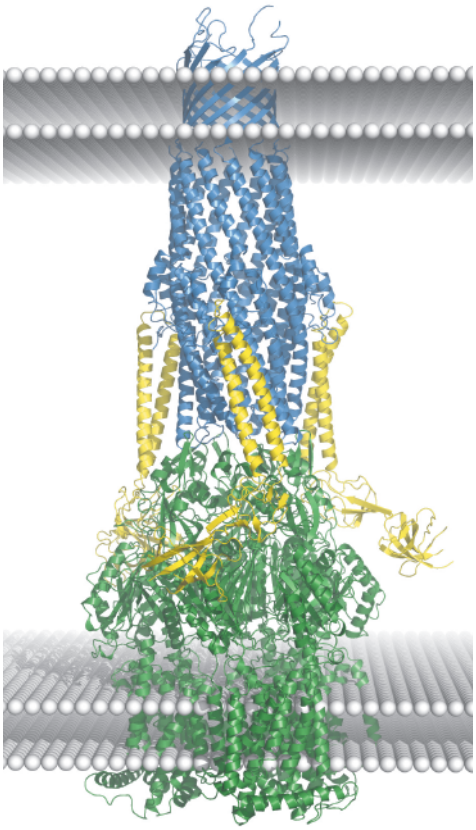

*Fig. 77:* A cartoon schematic showing a putative model of the AcrB/AcrA/TolC drug-efflux assembly. Crystal structures of the isolated components were docked to model the assembly. The TolC trimer is shown in blue, AcrB trimer in green, three AcrA molecules are coloured yellow. White sphere layers represent the two surfaces of each membrane; the two upper and two lower are from the outer membrane and inner membrane respectively. While the model presented here depicts a 3:3:3 assembly, other models, with different subunit compositions cannot be ruled out by the available data.

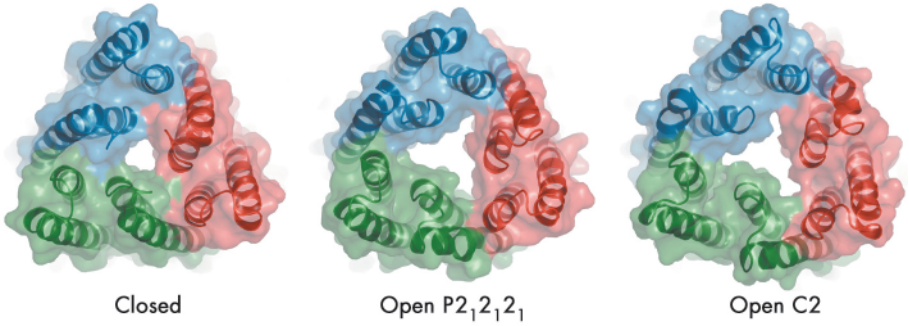


*Fig. 78:* Crystal structures of the open and closed states of the TolC channel protein. The view is along the three-fold axis of the TolC trimer at the periplasmic end that engages AcrB.

requires TolC to switch to an open conformation to allow transportation of the substrate.

In our study, we mutated TolC in order to disrupt a network of hydrogen bonding interactions at the periplasmic end that caused it to become leaky to bulky molecules *in vivo*. However, the mutations did not affect TolC function, since it retained the capacity to form a functional efflux assembly. We solved the crystal structure of the mutant in two crystalline forms at 3.2 and 3.3 Å resolution using data collected at beamline **ID23-2**. The crystal structures reveal that three of the six pairs of coiled coils at the closed end of TolC move radially outward from the central molecular axis to partially open the channel (**Figure 78**). Conformational changes associated with partial channel opening expose grooves which, we speculated, can accommodate periplasmic component AcrA. We developed a model of the interactions between AcrA and TolC, which successfully predicted a mutation pair in the proteins that compensate each other's disruptive effects. Using docking calculations, we generated a model in which the open form of TolC engages the periplasmic crown of AcrB, the inner membrane protein.

Despite the dramatic changes in the AcrB during its work cycle **[1,2]**, the TolC-interacting interface of AcrB changes little, suggesting that this interface might only partially transmit the conformational changes that trigger the opening of the TolC channel, and is likely only implicated in unlocking the periplasmic end of the channel, while additional energy is needed to drive the channel to fully open state. This suggests that AcrA is more than just a passive bridge between the energised AcrB and TolC, but likely also serves as an active transducer of energy from one to the other. The induced fit of the periplasmic partner into the partially opened grooves of TolC may complete the process of channel opening.

**References**
[1] S. Murakami, R. Nakashima, E. Yamashita, T. Matsumoto and A. Yamaguchi, *Nature* **443**, 173 (2006).
[2] M.A. Seeger, A. Schiefner, T. Eicher, F. Verrey, K. Diederichs and K.M. Pos, *Science* **313**, 1295 (2006).

# Structure of a "bonsai" Ndc80 complex sheds light on the mechanism of chromosome segregation

**Principal publication and authors**
C. Ciferri (a), S. Pasqualato (a), E. Screpanti (a), G. Varetti (a), S. Santaguida (a), G. Dos Reis (a), A. Maiolica (a), J. Polka (b), J.G. De Luca (c), P. De Wulf (a), M. Salek (d), J. Rappsilber (e), C.A. Moores (f), E.D. Salmon (b) and A. Musacchio (a), *Cell* **133**, 427 (2008).
*(a) Department of Experimental Oncology, European Institute of Oncology, Milan, (Italy)*
*(b) Department of Biology, University of North Carolina (USA)*
*(c) Dept of Biochemistry and Molecular Biology, Colorado State University (USA)*
*(d) Sir William Dunn Pathology School, Oxford (UK)*
*(e) Wellcome Trust Centre for Cell Biology, University of Edinburgh (UK)*
*(f) School of Crystallography, Birkbeck College, University of London (UK)*

Accurate chromosome segregation is a prerequisite for long-term cell and organism survival. To ensure this, the replicated chromosomes (known as sister chromatids) establish sturdy connections with a structure known as the mitotic spindle. Microtubules, which are polymeric structures based on the assembly of αβ-tubulin dimers, are the main component of the spindle. During the process of cell division, chromosomes assemble and expose a microtubule receptor known as the kinetochore. The crucial microtubule receptor at kinetochores is a 4-protein complex known as the Ndc80 complex. Our studies have provided a molecular understanding of the organisation of the Ndc80 complex and of its ability to bind microtubules.

The Ndc80 tetramer is assembled from two dimers, Ndc80:Nuf2 and Spc24:Spc25 (**Figure 79a**). The topology of interactions of these two dimers in the Ndc80 complex was known from previous studies. Ndc80:Nuf2 have globular N-terminal domains and are predicted to form a long parallel coiled-coil with their C-terminal regions. The Ndc80:Nuf2 coiled-coil ends in a tetramerisation domain where the Ndc80:Nuf2 dimer meets the Spc24:Spc25 dimer. The Spc24:Spc25 dimer contains another dimeric parallel coiled-coil that

engages the N-terminal regions of the Spc24:Spc25 subunits, and ends with a globular region. This organisation of the Ndc80 complex results in a very elongated and rather flexible structure, as shown by low-resolution electron micrographs on negatively stained samples. The globular regions at either end of the rod have been shown to mediate microtubule binding and kinetochore localisation.

Highly elongated and flexible structures are almost invariably difficult to crystallise. Thus, to gain high-resolution structural insight into the Ndc80 complex, we made an attempt to simplify its organisation. Because the topology of the Ndc80 complex suggested that the C-terminal moieties of the Ndc80:Nuf2 subunits are close to the N-terminal moieties of the Spc24:Spc25 subunits, we tried to fuse the chains two on two to create a dimeric strucure (**Figure 79b**). We then removed most of the intervening coiled-coil region to create a Bonsai Ndc80 complex containing only the "leaves" (the globular domains of Ndc80 and Nuf2), a small segment of the "trunk" (the coiled-coil), and the "roots" (the globular region of the Spc24:Spc25 dimer. The topology of this construct is shown in **Figure 79b**. The Ndc80$^{bonsai}$ construct retains the ability to bind microtubules and kinetochores.

Bonsai-Ndc80 proved to be very stable and crystallised readily. Using X-ray diffraction data collected on beamlines **BM16** and **ID23-1** we were able to determine the 2.8 Å crystal structure of the Bonsai-Ndc80 complex (**Figure 80a**). The structure revealed that the globular domains of Ndc80 and Nuf2 each contain a calponin-homology (CH) domain (**Figure 80b**). CH domains have been previously implicated in binding actin or microtubules. In the Ndc80:Nuf2 moiety, the CH domains are tightly packed and form a single large exposed surface. We have carried out an extensive mutagenesis analysis to demonstrate that this surface provides the main microtubule-binding area of the Ndc80 complex. Based on the structure of Bonsai-Ndc80 and of cross-linking and mass spectrometry data, we have generated a model for the

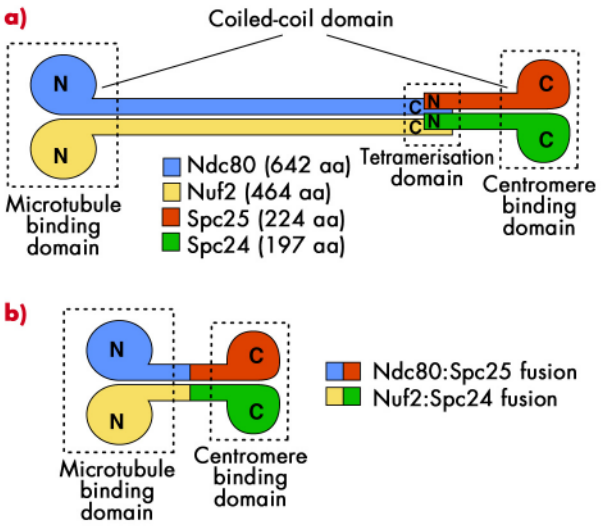


*Fig. 79:* **a)** The Ndc80 complex is a tetrameric arrangement of Ndc80, Nuf2, Spc25 and Spc24 subunits. Ndc80:Nuf2 and Spc25.Spc24 form dimeric arrangements containing microtubule-binding and kinetochore-binding domains, respectively. Overall, the complex is dumb-bell shaped consisting of two globular domains separated by a central coiled-coil rod. **b)** Bonsai version of the Ndc80 complex. The chains have been fused two-on-two and most of the coiled coil domain has been removed.

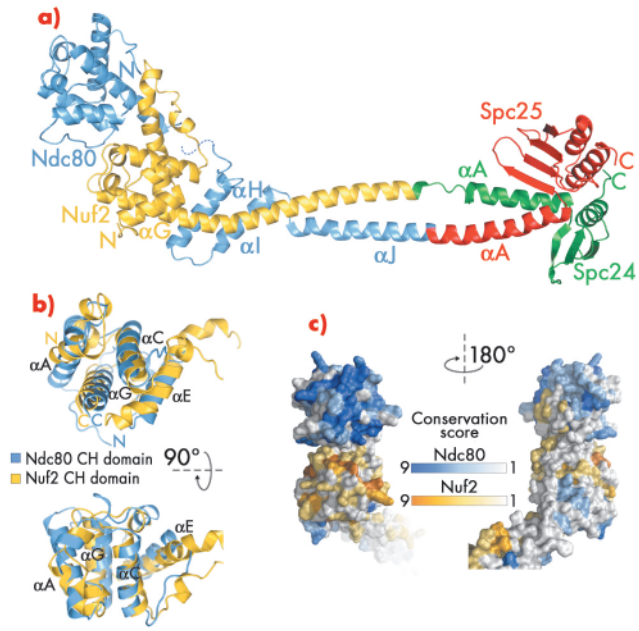


*Fig. 80:* **a)** Ribbon model of Bonsai-Ndc80. **b)** Superposition of the calponin-homology (CH) domains of Ndc80 (cyan) and Nuf2 (yellow). **c)** Map of evolutionary residue conservation on the surface of the Ndc80 complex identifies a microtubule-binding interface (left).

full-length Ndc80 complex and revealed the molecular basis of chromosome segregation, a process that is essential for the propagation of genetic information along successive generations. Our current analyses aim at understanding the broader organisation of multiple Ndc80 complexes around microtubules.

**Principal publication and authors**
P.R. Pryor (a), L. Jackson (b), S.R. Gray (a), M.A. Edeling (a), A. Thompson (c), C.M. Sanderson (c,d), P.R. Evans (b), D.J. Owen (a), J.P. Luzio (a), *Cell* **134**, 817-827 (2008).
*(a) Cambridge Institute for Medical Research and Department of Clinical Biochemistry, University of Cambridge, Addenbrooke's Hospital, Cambridge (UK)*
*(b) Medical Research Council Laboratory of Molecular Biology, Cambridge (UK)*
*(c) Medical Research Council Rosalind Franklin Centre for Genomics Research, Cambridge (UK)*
*(d) The Physiological Laboratory, School of Biomedical Sciences, University of Liverpool (UK)*

# Sorting SNAREs into clathrin-coated vesicles

The protein and phospholipid composition of cellular membranes defines the identity of that membrane; what binds to it and what reactions occur both on its surface and inside the cavity it surrounds. Components of the cell's limiting membrane are involved in cell signalling, homeostasis, cell contacts and recognition by the immune system. Glycosylation, proteolytic processing and degradation of transmembrane and luminal proteins occur within cells' organelles.

Transmembrane proteins with an enormous variety of functions are moved between cell membranes in transport vesicles. Once cargo has been sorted into a forming vesicle, the vesicle buds from the donor membrane and is then transported to and fuses with the target membrane. The directionality and specificity of this transport is regulated to a large extent by members of a family of small type II transmembrane proteins called SNAREs that are found in both vesicle and target organelle membranes.
After successful formation of a trans-four-helical bundle between homologous helices from a SNARE in one membrane and three SNAREs in the other, fusion of the vesicle with the target compartment can proceed. The specificity of SNARE complex formation, which leads to the specificity of vesicle/target membrane fusion, arises from the fact that only very limited combinations of SNAREs can form productive SNARE complexes.
The correct distribution and localisation of SNARE proteins are therefore critical: vesicles must contain sufficient SNAREs that can engage in complex formation at the target membrane as well as SNAREs that are being recycled to their donor compartment, most likely in an inactive form.

Post-Golgi transport is mainly mediated by clathrin-coated vesicles (CCVs), whose coats are composed of an outer clathrin scaffold linked to the membrane by clathrin adaptors. Clathrin adaptors have folded domains that bind to short-lived membrane components such as phospholipid headgroups and the GTP-bound forms of small GTPase proteins of the Arf superfamily and extended, flexible regions that contain multiple short motifs, which bind to clathrin and other CCV components. At least one of a very small number of transplantable 'tags', a short linear sequence motif, or alternatively a covalently attached ubiquitin molecule, are found on nearly all transmembrane proteins and bind to the folded domains of the most common clathrin adaptors, so marking the transmembrane protein for incorporation as general cargo into CCVs [1]. The mechanisms by which SNAREs are selected for incorporation into CCVs were unclear, although a lot was known about how SNAREs were incorporated into ER to Golgi COPII-coated vesicles.

Recent structural work carried out at beamline **ID14-4** has shed light on this issue (**Figure 81**). The SNARE VAMP7

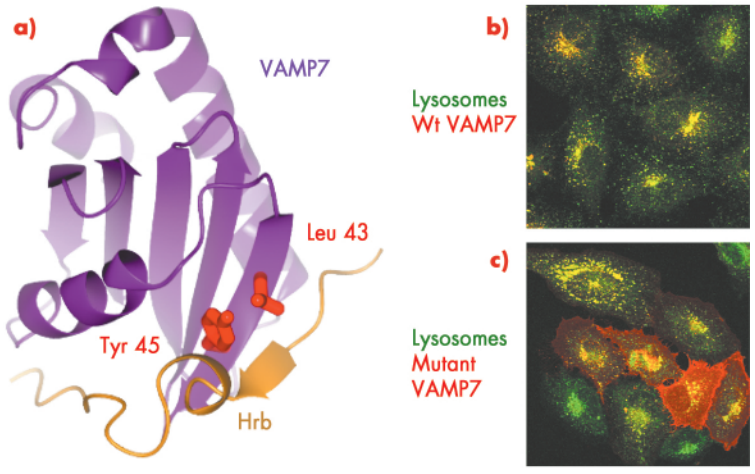


*Fig. 81:* **a)** Structure of the VAMP7 (purple): Hrb (gold) complex with key residues, whose mutation abolishes the interaction between the two proteins *in vitro,* highlighted in red. **b)** tagged VAMP7 (red) can be internalised from the cell surface to lysosomes and late endosomes (green) resulting in complete overlap of the two as indicated by the resulting yellow punctae. **c)** A version of VAMP7 harbouring mutations in the key VAMP7 residues Leucine43 and Tyrosine45 (red) cannot bind to Hrb and so cannot be internalised and builds up on the cell surface.

needs to be retrieved from the plasma membrane following its use in the fusion of late endosomes and lysosomes directly with the cell's limiting membrane, a process thought to be important in delivering new membrane to the cell surface during membrane repair or mitosis. This retrieval occurs through the interaction of VAMP7 with the low abundance clathrin adaptor Hrb. The structure of a complex between parts of VAMP7 and Hrb showed that a 20 residue stretch of largely hydrophobic amino acids in Hrb wraps around a groove in the folded longin domain of VAMP7 that preceeds its SNARE helix. Mutation of key residues in the VAMP7/Hrb interface that were identified from the structure of the VAMP7/Hrb complex, abolish the interaction between the two proteins both *in vitro* and *in vivo* where they result in altered trafficking of VAMP7.

Taken together with other recent studies [2,3], these data on the VAMP7/Hrb interaction suggest that two parallel pathways operate in post-Golgi CCVs for cargo selection: one for selecting general cargo that is mediated by the recognition of a few widely used tags, and the other for selecting the necessary SNAREs through the recognition of determinants that are each found on the surface of only a single SNARE. By having two non-competing cargo selection systems operating simultaneously, the cell ensures that CCVs incorporate sufficient amounts of the right SNAREs to allow fusion of the vesicle with its correct target organelle as well as standard 'bulk' cargo.

**References**

[1] J.S. Bonifacino and L.M. Traub, *Annu Rev Biochem* **72**, 395 (2003).
[2] S. Martinez-Arca, R. Rudge, M. Vacca, G. Raposo, J. Camonis, V. Proux-Gillardeaux, L. Daviet, E. Formstecher, A. Hamburger, F. Filippini, *et al.*, *PNAS* **100**, 9011 (2003).
[3] S.E. Miller, B.M. Collins, A.J. McCoy, M.S. Robinson, and D.J. Owen, *Nature* **450**, 570 (2007).

# Structural characterisation of IrisFP, a biological photoswitch from the green fluorescent protein family

Since the successful cloning of the green fluorescent protein (GFP) from the jellyfish *Aequorea victoria* in 1992, fluorescent proteins (FPs) have revolutionised Life Science. The 2008 Nobel Prize in chemistry was awarded to O. Shimomura, M. Chalfie and R.Y. Tsien for having, respectively, discovered GFP, introduced it in cells as a luminous genetic tag, and refining it to a palette of ever brighter fluorescent proteins with various colours. Using the fluorescent protein toolkit, cell biologists can image a very broad range of biological processes, including gene expression, protein translocation within cells, and cell movement during development [1].

In recent years, new fluorescent proteins have been identified, notably in *Anthozoa* species (*e.g.* corals and sea anemones found in tropical reefs), which display photo-activation properties [2]. Proteins from the "Kaede-family" undergo a photo-conversion from green to red upon illumination with UV light. Proteins from the "Dronpa-family" undergo on/off photo-switching upon illumination with UV/blue light. The use of photo-activatable fluorescent proteins provided new means to dynamically track proteins within live cells [3], and to develop "nanoscopy", a revolutionary set of techniques that defeat the diffraction barrier in light microscopy, achieving spatial resolution of ~10 nm with visible light [4]. Moreover, photo-activatable fluorescent proteins may find applications in nano-biotechnology, for example as novel data storage media [5].

All fluorescent proteins discovered so far display a so-called β-can structure, forming an almost perfect barrel composed of eleven β-strands. The chromophore is embedded at the heart of the β-can, and is made of 3 amino-acids (X-Tyr-Gly) that undergo post-translational modifications to form an extended π-electron system. Using X-ray crystallography, UV-vis spectroscopy and quantum chemistry, mechanistic details of the fluorescence mechanisms employed by photo-

**Principal publication and authors**

V. Adam (a), M. Lelimousin (b), S. Boehme (c), G. Desfonds (a), K. Nienhaus (c), M.J. Field (b), J. Wiedenmann (d), S. McSweeney (a), G.U. Nienhaus (c) and D. Bourgeois (a,b), *PNAS* **105**, 18343 (2008).

*(a) ESRF*
*(b) Institut de Biologie Structurale Jean-Pierre Ebel, Commissariat à l'Energie Atomique, Centre National de la Recherche Scientifique, Université Joseph Fourier, Grenoble (France)*
*(c) Institute of Biophysics, University of Ulm (Germany)*
*(d) National Oceanography Centre, University of Southampton (UK)*

activatable fluorescent proteins can be obtained, which can be of considerable value to rationally engineer new variants with improved properties. In a collaboration between the ESRF, University of Ulm and the IBS, we have developed such a complementary approach. In the course of this project, we discovered "IrisFP" (the Greek goddess Iris personifies the rainbow), a remarkable fluorescent protein that derives from the fluorescent protein EosFP [6] and combines the properties of Kaede-like and Dronpa-like proteins, *i.e.* photo-conversion and photo-switching (Figure 82). Following proper laser illumination schemes, IrisFP can be switched reversibly between fluorescent and non-fluorescent forms in its green state, then photo-converted irreversibly from green to red, and finally switched reversibly between fluorescent and non-fluorescent forms in its red state.

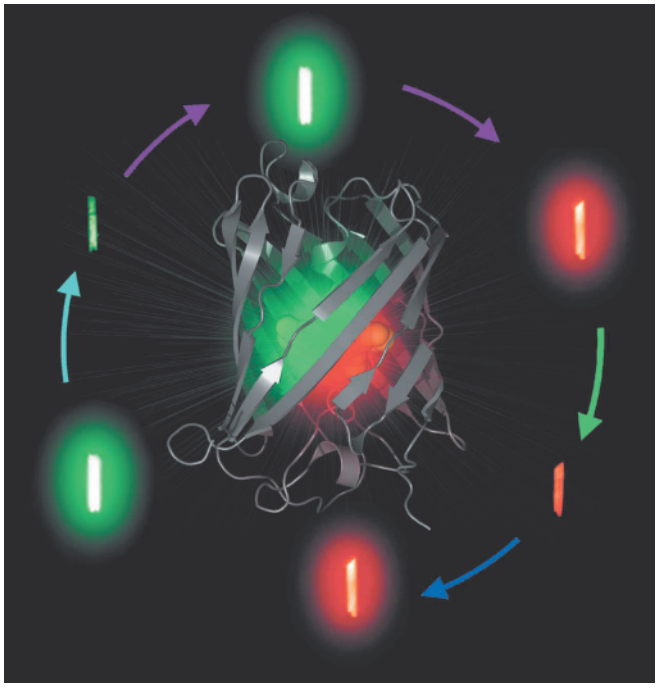

*Fig. 82:* The X-ray structure of IrisFP is shown at the centre. Around the structure are pictures of crystals of IrisFP in its different forms (switched on/off, green/red), recorded while fluorescing.

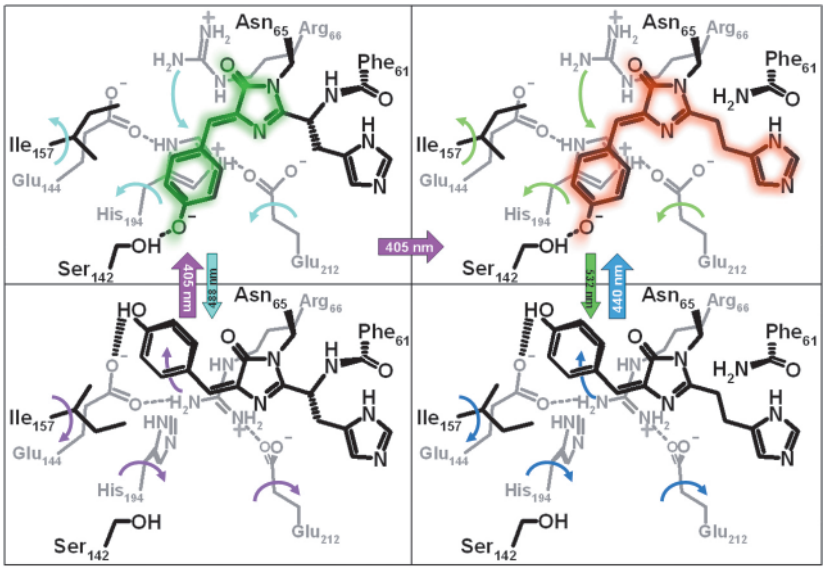


*Fig. 83:* Structural changes in IrisFP upon phototransformation. Structural motions induced by light are represented by curved arrows of the same colour as those used to represent light illumination at specific wavelengths.

We undertook a structural characterisation of IrisFP, in particular by using the Cryobench laboratory at the ESRF, which allows the illumination of crystals with a variety of lasers and the following of the induced colour changes by *in crystallo* spectroscopy. We discovered that photoswitching of green IrisFP involves a cis-trans isomerisation of the chromophore (Figure 83), accompanied by a major conformational change of the protein. In contrast, photo-conversion to the red-emitting state does not involve a large structural change, but results from a cleavage of the polypeptide backbone which induces an extension of the conjugated π-electron system of the chromophore. Photoswitching of the red form of IrisFP appeared similar to that of the green form, involving cis-trans isomerisation of the chromophore.

IrisFP holds great promises for applications in cell biology. Based on the mechanistic knowledge acquired in this work, rational engineering will be applied to further improve the behaviour of the protein. Applications taking advantage of the multiple phototransformations displayed by IrisFP will undoubtedly emerge, including two-colour nanoscopy for high-resolution spatio-temporal imaging, or sequential photo-activation schemes for unravelling complex protein-protein interactions. IrisFP also hints at the possibility of combining read-only and rewritable capabilities in future mass storage media.

**References**

[1] R.Y. Tsien, *Annu. Rev. Biochem.* **67**, 509 (1998).
[2] R. Ando *et al.*, *PNAS* **99**, 12651 (2002); *Science* **306**, 1371 (2004).
[3] K.A. Lukyanov *et al.*, *Molecular Cell Biology* **6**, 885 (2006).
[4] E. Betzig *et al.*, *Science* **313**, 1642 (2006).
[5] M. Andresen *et al.*, *PNAS* **102**, 13070 (2005).
[6] J. Wiedenmann *et al.*, *PNAS* **101**, 15905 (2004).

# Surface and Interface Science

## Introduction

With the ESRF Upgrade Programme launched in November, the starting signal was given for developing concrete plans for the future upgrade and refurbishment of the surface and interface science (SIS) beamlines. Conceptual design reports are required for the meeting of the Science and Advisory Committee in spring 2009. ID01 may be transformed into a 130 m long beamline for nanofocusing and coherent diffraction imaging (CDI) and ID03 may be relocated to another straight section. ID32 will most likely not be influenced immediately by the Upgrade Programme.

To explore the opinions and needs of the user community for the upgraded ID01 beamline, a highly successful brainstorming meeting with more than 30 participants was held at the ESRF in November. The diffraction analysis of MEMS/NEMS (micro/nano electro mechanical systems) was recognised as a brand-new and exciting avenue of research. With the novel ESRF *in situ* AFM at ID01 (see **Figure 84**), the X-ray analysis of mechanical interaction on the sub-μm scale has already been demonstrated, which may represent another prominent mission for the new ID01 beamline. The other two SIS beamlines had a busy time as well and improvements at ID03 have continued. In the ID03 UHV chamber in EH2, cooling was improved (< 30 K) and a high precision and rigid HEXAPOD for sample alignment with six degrees of freedom has now been installed. In EH1, a new small-volume flow-through reactor for *in situ* X-ray diffraction was commissioned, which permits rapid gas exchange and thus allows surface reactions to be followed at much increased speed (< sec). At ID32, the X-ray standing wave and photoelectron spectroscopy capabilities have been further upgraded. A new UHV system with a (presently unique) photoelectron analyser was installed in EH2. The analyser for HAXPES (hard X-ray photoelectron spectroscopy) studies is equipped with a low-noise 2D delay-line detector and, once fully commissioned, will permit the analysis of electrons with up to 15000 eV kinetic energy with very high resolution (nominally down to $\Delta E/E = 10^{-6}$). Fresnel zone plates, installed in front of the existing XPS system, have been tested and can deliver a beam as small as 3 μm for spatially-resolved XPS measurements.

Surface science is dead, yet long live surface science since with the advent of the fashionable term nanoscience, many fields of (classical) surface science underwent some metamorphosis, but

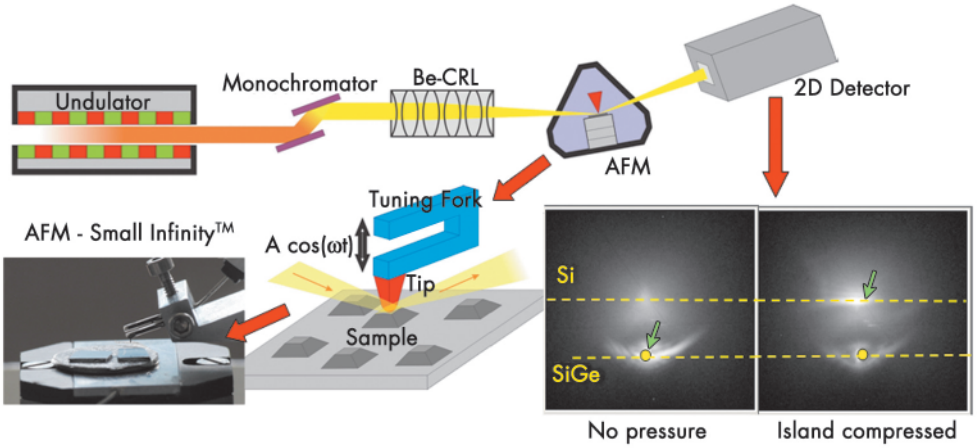


*Fig. 84:* A monochromatic X-ray beam of ~ 9.9 keV is focused by beryllium lenses (CRL) onto a single SiGe island while an atomic force microscopy (AFM) tip is used to apply pressure. A two dimensional image of the scattering close to the SiGe(004) Bragg peak is recorded. The shift in intensity (marked by the green arrows) reflects the compression of the island's lattice parameter (see http://www.esrf.fr/news/spotlight/spotlight63).

mostly in their labelling. However, a real shift in paradigm accompanied the change in the name of our group from surface science to surface and interface science (SIS) some years ago. The change reflected two aspects: firstly, the term surface for the truncated region of a solid suggest a purely two dimensional nature while the region affected by the truncation always extends into the third dimension. Secondly, it is apparent that the trend of science becoming more and more specialised is being reversed at present owing to the increasing interest in more complex systems. Thus, even the classical surface science has become more and more multidisciplinary. Surface scientists are looking at what's happening above and below where two agents meets, whether these are solid and vacuum, solid and solid, solid and liquid, etc. Contact points or phase boundaries are areas of interaction, interchange, and reaction and affect the properties of the materials involved. This is of interest to almost all fields in natural science and most industries. Noteworthy, the increased interaction extends to the scientists involved as well.

This year's SIS highlights are clearly testifying toward multidisciplinary interaction. Stadler *et al.* revealed that the cohesion among organic molecules can be tuned by the adsorption on a metal (silver) surface by using X-ray standing wave (XSW) studies with photoelectron spectroscopy at ID32. Dealing with a similar subject, also on the borderline between physics and chemistry, and likewise using the XSW method at ID32, Koch *et al.* find that the specific chemical/electronic interaction of molecules with a metal surface can lead to pronounced molecular distortions. The contribution of Le Bolloc'h *et al.* correlates structure and electronic properties for a subject of fundamental physics. An electronic excitation, a charge density wave, was studied by diffraction at ID01, and the authors discovered that it shows an intriguingly long coherence length of the order of µm. Making important progress toward the future mission of ID01, a joint team from DESY, IKZ Berlin, JKU Linz, and the ESRF (Zozulya *et al.*) managed to record CDI patterns from sub-µm small SiGe islands and to reconstruct their shape and density by a model-free phase retrieval approach.

While the last four contributions analysed in some detail some of the amazing features that Mother Nature is able to create on surfaces, in the following reports the authors watched over Mother Nature's shoulder when in action. Thus, Coati *et al.* observed the detailed nano-faceting of vicinal Ni surfaces induced by Ag deposit. Nolte *et al.* observe an oxygen-induced shape change of the Rh nanoparticles on a MgO(100) during oxidation and CO induced reduction that turns out to be fully reversible. Finally, in a collaborative effort, a team from MPI Halle, APS/ANL, and the ESRF studied the mesoscopic relaxations in cobalt nano-islands on Cu(001) and found experimental evidence for large contractions of the interatomic cobalt distances. With so many excellent results coming from the SIS beamlines, a selection of a few highlights is always difficult. I hope you enjoy our choice and I wish you a happy reading.

***J. Zegenhagen***

# Structure and electronic properties

## Tuning intermolecular interaction in long-range ordered sub-monolayer organic films

**Principal publication and authors**
C. Stadler (a), S. Hansen (a), I. Kröger (a), C. Kumpf (a,b) and E. Umbach (a,c), *Nature Physics*, DOI: 10.1038/nphys1176.
*(a) Universität Würzburg, Experimentelle Physik II, Am Hubland, Würzburg (Germany)*
*(b) present address: Forschungszentrum Jülich GmbH, Jülich (Germany)*
*(c) present address: Forschungszentrum Karlsruhe GmbH, Karlsruhe (Germany)*

The future development of organic electronic devices depends on the ability of tailoring the properties of thin-films and their interfaces with (metallic and insulating) substrates. The best results can be expected from well-ordered films with large crystalline grains and "perfect" interfaces. However, their properties are dominantly influenced by the formation of the first molecular layer on the surface representing a template for further growth. The development of the first layer – in turn – depends on the fine balance of molecule-substrate and molecule-molecule interaction. The latter usually is *attractive* due to van-der-Waals forces and causes formation of islands and small crystalline grains. Here we report on an organic adsorbate exhibiting a different behaviour: Sn-Phthalocyanine molecules show a *repulsive* intermolecular interaction when they are deposited on a Ag(111) surface in very thin films (coverage below one layer). This ensures a homogeneous filling of the surface terraces and hence the size of structural domains is only limited by the terrace width.

The phase diagram for SnPc/Ag(111) shows three different regions (**Figure 85**). A disordered overlayer is formed at low coverages and room temperature (RT). Like in a gas, the average intermolecular distance reduces with increasing density. This behaviour is proven by high-resolution low energy electron diffraction experiments (SPA-LEED images are shown for all regions as insets in **Figure 85**). In the second region at higher coverage, a series of well-ordered phases occurs, the structural parameters of which change continuously with coverage.
No discrete phase transitions are found in this regime, but a continuous rotation and deformation of the superstructure unit cell. This effect is caused by a substrate-mediated repulsive inter-molecular interaction between the molecules exceeding van-der-Waals and other attractive forces. The local molecular density is minimised at all coverages. Below 0.92 monolayers (ML), the repulsion can be reversibly switched to attraction by cooling. In this third region an additional site-specific interaction between molecules and substrate over-compensates the repulsion and leads to a rearrangement of the molecules in a commensurate pattern.

The key to understanding repulsive interaction is the charge transfer between molecule and substrate. From X-ray standing waves (XSW) measurements performed at beamline **ID32**, we found convincing indications for a significant overlap of molecular orbitals with the silver electronic states. The adsorption geometry differs for high and low coverages **[1]**. While in the monolayer-structure, all molecules adsorb with their Sn-atom below the molecular plane ("tin-down" position, **Figure 86a**), whereas a mixed "tin-up"/"tin-down" structure occurs at lower coverages. The molecule-surface distance is only about 3 Å, significantly below van-der-Waals bonding-distances. This indicates chemisorption and necessitates spatial overlap of molecular orbitals and surface electronic states.
An exchange of electronic charge (donation/backdonation) is the

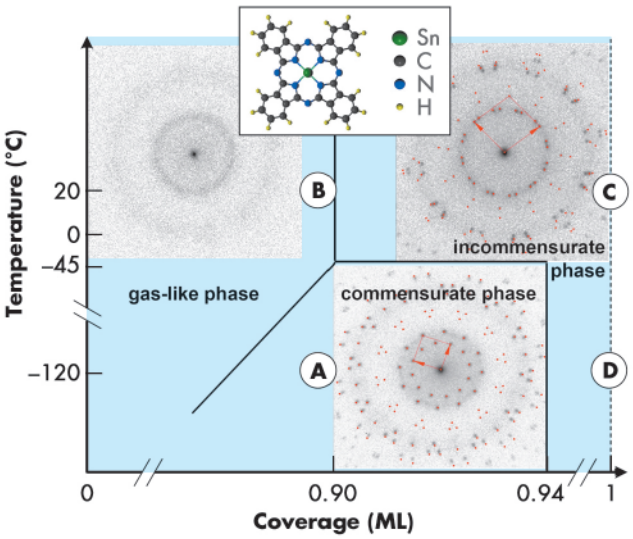


*Fig. 85:* Phase diagram of SnPc/Ag(111). Gas-like phases, a region with incommensurate structures, and a commensurate phase are identified. Typical SPA-LEED patterns and a model of the Sn-Phthalocyanine molecule are shown as insets. XSW experiments were performed at the points "A", "B", "C" and "D".

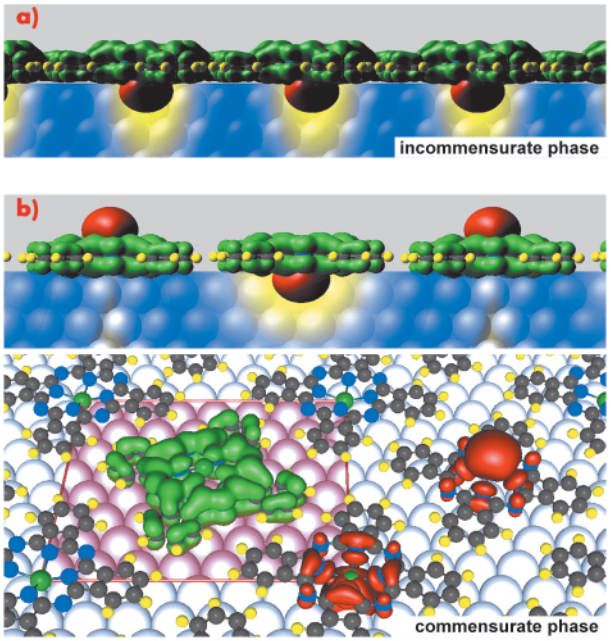


*Fig. 86:* Structural model and illustration of the donation/backdonation effect. **a)** Side view of the incommensurate monolayer structure ("C" and "D" in the phase diagram, coverage 1 ML). **b)** Side and perspective view of the commensurate LT structure ("A"). Molecular orbitals (HOMO-1 and LUMO) are drawn in red and green, respectively.

consequence. Density functional theory (DFT) calculations and ultraviolet photoelectron spectroscopy (UPS) confirmed this finding.

The donation/backdonation effect is also illustrated in **Figure 86**. Electron donation to the substrate just below the molecules (yellow area) displaces Ag electrons to the vicinity (blue). Backdonation to unoccupied orbitals of the molecule cannot completely compensate for this effect. Therefore neighbouring molecules – if they are identically oriented in "tin-down" position and located close to each other as is the case at high coverages (**Figure 86a**) – compete for the donation/backdonation effect which causes repulsion between the molecules. At lower coverages, the repulsion is reduced by the mixed "tin-up"/"tin-down"-orientation, but at room temperature (disordered, gas-like phase) it still remains dominant. Only upon cooling does the influence of the substrate overcome the repulsion, and an ordered structure is formed (**Figure 86b**).

Intermolecular repulsion in ordered organic overlayers is reported for the first time. It leads to a novel growth mode based on a homogeneous filling of surface terraces and results in large domain sizes. Just by tuning the temperature, the system can be switched from repulsive to attractive intermolecular interaction and back.

**Reference**
[1] C. Stadler, S. Hansen, F. Pollinger, C. Kumpf, E. Umbach, T.-L. Lee, and J. Zegenhagen, *Phys. Rev. B* **74**, 035404 (2006).

## Observation of correlations in sliding charge-density waves

**Principal publication and authors**
D. Le Bolloc'h (a), V.L. Jacques (a,b), N. Kirova (a), J. Dumas (b), S. Ravy (c), J. Marcus (b), and F. Livet (d), *Phys. Rev. Lett.* **100**, 096403 (2008).
*(a) Laboratoire de Physique des Solides bât 510, CNRS, Orsay (France)*
*(b) Institut Néel, CNRS Grenoble (France)*
*(c) Synchrotron SOLEIL, L'Orme des merisiers, Saint-Aubin (France)*
*(d) INP Grenoble CNRS St Martin d'Hères (France)*

To observe an electronic motion has always been a difficult task. For example, the sliding motion of a charge density wave (CDW) under an electric current has been observed only by a few experiments. Resistivity measurements were the first techniques able to observe this phenomenon **[1]**. In the sliding regime, the Ohm law is no longer fulfilled and a characteristic electronic noise appears. However, CDW systems, such as blue bronze, are rarely homogeneous and such macroscopic measurements fail to give information at the atomic scale.

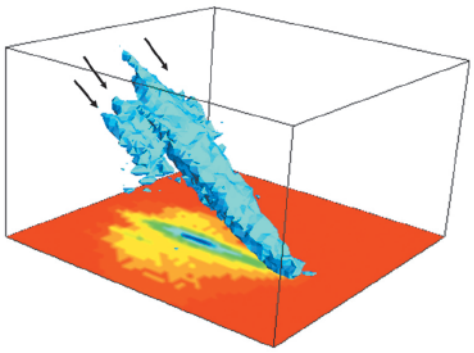

*Fig. 87:* 3D diffraction pattern of the $2k_F$ satellite reflection associated with the CDW. The central peak corresponds to the $2k_F$ satellite reflection. Periodic sequence of satellites flanking the $2k_F$ reflection appear in the sliding regime (indicated by arrows).

X-rays could in principle bring new information since the periodic displacement associated with the CDW can be easily measured by diffraction, leading to $2k_F$ satellite reflections, where $k_f$ represents the Fermi wave vector. Unfortunately, the loss of the phase prevents the observation of translation of a whole system by diffraction. Nevertheless, a few consequences of the sliding phenomenon have been measured. When the wave slides, the domain size decreases along the direction

transverse to the direction of sliding and the $2k_F$ wave vector changes close to the electric contacts. By using coherent X-ray diffraction at beamline **ID01**, we have observed another consequence. In the sliding regime, secondary satellites appear in the close vicinity of the $2k_F$ satellite reflection (**Figure 87**). The period of the corresponding modulation is particularly impressive since it is larger than a micrometre, *i.e.* 1000 times larger than the period of the charge density wave itself ($2\pi/2k_F$ = 10 Å). Such long-range electronic correlations are an unprecedented feature in electronic systems. The existence of this super long-range order could be a direct consequence of the incommensurability of the CDW. In blue bronze, the $2k_F$ wave vector is incommensurate along the chain axis **b***, but it is close to the commensurate value 0.750 **b***. Thus, the proximity to the commensurability point could result in a lattice of discommensurations, or soliton lattice with a periodic phase increment $\Delta\phi = 3\pi/4$, leading to the secondary satellites.

**Reference**
[1] P. Monceau, N.P. Ong, A.M. Portis, A. Meerschaut and J. Rouxel, *Phys. Rev. Lett* **37**, 602 (1976).

## Imaging of nanoislands by coherent GISAXS experiments

**Principal publication and authors**
A.V. Zozulya (a), O.M. Yefanov (a), I.A. Vartanyants (a), K. Mundboth (b,c), C. Mocuta (b), T.H. Metzger (b), J. Stangl (c), G. Bauer (c), T. Boeck (d), M. Schmidbauer (d), *Phys. Rev. B Rapid Commun.* **78**, 121304(R) (2008).
*(a) HASYLAB at DESY, Hamburg (Germany)*
*(b) ESRF*
*(c) Institut für Halbleiterphysik, Johannes Kepler Universität Linz, Linz (Austria)*
*(d) IKZ, Berlin (Germany)*

High-resolution imaging of nanoislands with hard X-rays is an experimental challenge due to the dramatic reduction of the scattered X-ray intensity from a sample when its size is in the submicrometre range. The lack of focusing optics with a nanometre focal spot at high X-ray energies is another bottleneck for a full-field imaging of nanoislands. In our work we use coherent X-rays in a grazing-incidence small-angle X-ray scattering (GISAXS) geometry to image SiGe nanoislands grown by liquid phase epitaxy (LPE) on Si(001). A significantly enhanced diffraction pattern is obtained from an average island as a result of the sum of the coherent scattering from individual islands. This is due to the narrow size distribution, identical shape, and orientation of the islands. We use iterative phase retrieval techniques for the reconstruction of the projected electron density of the islands with typical dimensions in the 100 nm range. We obtained a spatial resolution of 10 to 15 nm for such islands which is not achievable by other X-ray imaging methods.

In a conventional approach based on X-ray scattering methods, the structural information (shape, strain, and composition) is obtained indirectly by fitting the measured diffraction patterns with simulated ones derived from a realistic modelling of the nanostructures. Our model independent approach yields high resolution imaging of nanostructures. As an example, we determined the electron density of epitaxial SiGe nanoislands using coherent scattering in GISAXS geometry (**Figure 88**). In this scattering geometry, the recorded intensity distribution depends on the electron density distribution and the island shape and size, but not on strain. The GISAXS geometry provides an additional advantage to the conventional scattering techniques.The limited penetration of the X-rays into the substrate results in a considerable enhancement of the sensitivity to the nanoislands on the sample surface.

The experiments were performed at beamline **ID01**. The incidence angle $\alpha_i$ was taken equal to the critical angle $\alpha_c$ for the Si substrate $\alpha_i = \alpha_c = 0.22°$, for an X-ray energy of 8 keV. We used SiGe islands of 140 nm and 200 nm size as a model system. All islands exhibit a truncated pyramidal shape with a square base (see insets in **Figure 89**). In addition these islands typically have a narrow size distribution and the same

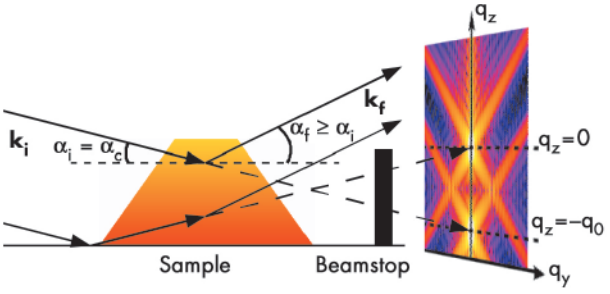


*Fig. 88:* Schematic diagram of the experiment in GISAXS geometry on a single island in the form of a truncated pyramid with a square base.

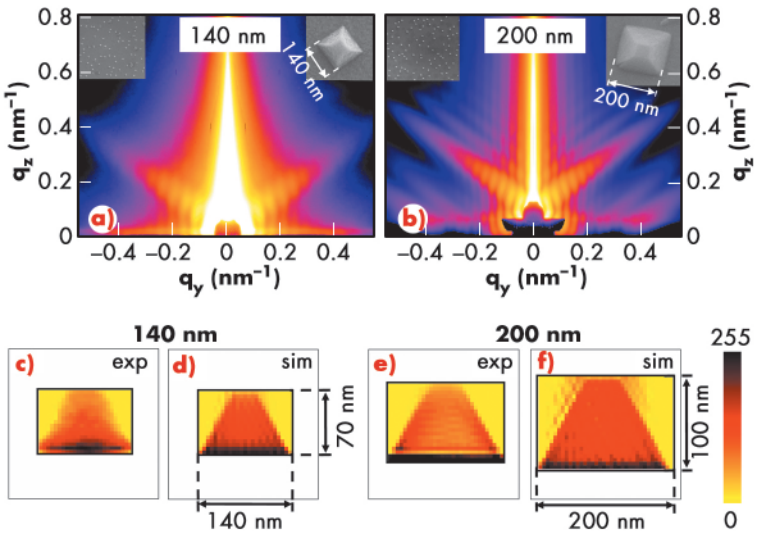


*Fig. 89:* GISAXS diffraction patterns measured for different island sizes, **a)** 140 nm and **b)** 200 nm. SEM images of the samples with different magnification are presented in the insets. **c)** and **e)** Results of the reconstruction of the islands electron density projections obtained from experimental GISAXS data. **d)** and **f)** The reconstruction of a single island electron density obtained from a simulated GISAXS pattern. The size of the rectangular support region used in each reconstruction is indicated by a black line.

**References**
[1] I.A. Vartanyants, *et al., Phys Rev. B* **77**, 115317 (2008).
[2] O.M. Yefanov and I.A Vartanyants, *Eur. Phys. J. Special Topics* **168**, 81 (2009).

crystallographic orientation on a Si surface. In GISAXS geometry with an incoming beam of a few hundreds of micrometres in size, a large number of SiGe islands, typically $10^6$, are illuminated simultaneously. Diffraction patterns measured under these experimental conditions are shown in Figure 89.

Results of the reconstruction of the islands electron density projection are presented in Figure 89. For comparison, a reconstruction of the island shape obtained from a simulated GISAXS pattern is also shown on the same Figure. We see that for our scattering conditions the projection of the electron density, the island shape, and their size are well reproduced.

We have demonstrated how the coherent GISAXS technique can be used to image nanometre-sized objects. The high resolution obtained in our experiment of about 10 to 15 nm is strongly related to the enhancement of the scattered signal from the simultaneous illumination of a large number of uniform islands. This approach does not depend on the crystalline structure of such an object and can, in principle, be applied to any material system. An important extension of this technique is its application to the collection of 3D data measured by rotating the sample around its axis perpendicular to the substrate surface, while maintaining grazing incidence conditions [1]. Such data can then be used for the reconstruction of the full 3D electron density of nanoislands [2].

## X-ray standing waves reveal the different bonding mechanisms of organic adsorbates

**Principal publication and authors**
N. Koch (a), A. Gerlach (b), S. Duhm (a), H. Glowatzki (a), G. Heimel (a), A. Vollmer (c), Y. Sakamoto (d), T. Suzuki (d), J. Zegenhagen (e), J.P. Rabe (a), F. Schreiber (b), J. *Am. Chem. Soc.* **130**, 7300 (2008).
*(a) Humboldt-Universität zu Berlin (Germany)*
*(b) Universität Tübingen (Germany)*
*(c) BESSY (Germany)*
*(d) Institute for Molecular Science (Japan)*
*(e) ESRF (France)*

Organic electronics have become increasingly popular for the various semiconductor applications that utilise conjugated organic materials. Tailoring the electronic and optical properties of such organic heterostructures, however, requires a detailed understanding of the interfaces between organic molecules and metal substrates [1]. A detailed characterisation of the first molecular layer on the substrate is crucial because this layer serves as a nucleus for the growth of the organic thin film, and thus largely determines the charge transfer into the organic layer. We have studied the adsorption behaviour of pentacene (PEN, $C_{22}H_{14}$) and perfluorinated pentacene (PFP, $C_{22}F_{14}$), two prototypical and widely studied organic semiconductor materials that are used in organic field-effect transistors with high hole (PEN) and electron (PFP) mobility.

The X-ray standing wave (XSW) data recorded at beamline ID32 reveal a surprisingly different bonding behaviour of PEN and PFP molecules on Cu(111). Like previous studies, which demonstrated the unique potential of this technique for organic systems [2,3], the new results are based on the high spatial resolution, the element specific information and the sensitivity to the chemical environment of the atoms. The bonding distances $d_0$ (Figure 90) derived from the photoelectron signals of PEN and PFP (Figure 91a) give direct evidence of their different interaction mechanism with the substrate.

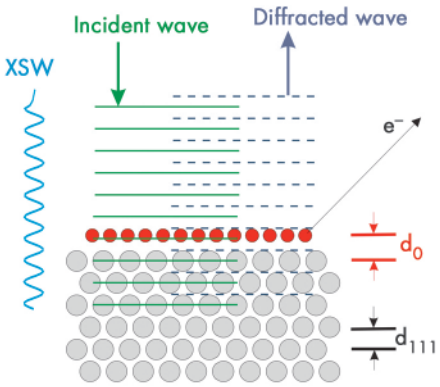


*Fig. 90:* An X-ray standing wave, with the periodicity of the substrate lattice $d_{hkl}$, is generated by Bragg reflection from a single crystal. By scanning the photon energy of the incident wave through the Bragg condition the phase of the interference field changes by $\pi$ and as a consequence the nodal planes of the standing wave field are shifting by $d_{hkl}/2$. Photoelectrons are used as element-specific signal. Depending on the site of the emitting atoms relative to the Bragg planes the photoelectron yield $Y_p(E)$ exhibits a characteristic shape which reveals the adsorption site $d_0$ of a given element.

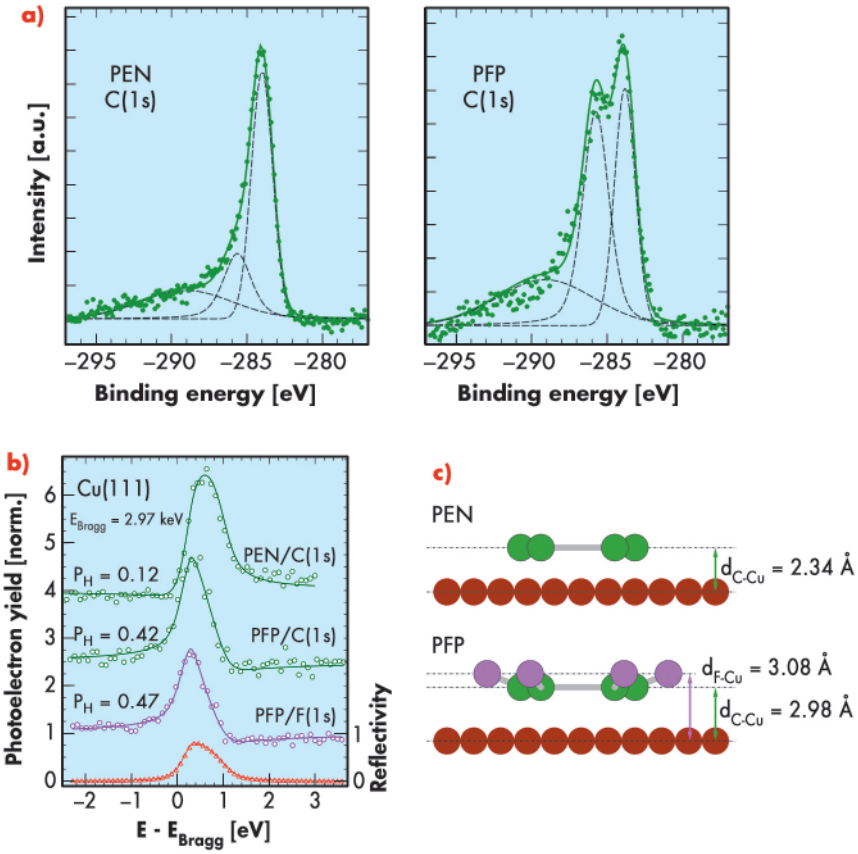


*Fig. 91:* **a)** Core-level spectra with the corresponding analysis for submonolayers of PEN and PFP on Cu(111) which were used for the XSW measurements. **b)** X-ray standing wave scans obtained on submonolayers of PEN and PFP on Cu(111). The symbols represent the photoelectron yield (circles) and substrate reflectivity (triangles) data measured for both adsorbate systems. The solid lines show least-squares fits based on dynamical diffraction theory which provide the coherent position $P_H$ ($d_0 / d_{111} = P_H$ , modulo n) and coherent fraction $f_H$ for each element **[2,3]**. The coherent position thus reveals the adsorption distance $d_0$ of PEN and PFP, whereas the coherent fraction (,$f_H < 1$) with $f_H = 0.55$ for PEN/C1s and $f_H = 0.41$ for PFP/C1s and PFP/F1s, is related to disorder in the adsorbate system. **c)** Schematic conformation of PEN (top) and PFP (bottom) on Cu(111) derived from XSW measurements, indicating the different average positions of the F and C atoms.

The analysis of the XSW data (**Figure 91b**) shows that PEN interacts strongly with the Cu(111) substrate and adsorbs with an average bonding distance of only 2.34 ± 0.02 Å, whereas the carbon core of PFP is located at $d_0$ = 2.98 ± 0.07 Å. Despite the relatively large distance from the surface, the PFP molecules exhibit an adsorption geometry that does not coincide with their planar gas phase structure (**Figure 91c**).

The considerable difference of 0.64 Å found for the positions of the carbon cores of PFP and PEN demonstrates that the later one interacts much stronger with the Cu(111) substrate. Unlike its perfluorinated counterpart PEN molecules obviously undergo a strong chemisorptive binding.
This observation is fully supported by complementary photoemission studies of the valence band structure.
The particular hole injection barriers for PEN and PFP on Cu(111) can be understood by taking into account that the non-planar conformation of PFP results in an adsorption-induced intramolecular dipole of ~0.5 Debye perpendicular to the surface. Overall the example illustrates how XSW measurements at **ID32** can be employed to study the subtle interplay between structural and electronic properties at organic/metal interfaces.

**References**
[1] N. Koch, A. Vollmer, S. Duhm, Y. Sakamoto, T. Suzuki. *Adv. Mater.* **19**, 112 (2007).
[2] L. Romaner, G. Heimel, J.L. Bredas, A. Gerlach, F. Schreiber, R.L. Johnson, J. Zegenhagen, S. Duhm, N. Koch, E. Zojer. *Phys. Rev. Lett.* **99**, 256801 (2007).
[3] A. Gerlach, F. Schreiber, S. Sellner, H. Dosch, I.A. Vartanyants, B.C.C. Cowie, T.-L. Lee, J. Zegenhagen. *Phys. Rev. B* **71**, 205425 (2005).

# *In situ* studies

**Authors**
C. Chambon (a,b), A. Coati (a), M. Sauvage (a) and Y. Garreau (a,b).
*(a) Synchrotron SOLEIL (France)*
*(b) MPQ Paris (France)*

## Nanofaceting of vicinal Ni surfaces induced by Ag deposit

The deposit of small amounts of atoms on surfaces may induce the formation of well-organised nanostructures with long-range order. In the case of a vicinal Cu surface [1], the adsorption of Ag induces well-defined, periodic facets of the surface. Moreover, the Ag coverage can be used to tune the periodicity and the orientation of these facets. The Ag/Ni couple was thought to be very similar to Ag/Cu: Ag and Ni are not miscible in the bulk, and their cohesive energies and atomic sizes are very different, leading to Ag segregation at the Ni surface and to an abrupt chemical interface. However, the faceting behaviour of vicinal surfaces under Ag adsorption was found to be different in the two cases, as observed by scanning tunnelling microscopy (STM) and confirmed quantitatively by Grazing incidence X-ray Diffraction (GIXD), performed on the ID03 beamline.

Ni (322) is a surface with a miscut of 11.42° with respect to the (111) planes and can be viewed as a regular succession of (111) terraces of 1.03 nm width separated by {100}-type monatomic steps. When Ag is deposited on this surface in the monolayer range, and after thermal annealing, periodic facets are indeed observed covering the whole surface, but only within a very narrow coverage range of around 0.6 monolayer. Figure 92 (a and b) shows this "ideal" faceted surface observed by STM and the corresponding X-ray reciprocal space map recorded at $k$ = 2 around two nickel Bragg peaks on which the scattering rods originating from the facets are well distinguished. Two orientations are observed for the facets: (111) and (211). The comparison with a corresponding map recorded around the Bragg peaks of the relaxed silver deposit at $k$ = 1.77, Figure 92c, which shows only (211) facet induced diffuse rods arising from the Bragg nodes, enables us to conclude that the surface is made of (111) bare Ni facets and (211) Ag covered facets. The narrow (111) oriented diffuse features in Figure 92c do not stem from silver Bragg peaks and are presumably linked to planar defects in the nickel near surface region.

For other coverages, in particular lower ones such as 0.3 monolayers, a surface phase separation between faceted regions similar to the case previously described (same facets with similar local periodicity) and bare vicinal nickel as shown in the STM image and the two corresponding maps in Figure 92 (d, e and f) are observed. The energetics of the system would need to be further investigated to understand this surface faceting decomposition.

In addition, as already visible in the STM image, Figure 92a, one of the

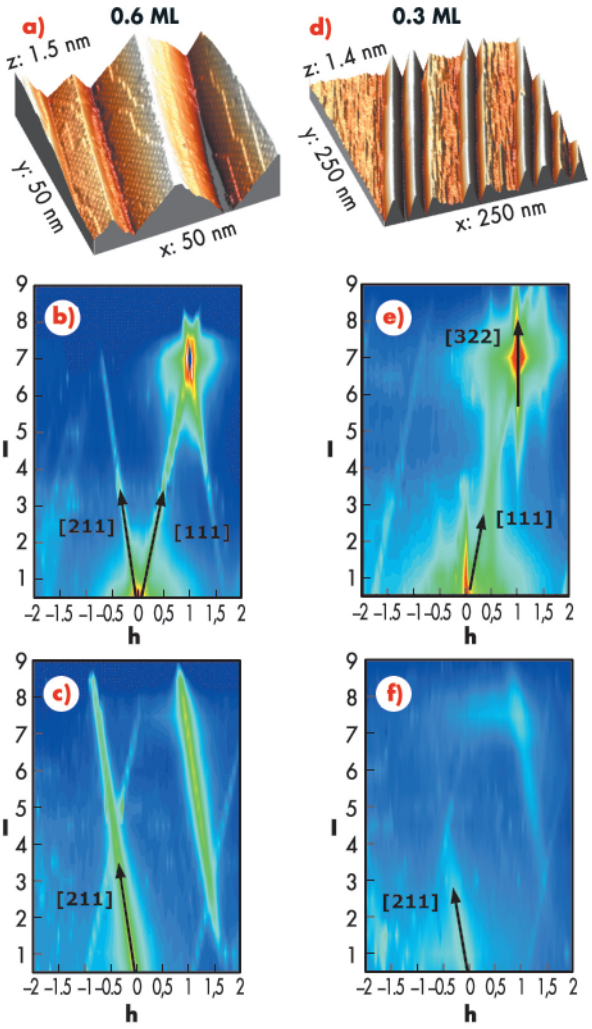


*Fig. 92:* Ni(322) surface after Ag deposit followed by annealing at 600 K. The Ag covered and bare Ni facets are clearly recognised. **a)**, **b)** and **c)** correspond to a 0.6 monolayer deposit, and **d)**, **e)** and **f)** to 0.3 monolayers. **a)** 3D STM image (50x50) nm²; **b)** *(h, l)* reciprocal space map at $k$ = 2; **c)** *(h, l)* reciprocal space map at k = 1.77; **d)** 3D STM image (250x250) nm²; **e)** *(h, l)* reciprocal space map at k = 2; **f)** *(h, l)* reciprocal space map at $k$ = 1.77.

facets shows a reconstruction. indeed, accurate GIXD data could be collected on the reconstructed Ag covered (211) facets (**Figure 93a**) corresponding to a (2 x *n*) surface cell (8 < *n* < 9). A starting model sketched in **Figure 93b** involving 6 silver rows on top of two successive (111) terraces of the (211) Ni substrate with (*n-1*) Ag atoms for *n* Ni atoms along the [01] direction has been used. When optimised by quenched molecular dynamics simulations involving 60 bulk layers, this model renders the diffraction data well but needs further refinement to quantitatively account for all measured in-plane and out-of plane structure factors. Mixing various coverages of the terraces is being investigated.

The knowledge of the system morphology and its surface structure are key parameters for its possible use as a nano-organised template for further growth of selected nano objects with magnetic or catalytic properties. This study shows that the coupling between GIXD, STM and atomistic simulations is necessary and fruitful to understand such phenomena.

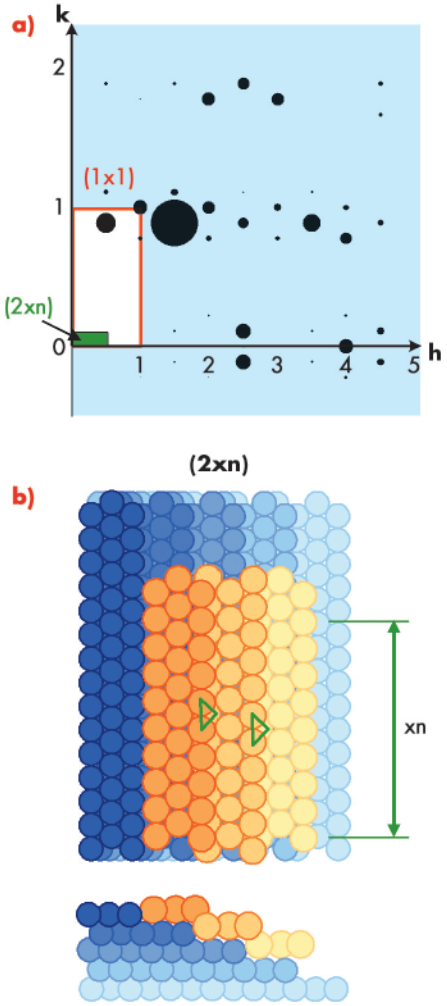


*Fig. 93:* Surface reconstruction induced by silver on the (211) facets. **a)** GIXD in-plane data which shows the (2x*n*) surface periodicity; **b)** model of the surface structure used for QMD simulations (Ag atoms in orange, Ni atoms in blue).

**References**
[1] A. Coati, J. Creuze, and Y. Garreau, *Phys. Rev. B* **72**, 115424 (2005); Y. Garreau, A. Coati, A. Zobelli, J. Creuze, *Phys. Rev. Lett.* **91**, 116101 (2003).

## The shape of supported rhodium nanoparticles during oxidation and reduction

**Principal publication and authors**
P. Nolte (a), A. Stierle (a), N.Y. Jin-Phillipp (a), N. Kasper (a), T.U. Schülli (b), H. Dosch (a), *Science* **321**, 1654 (2008).
*(a) Max-Planck-Institut für Metallforschung, Stuttgart (Germany)*
*(b) INAC/ SP2M Commissariat à l'Energie Atomique, Grenoble (France)*

The world market for the production of chemicals is estimated today to be around 1,300 billion Euros per year. More than 90% of these chemicals are produced via a catalytic process.

Catalysts also play an increasingly important role for the development of green chemistry and advanced renewable energy technologies.

A study on catalytic nanoparticles carried out on beamline **BM32** gives an example of how *in situ* X-ray scattering in dedicated sample environments can bridge the gap between structural and functional properties of nanostructures. In particular the interplay between the shape and size change of the nanoparticles and the oxidation/reduction process can be monitored.

The current challenge for fundamental research is to provide a detailed microscopic understanding of the different physical and chemical processes which take place at nanoparticles during catalytic reactions **[1]**. It is expected that nanoparticles should exhibit enhanced catalytic activity: (i) as they possess an increased number of under-coordinated atoms, and (ii) as different low index facets co-exist, facilitating mass transport and thereby lifting kinetic barriers known from single crystal surfaces. During catalytic cycling experiments, nanoparticles have been observed to undergo reversible size changes, which are associated with cyclic shape changes, material re-dispersion and sintering.

Here, we report an *in situ* high-resolution X-ray diffraction study of

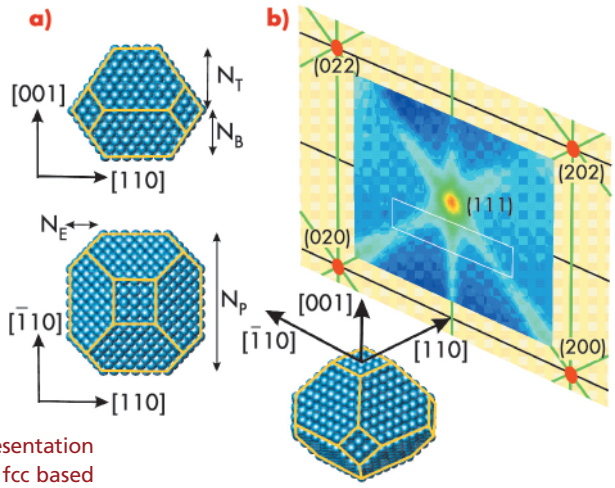


*Fig. 94:* **a)** Schematic representation of the particle shape for fcc based nanoparticles. The lateral particle size is characterised by $a_{fcc}/2 * N_P$, its height by $a_{fcc}/2 * (N_T+N_B)$ and the missing edge atoms by $N_E$. For a Wulff shaped particle (without substrate) is $N_T = N_B$ and $N_E = N_P-N_T$. **b)** (110) plane reciprocal space map of clean Rh nanoparticles on MgO(100) with an average lateral size of 8 nm (in fcc bulk coordinates). The white box indicates the area for high resolution scans.

epitaxial rhodium nanoparticles on MgO(100), during oxidation and CO induced reduction. This study brought to light a reversible facet rearrangement of the nanoparticles, which is in direct relation to the formation of oxygen-induced superstructures. We were able to access the average particle shape and size with atomic resolution from a quantitative fitting of the extended reciprocal space maps that were obtained at elevated temperatures and under varying gas atmospheres.

Rhodium nanoparticles were deposited *in situ* at a substrate temperature of 670 K in the **BM32** ultra-high vacuum (UHV) surface X-ray diffraction chamber, after cleaning the MgO substrates by sputtering and annealing under an oxygen atmosphere. The sample was annealed at 970 K to achieve the equilibrium shape of the nanoparticles (see **Figure 94a**). Grazing incidence small angle scattering was performed simultaneously to wide-angle diffraction reciprocal-space mapping.

High-resolution reciprocal space maps were recorded from (H,K) = (-0.5,0.5) to (0.5,-0.5) and from L = 0.6 to 0.84. **Figure 95a** (top) shows a high-resolution map of the clean particles, observed at 600 K under UHV conditions. The data can be understood in a straight forward way within kinematical diffraction theory which suggests nanoparticles with a truncated octahedral shape.

In the next step, the Rh nanoparticles are exposed to $3 \cdot 10^{-5}$ mbar $O_2$ at 600 K and simultaneously we recorded the X-ray diffraction pattern (**Figure 95 (b** and **c)**). We actually observe a very clear change in the X-ray diffraction signal (see difference map, **Figure 95b**) which consists of an intensity enhancement along the (001) rod and an intensity loss along the (111)-rods.

As a result of this analysis we find that the area both of the (100) side facets and (001) top facet increases upon oxidation, which is driven by the formation of ultrathin oxide layers. This implies that only intra particle mass transport takes place during the oxidation thereby removing Rh atoms from the (100) side and top facets. The average amount of atoms removed corresponds to the number of atoms

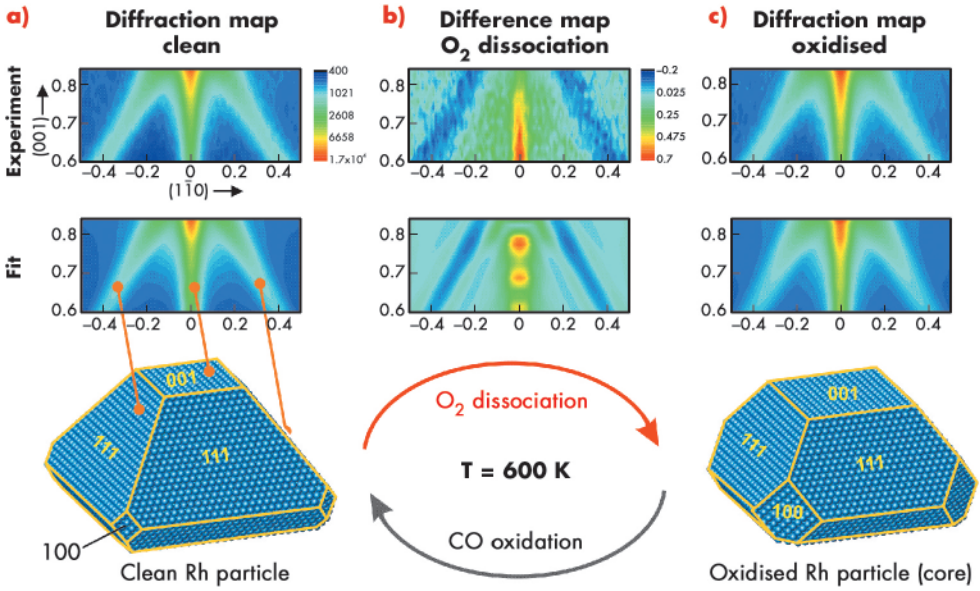


*Fig. 95:* **a)** (top) (110) Diffraction map of clean Rh particles at 600 K. (middle) Fitted diffraction map corresponding to the average particle shape given below. **b)** (top) Oxygen induced signal change in the (110) plane. (middle) Simulated signal change for particles with increased (100) side facet area. **c)** (top) Experimental (110) diffraction map at 600 K and $3 \cdot 10^{-5}$ mbar $O_2$ pressure. (middle) Fitted diffraction map for particles under oxygen exposure. (bottom) Best fit core particle shape after oxidation.

incorporated into the surface oxide layers on all facets. A further key observation is that the oxygen-induced shape change of the Rh nanoparticle is fully reversible when the surface oxide is removed by CO exposure (at $1 \cdot 10^{-5}$ mbar). We have demonstrated that *in situ* reciprocal space mapping can give an atomistic insight into the structure and morphology of catalytically-active nanoparticles on oxide supports.

**Reference**
[1] G. Ertl, H. Knözinger, F. Schüth, J. Weitkamp, *Handbook of Heterogeneous Catalysis*, Wiley-VCH, Weinheim (2008).

## X-ray study of mesoscopic relaxations in cobalt nanoislands on Cu(001)

**Principal publication and authors**
O. Mironets (a), H.L. Meyerheim (a), C. Tusche (a), V.S. Stepanyuk (a), E. Soyka (a), P. Zschack (b), H. Hong (b), N. Jeutter (c), R. Felici (c), and J. Kirschner (a), *Phys. Rev. Lett.* **100**, 096103 (2008).
*(a) Max-Planck-Institut f. Mikrostrukturphysik, D-06120 Halle (Germany)*
*(b) APS, Argonne National Laboratory, Argonne, IL 60439 (USA)*
*(c) ESRF*

Many atoms within nanostructures experience reduced coordination when compared to the bulk. This leads to strongly-modified chemical and physical properties, one being the rearrangement of the atoms in the structure. Despite its fundamental importance, knowledge of the atomic geometry in nanostructures is quite scarce. The interatomic distance represents the most important parameter and a theoretical study **[1]** on cobalt nanoislands on Cu(001) consisting of several tens of atoms has predicted that the interatomic distance is dramatically reduced from d = 2.51 Å for the bulk to values in the 2.4 Å range, *i.e.* considerably exceeding "usual" relaxations known for surfaces.

To provide direct evidence for the relaxations, we studied the registry of the cobalt-atoms with the Cu(001) substrate at beamline 33-ID-D (Advanced Light Source, ANL, USA) and at beamline **ID03**. In contrast to the common view that Co-atoms reside in hollow sites at a distance of d = 2.56 Å characteristic for the Cu(001) surface, a shortened interatomic distance (d = 2.40 Å) implies that cobalt atoms are not only located in hollow sites but also occupy low symmetry positions off the hollow site.

**Figure 96** shows the positions of 431 cobalt atoms within the surface unit cell derived from molecular dynamics calculations. The distribution of the cobalt atoms around the hollow site at (x,y) = (0,0) can be approximated by a Gaussian function of half width at half maximum of $\langle u \rangle = 0.18$ Å, corresponding to a Debye parameter of $B = 8\pi \langle u^2 \rangle = 2.56$ Å$^2$.
The determination of the static disorder of the adsorbed Co-atoms is the basis of the X-ray analysis.

The registry of the cobalt atoms is probed by the analysis of the intensity distribution along the substrate reflections, which are referred to as crystal truncation rods (CTR's).
The CTR's arise from the termination of the crystal leading to a continuous intensity distribution, $[I(q_z)]$ between the bulk Bragg-reflections. **Figure 97** shows the structure factor amplitudes

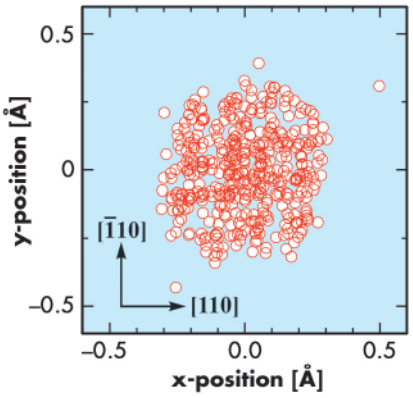


*Fig. 96:* Molecular dynamics calculation showing the positions of cobalt atoms in the Cu(001) unit cell. The centre at (x,y) = (0,0) corresponds to the hollow site.

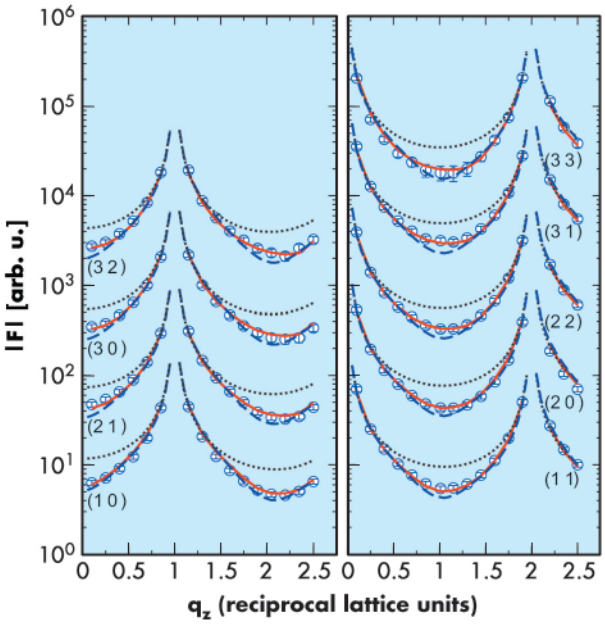


*Fig. 97:* Crystal Truncation Rods for 0.3 monolayer cobalt on Cu(001). Symbols and lines correspond to experimental and calculated structure factor amplitudes, respectively. Curves are shifted vertically for clarity.

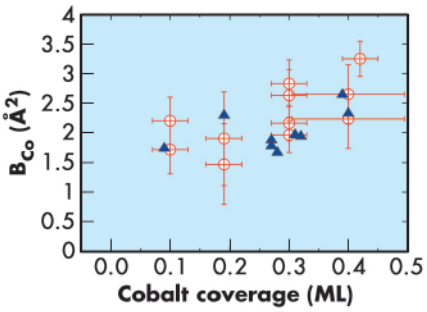


*Fig. 98:* Experimentally-derived Debye parameters $B_{Co}$ of cobalt atoms (circles) versus coverage. Triangles represent corresponding values determined by molecular dynamics calculation.

(|F| ∝ √I) along several CTR's. Dotted lines represent the calculated |F|-values for clean Cu(001), while solid and dashed lines are fits to the data (symbols) assuming hollow site adsorption with and without disorder of the cobalt atoms, respectively.

The solid line fits the data best especially close to the minima along the CTR's, which is the most surface sensitive position. **Figure 98** summarises the cobalt Debye-parameters B versus coverage. We find values in the B = 2.5 Å$^2$ range, in excellent agreement with calculated values shown as triangles. In summary, the analysis of the static disorder of surface adsorbed cobalt atoms on Cu(001) in combination with molecular- dynamics calculations based on STM images has provided experimental evidence for large contractions of the interatomic cobalt distances in monoatomic nanoislands.

**Reference**
[1] V.S. Stepanyuk, D.I. Bazhanov, A.N. Baranov, W. Hergert, P.H. Dederichs, and J. Kirschner, *Phys. Rev B* **62**, 15398 (2000).

# X-ray Absorption and Magnetic Scattering

## Introduction

Highlights are "snap shots" in time, they present the latest achievements, which are often the culmination of many years of work. This is not only true of the scientific programmes that lead to an experiment at the ESRF but also for the beamline facilities which have resulted from investment (human and financial) over the ~15 years that the ESRF has been operating. In that time, new instruments and support facilities have been built that allow today's state-of-the art experiments to be performed. So even if an experiment was conceived and the results published only recently, it is building on the work done and experience gained over the years. We are now at a point in time where the ESRF will start an Upgrade Programme. The aim is to allow experiments to be performed that cannot be done today. Although the gradual improvement of existing facilities is important and will allow new science in the future, the Upgrade Programme will take us a step further and enable the development of facilities that cannot be realised in this incremental manner. These developments will set the foundations for the scientific results of the next decade or more.

In the articles that follow there is a strong emphasis on magnetic materials, whether they are studies of dilute magnetic semiconductors, multiferroics or magnetostrictive materials. In addition, since absorption spectroscopy is a very powerful technique that can be applied to many problems, there are also highlights resulting from a variety of other studies. Examples include experiments on neptunium containing materials, which are interesting for environmental reasons; studies of the geologically important iron oxide, siderite, and research on alkali-doped fullerenes with the aim of producing new high-dimensional polymers. Also, the importance of industrial activities on the beamlines should not be forgotten. This is particularly evident at ID24 where Toyota has been an industrial user for several years and is well illustrated by the highlight article on vehicle exhaust catalysts (see **Figure 99**).

*Fig. 99:* An on-line approach to increasing catalyst lifetimes. X-ray studies by means of a special *in situ* cell were used to investigate auto-exhaust catalysts under realistic conditions at beamline ID24 (Image courtesy of TOYOTA Motor Corporation).

In the future we can expect studies of magnetism and of the electronic properties of materials to remain an exciting area of research. The Upgrade Programme will take these activities to new horizons. There will be more emphasis on "dynamical properties", "extreme conditions" and "science at the nanoscale" as these are some of the themes of the Upgrade Programme. There will undoubtedly be other important developments outside the Upgrade Programme. For instance, the possibility of having experimental facilities with very high static magnetic fields (> 30T) is being actively pursued. New and improved facilities for users will give us an even stronger basis for the highlights of the future.

***N.B. Brookes***

**Authors**
F. Wilhelm (a), P. Poulopoulos (b), V. Kapaklis (b), J.-P. Kappler (c), G. Schmerber (c), A. Derory (c), N. Jaouen (a), A. Rogalev (a), A.N. Yaresko (d), C. Politis (b,e).
*(a) ESRF*
*(b) University of Patras (Greece)*
*(c) IPCMS Strasbourg (France)*
*(d) MPI Dresden (Germany)*
*(e) INT Karlsruhe (Germany)*

# Au and Fe magnetic moments in disordered AuFe alloys

Recent developments in third generation synchrotron radiation facilities has made possible the element-specific determination of magnetic moments in multi-element materials via the X-ray magnetic circular dichroism (XMCD) technique. The limit of detection is now well below 0.01 $\mu_B$/atom even for thin films. Moreover, the ability to separate spin and orbital magnetic moment contributions has rendered XMCD as the most powerful tool for the complete magnetic characterisation of materials and for clarifying subjects that had remained controversial in the past.

In this work, we have determined the 5*d* induced magnetic moment of Au via XMCD, for disordered *fcc* and *bcc* AuFe alloys in the concentration range 25 - 97 at. % Fe. The exotic *fcc* phase is not predicted in the binary alloy phase diagram at room temperature.

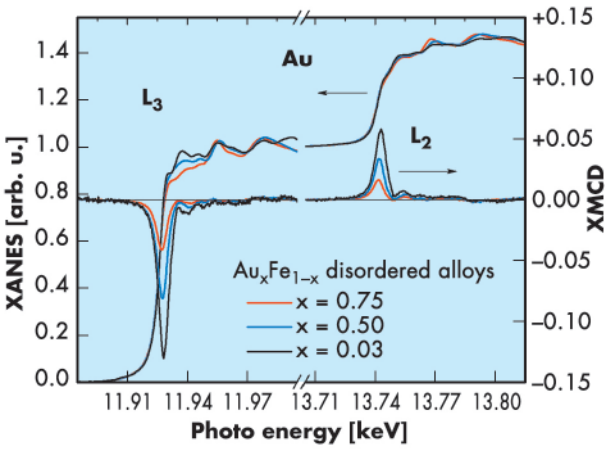


*Fig. 100:* Normalised XANES and XMCD spectra at the $L_{3,2}$ edges of Au in $Au_xFe_{1-x}$ alloys, x as indicated. The spectra reveal a straightforward relation between the 5*d* induced magnetic moments of Au and the number of Fe nearest neighbours.

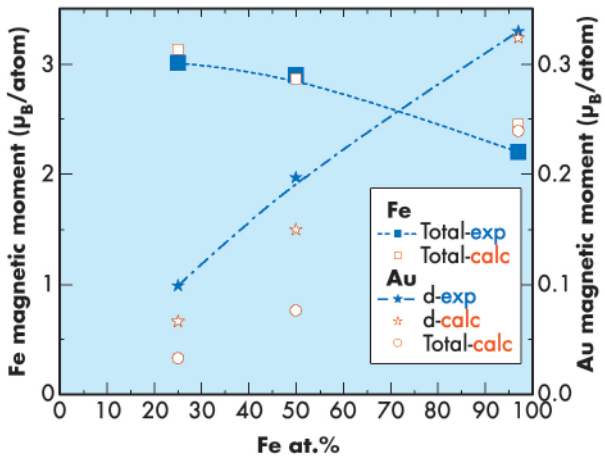


*Fig. 101:* Au and Fe magnetic moments by experiment and theory as a function of the Fe at. % concentration in disordered AuFe alloys. The lines are guides to the eye.

However, one may produce single phase *fcc* disordered AuFe alloys via rapid quenching of the molten alloy for concentrations up to 53 at. % Fe. Iron is in the regular low-spin state in the *bcc* Fe-rich alloys, but in the high-spin state in the ferromagnetic *fcc* alloys. This fact may further influence the Au induced magnetic moment and it makes the AuFe alloys extremely interesting from the point of view of magnetism; however, they could not be thoroughly studied in the past and controversial results were published, due to the lack of experimental techniques with element specificity and shell selectivity.

**Figure 100** presents the normalised XANES and XMCD spectra recorded at the $L_{3,2}$ edges of Au in $Au_xFe_{1-x}$ disordered alloys. The data were recorded at the beamline **ID12** using the fluorescence detection scheme. The intense photon flux of the Apple II undulator with a very high degree of circular polarisation was necessary in order for high quality data to be accumulated for the Au signal. The sizeable XMCD signal reveals that Au has acquired an induced magnetic moment. Knowing the direction of the magnetic field and the helicity of the beam we were able to conclude that Au is polarised parallel to the Fe magnetic moment. Our analysis followed the magneto-optical sum rules. The outcome was the precise determination of the 5*d* spin and orbital magnetic moment of Au in the disordered AuFe alloys. The results show that the total 5*d* induced magnetic moment of Au in the *fcc* alloys scales with the number N of nearest Fe neighbours, from $M_{Au}$ = 0.1 $\mu_B$/atom, for N = 3, to $M_{Au}$ = 0.2 $\mu_B$/atom, for N = 6. Iron in these alloys is in a high spin state carrying a total magnetic moment of about 3 $\mu_B$/atom as our superconducting quantum interference device (SQUID) magnetometry measurements have revealed. The maximum value of 5*d* induced magnetic moment of Au is 0.33 $\mu_B$/atom and is exhibited when Au is placed as an impurity in a *bcc* Fe

environment, *i.e.* when all its first neighbours are Fe atoms. In the bcc environment the total magnetic moment of Fe is 2.2 $\mu_B$/atom. Thus, one may conclude that the total 5*d* induced Au moment seem to follow a simple scheme of the type $M_{Au} \propto (N/N_{total})*M_{Fe}$ regardless of the crystallographic structure. Our experimental results for the Au and Fe magnetic moments compare well with first principle calculations, as **Figure 101** reveals.

In conclusion, the relationship between the induced magnetism of Au and the Fe magnetic moments for disordered *bcc* and *fcc* AuFe alloys have been found and a simple formula for the Au induced magnetic moments was deduced. The experimental results, recorded via a combination of XMCD and SQUID resolve previous controversial experimental data and are in good agreement with our *first principle* calculations **[1]**.

**Reference**
[1] F. Wilhelm, P. Poulopoulos, V. Kapaklis, J.-P. Kappler, N. Jaouen, A. Rogalev, A.N. Yaresko, and C. Politis, *Phys. Rev. B.* **77**, 224414 (2008).

# Absence of intrinsic ferromagnetic interactions in $Zn_{1-x}Co_xO$ with high structural perfection

**Principal publication and authors**
A. Ney (a), K. Ollefs (a), S. Ye (a), T. Kammermeier (a), V. Ney (a), T.C. Kaspar (b), S.A. Chambers (b), F. Wilhelm (c), and A. Rogalev (c), *Phys. Rev. Lett.* **100**, 157201 (2008).
*(a) Experimentalphysik, Universität Duisburg-Essen, Duisburg (Germany)*
*(b) Pacific Northwest National Laboratory, Richland, Washington, (USA)*
*(c) ESRF*

Dilute magnetic semiconductors are envisioned as sources of spin-polarised carriers for future semiconductor devices which simultaneously utilise spin and charge degrees of freedom. $Zn_{1-x}Co_xO$ (Co:ZnO) was thought a promising n-type dilute magnetic semiconductor for spintronics. Although Co:ZnO materials have been investigated intensively, their respective magnetic behaviours remain controversial from experimental and theoretical points of view. Claims of room-temperature ferromagnetism, or its absence, have been made by experimentalists and theoreticians **[1]**. Thus, the possibility that metallic Co nanoclusters account for the observed magnetic order has to be ruled out with great care.

Co:ZnO with 10.8% Co was grown by pulsed laser deposition onto c-plane sapphire substrates **[1]**, and studied with SQUID magnetometry and synchrotron radiation at the Zn and Co K-edges. X-ray absorption near-edge spectra (XANES) were recorded at beamline **ID12** in total fluorescence yield both with linear and circular polarised light under 10° grazing incidence. To record the X-ray linear dichroism (XLD) the polarisation was flipped using a quarter wave plate. The X-ray magnetic circular dichroism (XMCD) was recorded by reversing the circular polarisation as well as the magnetic field direction.

**Figure 102** shows the XANES and their respective XLD spectra recorded at the Zn and Co K-edges using linear polarised light. The XLD spectra show features typical for the wurtzite lattice of the ZnO host. In addition, simulations of the XANES and XLD spectra were made using FDMNES **[2]**, and the lattice parameters of ZnO for a Co:ZnO supercell with Co on Zn substitutional sites. The good agreement between experiment and simulation suggests that more than 95% of the Co dopant atoms are located on Zn substitutional sites. This result underlines the excellent structural quality of the Co:ZnO, devoid of metallic Co, small Co clusters or antisite disorder.

**Figure 103** summarises the magnetic properties of the Co:ZnO sample. M(H)-curves with H perpendicular to

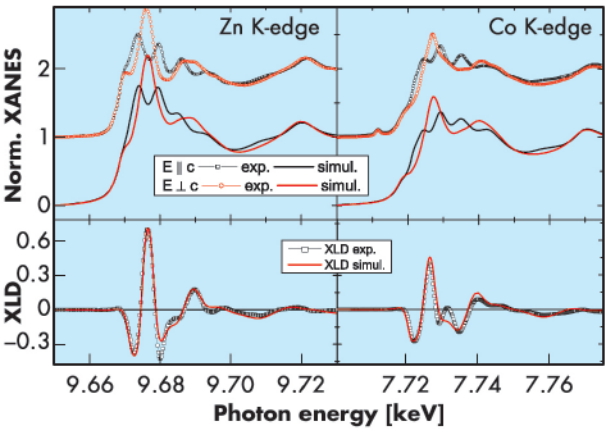


*Fig. 102:* XANES spectra at the Zn and Co K-edges recorded with two orthogonal linear polarisations and the respective XLD spectra. Simulations using the FDMNES code are also shown.

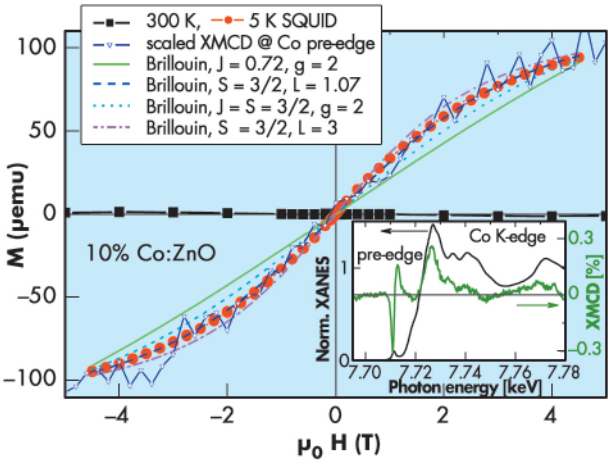


*Fig. 103:* M(H)-curves recorded at 5 K by SQUID and XMCD at the Co K-edge, respectively. The inset shows the respective XMCD spectrum. Lines are Brillouin fits (see text).

the c-axis were recorded using SQUID (full symbols) and XMCD at the pre-edge feature of the Co K-edge as indicated in the inset. This pre-edge feature is characteristic for $Co^{2+}$ in tetrahedral coordination [1] confirming the XLD results. The XMCD data were scaled to the SQUID data and both techniques consistently show paramagnetic behaviour with a comparable curvature of M(H). Three different fits using Brillouin functions for S = 3/2 and various L are scaled to the SQUID data. L = 3 reflects the maximum possible value of the magnetic moment for $Co^{2+}$ ($3d^7$) resulting in too strong a curvature, whereas the L = 0 fit has too weak a curvature to reproduce the data. Using L = 1.07, ($\mu_z = 4.1\mu_B$/Co atom), which results in an L/S-value of 0.7 that was already reported by means of XMCD data recorded at the Co $L_{3/2}$-edges, the curvature of the M(H) curves can be reproduced well. However, if one calculates the effective magnetic moment per Co atom from the measured magnetisation by SQUID, one finds only 1.44 $\mu_B$/Co atom which results in a linear M(H)-curve using the respective Brillouin function in disagreement with the data.
In other words, only 28(3)% of the magnetisation that can be expected from the curvature of M(H), are measured by SQUID. If one calculates the abundance of isolated Co atoms, Co-O-Co pairs, triples etc on Zn cation sites, *i.e.* an hcp sublattice with 12 next neighbours [3], this results in 28% of isolated Co atoms, 18% of pairs, 11% of triples etc. for 10.8% of Co in ZnO. Therefore, the magnetisation measured by SQUID can be readily explained by a paramagnetic behaviour of the isolated Co atoms, an antiparallel alignment of the Co-O-Co pairs and negligible contributions from larger cation clusters.

In conclusion we were able to demonstrate by means of XLD that the Co dopant atoms occupy exclusively substitutional Zn sites in high-quality Co:ZnO samples. In such samples, the isolated Co atoms behave as paramagnetic whereas the Co-O-Co pairs couple antiferromagnetically. Thus we find no signs of intrinsic ferromagnetic interactions.

**References**
[1] T.C. Kaspar, T. Droubay, S.M. Heald, P. Nachimuthu, C.M. Wang, V. Shutthanandan, C.A. Johnson, D.R. Gamelin, and S.A. Chambers, *New J. Phys.* **10**, 055010 (2008).
[2] Y. Joly, *Phys. Rev. B* **63**, 125120 (2001).
[3] R.E. Behringer, *J. Chem. Phys.* **29**, 537 (1958).

## Probing ion-specific magnetism in multiferroics

**Principal publication and authors**
R.D. Johnson (a), S.R. Bland (a), C. Mazzoli (b), T.A.W. Beale (a), C-H. Du (c), C. Detlefs (b), S.B. Wilkins (d) and P.D. Hatton (a), *Phys. Rev. B* **78**, 104407 (2008).
*(a) Department of Physics, Durham University (UK)*
*(b) ESRF*
*(c) Department of Physics, Tamkang University, Tamsui (Taiwan)*
*(d) Department of Condensed Matter Physics and Materials Science, Brookhaven National Laboratory, Upton (USA)*

Magneto-electric multiferroics are materials in which mutually-coupled magnetic and ferroelectric order-parameters coexist in a single phase. The recent discovery of such systems has lead to a boom in research in this field, not only due to their potential for technological application, but also because they offer an opportunity for detailed studies of coupled, and often competing order parameters [1]. In certain rare-earth manganites complex magnetic structures, such as cycloidal spin density waves, break inversion symmetry: the essential ingredient to obtain a spontaneous ferroelectric polarisation. Strong, intrinsic magneto-electric coupling can give rise to the condition whereby it is possible to manipulate the spontaneous electric polarisation by applying an external magnetic field, and thus produce a potentially important sensor material. For example, at low temperature $TbMn_2O_5$ displays a complete reversal of electric polarisation upon application of a modest external magnetic field of 2 T [2]. To completely understand this mechanism and to predict the macroscopic properties

observed, it is vital to unravel the complex magnetic structure. Ultimately this will allow the fabrication and optimisation of new devices. On substitution of the rare-earth ion, the $RMn_2O_5$ series ($R$ = rare-earth, Bi or Y) displays a rich phase diagram with a diverse range of macroscopic properties. Resonant X-ray scattering (RXS) selectively probes the long-range magnetic order present on a particular atomic species by tuning to an atomic transition corresponding to the excitation of a core electron. The subsequent recombination of the excited electron with the core hole emits a photon whose polarisation encodes precious information on the magnetic state of the resonating ions.

We have employed RXS to investigate the magnetic behaviour of the terbium ions in $TbMn_2O_5$ at 25 K, where the electric polarisation is most evident [3]. An energy scan through the terbium $L_{III}$ absorption edge at a constant wave-vector clearly showed two resonances, one just above the absorption edge and the other 8 eV lower. These originate from E1-E1 and E2-E2 transitions, respectively. In contrast to the E1-E1 transitions probing the band-like 5d levels that may hybridise with the neighbouring ions, the E2-E2 transitions directly probe the magnetism of the terbium 4f shell. The polarisation of the emitted photons is dependent upon the incident X-ray polarisation, magnetic moment direction and, in the case of the E2-E2 transition, wave-vector. This dependence is probed by full linear polarisation analysis as shown in **Figure 104**, a technique recently developed at beamline **ID20**. Simulations based upon the theory of Hannon *et al.* [4], of the scattered polarisation measured as a function of incident polarisation, allows one to refine the magnetic moment directions associated with both the terbium 5d and 4f states.

In $TbMn_2O_5$, manganese ions are found in two sublattices, $Mn^{3+}$ ions coordinated in $MnO_5$ square based pyramids and $Mn^{4+}$ ions in $MnO_6$ octahedra. These sublattices order below a Néel temperature of 43 K. It had been hypothesised that the

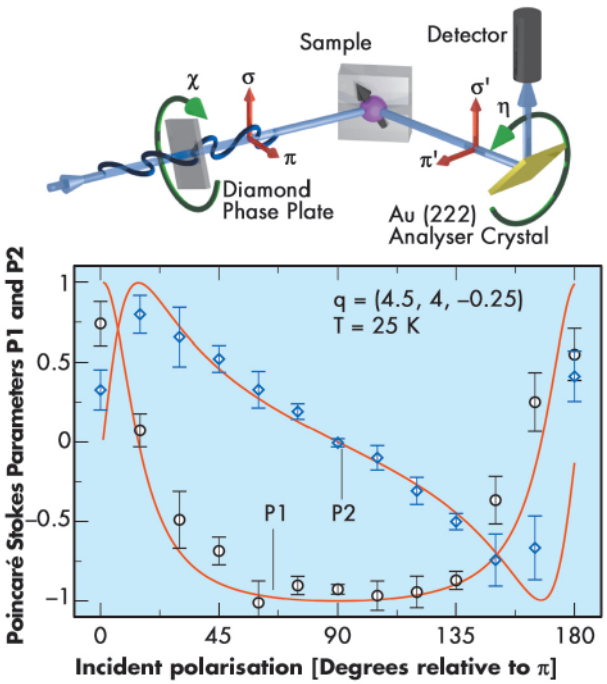


*Fig. 104:* Top: Experimental set up for full linear polarisation analysis. A diamond phase plate used in transmission geometry rotates the incident X-ray polarisation. The polarisation of the scattered beam may be measured in terms of Poincaré-Stokes parameters (P1 and P2) using an analyser crystal. Bottom: P1 and P2 of the (4.5, 4, -0.25) magnetic reflection at the E1-E1 transition at 25 K as a function of incident polarisation.

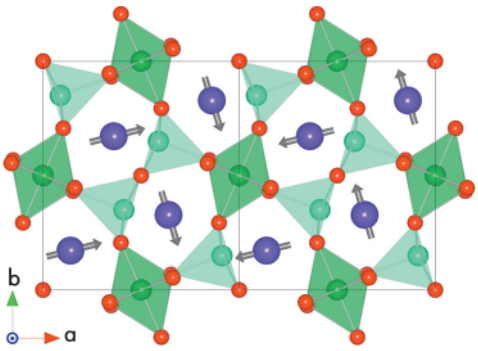


*Fig. 105:* The refined terbium magnetic structure of $TbMn_2O_5$ at 25 K. The magnetic moments lie in the *ab*-plane with a slight offset in the *c*-axis direction. Terbium ions are shown in purple, oxygen in red and $Mn^{4+}$ and $Mn^{3+}$ in dark and light green octahedral and square-based pyramid oxygen co-ordinations, respectively.

magnetic order on the terbium sublattice is induced through nearest neighbour interactions solely with $Mn^{4+}$ ions [5]. We have confirmed this scenario through the measurement of a superlattice reflection sensitive to the long range ordering of the magnetic moments which is shown to resonate at the binding energy for terbium, confirming an ordering of the terbium sublattice. Further analysis of the incident and exit photon polarisation confirms that the induced polarisation arises solely through interaction with $Mn^{4+}$ ions, shown by the red line in **Figure 104**. We were unable to reproduce the data when assuming a polarisation of the terbium ions due to the $Mn^{3+}$ ions, confirming the hypothesis of Blake *et al.* [5]. By performing a least squares fit to the polarisation analysis, taken when tuned to the E2-E2 resonance, we have refined the magnetic structure of the terbium ion sublattice as illustrated in **Figure 105**.

**References**

[1] M. Fiebig, *J. Phys. D: Appl. Phys.* **38**, R123-R152 (2005).

[2] N. Hur *et al.*, *Nature* **429**, 392 (2004).

[3] L.C. Chapon *et al.*, *Phys. Rev. Lett.* **93**, 177402 (2004).

[4] J.P. Hannon *et al.*, *Phys. Rev. Lett.* **61**, 1245 (1988).

[5] G.R. Blake *et al.*, *Phys. Rev. B* **71**, 214402 (2005).

**Authors**
S. Agrestini (a), A. Bombardi (b), C. Mazzoli (c), L. Chapon (d) and M.R. Lees (e).
*(a) Laboratoire CRISMAT, UMR 6508 CNRS-ENSICAEN, Caen (France)*
*(b) Diamond Light Source Ltd., Rutherford Appleton Laboratory, Chilton-Didcot (UK)*
*(c) ESRF*
*(d) ISIS Facility, Rutherford Appleton Laboratory, Chilton-Didcot (UK)*
*(e) Department of Physics, University of Warwick, Coventry (UK)*

# Revealing the magnetic ground state of $Ca_3Co_2O_6$

The study of frustration offers challenges to both theoreticians and experimentalists alike. New states, often characterised by peculiar static and dynamic properties, are created as a result of competing interactions. In particular, when acting in magnetic systems, frustration reveals many of its most intriguing aspects and careful investigations of specific systems can produce fascinating new science.

In this respect, $Ca_3Co_2O_6$ is a very interesting system, characterised by low dimensional magnetism and topological frustration. **Figure 106a**, shows the crystallographic structure of the compound, made up of chains of face-sharing polyhedra running along the c-axis, arranged in the ab-plane on a triangular lattice. Due to local symmetry, one half of the Co ions have a magnetic moment (Co(II), $\mu$ ~5.1 $\mu_B$), subject to (antiferro-)ferromagnetic (inter-)intrachain interactions. In the sketch, magnetic sites are located at the centre of dark blue polyhedra, representing oxygen cages with trigonal prismatic coordination.

$Ca_3Co_2O_6$ has been the focus of considerable experimental and theoretical attention due to its peculiar magnetic properties. Below the Neel temperature ($T_N$ ~25 K), 3D long range magnetic order is established. At low temperature, an unexpected evolution of the magnetic order parameter versus both temperature and magnetic field is observed. In particular, diffracted intensities corresponding to antiferromagnetic (AFM) reflections (**Figure 107** upper panel) decrease on cooling below 17 K, while the bulk magnetisation increases in a series of equally spaced steps versus the magnetic field, instead of smoothly approaching its saturation value. Depending on external conditions, the relaxation of the magnetisation towards its equilibrium state can also be dramatically modified.

It is clear that a simple AFM model is not able to account for the complexity of the magnetic ground state of $Ca_3Co_2O_6$. For this reason, we decided to investigate the magnetic properties of $Ca_3Co_2O_6$ using resonant magnetic X-ray scattering (RMXS) [1].
By studying AFM reflections in zero magnetic field and at low temperature, we found evidence that the system adopts an incommensurate magnetic state immediately below $T_N$. The characteristic temperature evolution of a typical Bragg forbidden AFM reflection in resonant conditions is shown in **Figure 107**. Our results rule out a number of previously proposed magnetic structures, and pose serious new constraints on the description of the system.

To complete the overview of the properties of the magnetic state and to access as much information as possible in reciprocal space, we performed a complementary neutron powder diffraction (NPD) experiment [2]. Using symmetry analysis and by considering the possible exchange pathways within the material (**Figure 106b**: exchange paths connecting magnetic trigonal sites are represented) we showed that $Ca_3Co_2O_6$ adopts a longitudinal incommensurate magnetic structure in the form of a sinusoidal wave propagating along the c-axis chains

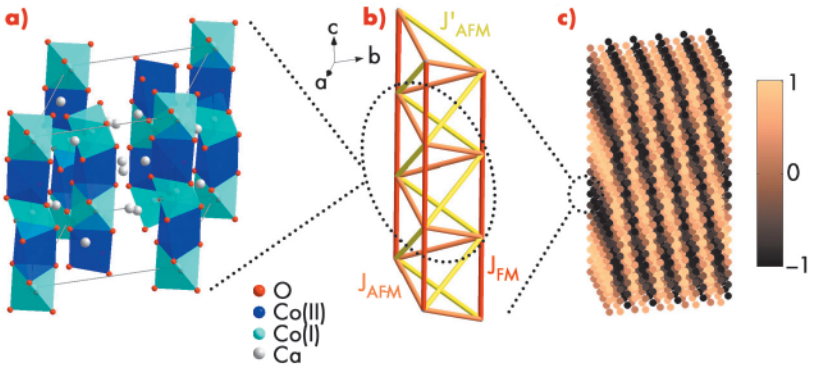


*Fig. 106:* **a)** $Ca_3Co_2O_6$ hexagonal cell, octahedral Co(I) and trigonal Co(II) sites are shown in light and dark blue, respectively; **b)** proposed magnetic exchange pattern between the Co(II) sites; **c)** sketch showing one possible arrangement of the normalised Co(II) magnetic moments in the incommensurate magnetic ground state ($\mu$ \\ c-axis, shown vertical). Some modifications to the cell and the propagation vector length have been applied for the sake of clarity.

(at T = 18 K the propagation vector is k~(0, 0, 0.01)). The modulation is phase shifted by 1/3 on moving from one chain to the next, resulting in the magnetic moment arrangement as shown in **Figure 106c**.

As a result of our investigations, exploiting RMXS and NPD techniques, we have demonstrated that the three dimensional nature of the magnetic exchange coupling in $Ca_3Co_2O_6$ must be taken into account in order to properly describe the magnetic ground state realised in this low dimensional system. **Figure 106b** shows a proposed exchange pattern ($J_{FM} >> J_{AFM}$, $J'_{AFM}$) compatible with the magnetic ground state. Our results challenge the existing theories describing the magnetic properties of $Ca_3Co_2O_6$ and provide a basis for future investigations of the unusual and as yet unexplained static (magnetisation steps) and dynamic (relaxation of the magnetisation) properties of this system.

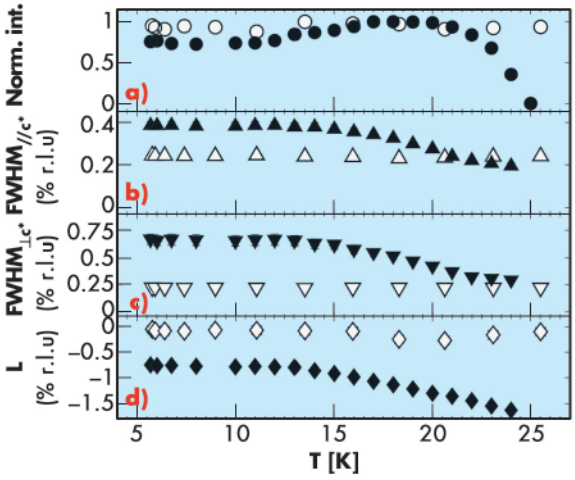


*Fig. 107:* Temperature evolution of a Bragg forbidden AFM reflection (320) and a charge reflection (330), in black and grey symbols, respectively.

**References**
[1] S. Agrestini *et al., Phys. Rev. B* **77**, 140403R (2008); A. Bombardi *et al., Phys. Rev. B* **78**, 100406R (2008).
[2] S. Agrestini *et al.,. Phys. Rev. Lett.* **101**, 097207 (2008).

# High domain wall velocity induced by low current densities in spin valve nanostripes

**Principal publication and authors**
S. Pizzini (a), J. Vogel (a), V. Uhlir (a), E. Bonet (a), N. Rougemaille (a), S. Laribi (b), F. Petroff (b), V. Cros (b), E. Jiménez (c), J. Camarero (c), C. Ulysse (d), G. Faini (d), C. Tieg (e), *Applied Physics Express*, accepted.
*(a) Institut Néel, CNRS and UJF, Grenoble (France)*
*(b) Unité Mixte de Physique CNRS/Thales and Université Paris Sud 11, Palaiseau (France)*
*(c) Dpto. Fisica de la Materia Condensada, Universidad Autonoma de Madrid and IMDEA-NANO, Madrid (Spain)*
*(d) CNRS, PhyNano Team, Laboratoire de Photonique et de Nanostructures, Marcoussis (France)*
*(e) ESRF*

Moving magnetic domain walls in nanostripes using electric currents via spin-torque effects rather than magnetic field pulses is one of the recent exciting developments in spintronics **[1]**. Achieving reproducible domain wall movements with low current densities and high domain wall velocities is the main challenge in this field of science. The critical current densities necessary to move a domain wall in single layer FeNi nanostripes are of the order of $10^{12}$ A/m$^2$ with zero magnetic field, while velocities spread from some m/s up to about 100 m/s. These current densities are too high for applications. Lower current density values have been found for spin-valve-based nanostripes. Our work shows the first direct evidence that in such materials very high domain wall velocities (exceeding 170 m/s) at zero field can be obtained for current densities much lower than for FeNi. We have used photoemission electron microscopy (PEEM) combined with X-ray magnetic circular dichroism (XMCD) to measure domain wall movements in the permalloy layer of 400 nm wide FeNi(5nm)/Cu(8nm)/Co(7nm)/CoO(3nm) nanostripes (**Figure 108a**). The measurements were performed at beamline **ID08**. The X-ray energy was tuned to the Ni $L_3$ absorption edge to probe the FeNi magnetic structure.

The remanent magnetic state obtained for a 90° angle zigzag nanostripe after application of an in-plane external field perpendicular to the zigzag long axis, is shown in **Figure 108b**. Magnetic domains with magnetisation pointing downwards/upwards along the nanostripe (white/black contrast) are separated by domain walls. A black-white-black-white contrast is visible at the bends. This contrast is due to the fact that the stray field generated by head-to-head or tail-to-tail domain walls in the bends of the Co layer induces a local antiparallel alignment

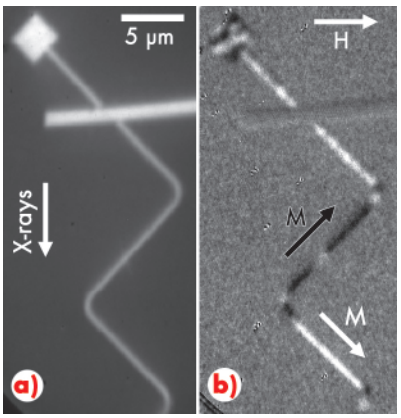


*Fig. 108:* Topographic **a)** and magnetic **b)** PEEM images of a spin-valve-like nanostripe with a zigzag angle of 90°, taken at the Ni $L_3$-edge. The sample is magnetised with a static in-plane magnetic field, as indicated by the white arrow. In (b), white (black) contrast corresponds to FeNi domains with a magnetisation component parallel (antiparallel) to the incoming X-ray direction.

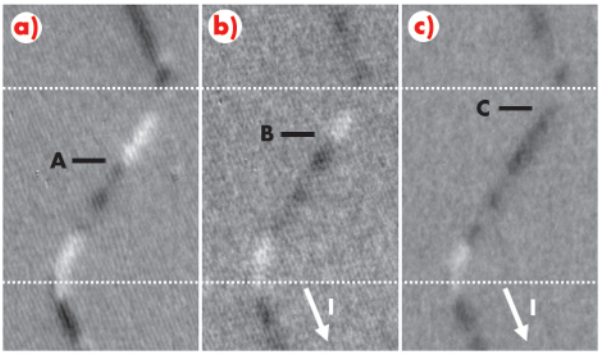


*Fig. 109:* XMCD-PEEM images of the FeNi layer in a zigzag nanostripe with angle of 120°; **a)** initial state with domain wall in position A; **b)** after application of one 100 ns current pulse of +2 mA, which shifts the domain wall to B; **c)** after application of a second 100 ns current pulse of +2 mA, which shifts the domain wall to C.

between Co and FeNi layers in the vicinity of the Co domain wall [2]. We found that these magnetostatic interactions prevent domain wall motion across the bends, but do not hinder domain wall motion away from the bends.

**Figure 109** shows current-induced domain wall motion in a stripe with zigzag angles of 120°. The initial magnetic state shown in **Figure 109a** was obtained reproducibly *in situ* by applying an ultrafast magnetic field pulse. **Figure 109b** shows the domain structure obtained after applying one 100 ns long current pulse with amplitude +2 mA. This current pulse causes a displacement of the domain wall initially in position A, towards position B in the images.

Note that the other domain walls present in the nanostripe are not affected by the current. This shows that the pinning strength can be very different at different sample positions.

A second current pulse with the same amplitude and length moves the same domain wall from B to C (**Figure 109c**). The two current pulses induce a domain wall movement of (1.7 ± 0.2) µm and (1.9 ± 0.2) µm respectively, resulting in domain wall velocities of the order of 20 m/s. When the current is increased to 5 mA the measured DW velocities are of the order of 170 m/s. The current density corresponding to this current value is 5 x $10^{11}$ A/$m^2$, if we consider a uniform current distribution through the trilayer stack. These domain wall velocities are well above literature values for single FeNi layers, for current densities that are at least a factor two smaller.

Currently used spin-torque phenomenological models do not allow such large domain wall velocities to be explained, and other spin transfer mechanisms should therefore be considered. In our spin-valve structures part of the incident spin flux in the FeNi layer is transformed, in the region around the domain wall, into spin accumulation in the Cu and Co layers. Spin accumulation in the Cu spacer below the domain wall induces a vertical spin current that flows into the domain wall and exerts an additional torque on the domain wall. Our results suggest that the yield of this additional vertical spin transfer channel is much higher than the yield of the in-plane spin transfer channel, as predicted recently by micromagnetic simulations on similar nanostructures containing a single domain wall.

Our direct observation of very fast current-induced domain wall motion confirms the potential application of spin-valve systems to domain wall-based magnetic memories and logic devices.

**References**
[1] S. Parkin, M. Hayashi, L. Thomas, *Science* **320**, 190 (2008).
[2] J. Vogel, S. Cherifi, S. Pizzini, F. Romanens, J. Camarero, F. Petroff, S. Heun, and A. Locatelli, *J. Phys.: Condens. Matt.* **19**, 476204 (2007).

# Magnon dispersion in antiferromagnetic cuprates measured by X-ray scattering

**Principal publication and authors**

L. Braicovich (a), L.J.P. Ament (b), V. Bisogni (c), F. Forte (b,d), C. Aruta (e), G. Balestrino (f), N.B. Brookes (c), G.M. De Luca (e), P.G. Medaglia (f), F. Miletto Granozio (e), M. Radovic (e), M. Salluzzo (e), J. van den Brink (b,g), and G. Ghiringhelli (a), *arXiv:0807:1140v1*, (2008).

*(a) CNR/INFM and Politecnico di Milano (Italy)*
*(b) Universiteit Leiden (The Netherlands)*
*(c) ESRF*
*(d) CNR/INFM and Università di Salerno (Italy)*
*(e) CNR/INFM and Università Federico II, Napoli (Italy)*
*(f) CNR/INFM and Università di Roma Tor Vergata (Italy)*
*(g) Radboud Universiteit Nijmegen (The Netherlands)*

In the early days of high temperature superconductivity it was already recognised that magnetic properties of these materials are intimately related to the superconducting ones. When doped, the long-range ordered antiferromagnetic background of pristine copper oxide insulators gets frustrated leading to short range antiferromagnetic fluctuations and superconductivity. That is why the magnetic properties of parent compounds have attracted so much attention since the discovery of superconductivity in cuprates. The spin dynamics of cuprates has been studied up to now mostly with neutron inelastic scattering.

Recently Hill *et al.* [1] have found that Cu K edge resonant inelastic X-ray scattering (RIXS) spectra of undoped antiferromagnetic cuprates at 20 K show a sizable peak around 500 meV when the transferred momentum $q$ corresponds to the $(\pi,0)$ point of the reciprocal space. This feature, suppressed by doping, has been assigned to the simultaneous excitation of two magnons. Magnons are collective excitations of a lattice presenting a long range magnetic order and they correspond to changing by one unit the magnetic moment of the system. Their non-local nature manifests itself in a dispersive behaviour, *i.e.* a non-constant relation between momentum and energy. Following that first indication, we have employed the same technique in the soft X-ray range, working at the $L_3$ edge ($2p \rightarrow 3d$ transition) of Cu. We have seen that Cu $L_3$ RIXS is an ideal technique to determine magnon dispersion in cuprates. In $La_2CuO_4$ and $CaCuO_2$ we have found dispersing spectral features both at room temperature and at 30 K.

**Figure 110** shows how Cu $L_3$ RIXS works in undoped cuprates, where all Cu sites are divalent ($3d^9$ configuration) and how two magnons can be thereby excited simultaneously. In undoped cuprates, a two-dimensional antiferromagnetic order of the spin 1/2 $Cu^{2+}$ sites always characterises the ground state. In the intermediate state, the $3d^{10}$ configuration (spin zero) makes the scattering site act as a magnetic impurity that quenches the super-exchange locally in the antiferromagnetic lattice. The screening by neighbouring sites can result in the generation of a couple of magnons. Similarly to optical Raman scattering, the total spin moment of the system is conserved, but finite energy and momentum have been transferred from the scattered photon to the system [2]. As opposed to K edge RIXS, a single magnon can also be excited in $L_3$ RIXS due to the strong spin-orbit interaction in the 2p core hole present in the intermediate state.

The measurements made at beamline **ID08** with the AXES spectrometer have a combined energy resolution of 400 meV, sufficient to resolve the magnetic excitation in the 100-400 meV energy range. We are working at present on the problem of separating single from mutliple magnons. The results, summarised in **Figure 111**, show a clear dispersive behaviour already in the raw data (left panel). The spectra are labelled as function of $q_n = q_{\|} \times a$; $q_{\|}$ is the transferred momentum component in the *ab* plane and *a* is the in plane lattice parameter, so $q_n$ is adimensional and equals $\pi$ at the zone boundary. In the right hand panel, the experimental data-points are compared to the single magnon results obtained on the same compound by inelastic neutron scattering and to the theoretical prediction for bi-magnons according to ref. [2].

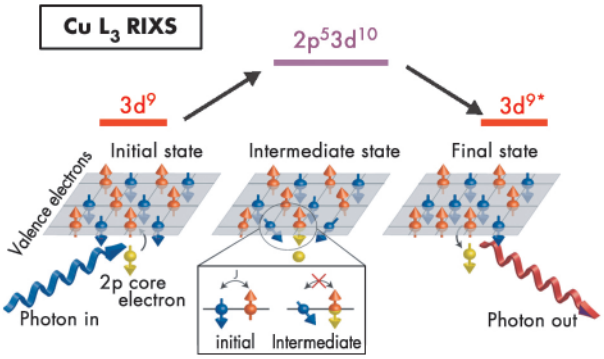


*Fig. 110:* Schematics of RIXS at the Cu $L_3$ edge and RIXS excitation of bi-magnons.

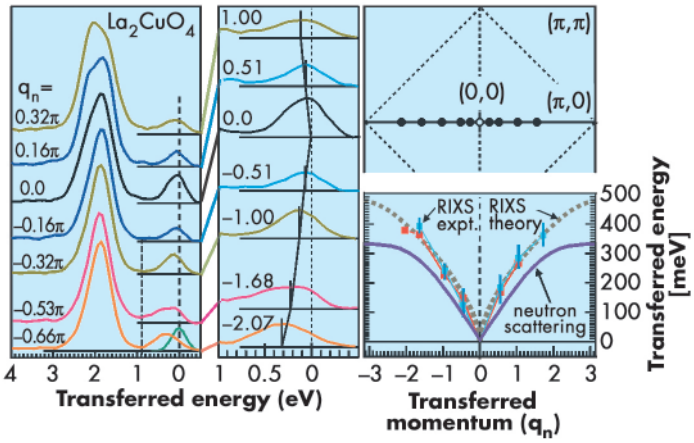


*Fig. 111:* Cu $L_3$ RIXS results of $La_2CuO_4$. The peak dispersion curve was extracted from the raw data (left panel) corresponding to the given dots in the Brillouin zone.

**References**

[1] J.P. Hill, G. Blumberg, Y.-J. Kim, D.S. Ellis, S. Wakimoto, R.J. Birgeneau, S. Komiya, Y. Ando, B. Liang, R.L. Greene, D. Casa, and T. Gog, *Phys. Rev. Lett.* **100**, 097001 (2008).

[2] F. Forte, L.J.P. Ament and J. van den Brink, *Phys. Rev. B* **77**, 134428 (2008).

These results provide the first direct measurement of the magnon dispersion made with inelastic X-ray scattering. As the peak position exceeds the energy of a single magnon excitation measured with neutrons, an important contribution has to come from two magnon excitations. A theoretical calculation for bi-magnons, after broadening for inclusion into the experimental resolution, agrees very well with the experimental data points. Nevertheless a contribution from single magnons cannot be excluded. In the doped $La_{1.85}Sr_{0.15}CuO_4$ sample we have measured a different dispersion curve, presenting a finite energy at $q_n = 0$. In the doped compounds the measured excitations might have mixed spin-charge character.

**Principal publications and authors**

M.P. Ruffoni (a), S. Pascarelli (a), R. Grössinger (b), R. Sato-Turtelli (b), C. Bormio-Nunes (c), R.F. Pettifer (d), *Phys. Rev. Lett.* **101**, 147202 (2008);
S. Pascarelli (a), M.P. Ruffoni (a), R. Sato-Turtelli (b), F. Kubel (b), R. Grössinger (b), *Phys. Rev. B* **77**, 184406 (2008).

*(a) ESRF*
*(b) Vienna University of Technology (Austria)*
*(c) Universidade de Sao Paulo, Lorena-SP (Brasil)*
*(d) University of Warwick, Coventry (UK)*

# Atomic-scale magnetostriction

Magnetostriction refers to the change in physical dimensions of a magnetic material, observed when there is a change in its magnetisation. It was first described by James Joule in 1842 and originates from spin-orbit coupling, where magnetic energy is converted to mechanical energy and vice versa. However, despite the obvious applications of such an effect in transducer devices, the strain produced in common magnetic materials is only a few tens of parts-per-million (ppm) at most. It was, therefore, not until the discovery of room-temperature 'giant' magnetostriction in rare-earth transition metal alloys in the 1970s that interest developed in magnetostrictive transducer technologies (**Figure 112**).

More recently, a different class of material based on binary metal alloys such as Fe-Al or Fe-Ga, have attracted considerable interest. It is well known that pure Fe exhibits only an extremely small magnetostriction (just 20 ppm), but experiments have revealed that when it is alloyed with certain nonmagnetic metallic elements, the magnetostriction can be enhanced by over an order of magnitude. Compositions of Fe-Ga with around 19at% Ga have reported strains of up to 400 ppm. Although this doesn't constitute a truly 'giant' magnetostriction, it is of interest for device applications since Fe-Ga is devoid of expensive rare-earth components, and possesses more desirable mechanical properties than, say, the much studied Terfenol-D alloy.

From a theoretical perspective, initial proposals for the source of this enhancement suggested it arose from clustering of the Ga atoms within a disordered Fe lattice, to provide both elastic and magnetoelastic defects. More recently, magnetostriction coefficients have been derived from first-principles calculations, and the magnetocrystalline anisotropy modelled, which together, suggested that such defects could be better formed by pairs of Ga atoms, arranged randomly throughout the material. To verify these proposals, it is clear that atomic-scale structure and strain measurements are needed. Yet this is where problems arise.

Experimentally, magnetostrictive strain is elusive at the atomic scale. Strains of the order of tens of ppm only generate displacements between atoms of the order of femtometres, which are extremely difficult to detect. Even commonly employed atomic probes, such as X-ray Absorption Spectroscopy (XAS), lack the sensitivity

to observe such motion by up to two orders of magnitude. As a result, experiments largely deal with magnetostriction in a scaled-up form. Typical measurements employ strain gauges on large, macroscopic samples, where the strain is easier to detect, but where atomic information is lost.

However, with the recent development of differential XAS (DiffXAS) on beamline **ID24** – a new technique designed specifically for the measurement of strains down to the scale of femtometres – such direct, atomic-scale measurements have become possible. When these are coupled to conventional XAS data (from beamline **BM29**), the static structure may also be obtained in the absence of an applied magnetic field, providing a complete picture of the sample behaviour.

Recently, we have carried out DiffXAS and XAS experiments on samples of $Fe_{81}Ga_{19}$, where the magnetostriction enhancement with respect to pure Fe is maximised. From the conventional XAS measurements, we were able to examine the static atomic structure immediately surrounding the Ga atoms, and found that there were no Ga clusters – in the first atomic coordination shell around Ga, there were no Ga-Ga bonds. Furthermore, in the second coordination shell, we found, on average, exactly one Ga-Ga bond – testifying to the presence of the Ga-Ga pair defects predicted by theory.

*Fig. 112:* In a typical magnetostrictive actuator, a magnetostrictive material (central rod) is wrapped in a metal coil, which is in turn housed in an outer casing. By passing a current through the coil, a magnetic field is formed within in, causing the rod to extend. Alternatively, the device may operate in reverse as a sensor, where external pressures change the length of the rod, which in turn generates a magnetic field that induces a measurable current in the coil. Such sensors are frequently employed for non-destructive testing applications, such as examination of suspender cables on bridges.

With an applied magnetic field, the DiffXAS measurements showed the way this structure deformed. By examining the surroundings of the Fe and Ga atoms individually, we established that the strain emanated from the environment around the Ga atoms. Here, the magnitude of the strain was about 400 ppm, compared to only 40 ppm around Fe. More importantly, negligible strain was found in the Ga-Ga pair defect itself. We could therefore conclude that the pair defect simply mediates the magnetostriction in the material rather than providing it directly. Instead, and in agreement with theory, the enhanced magnetostrictive strain in $Fe_{81}Ga_{19}$ arises from the Ga-Fe bonds in the immediate vicinity of the Ga-Ga pair defects.

## Controlled aggregation of magnetic cations in a semiconductor nitride matrix

The origin of the ferromagnetic behaviour persisting above room temperature (RT) and discovered in semiconductors doped with transition metals and rare earths may certainly be considered as one of the most controversial issues in today's materials science. Many misleading assumptions and conclusions on the actual magnetic interactions in magnetically doped semiconductors and oxides have been, until recently, caused by lack of a proper correlation between fabrication parameters and structural characterisation at the nanoscale.

Now, there is an increasing amount of evidence that, owing to specific features of magnetic impurities in semiconductors and oxides, the epitaxial growth of these systems can result in the self-organised aggregation of magnetically robust nanocrystals embedded in the host paramagnetic matrix. This finding holds enormous potential for the fabrication of a range of multifunctional nanosystems relevant to spintronics, nanoelectronics, photonics, and plasmonics. However, it has also been realised that difficulties in the experimental resolution and

**Principal publication and authors**

A. Bonanni (a), A. Navarro-Quezada (a), T. Li (a), M. Wegscheider (a), Z. Matěy (b), V. Holý (b), R.T. Lechner (a), G. Bauer (a), M. Rovezzi (c), F. D'Acapito (c), M. Kiecana (d), M. Sawicki (d), and T. Dietl (d), *Phys. Rev. Lett.* **101**, 135502 (2008).

*(a) University of Linz (Austria)*
*(b) Charles University Prague (Czech Republic)*
*(c) CNR-INFM-OGG c/o ESRF GILDA CRG Grenoble (France)*
*(d) Polish Academy of Sciences Warsaw (Poland)*

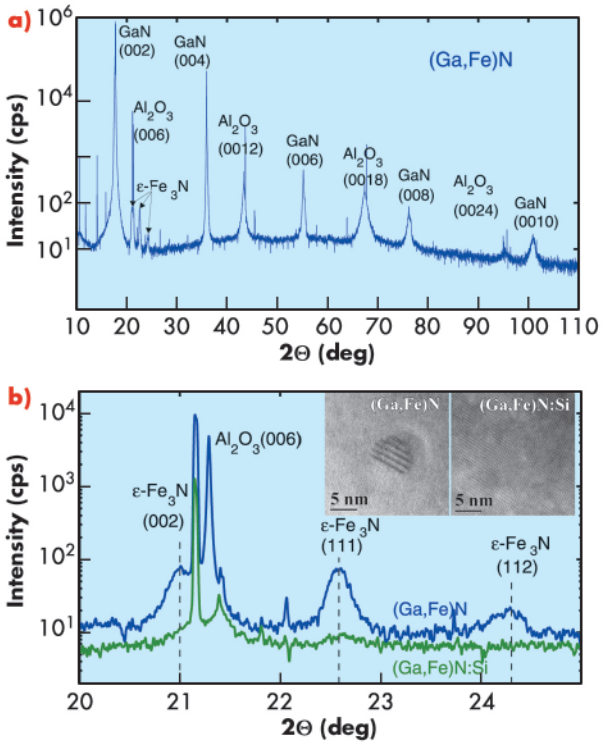


*Fig. 113:* Synchrotron radiation powder XRD spectra: effect of Si doping on the aggregation of Fe ions into the GaN matrix. **a)** full scan; **b)** reduced scan focussing on the region with the diffraction peaks from Fe-rich embedded nanocrystals. Inset: HRTEM images confirming the Fe aggregation hampered by Si doping.

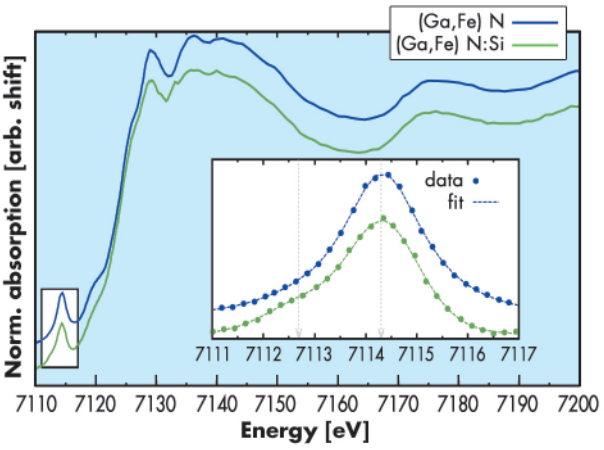


*Fig. 114:* XANES spectra with the region of interest expanded in the inset: in addition to the peak at 7114.3 ± 0.1 eV assigned to the $Fe^{3+}$ charge state, a shoulder at 7112.7 ± 0.1 eV is visible in the Si-doped samples pointing to the reduction of a part of the Fe ions to the $Fe^{2+}$ charge state by doping with donors.

identification of the embedded nanostructures endure and hamper the progress in the control of the mechanisms accounting for associated and hitherto unexplored nanoassembly processes. Synchrotron radiation microprobe [1] and other nanoanalytical synchrotron tools, in combination with high-resolution transmission electron microscopy (HRTEM) [2], represent a suitable blend of techniques that, when complemented by magnetic measurements, can lead to a thorough characterisation of magnetically doped semiconductors.

The model system (Ga,Fe)N has been found from SQUID magnetometry data to be ferromagnetic at RT for a concentration of magnetic ions above 0.4% under the employed growth conditions. While laboratory high-resolution X-ray diffraction (XRD) does not evidence any phase separation in these samples, powder diffraction XRD measurements carried out at the beamline **ID31** by using a photon energy of 15.5 keV reveal the presence of new diffraction peaks identified as the (002) and (111) of the phase ε-$Fe_3N$ with a Curie temperature $T_C$ ~ 575 K. Moreover, it has been possible to confirm a recent theory [3], according to which it is possible to modify the chemical valence of transition metal cations by doping with shallow acceptors (Mg in the case of GaN) or donors (Si for GaN), and, consequently, affect their aggregation in the semiconducting matrix. **Figure 113** indicates that doping with Si does indeed hinder the formation of Fe-rich regions: panel (a) reproduces the full ω/2θ scan and panel (b) a reduced scan with focus on the range with the diffraction peaks originating from the embedded nanocrystals. This is confirmed by the HRTEM images in the inset of **Figure 113**.

The results on the effect of Si on the aggregation of the Fe ions in the GaN matrix are also corroborated by X-ray absorption near-edge structure (XANES) measurements at the Fe K-edge carried out at the GILDA beamline (**BM08**). As evidenced in **Figure 114**, XANES data point to the expected presence of Fe in the $Fe^{3+}$ charge state in the nominally undoped (Ga,Fe)N samples, whereas they confirm the coexistence of $Fe^{3+}$ and $Fe^{2+}$ ions in the case of doping with Si, supporting the onset of a shift of the Fermi level and consequent modification of Fe charge state in the system. An analogous effect has been verified in the case of doping with Mg.

By combining HRTEM with synchrotron XRD and XANES it has been possible to identify the distinct ways by which Fe incorporates into the GaN lattice giving an important contribution to the elucidation of the origin of the ferromagnetic features in magnetically doped semiconductors. Importantly, the doping with either acceptors or donors hampers the nanocrystal assembling and offers a way to functionally control the aggregation of magnetic elements in a non-magnetic host.

**References**
[1] G. Martinez-Criado, A. Somogyi, S. Ramos, J. Campo, R. Tucoulou, M. Salome, J. Susini, M. Hermann, M. Eickhoff, and M. Stutzmann, *Appl. Phys. Lett.* **86**, 131927 (2005).
[2] M. Jamet, A. Barski, T. Devillers, V. Poydenot, R. Dujardin, P. Bayle-Guillmaud, J. Rotheman, E. Bellet-Amalric, A. Marty, J. Cibert, R. Mattana, and S. Tatarenko, *Nature Mater.* **5**, 653 (2006).
[3] T. Dietl, *Nature Mater.* **5**, 673 (2006).

# Alkali metal-intercalated fullerenes under high pressure

**Principal publications and authors**
R. Poloni (a), G. Aquilanti (b), S. Le Floch (c), M. V. Fernandez-Serra (d), S. De Panfilis (e), P. Toulemonde (f), D. Machon (c), G. Morard (b), D. Martinez-Blanco (g), W. Crichton (b), S. Pascarelli (b), A. San-Miguel (c), *Phys. Rev. B* **77**, 035429 (2008); *Phys. Rev. B* **77**, 205433 (2008).
*(a) ICMAB-CSIC, Barcelona (Spain)*
*(b) ESRF*
*(c) LPMCN, University of Lyon (France)*
*(d) Stony Brook, New York (US)*
*(e) INFM-CNR, Roma (Italy)*
*(f) Institut Néel, CNRS and UJF, Grenoble (France)*
*(g) Universidad de Oviedo (Spain)*

Alkali metal-intercalated fullerenes are attractive as precursors for new materials (high-dimensional polymers) exhibiting both superconducting and high hardness properties [1], that can be formed via high-pressure synthesis. Nevertheless, the strong ionic interactions between the alkali atoms and the $C_{60}$ molecule were predicted to give rise to a deformation of the $C_{60}$ the isolated icosahedral molecule [2]. This deformation could limit the pressure stability of the molecule. However, no experimental evidence of such deformation has been provided before our experiments. Therefore, exploration of the P-T phase diagram of alkali metal-intercalated fullerenes is of particular interest because of these predictions.

We studied the body-centered cubic (bcc) $Rb_6C_{60}$ (a = 11.54 Å) and $Cs_6C_{60}$ (a = 11.79 Å) systems by employing different complementary techniques: X-ray diffraction (XRD), X-ray absorption fine structure (XAFS) and Raman spectroscopies. XRD (beamline ID27) and XAFS measurements (beamline BM29) were carried out up to 15 GPa at room temperature on both systems. By comparing the compressibility of the total volume obtained by XRD data with the compressibility of the interstitial volume between the $C_{60}$ and the alkali atoms obtained by XAFS, we observed that its compression is accompanied by a shape-changing deformation under pressure, this is reported in Figure 115.

The distortion of the molecule is probably due to an enhancement of the Coulomb interaction with the surrounding ions, effectively increasing the difference between the distances from each molecule's centre to those 36 carbons closest to the alkali metals (grey atoms in Figure 115), on one hand, and to those 24 carbon atoms located closest to other $C_{60}$ molecules (white atoms in Figure 115), on the other hand. This deformation is analogous to pulling the molecule through the three orthogonal axes pointing towards the bcc faces containing the alkali metals.

The deformation of the fullerene molecule is greater (54% at 15 GPa) for Rb than for Cs intercalation, this too confirmed by our *ab initio* calculations for both systems.

In spite of such slight deformation due to the pressure enhanced Coulomb interaction, Raman measurements performed under pressure on $Cs_6C_{60}$ indicated that the $C_{60}$ cage is preserved up to a pressure two times higher (45 GPa) than for pristine $C_{60}$, which was observed to amorphise at 22 GPa.

Conversely, XRD, XAS (beamline ID24) and Raman spectroscopy measurements for $Rb_6C_{60}$ under HP-HT conditions showed the existence of a first-order phase transition at around 35 GPa from the bcc towards a hexagonal phase accompanied by a discontinuous decrease of the unit cell volume. Both XRD and Raman data collected under pressure are shown in Figure 116. The lattice parameters of the hexagonal unit cell (a = 8.360 Å and c = 14.830 Å) are compatible with a distance between molecules previously observed in the case of polymerised $C_{60}$. In addition, in correspondence with the transition, the Raman data show a discontinuous change in the frequency of the intramolecular vibrations. This is probably associated with the breaking of some intramolecular bonds concomitant with the formation of intermolecular covalent bonds, as

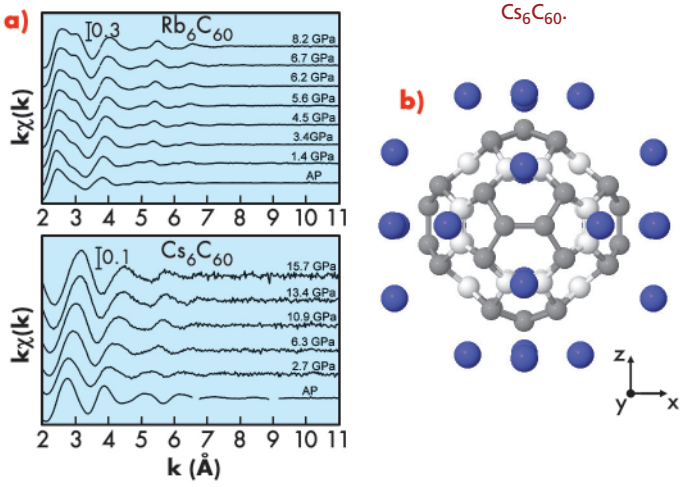


*Fig. 115:* **a)** Pressure evolution of the XAFS signal; **b)** Pressure-induced distortion (amplified by a factor of 30) of the $C_{60}$ molecule at 15 GPa observed in $Rb_6C_{60}$ and $Cs_6C_{60}$.

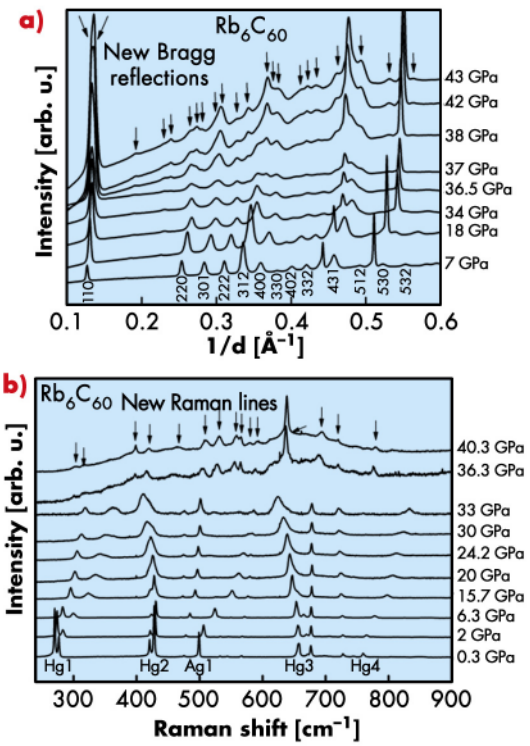


*Fig. 116:* **a)** Pressure evolution of XRD, and **b)** Raman measurements for $Rb_6C_{60}$. The occurrence of a phase transition at around 35 GPa is indicated by the appearance of new Bragg reflections and Raman lines, respectively.

occurs in cycloaddition processes characteristic of the $C_{60}$ polymerisation. Hence, we suggest that the hexagonal HP phase could be associated to the formation of 2D polymers in the (001) plane of the hexagonal structure.

The lower pressure stability of the cubic phase (and of the molecular character) observed in $Rb_6C_{60}$ compared to $Cs_6C_{60}$ is concomitant with a more pronounced distortion of the molecule in the first compound compared to the latter. Nevertheless, both fullerides show a much higher pressure stability of the molecular character of the system, compared to the solid $C_{60}$. We therefore infer that the presence of such ionic host-guest interactions could be responsible for the high pressure stabilisation of the $C_{60}$ molecules.

**References**
[1] Connétable *et al., Phys. Rev. Lett.* **91**, 247001 (2003).
[2] Andreoni *et al., Phys. Rev. Lett.* **68**, 823 (1992).

# Isotopic effect in extended X-ray absorption fine structure of germanium

**Principal publication and authors**
J. Purans (a,b), N.D. Afify (a), G. Dalba (a), R. Grisenti (a), S. De Panfilis (c,d), A. Kuzmin (b), V.I. Ozhogin (e), F. Rocca (f), A. Sanson (f), S.I. Tiutiunnikov (g) and P. Fornasini (a), *Physical Review Letters* **100**, 055901:1-4 (2008).
*(a) Department of Physics, University of Trento (Italy)*
*(b) Institute of Solid State Physics, Riga (Latvia)*
*(c) Res. Centre Soft INFM-CNR, Roma (Italy)*
*(d) ESRF*
*(e) Res. Centre "Kurchatov Institute", Moscow (Russia)*
*(f) CNR-IFN and FBK-CeFSA, Trento (Italy)*
*(g) JINR, Dubna (Russia)*

The structural, electronic and dynamical properties of crystals are mainly dependent on the atomic number of the constituent atoms. However, the isotopic composition has subtle but non-negligible influence on some basic properties, like density, phonon widths, and electronic energy gaps [1]. Isotopic effects are relevant not only for their basic scientific interest, but also for several possible technological applications [2].

The dependence of the dynamical properties of crystals on the isotopic composition is of primary importance. The force constants depend on atomic species and crystal structure. However, the zero-point amplitude of atomic vibrations is also influenced by the nuclear masses, the lighter isotopes undergoing larger oscillations than the heavier ones. As a consequence of anharmonicity, the difference in zero-point amplitude of motion reflects on a difference of interatomic equilibrium distances and lattice parameters [1]. In the case of germanium, the expected relative change in the lattice parameter between $^{70}$Ge and $^{76}$Ge is as small as $\Delta a/a \approx 5 \times 10^{-5}$. Note that these effects, of genuine quantum origin, disappear progressively when temperature increases.

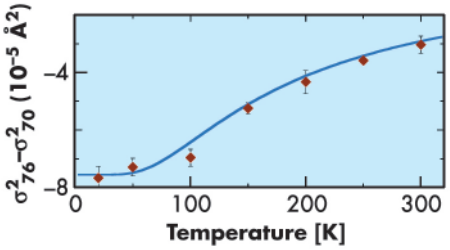


*Fig. 117:* Difference of the EXAFS MSRDs as a function of temperature for the two isotopes $^{70}$Ge and $^{76}$Ge. The solid line shows the difference between two Einstein models.

An investigation of the isotopic effect on the amplitudes of nearest-neighbours relative vibrations (parallel mean square relative displacement (MSRD)) and on the nearest-neighbours average distance in powdered samples of $^{70}$Ge and $^{76}$Ge has been performed by extended X-ray absorption fine structure (EXAFS) spectroscopy.

Two highly isotopically enriched Ge samples with the degrees of enrichment 98.2% for $^{70}$Ge and 99.9% for $^{76}$Ge were produced at the

Kurchatov Institute (Russia), and their Ge K-edge EXAFS spectra recorded with high accuracy from 20 to 300 K, at beamline **BM29**.

The difference of the MSRD values for two isotopes has been clearly evidenced (**Figure 117**) and is in good agreement with a behaviour expected from the Einstein model based on the single force constant $k_0$ = 8.496(40) eV/Å$^2$ and two characteristic frequencies: 7.70(2) THz for $^{70}$Ge and 7.39(2) THz for $^{76}$Ge.

The effect of isotopic mass has also been revealed in thermal expansion (**Figure 118**). The zero-point values of the nearest-neighbours average distance measured by EXAFS are consistent with the values of distance between average positions measured by Bragg diffraction, once the effects of vibrations perpendicular to the bond are taken into account. The possibility of detecting relative distance variations smaller than 10 femtometres by means of a conventional transmission EXAFS apparatus and a standard procedure of data analysis has been demonstrated.

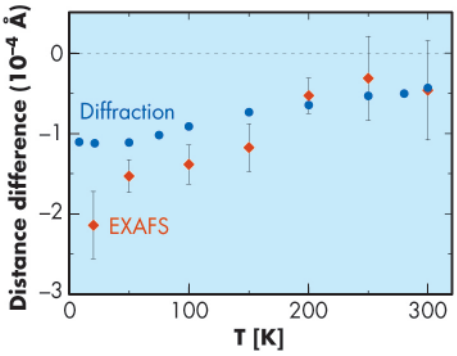


*Fig. 118:* Difference of the nearest-neighbour average interatomic distance in $^{76}$Ge and $^{70}$Ge, determined from EXAFS analysis (diamonds), compared with the difference of distances between average positions determined from X-ray backscattering (circles).

**References**
[1] M. Cardona and M.L.W. Thewalt, *Rev. Mod. Phys.* **77**, 1173 (2005).
[2] V.G. Plekhanov, *Prog. Mater. Sci.* **51**, 287 (2006).

## *In situ* redispersion of platinum nanoparticles on ceria-based oxide for vehicle exhaust catalysts

Supported precious metals are used to facilitate many industrial catalytic processes. Platinum (Pt) in particular is used for the cleaning up of vehicle exhaust emissions. When the vehicle exhaust catalyst is exposed to high temperatures (~800°C and above), the highly dispersed metal nanoparticles agglomerate and sinter, decreasing the active surface area, which causes a loss of catalytic activity (*i.e.* deactivation). Exhaust gases exiting from gasoline engines change quickly during operation. Temperatures can rise transiently to around 1000°C and the exhaust gas composition itself fluctuates quickly between oxidative and reductive compositions. Hence, *in situ* dynamic observation on the sintering and redispersion phenomena of the precious metal in the automotive catalysts is very important indeed.

Real-time observation of the sintering/redispersion behaviour of Pt was made possible by the fluorescence yield variant (Turbo-XAS) of energy dispersive XAFS developed by Pascarelli *et al.* at **ID24** **[1]**.

An *in situ* cell optimised for fluorescence detection was designed for this experiment **[2]**. Fluorescence yield Turbo-XAS data collected at the Pt $L_{III}$ edge on 2 wt% Pt/Ce-Zr-Y mixed oxide (referred to as CZY) catalysts under *in situ* conditions are shown in **Figure 119**. The signal to noise ratio on this data is improved with respect to our previous transmission XAS study on Pt/CZY, which showed that the combination of low levels of Pt in the catalysts, with high levels of heavy, absorbing, elements such as Ce and Zr severely compromises the conventional, transmission based experiments, making quantitative analysis very difficult **[3]**.

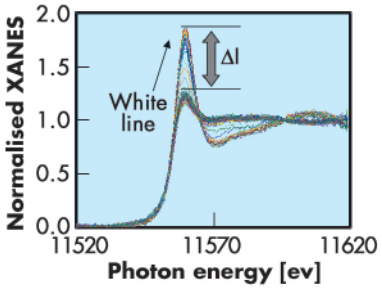


*Fig. 119:* Serial time-resolved Pt $L_{III}$ edge XANES spectra (6 seconds each) of 2 wt% Pt/CZY catalyst under cyclical oxidising/reducing. Variation in the first hundred spectra under oxidising/reducing atmosphere at around 400°C.

**Principal publication and authors**
Y. Nagai (a), N. Hara (b), K. Dohmae (a), Y. Ikeda (b, g), N. Takagi (c, g), T. Tanabe (a), G. Guilera (d, h), S. Pascarelli (d), M.A. Newton (d), O. Kuno (e, i), H. Jiang (e), H. Shinjoh (a), S. Matsumoto (f), *Angew. Chem Int. Ed.* **47**, 9303 (2008).
*(a) TOYOTA Central R&D Labs., Inc., Aichi (Japan)*
*(b) TOYOTA Motor Europe Technical Centre, Zaventem (Belgium)*
*(c) TOYOTA Motor Corporation Higashi-Fuji Technical Center, Shizuoka (Japan)*
*(d) ESRF*
*(e) TOYOTA Motor Engineering & Manufacturing North America, Inc., Michigan (USA)*
*(f) TOYOTA Motor Corporation, Toyota (Japan)*
*(g) Current Address: (f)*
*(h) Current Address: ALBA-CELLS, Barcelona (Spain)*
*(i) Current Address: (c)*

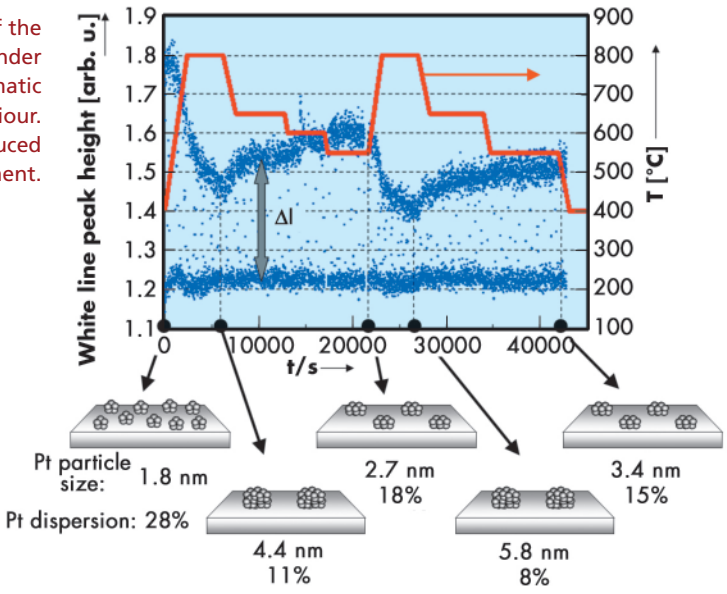


*Fig. 120:* Temporal dependence of the white line peak height of the Pt $L_{III}$ edge XANES for the fresh 2 wt% Pt/CZY catalysts under oxidising/reducing atmosphere at 400 ~ 800°C and the schematic representation of the sintering/redispersion behaviour. 4 or 20% $O_2$/He gas and 3% $H_2$/He gas were alternately introduced into the cell every 60 seconds throughout the measurement.

**Figure 120** shows the variation of the white line peak height of the normalised XANES for the fresh Pt/CZY catalysts under cyclical oxidising/reducing condition at 400 ~ 800°C. $\Delta I$ in **Figure 120** denotes the difference between the white line peak height of the oxidised and reduced samples. From a previous experiment **[3]**, we found that the $\Delta I$ increased with decreasing Pt particle size. Using the correlation between the Pt particle size and $\Delta I$, we observed that the Pt particle size changed with temperature. The Pt particle size of the fresh catalyst increases from 1.8 to 4.4 nm while temperature is increased from 400 to 800°C, but then decreases to 2.7 nm as temperature is lowered to 550°C. It is particularly interesting to note that the sintering/redispersion phenomena occur reversibly and can be controlled using the temperature. During the redispersion process, the Pt particle size was recovered from 4.4 to 2.7 nm at first, and then from 5.8 to 3.4 nm. In contrast, only facile sintering of Pt particles occurs in alumina supported Pt catalysts ($Pt/Al_2O_3$), and Pt redispersion is not achieved at any temperature. Therefore, the Pt redispersion on CZY can be reasonably attributed to the strong Pt-ceria support interaction **[4]**. Through further kinetic measurements, using XAS and *in situ* transmission electron microscopy, an atomic migration mechanism is shown to account for the observed redispersion through the trapping of atomic Pt species at sites on the Ce support that exhibit a strong Pt-oxide-support interaction.

In conclusion, we have made the first *in situ* time-resolved fluorescence XAS measurements from a dilute sample using the Turbo-XAS acquisition mode. This technique allowed us to shed light on catalytic processes on the second timescale for Pt supported on a ceria-based oxide. Analysis of the data led to the discovery of an unexpected phenomenon, *i.e.* an efficient oxidative redispersion of Pt nanoparticles during quick (~ 60 seconds) redox cycling. This redispersion process does lead to a tangible potential for incorporation into "on board" methodology for extending vehicle catalyst lifetime through curtailing or reversing the effects of metal sintering during operation.

**References**

[1] S. Pascarelli, T. Neisius, S. De Panfilis, *J. Synchrotron Rad.* **6**, 1044 (1999).

[2] G. Guilera, B. Gorges, S. Pascarelli, H. Vitoux, C. Prestipino, Y. Nagai, N. Hara, submitted to *J. Synchrotron Rad.*

[3] Y. Nagai, N. Takagi, Y. Ikeda, K. Dohmae, T. Tanabe, G. Guilera, S. Pascarelli, M.A. Newton, H. Shinjoh, S. Matsumoto, *AIP conference proceedings.* **882**, 594 (2007).

[4] Y. Nagai, T. Hirabayashi, K Dohmae, N. Takagi, T. Minami, H. Shinjoh, S. Matsumoto, *J. Catal.* **242**, 103 (2006).

# Structural determination of neptunium redox species in aqueous solutions

**Principal publication and authors**
A. Ikeda-Ohno (a,b), C. Hennig (a), A. Rossberg (a), H. Funke (a), A.C. Scheinost (a), G. Bernhard (a), T. Yaita (b), *Inorg. Chem.* **47**, 8294 (2008).
*(a) Institute for Radiochemistry, Forschungszentrum Dresden-Rossendorf (Germany)*
*(b) Synchrotron Radiation Research Center, Japan Atomic Energy Agency (Japan)*

Neptunium ($_{93}$Np) is one of the most critical elements for the geological disposal of high-level radioactive wastes because of its considerable content in such wastes, and the high radioactivity, half-lives and radiotoxicity of its nuclides. From a chemist's point of view, it is also a very interesting element because of its diversity of oxidation states from III to VII [1]. Whether Np may be retained in the waste repository for millions of years, or whether it will migrate to the biosphere, depends heavily on its chemical forms (speciation). We assume that oxidation state will have a strong influence on the speciation. Therefore detailed knowledge about the interrelation between oxidation state and the structure of chemical species is critical for the development of safe nuclear waste repositories. This motivated us to perform X-ray absorption fine structure (XAFS) studies to determine the complex structure of Np species in aqueous solutions at different oxidation states. The experiments were performed at the Rossendorf Beamline (BM20), the only beamline at the ESRF where such studies with aqueous Np samples can be performed.

The solution samples investigated in this study were prepared by dissolving $Np^{VI}O_2(ClO_4)_2{\cdot}nH_2O$ into aqueous solutions, to give a Np concentration of 0.04 M. The oxidation state of Np in the samples was electrochemically adjusted. Np $L_{III}$-edge (17.625 keV) XAFS measurements were carried out in transmission mode using a Si(111) double-crystal monochromator, and two Pt-coated mirrors for rejection of higher harmonics.

**Figure 121** shows the $k^3$-weighted Np $L_{III}$-edge extended X-ray absorption fine structure (EXAFS) spectra for Np(IV), -(V), and -(VI) in 1.0 M $HClO_4$ (left), and their corresponding Fourier transforms (right). Perchlorate is known to be a noncomplexing ligand to actinide ions in aqueous solution, and hardly coordinates to the primary coordination sphere of actinide ions [2].

Accordingly, the chemical species formed in aqueous $HClO_4$ solution are considered to be pure hydrate species. The EXAFS spectrum of Np(IV) is composed of a single oscillation pattern, giving a single peak at 1.9 Å in the Fourier transform. The structural parameters determined by shell fitting are a Np-O distance ($R_{Np\text{-}O}$) of 2.40 Å with a coordination number (CN) of 10.4, corresponding to water molecules of the primary coordination sphere. The EXAFS spectra for the two higher oxidation states, V and VI, exhibit more intricate oscillation patterns and the corresponding Fourier transforms show several significant backscattering peaks. The most prominent peak at around 1.4 Å arises from the single scattering of the double-bond axial oxygen atoms ($O_{ax}$), indicative of the neptunyl unit ($NpO_2^{n+}$). The following two peaks at around 1.9 Å arise from oxygen atoms of the water molecules in the neptunyl equatorial plane ($O_{eq}(H_2O)$, while the small but sufficiently distinguishable peak at 2.9 Å is due to the multiple scattering of $O_{ax}$, respectively. The shell fitting results reveal that the neptunyl(V) ion is coordinated in its equatorial plane by 5.2 water molecules with O atoms at a distance of 2.49 Å, whereas the neptunyl(VI) ion is coordinated by 5.3 water

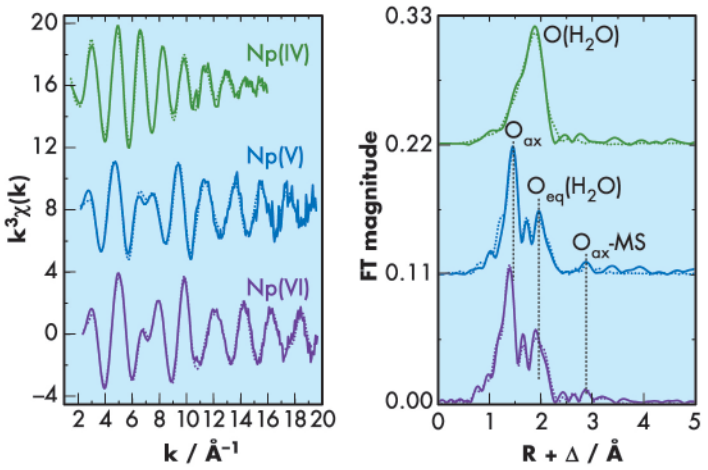


*Fig. 121:* **a)** $k^3$-weighted Np-$L_{III}$ edge EXAFS spectra, and **b)** their corresponding Fourier transforms for Np(IV), -(V), and -(VI) in 1.0 M $HClO_4$. Solid lines represent experimental data and dotted lines represent theoretical fit. The line colours reflect the actual colour of sample solutions.

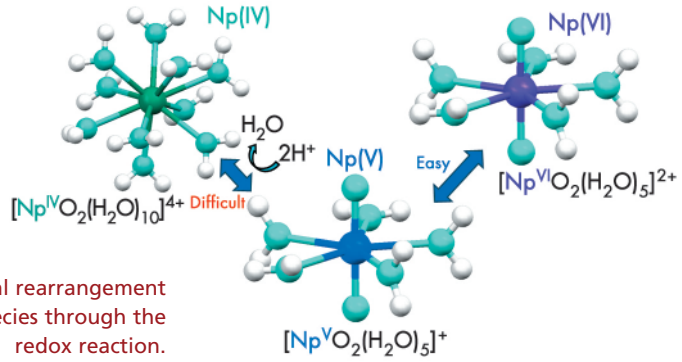


*Fig. 122:* Structural rearrangement of Np hydrate species through the redox reaction.

molecules with a shorter interatomic distance of 2.42 Å.

Our EXAFS data show therefore a structural rearrangement of Np hydrate species with oxidation state as illustrated in **Figure 122**: both Np(V) and (VI) ions exist predominately as pentaaquo neptunyl complexes, $[NpO_2(H_2O)_5]^{n+}$ ($n$ = 1 for Np(V) and 2 for Np(VI)), whereas the Np(IV) ion forms a spherically coordinated decaaquo complex, $[Np(H_2O)_{10}]^{4+}$. It is this drastic change in complex structure between Np(IV) and Np(V), which makes the transition between these two redox states almost irreversible ($\Delta E$ ~0.9 V), while the transition between Np(V) and Np(VI) requires no structural change, hence is quasi-reversible ($\Delta E$ = ~0.2 V). These results support our initial hypothesis that there is a strong relationship between the electrochemical behaviour of Np and its complex structure.

**References**
[1] Z. Yoshida, S.G. Johnson, T. Kimura, J.R. Krsul, *in The Chemistry of the Actinide and Transactinide Elements (3rd Ed.)*, L.R. Morss, N.M. Edelstein, J. Fuger (Eds.), Springer, Dordrecht, The Netherlands, 699 (2006).
[2] L. Sémon, C. Boehme, I. Billard, C. Hennig, K. Lützenkirchen, T. Reich, A. Rossberg, I. Rossini, G. Wipff, *ChemPhysChem* **2**, 591 (2001).

**Acknowledgement**
This work was supported by the Deutsche Forschungsgemeinschaft (DFG) under Contract HE2297/2-1.

## Kinetics and thermodynamics of siderite dissolution at 300 bar between 50°C and 100°C

**Principal publication and authors**
D. Testemale (a), F. Dufaud (b), I. Martinez (b), P. Bénezeth (c), J.-L. Hazemann (a), J. Schott (c), F. Guyot (b,d), *Chemical Geology*, doi:10.1016/j.chemgeo.2008.08.019 (2008).
*(a) Institut Néel and FAME/ESRF, CNRS, Grenoble (France)*
*(b) $CO_2$ storage research center. Institut de Physique du Globe, Paris (France)*
*(c) Laboratoire de Mécanismes des Transferts en Géologie, CNRS-IRD-OMP, Toulouse (France)*
*(d) Institut de Minéralogie et de Physique des Milieux Condensés, CNRS-Paris6-Paris7, Paris (France)*

Iron-bearing minerals are reactive phases of the subsurface environment. Siderite ($FeCO_3$) is one of the most abundant of these and it plays a major role in the deep geological storage of $CO_2$, both by its presence in the reservoir rock where the injection might be done, and by its own constitution, being a form of precipitated $CO_2$ during its injection in deep aquifers. It is thus of utmost importance to precisely model the stability and dissolution kinetics of siderite under hydrothermal subsurface conditions.

The dissolution of siderite $FeCO_3$ in acidic hydrothermal conditions (50-100°C, 300 bar, 0.1 M HCl) has been studied by X-ray Absorption Spectroscopy. The absorption spectra are the data on which our methodology is based. Taken at the Fe K-edge, and measured on the aqueous solution in contact with the dissolving mineral they allow:

- determination of the dissolution rate of siderite, as a function of time, from the absorption value of the solution.
- determination of the speciation of dissolved iron by comparing the absorption spectra with reference spectra of iron complexes in hydrothermal conditions.
- *in situ* measurement in a high pressure-high temperature autoclave which permits working with macroscopic samples (siderite samples are millimetric single crystals) + 50 $mm^3$ of solution, **[1]**). Results are directly related to subsurface $CO_2$ storage conditions.

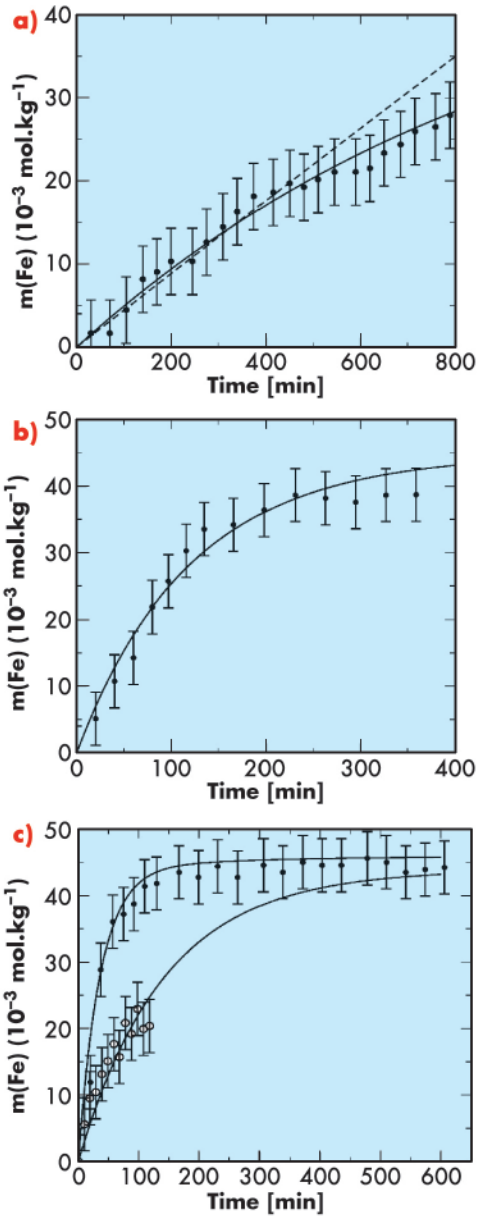


*Fig. 123:* Iron molality as a function of time for siderite dissolution at 300 bar and 0.1 m HCl at **a)** 50°C, **b)** 75°C, **c)** 100°C. The experimental data points are shown as filled circles (empty circles in **c)** are for a 1 mol/Kg NaCl solution). The continuous lines are calculated with the Chess software using the dissolution rate constants measured in this study [2].

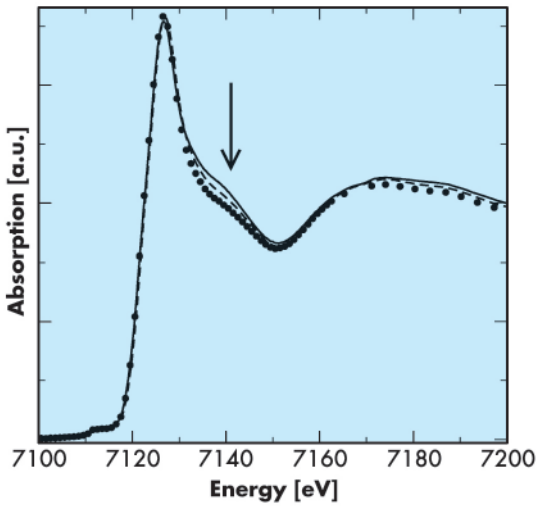


*Fig. 124:* Comparison of XANES spectra obtained for hydrated $Fe^{2+}$ (solid line) and at the end of the siderite dissolution experiment at 100°C (dashed lines: without NaCl; filled circles: with 1 mol $kg^{-1}$ NaCl). The three spectra are very close and mainly differ in the 7130–7150 eV region (indicated by the arrow), with slight differences in the 7170–7200 eV region. All the spectra show the dominance of hydrated $Fe^{2+}$ species. The differences are interpreted by minor occurrence of $FeCl^{+}$ and/or $FeCl_2$ species, more significant, as expected, in 1 mol $kg^{-1}$ NaCl.

**Figure 123** and **Figure 124** summarise the data collected in our experiment. Using the molalities of Fe(II) in the aqueous phase (**Figure 123**), a geochemical model was built using Chess [2] from which kinetics rate constants are derived at each temperature, as well as the activation energy of the system. Thanks to this model, the distribution of iron aqueous species is also calculated, and compared with a very good agreement with the speciation derived from the XANES measurements (**Figure 124**). This XANES signal is characteristic of the hydration structure of dissolved iron, and it is interpreted thanks to a parallel study where the speciation of iron is determined as a function of temperature, pressure and chloride concentration by EXAFS analysis and XANES *ab initio* calculations.

The kinetics rate constants obtained in these closed-reactor pH-varying experiments compare favourably with values from recent experiments carried out at constant chemical affinity [3]: this indicates that we can retrieve kinetics parameters from batch micro-reactor experiments conducted at synchrotron radiation facilities that can be coupled with spectroscopic speciation results. These data are now incorporated in geochemical software modelling fluid-rock interactions under $CO_2$ storage conditions.

**References**

[1] D. Testemale, R. Argoud, O. Geaymond, J.-L. Hazemann, *Rev. Sci. Instrum.*, **76**, 043905 (2005).

[2] J. van der Lee, Technical Report LHM/RD/98/39, CIG, Ecole des Mines de Paris, http://chess.ensmp.fr/

[3] S. V. Golubev, P. Bénézeth, J. Schott, J.-L. Dandurand, A. Castillo, *Chem. Geol., Special issue on $CO_2$ geological sequestration*, in press.

# X-ray Imaging and Optics

## Introduction

The importance of X-ray imaging techniques for innovative research is now widely recognised among the synchrotron radiation user communities. A number of X-ray imaging beamlines are being built in new synchrotron facilities that are emerging all around the world. Two new biomedical beamlines have entered into operation at the end of 2008, in Canada and Australia. The upgrade programmes of major facilities such as the ESRF and APS strongly emphasise X-ray imaging as one of the five "highlight areas" and one of the two "compelling avenues for research" respectively.

This gain in visibility results from the increased number of scientific communities that use X-ray imaging techniques for their research, as reflected by the present chapter. The highlight contributions originate from several scientific areas, which include:

- **Biomedical** applications, with the investigation of novel contrast agents, an improved knowledge of the effect of microbeams, potentially very important for clinical radiotherapy applications, and the characterisation of stem cells using infrared spectromicroscopy.
- **Materials Science** studies, with the observation of intergranular stress corrosion cracking in a grain-mapped polycrystal, and the local structure of GaGdN, investigated with a microprobe beam and several complementary techniques.
- **Cultural Heritage**, where synchrotron techniques revealed the unexpected presence of oil in very ancient paintings of the Bamiyan Buddhist murals, the presence of relics hidden in Middle Age artistic objects, and where phase contrast imaging was used for paleontological purposes, to study fossil evidence hidden in Early Cretaceous opaque amber.
- **Environmental Sciences** with the investigation, using a 80 x 90 nm spot, of cometary grains collected during the NASA Stardust mission, or helping to characterise the impact of carbon nanotubes on human health.

Another point we wish to emphasise is the importance of the effort, made by the ESRF staff and users, to implement new (or new combinations of) imaging techniques, opening new ways for scientific research. This is exemplified, by the first results obtained with an improved diffraction tomography method, as well as the biomedical phase contrast images provided by a grating inteferometry-based technique. The latter can be applied to a wide variety of materials: **Figure 125** shows a slice of kiwi fruit in different contrast modes, obtained from a single phase-stepping interferogram series.

The trends, challenges and new opportunities associated with synchrotron radiation-based imaging are clearly defined for the next few years; if we wish to be able to contribute substantially to emerging topics in areas like nanosciences, health and environment preservation, or cultural heritage, we must improve both the spatial (towards the nanometre scale) and temporal resolutions (for the investigation of evolving systems), and be able to achieve higher chemical sensitivity for micro- or nano-analysis. In addition, we have to pursue the implementation of new imaging techniques and the *in situ* combination of techniques. All this will be performed in a highly competitive international context.

The ESRF upgrade programme, where X-ray imaging plays a substantial role, intends to give an answer to these

trends and challenges, through several projects, which include very long (up to 200 m) beamlines for Nano Imaging and Nano Analysis (NINA), and parallel and coherent beam Micro-Imaging Applications (MIA). In addition, the next two years will be crucial for the implementation of clinical radiotherapy programmes, at the recently refurbished biomedical beamline. All these upgrades, coupled with the scientific know-how already acquired using X-ray imaging at the ESRF, will constitute a great incentive for both the ESRF staff and users to push the present limits of the techniques to reach new, currently unobtainable, scientific heights.

***J. Baruchel***

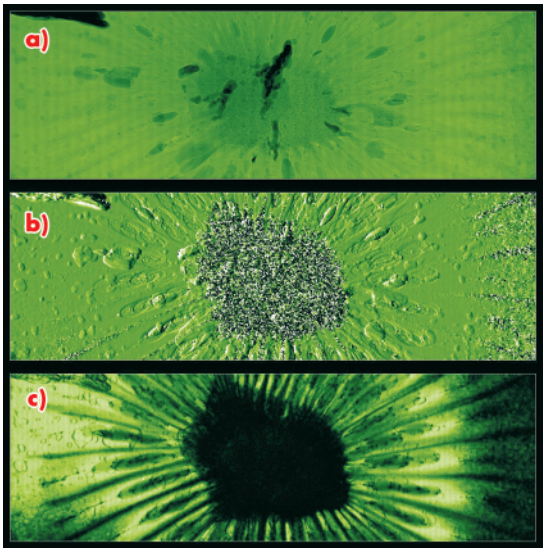


*Fig. 125:* Grating interferometric radiographs of a slice of kiwi fruit (ID19, 27 keV): **a)** absorption image; **b)** differential phase contrast image (the scattering is so strong in the centre that the phase is not well defined); **c)** dark-field (*i.e.*, scattering-contrast) image, showing features that are not visible in the absorption and the phase images. The field of view of each frame is 36.5 mm wide and 11.5 mm high; the detector pixel size was 30 µm (Image courtesy: T. Weitkamp, E. Reznikova, C. David *et al.*).

# New X-ray imaging methods

## 3-D imaging of multi-phase polycrystalline materials by diffraction microtomography

**Principal publication and authors**
P. Bleuet (a), E. Welcomme (b), E. Dooryhée (c), J. Susini (a), J-L. Hodeau (c), P. Walter (b), *Nature Materials* **7**, 468 (2008).
*(a) ESRF*
*(b) Centre de Recherche et de Restauration des Musées de France, CNRS-UMR 171, Palais du Louvre, Paris (France)*
*(c) Institut Néel, CNRS-UPR 2940, Grenoble (France)*

Powder X-ray diffraction is a technique used to solve new crystalline structures, identify phases, analyse phase transformation, and examine micro-structural features. With the recent improvements in X-ray optics and detection, powder microdiffraction experiments can be carried out that provide researchers with images of high lateral resolution in a reasonable scanning time. However, such two-dimensional mappings only provide a global integral of all the diffracted intensity along the X-ray path, thus preventing us from gaining depth resolution information. To study bulk materials, we also require depth resolution information. A local structural probe providing depth resolution images is mandatory in cases where the materials present structural heterogeneities. Three-dimensional diffraction tomography has already been demonstrated for several applications: WAXS was used to study soft tissue achieving millimetre resolution for biological applications, and SAXS was used to study polymers. Furthermore, Laue diffraction and topotomography was used to build 3D mappings of individual grains **[1,2]**.

Here we introduce a new scanning method for synchrotron X-ray diffraction tomography in order to reconstruct cross-section images of unidentified phases in nanomaterials and polycrystalline materials.
The technique is a further extension of the X-ray fluorescence micro-tomography technique that has recently been developed at **ID22**.
It involves simultaneous measurement of the absorption, fluorescence and diffraction data while translating (along **y**) and rotating (around **ω**) a sample illuminated by a focused -or pencil- beam (**Figure 126**). Thanks to the high flux combined with the use of a fast readout and low noise camera (FRELON) equipped with a taper, the scanning time for a 100 µm$^3$ sample is about 6 hours. This process produces a stack of diffraction images, fluorescence spectra and absorption

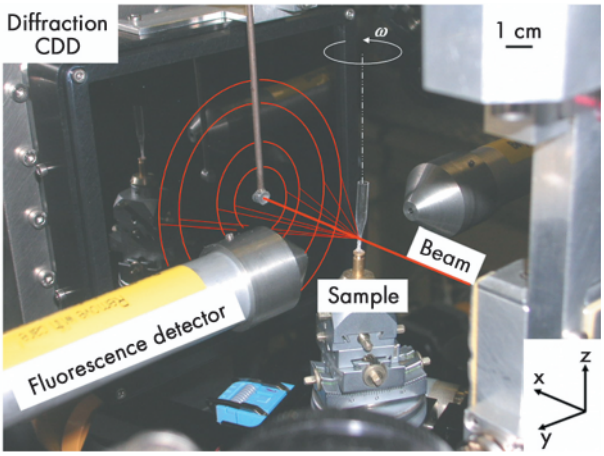


*Fig. 126:* The ID22 sample environment.

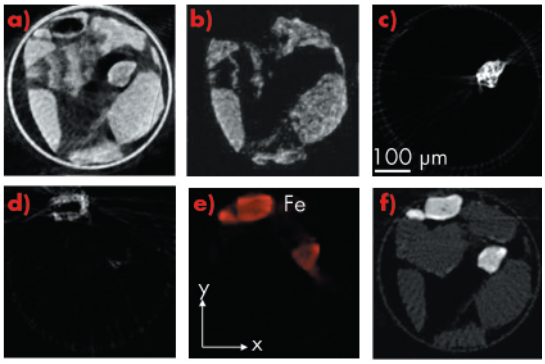


*Fig. 127:* Reconstructed cross-sections corresponding to: **a)** the entire diffracted intensity; **b)** chalcedony; **c)** hematite and siderite; **d)** hematite and greenalite; **e)** fluorescence imaging; **f)** absorption imaging.

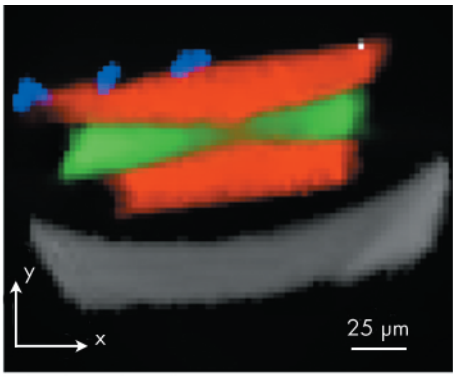


*Fig. 128:* Cross-section reconstruction of the diamond sample. Glass capillary (gray), sp3 amorphous (red), cubic diamond (red), ferrite (blue) and calcite (white).

sinograms. These sinograms are a representation (y,ω) of a particular crystalline phase, elemental distribution, and attenuation coefficient, respectively. Starting from this set of sinograms, a mathematical inversion formula gives rise to cross-section images for each one of the three modalities.

This multi-modal tomographic scheme was first tested on a textbook powder with various grain sizes: a 300 µm capillary was filled with a mixture of chalcedony and iron pigments containing hematite ($\alpha$-$Fe_2O_3$). Chalcedony is composed of long quartz micro-fibres, generally less than 100 nm in diameter. A single cross-section image was measured and reconstructed (**Figure 127**). Even if chalcedony is by far the dominant phase, at least two types of iron grains were observed: hematite and siderite on the one hand, and hematite and phylosilicate phases including greenalite on the other hand. For each grain, a diffraction diagram can be extracted from extremely tiny volumes of powder (as small as the voxel size), allowing subsequent data simulation or structural refinement.

Another carbon-based sample of similar composition and density was also analysed. Five phases were identified and located within the sample (**Figure 128**). Well-crystallised cubic diamond was located in the central part of the sample, embedded within an amorphous carbon $sp^3$ phase matrix. Furthermore, crystallised ferrite ($\alpha$-Fe) grains located at the sample surface were identified as well as one single impurity grain of calcite ($CaCO_3$), outlining the sensitivity of the method. Ferrite comes from some contamination from the razor blade during sample extraction while calcite is probably a dust particle in contact with the pressure cell. For this weakly-absorbing material, absorption and fluorescence tomography do not provide any contrast, while diffraction tomography reveals the distribution of phases (crystalline and amorphous) inside the sample.

Pencil-beam diffraction tomography bridges the gap between the quantitative structural global probe, such as X-ray and neutron diffraction methods, and the local compositional probe, such as X-ray fluorescence and absorption computed-tomography techniques or electron diffraction. Though limited by the number of crystallites in the gauge volume and their size, this method presents a number of advantages. It can obtain contrast where other modalities cannot, provide multi-modal images for a complete sample characterisation and allow the reconstruction of unknown crystalline phases without any *a priori* information. Furthermore, it is extremely sensitive due to the quantity of diffraction images recorded at different positions and angles of the sample.

**References**
[1] W. Ludwig, E.M. Lauridsen, S. Schmidt, H.F. Poulsen, J. Baruchel. *J. Appl. Cryst.*, **40**, 905 (2007).
[2] B.C. Larson, W. Yang, G.E. Ice, J.D. Budai and J.Z. Tischler. *Nature* **415**, 887 (2002).

# Biomedical phase-contrast tomography

**Principal publication and authors**
F. Pfeiffer (a,b), C. David (a), O. Bunk (a), T. Donath (a), M. Bech (c), G. Le Duc (d), A. Bravin (d), and P. Cloetens (d), *Phys. Rev. Lett.* **101**, 16810 (2008).
*(a) Paul Scherrer Institut, Villigen (Switzerland)*
*(b) EPFL, Lausanne (Switzerland)*
*(c) Niels Bohr Institute, Copenhagen (Denmark)*
*(d) ESRF, Grenoble (France)*

X-ray computed tomography (CT) is an invaluable three-dimensional non-destructive imaging method with numerous applications in life and material science. The technique yields excellent results where highly absorbing structures are embedded in a matrix of relatively weakly absorbing material (like bones and tissue in the human body). However, for the differentiation of weakly absorbing soft matter, *e.g.*, pathologies in the soft-tissue structure, the contrast achieved by the currently existing, absorption-based X-ray methods is limited, unless contrast agents are used.

Phase-sensitive X-ray imaging can overcome these limitations and yield good contrast for soft-tissue structures. Phase-contrast imaging relies on refraction, or changes in the angular trajectory of X-rays. Just as light rays bend when they enter water from air, X-rays deflect as they travel through objects of varying densities. We used grating interferometry at **ID19** to measure this effect and thus obtain detailed radiographic phase-contrast X-ray images. This approach can be extended to three-dimensional phase-contrast computed tomography (PC-CT) by rotating the specimen around an axis perpendicular to the X-ray beam and recording several hundred differential phase-contrast projections **[1,2]**. Using specially developed filtered back-projection algorithms, a quantitative three-dimensional volume data set of the specimen can then be reconstructed by computer.

To evaluate the potential impact of this novel grating-based PC-CT method particularly for biomedical imaging applications, we carried out several in-vitro synchrotron experiments on biological specimens. As an example, **Figure 129** shows results for a rat brain specimen, fixed in formalin solution. The data reveals two interesting findings. Firstly, there is good contrast between the brain's white and grey matter. This can be seen in the image of the region containing the rat's cerebellum (centre). Although such differentiation is rarely possible with absorption-based X-ray CT scans, our method clearly resolves these small density differences between the two brain tissues. Secondly, pathologies such as tumours can be clearly distinguished. The right panel of **Figure 129** shows a section through a region in the brain containing a tumour, where we can clearly see the presence of a 9L gliosarcoma (rat brain tumour) in the right caudate nucleus of the brain, even though no contrast agent was used in the experiments. This again confirms the enhanced tissue sensitivity of the method. **Figure 130** shows a comparison between the phase-contrast CT results (left panel), and the corresponding tomographic slice obtained by conventional absorption-based CT reconstruction (right panel). Both results were obtained from the same data set, *i.e.*, with the same exposure time.

With this work we have demonstrated how grating-based phase-contrast CT can yield images of biomedical specimens with unprecedented soft tissue sensitivity thanks to the high spatial coherence of the synchrotron beam at **ID19**. In particular, we have shown that this X-ray method can be used to discern between subtle details

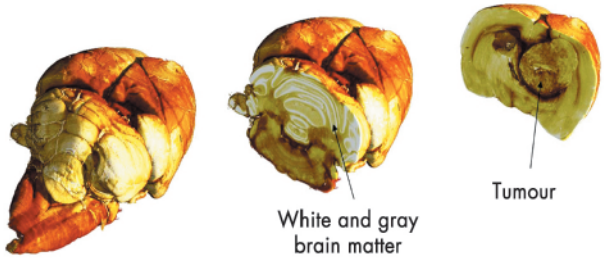


*Fig. 129:* Post mortem three-dimensional X-ray phase-contrast CT images of a rat brain bearing a 9L gliosarcoma (rat brain tumour), obtained at ID19. The images show three-dimensional renderings of the reconstructed data set.

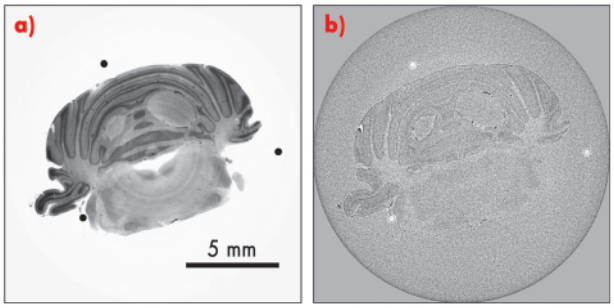


*Fig. 130:* Reconstructed tomographic slices through the rat's cerebellum.
**a)** Phase-contrast CT results,
**b)** Conventional absorption CT results.

**References**
[1] T. Weitkamp, A. Diaz, C. David, F. Pfeiffer, M. Stampanoni, P. Cloetens, and E. Ziegler, *Opt. Express* **13**, 6296 (2005).
[2] F. Pfeiffer, O. Bunk, C. David, M. Bech, G. Le Duc, A. Bravin, and P. Cloetens, *Phys. Med. Biol.* **52**, 6923 (2007).
[3] F. Pfeiffer, C. Kottler, O. Bunk, and C. David, *Phys. Rev. Lett.* **98**, 108105 (2007).

in the tissue structure of animal brains, an application field which until now has almost exclusively been reserved for other techniques such as histology and non-functional imaging techniques. Furthermore, the approach can be combined with local tomography to obtain a detailed view of a region of interest within a large sample. We believe that this method can be applied to a range of biomedical investigations immediately, including studies of the development of certain pathological features associated with neurodegenerative diseases (Alzheimer's disease), or the complex formation of blood vessels in tumour models. These results are also potentially interesting from a clinical point of view, since a similar approach can be implemented with standard X-ray tube sources [3].

# Biomedical applications

## Gold nanoparticles functionalised by gadolinium chelates as contrast agent for both X-ray computed tomography and magnetic resonance imaging

**Principal publication and authors**
C. Alric (a), J. Taleb (b), G. Le Duc (c), C. Mandon (b), C. Billotey (b), A. Le Meur-Herland (b), T. Brochard (c), F. Vocanson (d), M. Janier (b), P. Perriat (e), S. Roux (a), O. Tillement (a), *J. Am. Chem. Soc.* **130**, 5908 (2008).
*(a) LPCML, Villeurbanne (France)*
*(b) Créatis – LRMN, Villeurbanne (France)*
*(c) ESRF, Grenoble (France)*
*(d) Laboratoire Hubert Curien, Saint-Étienne (France)*
*(e) MATÉIS, Villeurbanne (France)*

There is a considerable need for better contrast agents both for cancer diagnosis and for monitoring treatments. Commercial contrast agents used in X-ray imaging and magnetic resonance imaging (MRI) – two anatomic techniques widely used to detect tumours – are not sensitive enough to be used with small animals. Indeed, the small molecular size of the contrast agents results in their rapid elimination by the kidneys. Moreover, most of them are specific for one imaging technique alone, whereas to use a combination of imaging techniques would be desirable. Numerous nanoparticulate contrast agents have been recently proposed to overcome these limitations. Their longer vascular half-life renders them suitable for long-term studies of biodistribution, and to evaluate the animal models response to a specific treatment. Another great advantage of the nanoparticle contrast agents lies in their ability to display several complementary properties in the same object. Consequently, some multifunctional nanoparticles that can be detected by several *in vivo* imaging techniques have been described.

We have recently developed a synthesis of gold nanoparticles functionalised by gadolinum chelates (Au@DTDTPA-Gd). These contrast agents are composed of a gold core (mean diameter of ~ 2.5 nm) encapsulated within a multilayered organic shell of ~ 150 gadolinium chelates (DTDTPA-Gd). These paramagnetic gold nanoparticles are able to induce a contrast enhancement in magnetic resonance images *in vitro* [1] thanks to the presence of the gadolinium (III) ions inside the organic shell. The aim of the present study was to investigate the *in vivo* contrast enhancement of Au@DTDTPA-$Gd_{50}$ nanoparticles (*i.e.* Au@DTDTPA nanoparticles with ~ 50 $Gd^{3+}$ ions trapped in the organic shell) for both MRI (gadolinium ions) and X-ray imaging (thanks to the strong X-ray absorption of the gold core).

The biodistribution of these nanoparticles was monitored by MRI (at 7T) and X-ray imaging, following their intravenous injection into mice and rats. X-ray imaging was performed at the biomedical beamline (ID17),

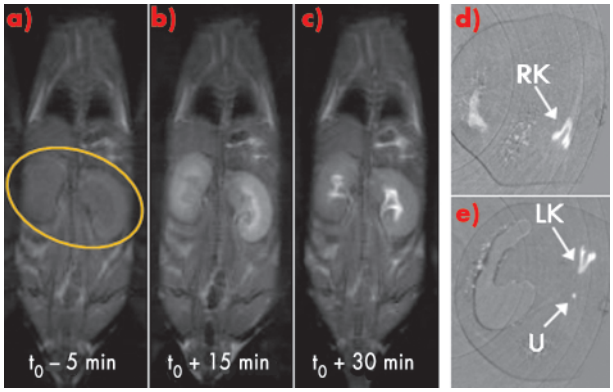


*Fig. 131: T1*-weighted images of a mouse before **a)** and after **b)c)** the Au@DTDTPA-$Gd_{50}$ nanoparticles injection. X-ray images in tomographic mode of a rat at right kidney level **d)** and left kidney level **e)**. RK and LK for right and left kidneys respectively; U for ureter.

using two monochromatic X-ray beams bracketing the gold K-edge energy. Both techniques led to the same observations: some areas in the body present an enhanced signal due to the accumulation of paramagnetic gold nanoparticles, this only a few minutes after injection. The contrast enhancement occurs first in the kidneys (**Figure 131**) and then in the bladder. Thus, the Au@DTDTPA-$Gd_{50}$ nanoparticles freely circulate within the vascular system without undesirable accumulation in liver and in spleen and are efficiently cleared by renal elimination. This was confirmed by ICP analysis: the gold element was essentially present in the urine and kidneys. Moreover, for both MRI and X-ray *in vivo* experiments, the contrast induced by these paramagnetic gold nanoparticles allow their monitoring over a long time period compared with molecular contrast agents.

The high photons flux of the biomedical beamline offers two advantages over conventional CT scanners. First, the synchrotron imaging technique requires only low gold concentrations (gold content for X-ray imaging is similar to that used in MRI). Thus, the injection of the contrast agent is less invasive. Another key advantage lies in the quantification of the contrast agent concentration in the tissues. Prior to *in vivo* imaging studies, *in vitro* experiments were carried out with aqueous solutions of Au@DTDTPA nanoparticles containing various concentrations of gold (**Figure 132a**). We can note the concordance between the experimental gold concentration (Exp) and the measurements (Meas) by synchrotron radiation computed tomography (SRCT). The ability to determine quantitatively the gold content in the tissues was used to monitor the biodistribution of paramagnetic gold nanoparticles *in vivo* and in "real time" (**Figure 132b**), without sacrifice of the animal. Moreover, another great advantage of the **ID17** beamline is its ability to perform radiotherapy **[2]**.

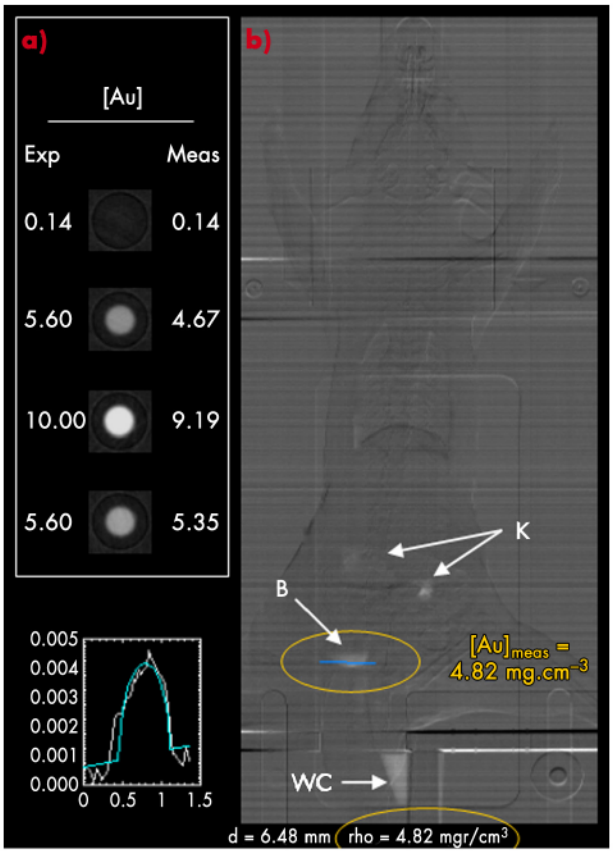


*Fig. 132:* **a)** Phantom images of samples containing differents gold concentrations ('Exp') measured by SRCT ('Meas'). The last phantom contains Au@DTDTPA-$Gd_{50}$ nanoparticles. **b)** *In vivo* measurement of gold concentration ($[Au]_{meas}$) in the bladder of a rat by SRCT (blue line). B for bladder; K for kidneys and WC for the tube collecting the urine.

In conclusion, this study confirms that Au@DTDTPA-$Gd_{50}$ nanoparticles freely circulate in the vascular system and that they can be used *in vivo* as a bimodal contrast agent for medical imaging. The MRI contrast enhancement comes from the presence of gadolinium ions in the organic shell of the nanoparticles, whereas the gold core provides strong X-ray absorption. These nanoparticles could therefore be a promising tool for preclinical studies in oncology.

**References**

[1] P.-J. Debouttière, S. Roux *et al., Adv. Funct. Mater.*, **16**, 2330 (2006).

[2] C. Alric, R. Serduc *et al. Gold Bull.*, **41**, 90 (2008).

## Brain tumour and normal vessel responses to synchrotron microbeam radiation therapy

Microbeam radiation therapy (MRT) is a pre-clinical form of radiosurgery initially dedicated to the treatment of brain tumours **[1]**. MRT requires very intense X-rays produced by a third generation synchrotron. The treatment is based on spatial fractionation of the radiation dose instead of conventional clinically-used temporal fractionation. Tumours are irradiated with very high doses (~150-625 Gy) by an array of parallel microbeams (~25-50 µm width), 100 to 400 µm spaced on-centre.

**Authors**
R. Serduc (a,b,c), T. Christen (a,b), J. Laissue (d), R. Farion (a,b), A. Bouchet (a,b), B. van der Sanden (a,b), C. Segebarth (a,b), E. Bräuer-Krisch (e), G. Le Duc (e), A. Bravin (e), C. Rémy (a,b) and E.L. Barbier (a,b).
*(a) INSERM, U836, Grenoble (France)*
*(b) Université Joseph Fourier, Grenoble Institut de Neurosciences, Grenoble (France)*
*(c) Present address: Centre de Recherche Cerveau et Cognition, UMR5549 CNRS-Université Toulouse, and visiting scientist, ESRF.*
*(d) Institute of Pathology, University of Bern (Switzerland)*
*(e) ESRF*

Previous preclinical studies on rodents have shown that normal tissue presents a particularly high tolerance to radiation delivered *via* microbeams and MRT has been proven to have palliative and even curative effects on cerebral tumours implanted in rat brain. These studies showed that MRT yields a better therapeutic index than conventional, non-spatially fractionated, radiotherapy. This has been largely attributed to a stronger effect of microbeam irradiation on tumoural vessels than on normal vessels. It has been hypothesised that MRT-damaged microsegments in poorly differentiated neovasculature of brain tumours may not be efficiently repaired, in marked contrast to the rapid repair of radiation-damaged normal vessels [2,3].

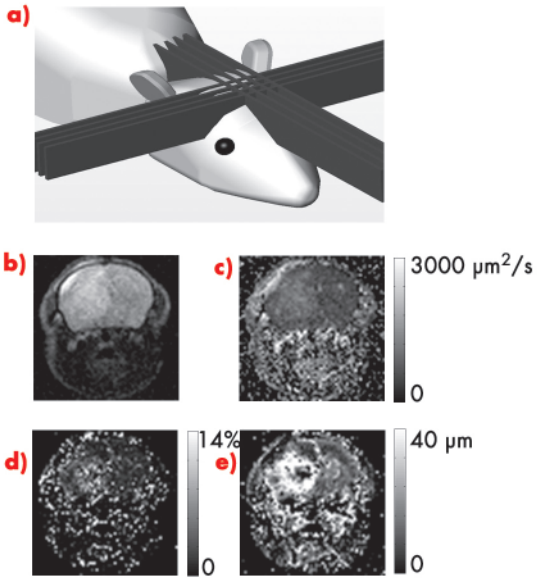


*Fig. 133:* **a)** Schematic representation of the irradiation geometry. Each microbeam array contains 28 microbeams (25 µm width, 211 µm on-centre distance, in-beam dose: 500 Gy). The two orthogonal irradiations produce a composite irradiation volume in the brain of 6 x 6 x 6 mm at the tumour site. MR images from one mouse obtained 21 days after tumour implantation: **b)** $T_2$-weighted image and **c)** related apparent diffusion coefficient, **d)** blood volume, and **e)** vessel size index maps. The tumour, readily visible in the left hemisphere, presents increased ADC, BV and VSI.

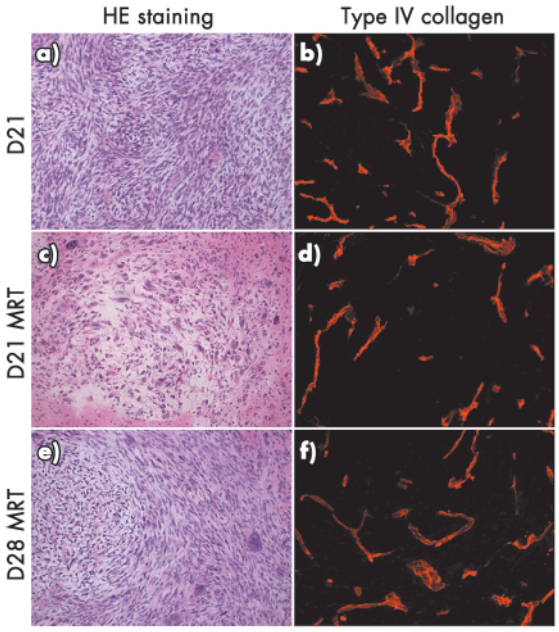


*Fig. 134:* HE staining **a), c), e)** and type IV collagen immunochemistry **b), d), f)** of transversal sections of 9L tumour implanted in nude mice. Untreated (**a**, **b**) and MRT-treated (**c**, **d**) tumour 21 days after tumour inoculation. MRT treated at D28 tumour (**e**, **f**).

This tumour vessel necrosis would lead to tumour asphyxia and lesion cure.

In this work, we characterised by MRI and histology the acute response of a 9L tumour implanted in the mouse brain (D0) and its vasculature to crossfired MRT performed on day 13 (**Figure 133**).

The mean survival time of 9L tumour bearing mice increased significantly for MRT-treated as opposed to untreated groups (x1.34, $p<0.0001$). A significant increase of apparent diffusion coefficient (ADC) was observed 24 hours after MRT in irradiated tumours versus non-irradiated ones. ADC reflects a radiation-induced increase in tumour vessel permeability which could be exploited to specifically deliver chemo-agents to brain tumours *via* the circulatory system. Indeed, no change in vessel permeability was observed in the contralateral, unidirectionally irradiated, hemisphere. In the untreated group, both tumour size and vessel size index (VSI, *i.e.*, mean vessel diameter) increased significantly (from 7.6 ± 2.2 to 19.2 ± 4.0 $mm^2$ and +21%, respectively) between the fourteenth and the twenty-first day after tumour cell inoculation. During the same period, in the MRT-treated group, no difference in tumour size was observed. Vessel size index measured in MRT-treated group increased significantly (+26%) but only between 21 and 28 days of tumour growth. We did not observe significant difference in blood volume between the MRT-treated and untreated groups. Histological analysis performed at different periods after irradiation revealed that MRT presented an important cytotoxic effect on tumoural cells while sparing unidirectionally irradiated normal brain tissue (**Figure 134**). However, tumour vessel labelling (**Figure 134**) and MRI data suggest that MRT does not reduce blood volume in this tumour model (and therefore the blood supply to the tumour remains practically unchanged), the opposite to expectations from Dilmanian *et al.* [2].

To conclude, this study shows that MRT slows the 9L tumour growth in nude mouse brain. MRI and histological

results suggest that the increase in survival time may be due to cytoreduction rather than to a short-term effect of ionising radiation on 9L tumour vessels. Tumour vessels were detected and appeared perfused up to 28 days after irradiation. This implies that our MRT parameters should be optimised and that even higher doses could be delivered to increase the damage to tumour vessels. In this study, measured microvascular parameters suggest that the action mechanism of MRT on 9L gliosarcoma tumour, at least under our experimental conditions, do not involve a significant microvascular component and that the cellular processes involved require further investigation.

**References**
[1] D.N. Slatkin, F.A. Dilmanian, P. Spanne, *Method for microbeam radiation therapy*, US Patent (1994).
[2] F.A. Dilmanian, T.M. Button, G. Le Duc, *Neuro-oncol* **4**, 26 (2002).
[3] J.A. Laissue, G. Geiser, P.O. Spanne, *et al., Int J Cancer* **78**, 654 (1998).

## Stem cell characterisation in the human intestine derived by mid-infrared light

**Principal publication and authors**
M.J. Walsh (a), T.G. Fellous (b), A. Hammiche (a), W.R. Lin (b), N.J. Fullwood (a), O. Grude (a), F. Bahrami (c), J.M. Nicholson (c), M. Cotte (d), J. Susini (d), H.M. Pollock (a), M. Brittan (b), P.L. Martin-Hirsch (a), M.R. Alison (b) and F.L. Martin (a), *Stem Cells* **26**, 108 (2008).
*(a) Lancaster University (UK)*
*(b) Queen Mary's School of Medicine and Dentistry (UK)*
*(c) Daresbury Laboratory (UK)*
*(d) ESRF*

The human body is comprised of different cell types, which together form complex tissues. Cells are evolved structures composed of biomolecules, such as proteins, lipids, DNA, RNA, glycoproteins and carbohydrates; their make-up differs with function. Stem cell populations are believed to be slow-cycling, possessing an infinite proliferative capacity and giving rise to transit-amplifying (TA) cells; these then differentiate into functional terminally-differentiated (TD) cells.

Identification of stem cells is important in order to understand fundamental tissue biology. However, robust markers for adult stem cells remain elusive because many approaches have relied on the expression of a single cell-surface marker. The most regenerative tissue in the human and an important stem-cell system which should be amenable to characterisation, due to its well-compartmentalised structure, is the gastro-intestinal (GI) tract containing the crypts of the small and large intestine. The GI tract is a model system as the putative stem cells are generally believed to reside towards the base of the crypt; these divide slowly migrating upwards to form TA cells, which form TD cells after further cell divisions. It has always been something of a conundrum that we seem to know a great deal about intestinal stem cells and yet reliable markers have proved to be elusive. However, it is generally agreed that in the small intestinal crypt, the stem cells are located, at approximately cell positions 4-5 (counting from the crypt base), whereas in the large intestinal crypts, they are at the very base.

Because of their different *in situ* roles, one might expect that these cell populations would have differing biochemical profiles giving differing infrared spectral fingerprints (**Figure 135**). Cellular biomolecules absorb the mid-infrared ($\lambda$ = 2-20 μm) *via* vibrational transitions that are derived from individual chemical bonds; this may yield richly structured "fingerprint" spectra relating to structure and conformation **[1]**. Synchrotron infrared sources such as at ESRF generate a highly collimated beam of photons of high brilliance that may be delivered through a very small aperture.

We set out to determine whether specific biomolecular fingerprints derived using infrared microspectroscopy could be attributed to different regions. Marked differences (including peak location and intensity) were observed throughout the infrared spectral "fingerprint" region (900 $cm^{-1}$ to 1,800 $cm^{-1}$). Large numbers of variables sometimes make it difficult to identify underlying variance **[2]**. Such data may be interrogated using principal component analysis (PCA). PCA was used for data reduction, and the

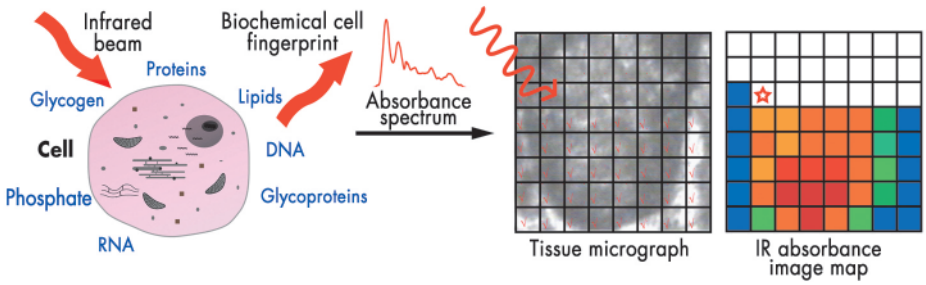


*Fig. 135:* Biomolecules absorb in the mid-infrared allowing interrogation of cells with differing biochemistry. Chemical entities may be tracked in a pixel-by-pixel fashion.

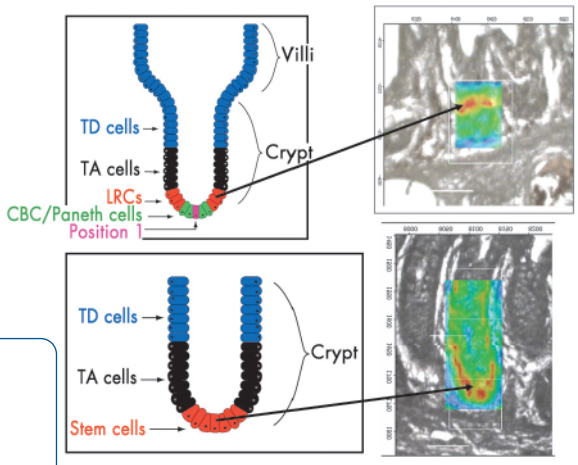


*Fig. 136:* Stem cell hierarchy of small and large intestine stem cells. Infrared spectral image maps highlight $\nu_s PO_2^-$ in the different putative regions.

**References**
[1] M.J. Walsh, M.J. German, M. Singh, H.M. Pollock, A. Hammiche, M. Kyrgiou, H.F. Stringfellow, E. Paraskevaidis, P.L. Martin-Hirsch and F.L. Martin, *Cancer Lett.* **246**, 1 (2007).
[2] M.J. German, A. Hammiche, N. Ragavan, M.J. Tobin, N.J. Fullwood, S.S. Matanhelia, A.C. Hindley, C.M. Nicholson, H.M. Pollock and F.L. Martin, *Biophys. J.* **90**, 3783 (2006).

output was processed using linear discriminant analysis (LDA). This allowed new variables to be found such that the ratio of the between-cluster (*i.e.*, category of cell type based on locations) variance to the within-cluster variance was maximised. PCA-LDA highlighted $\nu_s PO_2^-$ (1,080 $cm^{-1}$) as being a major contributor to segregation, pointing to an important role of alterations in the structure of chromatin.

Infrared spectral image maps allow one to track the spatial distribution of chemical entities based on levels of relative absorbance intensity at a wavenumber in a pixel-by-pixel fashion (**Figure 136**). Tissues analysed at the high resolution (8 μm × 8 μm) possible at ESRF generated such image maps that were then superimposed exactly on the interrogated regions (**Figure 136**). Our findings highlighted $\nu_s PO_2^-$ with greatest intensity located in a ring in the small intestinal crypt, at approximately cell positions 4-5 near the base, whereas in the large bowel crypts, this occurred primarily at cell positions 1-4, at the base. This suggests that this approach is a powerful adjunct to our understanding of stem cell biology.

# Materials science

## Grain mapping of stress corrosion cracks by diffraction contrast tomography

**Principal publication and authors**
A. King (a,b), G. Johnson (a,b), D. Engelberg (a), W. Ludwig (b,c) and J. Marrow (a), *Science* **321**, 382 (2008).
*(a) Manchester University (UK)*
*(b) ESRF*
*(c) MATEIS, INSA de Lyon (France)*

Stainless steels can suffer from intergranular stress corrosion cracking in certain conditions. Damage occurs via the nucleation and growth of cracks by localised corrosion of susceptible, sensitised grain boundaries under the action of stress. It is a potential failure mechanism in some power station components, where sensitisation can result from heat treatments, or fast neutron irradiation **[1]**. The susceptibility of grain boundaries to sensitisation depends on their structure at the atomic level, which depends on the relative crystal orientations of the grains at the boundary, as well as the orientation of the boundary relative to the grains. Certain special boundaries resist sensitisation, and previous experiments at the ESRF have shown that these resistant boundaries can form bridges across the advancing crack **[2]**, increasing the resistance to stress corrosion cracking **[3]**. Hence, grain boundary engineering aims to improve material performance by maximising the fractions of resistant boundaries **[4]**.

Diffraction contrast tomography (DCT) is a technique recently developed at the ESRF for mapping 3D grain shape and orientation in polycrystalline materials **[5]**. A technique related to the **ID11** 3D X-ray microscope project, DCT combines microtomography with an analysis of the diffraction spots arising from grains in the sample. As well as work reported here, other current research projects are using DCT to investigate the growth of grains during annealing, the interaction of fatigue cracks with microstructures, and on the distribution of strains and stresses in elastically anisotropic materials.

In the stress corrosion cracking project, DCT was used to map the grain structure of a sensitised stainless steel sample (**Figure 137**). This revealed the

crystallographic orientation of the grains on either side of each boundary, as well as the orientation of the grain boundary planes, which provides the required full macroscopic description of grain boundary structure. Because DCT is a non-destructive technique, the sample was then available for a subsequent *in situ* stress corrosion cracking investigation using standard microtomography. Both the grain mapping and *in situ* cracking observations were made using beamline **ID19**. We were able to align the crack path with the grain boundaries as shown in **Figure 137**, and thus associate bridges across the crack with particular grain boundaries (**Figure 138**). We could then examine the structure of these special grain boundaries, and compare them to the population of grain boundaries in the sample (~1600 boundaries in total) and also to the subset of grain boundaries that failed by stress corrosion cracking.

In conclusion, diffraction contrast tomography was used to map the grain shapes and orientations in a polycrystalline stainless steel sample, revealing the crystallographic character of the grain boundaries.


*Fig. 137:* Part of the DCT grain map of a stainless steel sample, combined with the crack path (shown in white).

We could then grow an intergranular stress corrosion crack in the sample, and make *in situ* tomographic observations of how the crack interacted with the microstructure, revealing which boundary types tend to resist crack propagation.

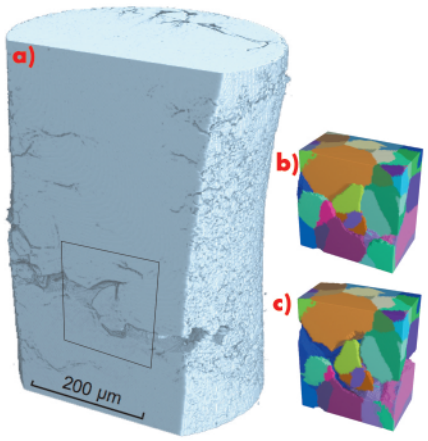


*Fig. 138:* **a)** A bridge across the crack, **b)** a rendering of the grains around this feature, and **c)** the grains with the crack opening displacements applied.

**References**

[1] P.M. Scott, *Corrosion* **56**, 711 (2000).
[2] L. Babout *et al., Mater. Sci. Technol.* **22**, 1068 (2006).
[3] A.P. Jivkov, T.J. Marrow, *Theoret. App. Fracture Mechanics* **48**, 187 (2007).
[4] D.L. Engelberg, R.C. Newman, T.J. Marrow, *Scripta Mat.* **59**, 554 (2008).
[5] G. Johnson *et al., J. Appl. Crystallogr.* **41**, 310 (2008).

## Local environment of Gd in GaN

Recently, Teraguchi *et al.* **[1]** observed a Curie temperature larger than 400 K in $Ga_{0.94}Gd_{0.06}N$. Additionally, Dhar *et al.* **[2]** reported an extraordinarily large magnetic moment of Gd in weakly Gd doped GaN layers as well as ferromagnetism above room temperature. Despite the great potential, there are some controversial results on the ferromagnetic interactions in $Ga_{1-x}Gd_xN$. Some findings suggest that the crucial mechanism is either the electric polarisation of the hexagonal GaN, or a strong long-range interaction between Gd atoms and certain defects. On the other hand, Gd might be inducing a magnetic moment in Ga and/or N interstitials were being detected; others have attributed the stabilisation of ferromagnetism to nitrogen or gallium vacancies. Moreover, according to a recent theoretical study **[3]**, Ga vacancies are the most effective source of localised holes necessary for a strong ferromagnetic *p-d* exchange coupling in GaGdN. In addition, several reports have not detected the formation of any secondary phases in GaN, whereas in Gd implanted GaN the presence of precipitates of $Gd_3Ga_2$, GdN, and Gd has been observed with high saturation magnetisation. **[4]** Therefore, the role of Gd on the defect formation, local atomic site configuration, and/or phase separation in GaN is of key importance.

We have studied the incorporation of Gd on 0.5 µm thick GaN films grown by molecular beam epitaxy (concentrations ranging from $1.14 \times 10^{17}$ to $1.18 \times 10^{19}$ $cm^{-3}$). All GaGdN layers are ferromagnetic at room temperature, as measured by

**Principal publication and authors**

G. Martínez-Criado (a), O. Sancho-Juan (b), N. Garro (b), J.A. Sans (a), A. Cantarero (b), J. Susini (a), M. Roever (c), D.-D. Mai (c), A. Bedoya-Pinto (c), J. Malindretos (c) and A. Rizzi (c), *Appl. Phys Lett.* **93**, 021916-1-3 (2008).
*(a) ESRF*
*(b) ICMUV, 46071-València (Spain)*
*(c) VISel, D-37077 Göttingen (Germany)*

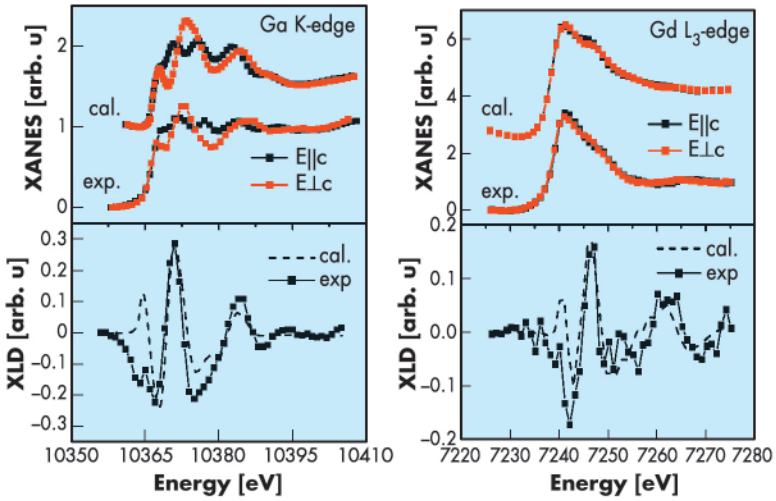


*Fig. 139:* XANES and XLD signals recorded at the Gd $L_3$ and Ga *K* edges from the GaN (0.027% Gd).

**References**

[1] N. Teraguchi, A. Suzuki, Y. Nanishi, Y.K. Zhou, M. Hashimoto, and H. Asahi, *Solid State Commun.* **122**, 651 (2002).

[2] S. Dhar, O. Brandt, M. Ramsteiner, V.F. Sapega, and K.H. Ploog, *Phys. Rev. Lett.* **94**, 037205 (2005).

[3] L. Liu, P.Y. Yu, Z. Ma, and S.S. Mao, *Phys. Rev. Lett.* **100**, 127203 (2008).

[4] S.Y. Han, J. Hite, G.T. Thaler, R.M. Frazier, C.R. Abernathy, S.J. Pearton, H.K. Choi, W.O. Lee, Y. D. Park, J.M. Zavada, and R. Gwilliam, *Appl. Phys. Lett.* **88**, 042102 (2006).

[5] A. Ney, T. Kammermeier, E. Manuel, V. Ney, V.S. Dhar, K.H. Ploog, F. Wilhelm, and A. Rogalev, *Appl. Phys. Lett.* **90**, 252515 (2007).

superconducting quantum interference device magnetometry (SQUID). X-ray absorption near edge structure (XANES) and scanning X-ray fluorescence (XRF) measurements were carried out at the microprobe at **ID22**. It has been argued that high-temperature ferromagnetism in magnetically doped nitrides results from nanoscale regions containing a high concentration of the magnetic constituents. However, at the length scale of the beam size (1.5 x 3.5 μm$^2$), uniform patterns with no intensity changes (< 0.02%) were observed, showing a homogeneous distribution of Ga and Gd. Whereas the expected impurity aggregation effects are observed in heavily rare earth doped GaN, our results suggest no tendency to agglomerate at those low Gd levels.

The comparison of the X-ray linear dichroism (XLD) of the XANES at the Gd $L_3$ and Ga *K* edges supports the tetrahedral 6d$^{3+}$ site distributions in the highest Gd doped GaN (0.027%). **Figure 139** shows the XANES recorded with the electrical field vector parallel and perpendicular to the *c* axis of the GaGdN as well as the respective XLD signal, reflecting directly the anisotropy of the unoccupied density of states of the 5*d* and 4*p* shells of the Gd and Ga atoms. The simulations of the XLD performed with FEFF8 code were rescaled with respect to the experimental ones. The Gd $L_3$ edge XLD signal is similar to the one observed at the Ga *K* edge but with smaller amplitudes. The results show a strong anisotropy exhibiting the signature of the hexagonal GaN. There is no remarkable damping effect revealing a strong influence of the Gd impurities in any preferential crystallographic direction. For other possible Gd site occupation rather than substitutional, the spectral shape and amplitude of XLD signal is drastically different **[5]**.

In summary, structural analysis based on XANES and XLD revealed Gd ions in a predominantly trivalent state with tetrahedral coordination, occupying Ga sites in the wurtzite structure. In addition, EXAFS collections around Ga atoms have shown no local atomic distortion as a function of Gd fraction providing direct evidence for the highly short range structural order. Although the presence of very small amounts cannot be completely excluded, within the sensitivity of our experimental techniques, neither secondary phases nor Ga vacancies were observed.

# Cultural Heritage

## Secrets of Bamiyan Buddhist murals

Forceful blasts aimed at destroying the two Giant Buddha statues at the Bamiyan site and vandalism following these 2001 explosions damaged more than just the statues. They were also directly responsible for shattering important mural paintings that had once existed on the niches above the Buddhas as well as other valuable paintings inside the hundreds of caves (**Figure 140**).

The Bamiyan site is important both historically and artistically for its place along ancient cultural and material routes on the Silk Road linking the East and the West. It was included in the World Heritage List in Danger in 2003

and designated as a subject to be protected through international cooperation. This project has been funded by the UNESCO/Japanese Funds-in-Trust so that the conservation project 'Safeguarding of the Bamiyan Site' could be overseen by UNESCO. In order to perform satisfactory conservation intervention and provide a deepened knowledge of painting technologies stemming from Bamiyan along the vast Silk Road area, a wide range of scientific diagnosis has been used to reveal the manufacturing techniques and deterioration mechanisms of various mural paintings from over 50 caves dating back to a period between the 5th and 9th centuries AD. In particular, synchrotron-based analyses were performed at the ESRF with the aim of identifying the inorganic pigments and alteration products, and also the organic binders. Thus, a multi-modal analysis was carried out on both beamline **ID18F** (micro X-ray fluorescence, μXRF, and micro X-ray diffraction, μXRD) and beamline **ID21** (micro Fourier Transform Infrared, μFTIR).

Elemental analyses were a first step to identifying the pigments and grounds. We found compounds containing metals such as lead, copper, calcium, mercury, iron and arsenic. These preliminary data were then refined thanks to micro X-ray diffraction. This technique is highly valuable for the precise identification of phases. It was particularly useful to distinguish pigments sharing common elemental composition. For example, various lead pigments were identified such as oxides, sulphates, carbonates, chlorides. It was also possible to distinguish various compositions of the same pigment, for example lead whites, containing differing proportions of lead carbonates (cerussite, $PbCO_3$) and lead hydroxycarbonates (hydrocerussite, $Pb_3(CO_3)_2(OH)_2$). Such identification is very important because it can give indication of a possible choice of pigment quality and/or a specific use of these pigments by the painter. In parallel to these identifications, phases were mapped across transversal cross-sections to reveal their distribution. Indeed, these Buddhist paintings usually present a very complex stratigraphy with the superposition of often 5 or 6 layers (**Figure 141**). To look at this stratigraphy, μFTIR 2D-mappings were acquired. This permitted an identification of the organic binders as well as their localisation within the painting's multi-layered structure.

Interestingly, the organic components also revealed complex compositions and distributions. A wide variety of organic materials were used, with an apparent intentional choice correlating to their role and their location (*e.g.* within sizing layers, paint layers, mordant, varnish and glaze). Oil was identified in many fragments, in addition to proteins, resins and polysaccharides. This discovery of mid-seventh century oil paintings is one of the oldest known to date.

Even more surprisingly, μFTIR enabled an identification of hydride materials, obtained by reaction of metallic (such as lead or copper) compounds with oil, leading to metallic carboxylates (soaps). The use of a similar formulation was already established in ancient cosmetics, but once again, their presence in such ancient paintings was a real discovery.

**Principal publication and authors**

M. Cotte (a,b), J. Susini (b), V. Armando Solé (b), Y. Taniguchi (c), J. Chillida (d), E. Checroun (e), P. Walter (a), *J. Anal. At. Spectrom.* **23**, 820 (2008).

*(a) Centre of Research and Restoration of the French Museums - UMR171 CNRS, Paris (France)*
*(b) ESRF*
*(c) Japan Center for International Cooperation in Conservation – National Research Institute for Cultural Properties, Tokyo (Japan)*
*(d) Painting restorer, Barcelona (Spain)*
*(e) Painting restorer, Paris (France)*

*Fig. 140:* A painting fragment from the Foladi cave. This painting of a Buddha figure was identified as an oil painting (© NRICPT).

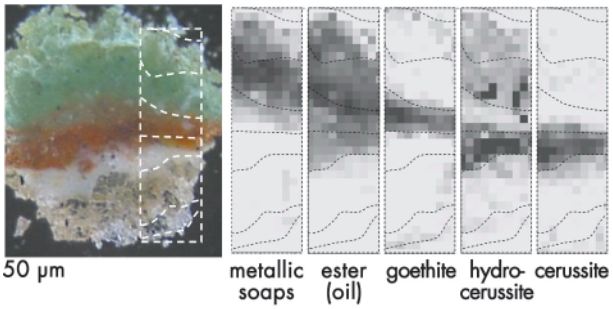


*Fig. 141:* Micro-FTIR analysis of a pressed painting fragment from Foladi. Visible light picture (left). Some of the ingredients (organic binders and pigments) identified and mapped by μFTIR (right).

The chemical and structural study of a complex multi-layered system such as these paintings exemplifies the potential of a correlative analysis using micro- synchrotron-based techniques. The high spatial resolution associated with a high detection limit and short dwell time allows precise 2D chemical and/or structural mappings. On a more general level, this type of 2D information together with advanced data processing should lead to a better understanding of painting techniques, both of the material compositions and the manner in which the paint was applied. These results have given us a completely new view on painting history and will certainly encourage similar analyses of ancient paintings worldwide.

**Principal publication and authors**
K. Krug (a), L. Porra (b, c), P. Coan (b), A. Wallert (d), J. Dik (a), A. Coerdt (d), A. Bravin (b), P. Reischig (a, e), M. Elyyan (e), L. Helfen (b, e) and T. Baumbach (e), *J. Synchrotron Rad.* **15**, 55 (2008)
*(a) Department of Materials Science, Delft University of Technology (the Netherlands)*
*(b) ESRF*
*(c) Department of Physical Sciences, University of Helsinki (Finland)*
*(d) Rijksmuseum, Amsterdam (The Netherlands)*
*(e) ANKA/IISS, Forschungszentrum Karlsruhe (Germany)*

## X-ray imaging in the study of paintings

During the Middle Ages, Christianity attached great value to relics, *i.e.* physical remnants from the life of Christ or remains of a saint, such as a piece of bone, textile or paper. The Scripture refers to the healing power of objects that were touched by Christ or his Apostles. Similar to modern homeopathy, it was thought that such remains, even when present in small doses, could have a beneficial effect.

In some cases relics have been hidden inside an art object without any external physical evidence of the relic's presence. This seems to have been the practice notably with sculpture, and in some rare instances also with altarpieces. A good example is the Norfolk triptych from the collection of the Museum Boymans-van Beuningen in Rotterdam, which is considered to be one of the oldest paintings in The Netherlands.

The main scene in the central panel represents the Deposition of Christ (**Figure 142**). The X-ray transmission radiography of this area shows that an inset was made into the panel, into which a thin plank of softwood was inlaid with its grain direction perpendicular to the grain direction of the altarpiece. The primer and paint layer have been painted on top and therefore cover the wooden inlay. This raises the question of whether some sort of relic could be hidden behind this inset (**Figure 142**). The object could be a piece of textile related to the Shroud of Christ, depicted in the painting itself, or a small piece of paper with an inscription, or maybe even a bone or piece of wood from the cross of Christ.


*Fig. 142: Christ as the man of Sorrows*, also known as the 'Norfolk tryptych' ca. 1415–1420, Museum Boymans-van Beuningen, Rotterdam, The Netherlands. The white frame corresponds to the X-ray radiography of the central panel showing the wooden inlay and its perpendicular grain direction.

Regular X-ray transmission radiography has failed to properly image what is hidden behind the panel inlay. Conventional radiography provides no three-dimensional insight into the construction of the panel. However, a more significant limitation is the low sensitivity of X-ray absorption to low-Z materials. The paint layer on the front contains heavy metals like Pb and Hg in pigments such as lead white and cinnabar. The wooden panel has a thickness of about 4 cm. Any organic materials such as paper or textile sandwiched in between the paint and the wood are therefore virtually transparent at the relatively high energies needed to penetrate the entire object (> 25 keV).

The present study describes the first-time application of two synchrotron-based imaging techniques in the study of paintings: X-ray computed tomography (**ID17**) and X-ray computed laminography (**ID19**). Both setups have phase-contrast imaging capability, being analyser-based and

propagation-based, respectively. The tomography setup had a 0.35 mm resolution with a 15 cm field of view, while laminography had a 7.5 micrometre resolution with a 15 mm field of view, which allowed a more detailed inspection. The aim of this experiment was to see whether three-dimensional phase-contrast imaging would be adequate for the visualisation of an organic, fibrous object imbedded inside a painting.

We prepared a test panel into which a small inset was cut, mimicking the suspected construction of the Norfolk panel. Behind the inset we placed a small folded piece of paper with a short inscription in organic ink. The panel was given an authentic chalk-based priming layer and several layers of various paints containing heavy metals like Hg and Pb.

A computer tomography scan with 0.35 mm resolution provided the three-dimensional structure of the entire panel, visualising features such as wood grain, and accumulation of glue and voids inside the panel. Computed laminography with spatial resolution on the micrometre scale allowed us to image local volumes, *i.e.* three-dimensional regions of interest, within the panel. In combination with propagation-based phase-contrast imaging, we succeeded in three-dimensionally imaging the piece of paper sandwiched in the wooden inset, the heavy metal paint layers and the bulk panel (**Figure 143**). The phase-contrast capability proved very effective in enhancing image contrast (at all material interfaces and especially between paper and air) which otherwise would have been dominated by the attenuation of the highly absorbing paint layer.

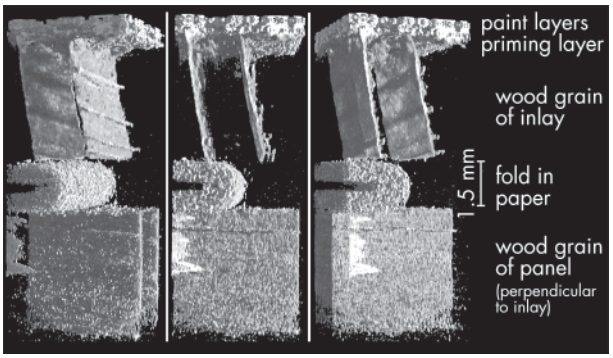


*Fig. 143:* Three-dimensional rendering of a mockup panel under different viewing angles, obtained by synchrotron-radiation computed laminography. The paint layer at the top, the perpendicular grain directions in the inlay (below) and the panel (bottom), and the folded paper (centre) are clearly visible.

In addition to the propagation-based setup we also imaged our panel with the analyser-based phase-contrast imaging. This phase-contrast method is particularly well suited to the detection of steady variations of the projected refractive index distribution. It permitted the hidden paper to be imaged, and even the contours of the ink writing on the paper were visible. The contrast in these images strongly depends on the refraction angle, the orientation of the analyser crystal with respect to the wood grain and, to a lesser extent, the density of the grain being imaged. The future availability of a laminography setup using an analyser-based phase contrast could significantly improve the detectability of such written texts. Plans are underway to examine the actual artwork, the Norfolk triptych, with techniques described above.

## Early structure of feathers revealed by phase contrast X-ray synchrotron imaging

A 4-cm piece of amber discovered among thousands of others in a quarry from southwestern France is helping to bridge a gap in our knowledge of the early development of feathers. The amber dates from the Early Cretaceous period, around 100 million years ago, and encases at least seven beautifully preserved feathers of a primitive type never seen before. They represent a critical stage in the evolution of feathers.

Conventional imaging techniques using transmitted light microscopes were used first (**Figure 144**) but this did not reveal sufficient information for a precise assessement of the morphology of the feathers. Phase contrast X-ray synchrotron imaging techniques have already demonstrated their power on fossil inclusions in amber **[1]**, so we decided to apply such methods to image the unique fossil feathers. To reveal the finest structures

**Principal publication and authors**
V. Perrichot (a), L. Marion (b), D. Néraudeau (c), R. Vullo (c), P. Tafforeau (d), *Proc. Roy. Soc. B*, **275**, 1197 (2008).
(a) University of Kansas (USA)
(b) Ecobio, UMR 6553, Rennes (France)
(c) Géosciences Rennes, UMR 6118, Rennes (France)
(d) ESRF

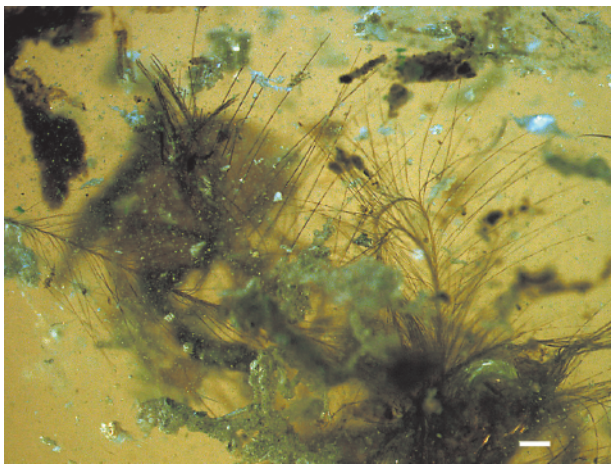

*Fig. 144:* Fossil feathers preserved in a 100 million-year-old piece of amber from France, observed by transmitted light microscopy. Scale bar 0.1 mm.

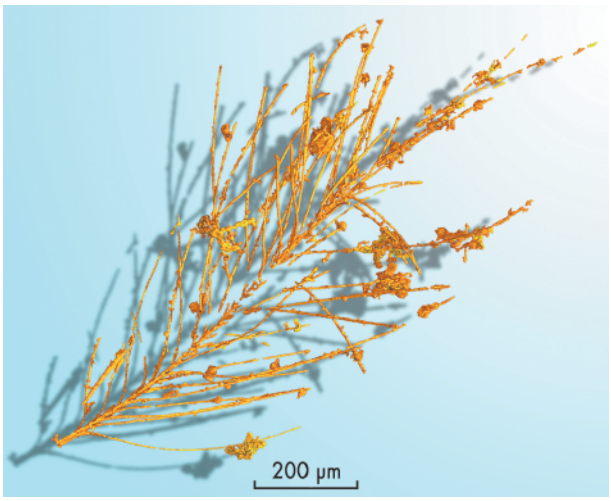


*Fig. 145:* 3D virtual reconstruction of the best-preserved fossil feather using holotomography: long filaments inserted parallel and opposite on each side of a flattened primary shaft initiate the planar form of later feathers.

of the feathers in three dimensions, a mosaic of 6 scans was performed using a single-distance phase retrieval approach (holotomography) with a voxel size of 0.7 micrometres, at beamline **ID19**. Complex multistep data processing allowed an enhancement of the visibility of the feathers and other fine structure and then the virtual extraction of the most well-preserved feather from the resin.

Detailed holotomographic images (**Figure 145**) revealed a unique structure in the feathers morphology that was previously unknown. The fossils display a flattened primary shaft – or rachis – composed of the not-yet-fused bases of the secondary branches – or barbs – that initiate the planar form of later feathers. The barbs fuse progressively and lack the complete fusion that is observed in the rachis in all other fossil and modern feathers. The planar form of the fossil feathers was observed here for the first time. It results from the insertion of barbs on the two opposite sides of the shaft whose shape is flattened with respect to modern feathers.

This structure represents an intermediate and critical stage in the incremental evolution of feathers. It had been predicted by developmental theories **[2]** but was hitherto undocumented by evidence from the recent or the fossil record. Primitive and derived feathers occur in both early birds and some dinosaurs known as theropods. Interestingly, teeth from two species belonging to this group of feathered dinosaurs were found fossilised in the same quarry as the amber, raising the possibility that the feathers come from a dinosaur rather than a bird.

In conclusion, the feathers' primitive feature differs from all other known morphologies, both modern and fossilised. It provides evidence for a key step in the evolution of feathers leading towards feathers for the purpose of flight, thus in the transition between dinosaurs and birds.

**References**
[1] M. Lak *et al., Microsc. Microanal.*, **14**, 251 (2008).
[2] R.O. Prum and A.H. Brush, *Q. Rev. Biol.*, **77**, 261 (2002).

# Environmental Sciences

## Hard X-ray nanoscale fluorescence imaging of Earth and Planetary Science samples

Synchrotron-based microanalysis can be used to analyse fragile and minute samples because it offers a unique way to study the bulk morphology, internal structure, crystallography, and trace composition of sub-millimetre grains at the micrometre scale. Some scientific applications, however, require even higher resolution than currently available which leads to an advancement of the techniques. For instance, nondestructive observation

of Earth and Planetary Science materials requires multiscale analysis because samples can often feature chemical and structural heterogeneities that span scales from the millimetre to the nanometre [1].

Here we present the new imaging capabilities of the nano-imaging beamline end-station (ID22NI) for the non-invasive study of planetary science samples. The setup is based on a focusing system permitting large bandwidth and fast nanoscale mapping optimised for fluorescence imaging.

The optics scheme of ID22 beamline has to be suitably tuned in order to obtain decananometre X-ray spot sizes with comparable horizontal and vertical dimensions. First, the horizontal source was reduced to about 25 micrometres by means of slits, thus creating a secondary horizontal source 28 metres away from the synchrotron source. The loss of intensity is compensated for by switching to the "pink beam" mode, whereby there is no crystal monochromator in the beam. Thus the only optical element between the source and the focusing device is a flat Si mirror with Pd or Pt stripes that filters out high incident energies. This dramatically increases the photon flux and improves the performance and stability of the focus at the expense of the energy resolution $\Delta E/E$ which increases by two orders of magnitude up to $10^{-2}$. At 63 metres away from the synchrotron source, the beam is focused using a Kirkpatrick-Baez (KB) system that consists of two independent mirrors for focusing the beam vertically and horizontally (Figure 146). The primary mirror, coated with a graded multilayer, acts both as a vertical focusing device and a monochromator, yielding very high flux of about $10^{12}$ photons/s for X-rays in the 15-20 keV range. The minimal spot size achieved was 80 nm in two dimensions and 40 nm in one dimension [2]. The nanoprobe features a flux density of up to $5.10^{13}$ ph/s/μm², largely superior to the microprobe's $10^{11}$ ph/s/μm², thus exhibiting much higher sensitivity for (ultra-) trace element detection and allowing mapping with a greatly reduced dwell time.

Samples are placed in the focal spot of the KB system on a 4-axis stage and can be raster scanned on three axes plus one rotation. At each position a fluorescence spectrum which gives information about the sample elemental composition is collected. The spectra are measured using a SII Nanotechnology Vortex 50 mm² silicon drift diode (SDD) collimated detector placed in the horizontal plane at 75 degrees from the incident beam. SDD detectors provide an excellent trade-off between output count rate (approximately 600 kcps at 0.25 μs peaking time) and energy resolution (140 eV), although displaying lower peak-to-valley ratios than standard Si(Li) detectors. A scanning mode based on the acquisition of data while continuously translating the sample with a piezo-driven stage speeds up the measurement by up to 50%.

A cometary grain from the NASA Stardust cometary mission collection was studied [1]. The sample was measured *in situ*, in the original low density (approx. 0.01 g/cm³) silica aerogel, in which it was trapped after its few millimetres penetration track.

Figure 147 shows the superposition of the Fe 2D map with the Ca and Ni

**Principal publication and authors**

P. Bleuet (a,d), A. Simionovici (b), L. Lemelle (c), T. Ferroir (c), P. Cloetens (a), R. Tucoulou (a), J. Susini (a), *Applied Physics Letters* **92**, 213111 (2008).

*(a) ESRF*

*(b) LGIT, OSUG, Université J. Fourier, CNRS UMR 5559, Grenoble (France)*

*(c) LST, Université de Lyon, Ecole Normale Supérieure de Lyon, UMR5570-USR3010 (France)*

*(d) Present address: CEA, LETI, MINATEC (Grenoble)*

*Fig. 146:* Schematic view of the experimental setup of the ID22NI end-station.

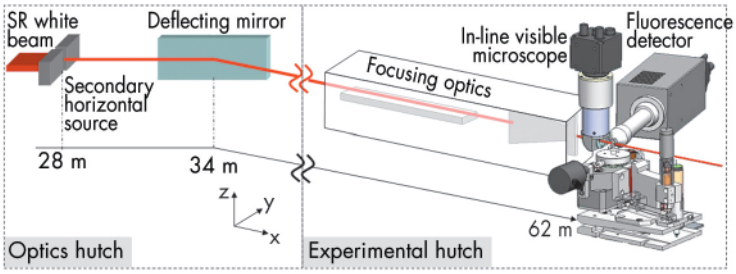


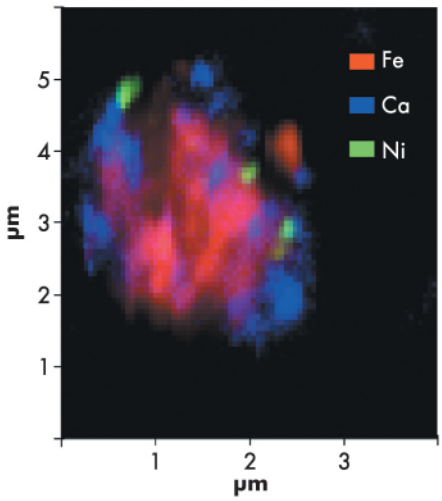


*Fig. 147:* Colour-coded map of the distribution of Fe, Ni and Ca in the cometary grain.

maps, respectively, the two other major elements in the grain. A chemical heterogeneity at the sub-micrometre scale is evident in this view. No post-processing of the image has been done so that strong heterogeneities from one 50 nm pixel to the other are shown. Micrometre Ca-rich zones and hundreds of nanometres Ni-rich phases are embedded in an Fe-rich matrix. This chemical view starts to be consistent with the classical petrology of the cometary grains composed of micrometre Fe-rich crystals of olivines and pyroxenes, Ca-rich pyroxenes and plagioclases, nanometre Fe-Ni precipitates, all embedded in a silica matrix. These excellent results suggest that XRF studies of Stardust grains could be used to obtain petrology information in place of the alternative more destructive analyses.

Further analyses must be carried out to better establish the shape and 3D quantitative chemical composition of the grain. They include 2D/3D morphology, crystallinity and oxidation state by means of nano-tomography, diffraction or spectroscopy.

**References**
[1] G.J. Flynn *et al., Science* **314**, 1731 (2006).
[2] R. Ortega, P. Cloetens, G. Devès, A. Carmona, and S. Bohic, *PLoS ONE* **9**, e925 (2007).

## Carbon nanotubes in macrophages: imaging and chemical analysis by synchrotron X-ray fluorescence microscopy

**Principal publication and authors**
C. Bussy (a,b), J. Cambedouzou (a), S. Lanone (b), E. Leccia (a), V. Heresanu (a), M. Pinault (c), M. Mayne-l'Hermite (c), N. Brun (a), C. Mory (a), M. Cotte (d), J. Doucet (a), J. Boczkowski (b), and P. Launois (a), *Nano Letters* **8**, 2659 (2008).
*(a) Laboratoire de Physique des Solides, CNRS-Université Paris-Sud 11, Orsay (France)*
*(b) Institut Mondor de Recherche Biomédicale, INSERM-Université Paris Val de Marne/Paris 12, Créteil (France)*
*(c) Laboratoire Francis Perrin, CEA-CNRS, Saclay (France)*
*(d) ESRF*

The human health impact associated with carbon nanotubes (CNT) is a critical issue considering their numerous potential applications. Basic research on interactions between carbon nanotubes and cells is needed, especially for their localisation within cells. A second requirement is to have information about cell modifications after contact with carbon nanotubes. Both points can be addressed using synchrotron-based X-ray fluorescence microscopy (μXRF), used here for the first time to study carbon nanotube-cell interactions.

In this study, we consider murin macrophages exposed to unpurified or purified single-walled (SW) CNT or to multi-walled (MW) CNT, the choice of macrophage cells being dictated by their key role in host responses to exogenous agents (**Figure 148**). Two-dimensional fluorescence scans have been performed on cryofixed samples, on beamline **ID21**, with a beam size of 1.5 μm x 0.5 μm and with incident X-ray energy of 7.2 keV. This energy was chosen to excite the K-lines of elements of atomic number up to Z = 26, corresponding to iron, which is the catalyst of the growth of the studied nanotubes. Iron particles are found inside MWCNT or bound to SWCNT bundles, and can therefore be used as a nanotube tracer inside cells. The purification process considered in SWCNT samples leads to a decrease of the amount of iron from 20 wt% to 2wt% in unpurified and purified samples, respectively.

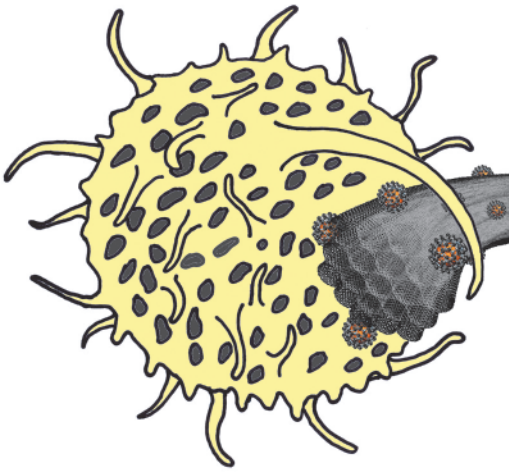

*Fig. 148:* Artistic view of a macrophage cell engulfing a bundle of single-walled carbon nanotubes. Iron catalytic particles, surrounded by carbon shells and bound to nanotubes, are shown in orange (not to scale).

**Figure 149a** shows fluorescence spectra and elemental maps of an unexposed cell obtained using μXRF. Phosphorus and potassium are constitutive elements of cells and their spatial repartition delimitates the cell shape. The P and K-rich zones in the central part of the cell can be attributed to the nucleus. Iron signal is found to present a rather homogeneous distribution and is attributed to experimental background.

Considering carbon nanotube-exposed cells, iron maps reveal one or several iron-rich zone(s) inside or close to the

cell contours (see **Figure 149b**). These zones correspond to CNT localisation. Iron-based catalyst particles could even be detected in the case of cell exposure to purified SWCNT, for which iron amount is minimised, thus highlighting the high sensitivity of the μXRF method. In the case of macrophages exposed to unpurified SWCNT, an additional calcium signal following the cell-shape can be evidenced (**Figure 149b**) although no calcium signal is detectable in unexposed cells. This finding of extra-cellular calcium uptake by exposed cells could be of strong importance in the perspective of understanding the toxicological mechanisms of CNT **[1,2]**. Moreover, pharmacological assays with calcium chelators and inhibitors, performed following this μXRF experiment, point toward the key role of calcium in carbon nanotube cytotoxicity.

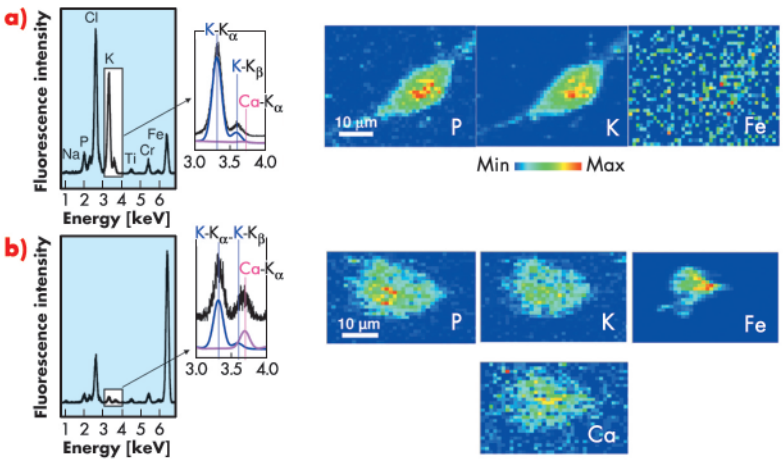


*Fig. 149:* X-ray fluorescence spectra integrated over the whole scanned areas of a typical control cryo-fixed macrophage **a)** and of a macrophage exposed for 24h to an unpurified SWCNT suspension at 100 μg/mL **b)**. Enlarged areas around the positions of the Kα and Kβ fluorescence peaks of potassium and of the Kα peak of calcium are shown, together with fits of the potassium and calcium contributions, in blue and in purple, respectively. Elemental maps of phosphorus (P), potassium (K), iron (Fe) and calcium (Ca) are drawn. Pixel size is 1 μm x 1 μm.

Calcium uptake was shown in part of the cells exposed to unpurified SWCNT or MWCNT but in none of those exposed to purified SWCNT. Chemical or physical parameters of CNT, such as their catalyst content (higher in unpurified SWCNT and MWCNT than in purified ones) or their surface properties (which are modified during purification process) could be crucial determinants in their toxicity. Effect of the nanotube aspect ratio and length may also be relevant. ESRF capabilities could allow one to go further in the understanding of carbon nanotube-cell interactions: micro-XANES could be used to identify putative changes in the chemical state of the iron nanoparticles during cell contact and nano-XRF tomography could give new information about CNT toxicity at the sub-cellular level.

**Acknowledgement**
The authors acknowledge financial support from the *Agence Nationale de la Recherche* and C'Nano Ile de France.

**References**
[1] D.M. Brown, *et al., Am. J. Physiol. Lung Cell. Mol. Physiol.* **286**, L344 (2004).
[2] K. Donaldson, *et al., Free Radical Biol. & Med.*, **34**, 1369 (2003).

# Methods and Instrumentation

## Introduction

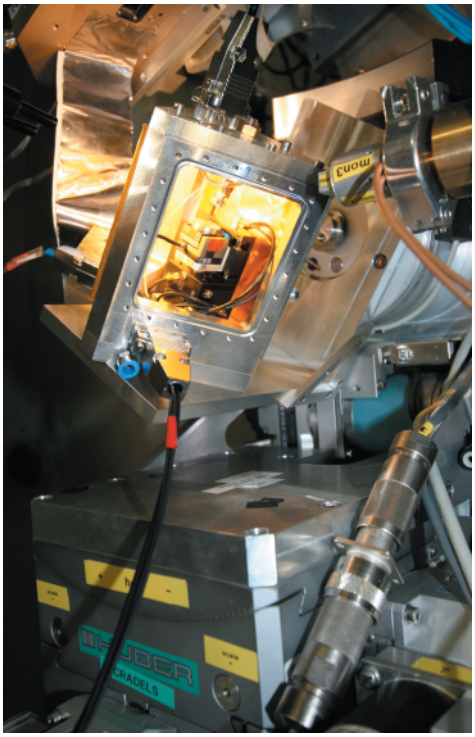

*Fig. 150:* The atomic force microscope installed in the end station of beamline ID01. The AFM is used to visualise both the beam and the sample and to manipulate the sample (Courtesy O. Dhez).

Instrumentation development and the deployment of new methodology are fundamental to synchrotron radiation research. At the ESRF, close collaboration between the instrumentation support teams and the beamline scientists has been the traditional source of most developments. In the future, the exploration of new techniques, the need for instrument integration, the quest for stability, automation, and user-friendly operation will call for an even closer collaboration between beamlines and developers.

A new division, the Instrumentation Services and Development Division, ISDD, will gather together support groups presently distributed among the Experiments, Computer Services and Technical Services Divisions in view of the Upgrade Programme, which will dedicate the greatest part of its funding to new beamlines and instrumentation development. The new division, together with a newly introduced project management system, will permit an enhanced effort, capable of responding to the instrumentation challenges set by the Upgrade Programme.

The main themes of instrumentation development for the next few years will be based on the integration of very different technical domains and the use of the most recent discoveries in nanotechnology. Integration of different characterisation techniques into the crowded environment surrounding the sample is one of the challenges of the entire programme. In 2008, an important breakthrough was made in this direction: a beamline specific atomic force microscope (AFM) was developed and has been tested on selected ESRF beamlines. The microscope is designed to visualise and position nanostructures, track the beam profile, and manipulate and exert force on the sample while doing X-ray experiments. In one of the first experiments, it has made the measurement of the Young's modulus possible for a single nanodot **[1]**.

The small dimensions of the atomic force microscope are advantageous for its installation in the beamlines, facilitating its integration (see **Figure 150**). Smaller devices naturally offer much higher cut-off frequencies, and hence faster responses. For these reasons they will be important players in the instrumentation theatre of the next few years. The first contribution in this chapter dedicated to methodologies and instrumentation, shows how a simple silicon cantilever can be used as a fast X-ray chopper. This simple experiment opens the way to the use of fast responding MEMS and NEMS in synchrotron radiation technology.

Miniaturisation is also the driving force of the second contribution where a laser beam is used to drill small holes in the gaskets of diamond anvil cells. The next two contributions are relevant to X-ray optics, one suggesting a method for easier retrieval of information on layered systems and the second showing again that silicon technology applied to synchrotron radiation can provide easy to use X-ray interferometry up to 100 keV. The last two contributions illustrate the range of instrumentation advances made possible by the close collaboration between the Macromolecular Crystallography Group and the various support teams. In the past years this close collaboration has led to the development of beamline automation that earned the Bessy Innovation Award for the teams involved. Their work has permitted the launch of remote access to the macromolecular crystallography beamlines, this is described in the final article.

***F. Comin***

**Reference**
[1] T. Scheler, M. Rodrigues, T.W. Cornelius, C. Mocuta, A. Malachias, R. Magalhães-Paniago, F. Comin, J. Chevrier, and T. H. Metzger, *Appl. Phys. Lett.* **94**, 023109 (2009).

# MEMS based high-frequency chopper

**Authors**
A. Siria (a,b), O. Dhez (c), W. Schwartz (a,b), G. Torricelli (d), F. Comin (c) and J. Chevrier (a).
*(a) Institut Neel, CNRS-Université Joseph Fourier, Grenoble (France)*
*(b) CEA/LETI-MINATEC, Grenoble (France)*
*(c) ESRF*
*(d) Department of Physics and Astronomy, University of Leicester (UK)*

Many experiments in physics, biology, chemistry and material science require short bursts of X-ray radiation to study the detailed time response of a sample under a particular excitation [1].

X-ray techniques are extremely important for the investigation of the chemistry and structure of materials. In a typical experiment, the system to be analysed is excited by a short X-ray burst and information about the response is obtained by studying the fluorescence emitted during the system's de-excitation. In a pump-probe experiment, the sample is pumped in a metastable state by laser excitation and a delayed X-ray pulse is used to monitor the time evolution of the system.

The duration of the X-ray pulse is critical to a pump-probe experiment. Since the timescale involved can be smaller than a microsecond, X-ray pulses with duration less than a microsecond are required. Short-duration X-ray bursts are produced when a continuous X-ray beam passes through a mechanical shutter that is open for a short time. The major limitations of rotating mechanical shutters are their relatively large size and the constraints imposed by the operating environment. For example, they may have to work under vacuum conditions, especially if a very short X-ray pulse is required.

A combination of X-ray techniques and micro-electro-mechanical systems (MEMS) technology has recently been demonstrated in a setup where a modulated X-ray beam was used to excite a mechanical system around its first order resonance [2]. We show here that the inverse mechanism can be used to modulate an X-ray beam.

Figure 151 shows the experimental setup. The mechanical system is a standard Si (100) atomic force microscope (AFM) cantilever with dimensions 300 x 35 x 2 µm. The cantilever displacement is measured by the interference between the light reflected from the end of a cleaved

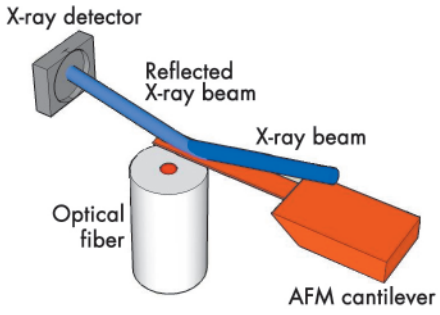


*Fig. 151:* Schematic representation of the experimental setup. The AFM cantilever (red) is used to modulate the X-ray beam (blue) impacting around the Bragg angle. The reflection of the X-ray beam is detected with a photodiode. The lever position is detected via the optical fibre (white).

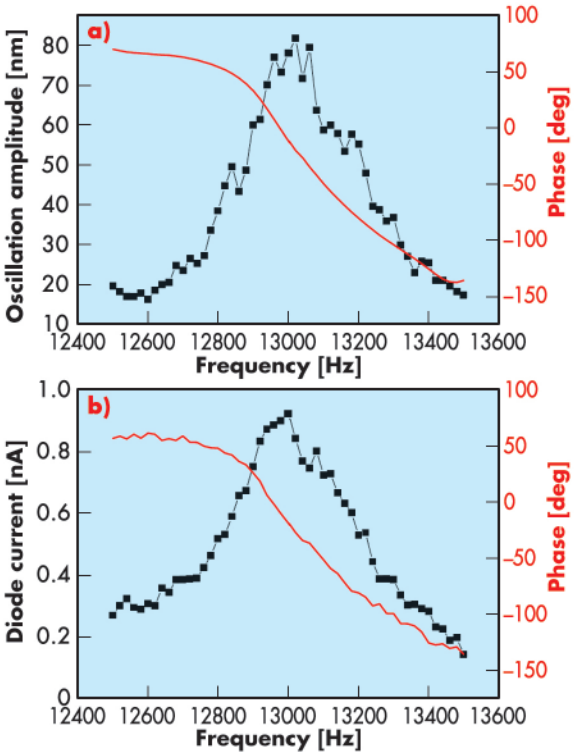


*Fig. 152:* **a)** Optically measured response of the AFM cantilever when it is excited around its first resonant frequency. **b)** Diode photo-current measured by the photodiode at 2θ Bragg position. In both **a)** and **b)** the black curve represents the oscillation amplitude and the red curve the phase lag.

optic fibre and the beam reflected by the back of the lever. When at rest, the cantilever is in Bragg conditions and the photodiode will detect a constant photon flux. Whereas, when the AFM lever is excited by a piezo-electric ceramic, the X-ray incidence angle is modified by the lever motion. If the lever oscillation amplitude is larger than the Bragg peak width, the cantilever will periodically sweep through the Bragg conditions. Therefore, a periodically-modulated current will be measured at the output of the photodiode. The amplitude of the photon flux oscillation is thus directly controlled by the oscillation amplitude of the cantilever.

The experiment was carried out at the surface X-ray diffraction (SXRD) beamline, **ID03**. The incoming X-ray beam set to 18.98 keV impinged on the cantilever at rest at Bragg condition and the X-ray photo detector was positioned at the corresponding 2θ angle. The spot size of the incoming beam was 50 x 50 µm with $10^{10}$ ph/s. **Figure 152a** shows the cantilever oscillation amplitude and phase lag as a function of frequency when the mechanical system is mechanically excited at the resonance. **Figure 152b** shows the current (amplitude and phase) at the output of the X-ray photodiode as a function of the frequency.

We have shown that an X-ray beam can be modulated in intensity by an oscillating AFM lever. In this experiment the X-ray beam was chopped at 13 kHz. This operating frequency was related to the resonance frequency of the AFM lever used, however it could easily be increased to values much higher than 100 kHz by using others types of cantilever. Specific setups based on MEMS could be designed so that efficient X-ray choppers could operate at frequencies in the MHz regime, potentially opening a wealth of new experiments based on X-ray examination of time dependent processes requiring high repetition speed.

**References**
[1] C. Rischel, *et al., Nature* **390**, 490-492 (1997).
[2] A. Siria, *et al., Nanotechnology* **19**, 445501 (2008).

# Laser drilling of DAC gaskets

**Authors**
P. van der Linden (a), M. Mezouar (a), N. Guignot (b), Y. Dabin (a), J. Jacobs (a) and D. Gibson (a).
*(a) ESRF*
*(b) Synchrotron SOLEIL (France)*

Diamond anvil cells have been used increasingly on synchrotron X-ray beamlines over the past decade due to the pressure and temperature range they permit, and the match between available sample volume and beam size. As the availability of micrometre sized beam grows, smaller samples may be used with smaller diamond culets in order to reach higher pressures, up to and above one megabar. This means of course that the hole for the sample in the gasket which is clamped between the two diamonds also has to follow the same reduction in size. The classical method of drilling the hole in the gasket by electro-erosion becomes increasingly difficult when the hole size goes below 100 micrometres. The laser drill we have developed allows the drilling of holes with sizes ranging from 25 µm up to 1 mm with a precision of 2 µm. Additionally, in contrast to electro-

erosion drilling that can only be used for metals, the laser drill can be used for materials such as ceramics, salts and even diamond.

The setup (**Figure 153**) uses a pulsed Nd:$YVO_4$ laser at a wavelength of 1064 nm which was selected for its short pulse length of 10 ns. This allows more efficient ablation of the material and reduces the heat affected zone. A standard beam expander and microscope objective focus the laser beam on the gasket. The gasket is fixed on a high precision spindle which was developed in house. The first alignment stage of the spindle is for pre-alignment by means of simple screws; the second alignment stage is a rotating XY piezo mounted on the axis; the mechanical support consists of the bearing cage, motor and slip ring contacts. The combination of axis and bearing cage was designed to compensate for temperature changes; the axis is belt driven by an offset motor to minimise the mechanical noise. Special care was taken to optimise the visualisation; the constant focus zoom allows on screen images from 900 to 120 micrometres in diameter.

The laser drill was first developed to gain time drilling micro-holes for multimegabar X-ray experiments. One of the very first experiments requiring the use of the laser drill was run in parallel on **ID27** and **ID24** for the study of phase transformations at the deep earth pressure and temperature conditions (**Figure 154**). On the high pressure beamline **ID27** the samples were synthesised *in situ* by laser heating, using X-ray diffraction to verify the crystalline structure. In the second part of the experiment the oxidation state of iron was measured by EXAFS on the dispersive beamline **ID24**.

New applications have also become possible: the use of non metallic materials in built up gaskets (**Figure 155**; S. Petitgirard / ID22; V. Giordano / ID16; G. Garbarino / ID27), cutting small samples (A. Bosak / ID28). Some tests have been done on the drilling of pinholes which are to be used as beam cleaning elements. Future possibilities include drilling of multiple holes in one gasket to use multiple samples or to separate the pressure measurement ruby from the sample.

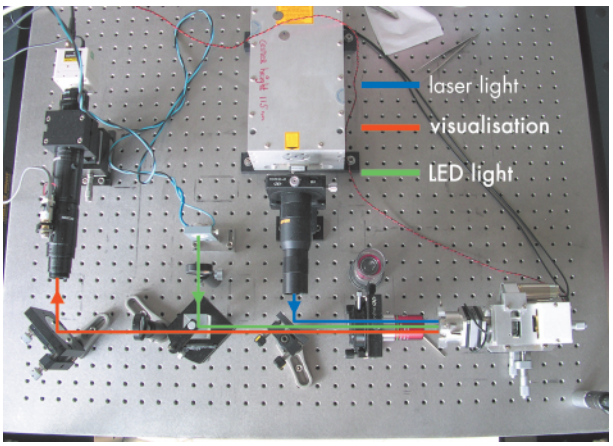


*Fig. 153:* Setup of the laserdrill.

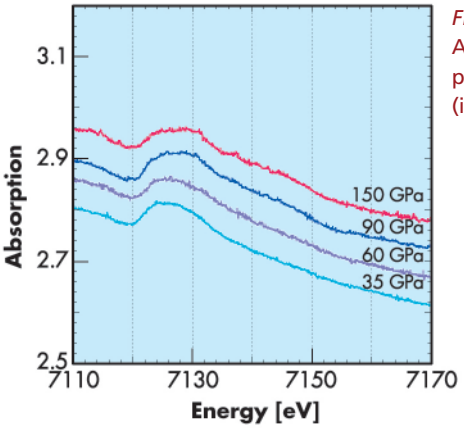


*Fig. 154:* Fe K-edge XANES analysis of Al-bearing(Mg,Fe)$SiO_3$ Perovskite and post Perovskite phases up to 1.5 Mbar (image courtesy D. Andrault).

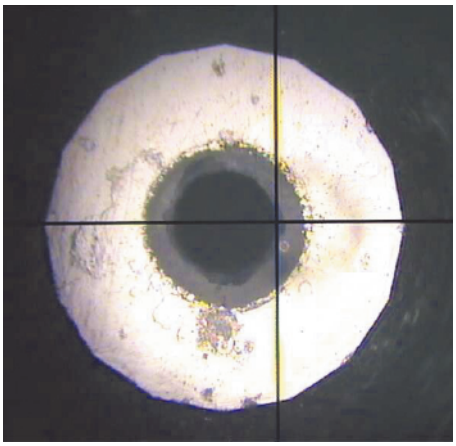

*Fig. 155:* Gasket drilled / filled with NaCl / drilled to avoid contact between the molten Tellurium sample and Rhenium gasket (courtesy V. Giordano / ID16). The hole in the centre is dark, the salt is the grey ring. The bigger white ring is the imprint of the diamond, 600 micrometre in size.

The authors would like to thank their colleagues who have made the examples available for this highlight: S. Pascarelli, V. Giordano. They also would like to thank R. Boehler of the Max Planck Institute who has built the first laser drill; P. Duboc for help with the drawings of the spindle and I. Snigireva for electron microscope work.

**Principal publications and authors**
I. Kozhevnikov (a), L. Peverini (b) and E. Ziegler (b), *Optics Express*, **16**, 144 (2008);
*J. Appl. Phys*, **104**, 054914 (2008).
*(a) Institute of Crystallography, Moscow (Russia)*
*(b) ESRF*

# *In situ* X-ray reflectometry can solve the phase problem

X-ray reflectometry is widely used to determine the depth distribution of the dielectric constant in layered systems. This involves an inverse problem, where one attempts to infer the causes from observation of the effects. Solving it may be hampered by the ambiguity in the solution, essentially due to the absence of information about the phase of the amplitude reflectivity [1].

We have developed a method of exact phase retrieval that is applicable to a layered film for which the reflectivity has been measured *in situ* during growth. In the simplest case, the angle between the X-ray beam and the film surface is fixed, while, at a point $t$ in time, both the reflectivity $R(t) = |r(t)|^2$ and the derivative $dR/dt$ are measured. In this case, both the real $\mathcal{R}[r(t)]$ and imaginary $\mathcal{I}[r(t)]$ parts of the amplitude reflectivity $r(t)$, hence the phase, can be pinpointed exactly.

Using the first order differential equation describing the variation of the amplitude reflectivity with the film thickness we deduced the following accurate equation to describe the variation of the reflectivity with time $dR/dt = A(q, f, R)\,\mathcal{R}[r(t)] + B(q, f, R)\,\mathcal{I}[r(t)]$ (Eq. 1), where $A$ and $B$ are real functions that do not explicitly contain the film's parameters. They only depend on the reflectivity $R(t)$ and on the incident flux of particles $q(t)$ and their chemical composition via the complex atomic scattering factor $f(t)$. $q$ and $f$ can vary with time.

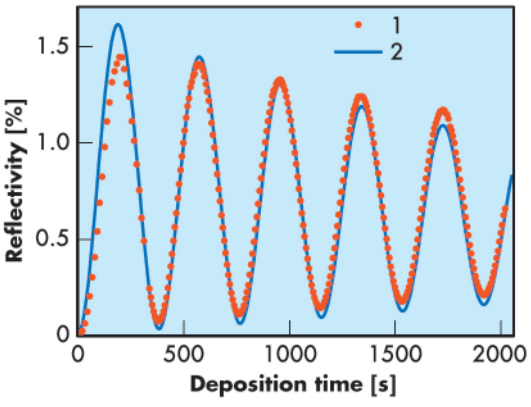


*Fig. 156:* Reflectivity versus deposition time from a growing tungsten film measured at an X-ray energy of 17.5 keV and with a grazing angle θ = 0.5° (dots). The solid curve was calculated assuming constant density in the depth of the film.

When performing *in situ* reflectivity measurements $R$ and $dR/dt$ are known so that Eq. (1) is no longer a differential equation for the function $R(t)$. As a linear algebraic equation for the real and imaginary parts of the amplitude reflectivity, Eq. (1) can now be solved together with the obvious relation $R(t) = \{\mathcal{R}[r(t)]\}^2 + \{\mathcal{I}[r(t)]\}^2$ (Eq. 2) to determine both $\mathcal{R}[r(t)]$ and $\mathcal{I}[r(t)]$ directly from the experimental data, without using any model for describing the reflection from the media.

Thus, knowing $R$ and $dR/dt$ at a point $t$ in time we determine the phase of the reflected wave at the same point, *i.e.*, the phase can be found without any knowledge of the pre-history of the structure growth, and independent of the chemical composition inside the structure, the presence of interlayers, and of the substrate composition. The equation was deduced while making two important assumptions: (a) the material polarisability is proportional to the density, and (b) the dielectric permeability inside the film remains unchanged.

The reflectivity (17.5 keV X-ray energy, 0.5° grazing angle) measured *in situ* at the **BM05** beamline [2] during the growth of a tungsten film on a Si substrate is shown in **Figure 156**. The incident flux $q = 7.26 \cdot 10^{13}$ atom/cm$^2$/s results in a typical growth rate of 12 pm/s. The measurements were performed every 7 s which corresponds to an increase of the film thickness of about 80 pm, equivalent to one third of a monolayer of tungsten. The phase of the amplitude reflectivity extracted from the experimental curve $R(t)$ is presented in **Figure 157**. As Eq.(2) has a quadratic form, there are two possible solutions for the phase retrieval problem (red curves 1 and 2). Curve 3 in **Figure 157** and curve 2 in **Figure 156** were calculated using the simplest model possible, *i.e.*, assuming a constant film density with depth. Since curves 1 and 3 in **Figure 157** are close to each other, we selected curve 1 as the solution to the phase retrieval problem. Nonetheless, both the

reflectivity and the phase inferred from the experimental data differ noticeably from the model calculation, suggesting that this simplest model is not fully correct.

We also reconstructed the depth-distribution of the tungsten density using the approach described in [1], which is based on the analysis of the angular dependence of the reflectivity measured after deposition of a 24.6 nm thick film. Two particular features can be clearly observed on the density profile: (a) the reduced density as compared to bulk tungsten in a region about 2 nm thick near the substrate and (b) the exponential decrease of tungsten concentration over a depth of about 1 nm within the Si substrate, probably caused by diffusion and implantation processes. These two features permit a complete explanation of both the reflectivity and the phase curves.

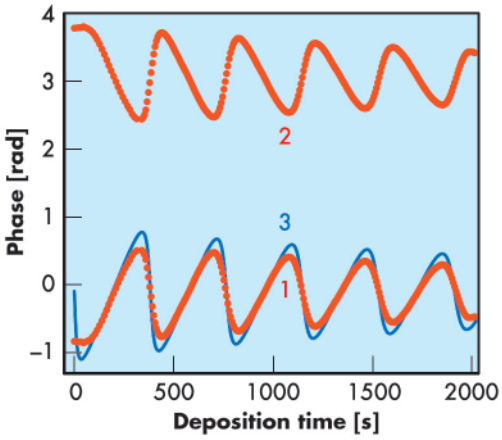


*Fig. 157:* Solutions of the phase retrieval problem (curves 1 and 2) found directly from the experimental curve shown in Figure 156. Curve 3 shows the phase evolution calculated assuming a uniform tungsten film with constant density. For illustrative purpose, we assumed the phase to vary within the $[-\pi / 2, 3\pi / 2]$ interval.

In the future, we plan to investigate the possibility of performing a complete angular reflectivity curve $R(\theta, t)$ instead of a single angular value at any point in time. That would allow us to find the phase versus angle, to solve the inverse problem of X-ray reflectometry more correctly, and to analyse the variations of the dielectric constant profile with time.

**References**
[1] I.V. Kozhevnikov, *Nucl. Instrum. Methods A* **508**, 519 (2003).
[2] L. Peverini, E. Ziegler, T. Bigault, I. Kozhevnikov, *Phys. Rev. B* **72**, 045445 (2005).

## Hard X-ray interferometer based on a silicon refractive bi-lens system

**Authors**
A. Snigirev (a), V. Kohn (b), I. Snigireva (a), M. Grigoriev (c), S. Kuznetsov (c), V. Yunkin (c), T. Roth (a), C. Detlefs (a) and G. Vaughan (a).
*(a) ESRF*
*(b) Kurchatov Instititute, Moscow (Russia)*
*(c) Institute of Microelectronics Technology, Chernogolovka (Russia)*

Optical interferometers are widely used for diagnostics and metrology because of the availability of lasers with a high degree of spatial coherence. X-ray interferometry, however, has long been hampered by the lack of coherent sources. To circumvent this problem, the first X-ray interferometers used the so-called perfect crystal optics in the regime of dynamical diffraction. Due to the coherent interaction of the X-rays with a three-dimensional crystal structure, the crystal becomes an intrinsically coherent device and therefore does not require spatial coherence of the incident radiation. The classical example is the Bonse-Hart interferometer, which utilises both transmission (Laue) and surface reflection (Bragg) diffraction components.

Nowadays, the widespread availability of bright X-ray sources with sufficiently large spatial coherence, such as third-generation synchrotrons, allows researchers to observe interference by division of the wave front, similar to the classical Young's experiment. Recently a Fresnel double slit, a Fresnel double prism and a Fresnel double mirror were applied to measure the spatial coherence of synchrotron beams.

Following the successful development and application of refractive optics for high energy X-rays [1,2], we have constructed an X-ray bi-lens interferometer similar to the Billet split

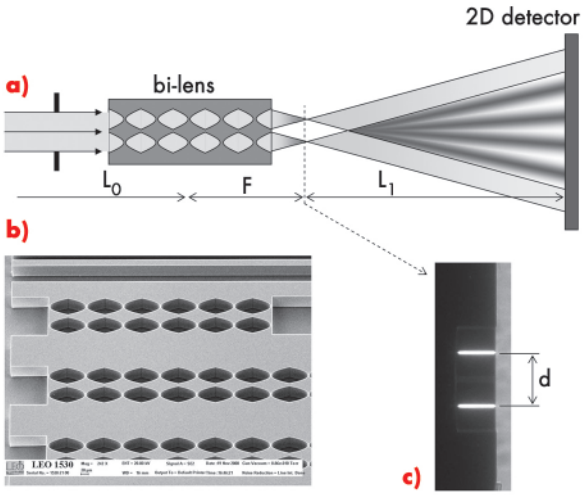


*Fig. 158:* **a)** Schematic drawing of the experimental set-up used for the bi-lens test. **b)** Scanning electron microscope micrograph showing a fragment of silicon bi-lenses chip. **c)** Image of the bi-lens foci recorded at a distance $F$ = 35 mm shows the lenses split distance $d$ = 60 µm.

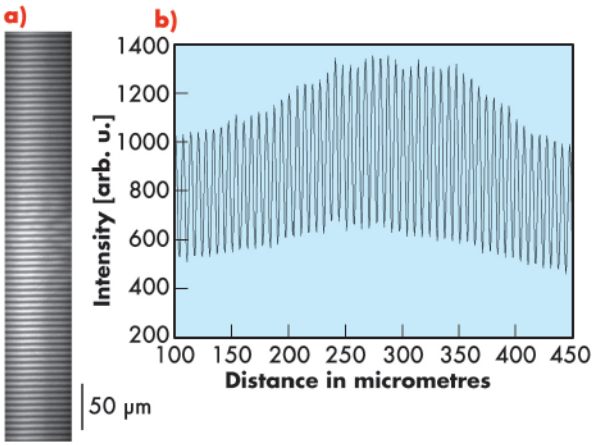


*Fig. 159:* **a)** Interference pattern obtained using the bi-lens interferometer of Figure 158, recorded at a distance 4 m with monochromatic beam at energy E = 12 keV. **b)** Intensity variation for a line through the centre of the fringe pattern shows a visibility (contrast) of approximately 40% corresponding to a source size S = 45 µm vertically (FWHM).

lens in classical optics. The schematic diagram of our X-ray bi-lens interferometer is shown in **Figure 158**. It consists of two identical parallel planar compound refractive lenses (CRLs) separated by a certain distance, *d*. Each lens produces an image of the source. When the lens split distance *d* is smaller than the spatial coherence length of the incoming beam, these images are diffraction limited and can be treated as coherent secondary sources. At a distance of more than twice the lens focal distance, *F*, the radiation cones diverging from these coherent secondary sources overlap, and interference occurs in the region of superposition (see **Figure 158**). Identically to the Fresnel double slit, the visibility (or contrast) of the recorded interference pattern can be used as a measure of the degree of a spatial coherence of the incident beam, or of an equivalent effective source size.

A silicon chip with a set of different linear (1D) bi-lenses was manufactured using semiconductor microfabrication technology (**Figure 158b**). The length of each single, individual lens was 100 µm and the aperture was 50 micrometres. The radius of the parabola apex was 6.25 µm. The compound refractive lenses were separated by a distance $d$ = 60 µm.

The bi-lens interferometer was tested at beamline **ID06**. The liquid -nitrogen cooled Si-111 double crystal fixed exit monochromator (manufactured by CINEL, Italy) was used at an X-ray energy of 12 keV. The Si bi-lens chip was mounted on the microoptics test bench optics stage at a distance $L_0$ = 55 m from the source.

All measurements of bi-lens interference patterns were made in a vertical plane. The interference patterns were recorded by means of the high resolution X-ray CCD Sensicam camera with a spatial resolution about 1.3 µm (0.645 µm pixel size). The typical exposure time was 5-10 sec. during 16-bunch filling mode.

The observed interference pattern is shown in **Figure 159**. The fringe spacing or peak-to-peak width of the fringes is given by $\Lambda = \lambda L_1/d$, where $\lambda$ is the wavelength, and $L_1$ is the distance from the bi-lens focus plane to detector plane. The measured spacing, $\Lambda$ = 6.25 µm, is in very good agreement with calculations. The quality of the fringes produced by a bi-lens system can be described quantitatively using the visibility $V = (I_{max} - I_{min})/(I_{max} + I_{min})$, where $I_{max}$ and $I_{min}$ are the irradiances corresponding to the maximum and adjacent minimum in the fringe system. It is easy to show that the visibility $V$ is directly related to the source size, $S$, as follows:

$$S = \frac{\Lambda L_0}{L_1}\left(-\frac{\ln V}{3.56}\right)^{1/2}$$

The measured visibility was close to 40%, corresponding to an effective source size in the vertical direction of about 45 µm (FWHM).

The bi-lens interferometer presented here has major advantages over existing methods. Manufacturing of micro-slits, mirrors and prisms for hard X-rays is a challenging technological task considering the requirements to the surface and shape (edges) quality. Whereas for silicon planar lenses, the well-developed microelectronics technology is used providing superior lens quality **[3]**. Compared to slits, mirrors and prisms, the compound refractive bi-lens system can be used at high photon energies up to 100 keV.

The applications of the bi-lenses are not limited to coherence characterisation. They can easily be extended to coherent imaging techniques. As with a classical interferometer, the bi-lens interferometer generates two coherent beams separated in space and then coherently recombines them

**References**

[1] A. Snigirev, V. Kohn, I. Snigireva, B. Lengeler, *Nature* **384**, 49 (1996).

[2] V. Aristov, M. Grigoriev, S. Kuznetsov, L. Shabelnikov, V. Yunkin, T. Weitkamp, C. Rau, I. Snigireva, A. Snigirev, M. Hoffmann, E. Voges, *Appl. Phys. Lett.* **77**, 4058 (2000).

[3] A. Snigirev, I. Snigireva, M. Grigoriev, V. Yunkin, M. Di Michiel, S. Kuznetsov, G. Vaughan, *SPIE* **6705**, 670506-1 (2007).

producing the interference pattern. One can easily insert a sample into one of the beams while they are separated. Any interaction with the beam would then induce significant changes in the interference pattern. From the new phase pattern, one should then be able to extract information concerning the nature and degree of interaction of the sample with the beam, leading, eventually, to a holographic reconstruction of the sample.

# Capturing the shape of macromolecular crystals in 3D

Absorption correction algorithms have been used for decades, in particular by crystallographers. The first approaches to reduce the effects of absorption were made by physically reshaping the sample to reach simple geometries, such as spherical or cylindrical, so that tabulated corrections could be applied easily. When the crystal could not be reshaped, Albrecht's [1] method was widely used, it relies on a precise description of the crystal geometry in order to determine the correction graphically.

However, macromolecular crystallography (MX) demanded a different approach. During MX experiments an undefined volume of cryoprotectant buffer is used to hold the macromolecular crystal within a nylon or Kapton loop prior to vitrification and data collection at cryotemperatures (100 K). Such a complex system, often with highly irregularly shaped crystals, is almost impossible to characterise manually with a description of all of the elements contributing to the absorption process, particularly the liquor surrounding the crystal. Most scaling software used in MX today employs an entirely empirical function which minimises the differences between symmetry-equivalent reflections to correct for absorption effects (as well as for the correlated crystal decay and beam effects). With the use of increasingly fragile samples having high radiation sensitivity, complete and redundant data sets may not be obtainable from a single crystal, in turn defeating the fully empirical method. Other methods are therefore needed to optimise such data sets – of particular importance where small signals are being recorded, such as anomalous data from sulphur or phosphorus atoms that commonly occur naturally in proteins or nucleic acids.

Studies on two methods to supply three-dimensional shape information recorded directly from the cryocooled crystals in vitrified buffer and supporting loop have been carried out. One uses the standard visible-light microscope systems installed on all of the ESRF MX beamlines to build a three-dimensional model based on reconstruction from shape-from-silhouettes of the crystal, buffer and loop components; the second uses X-ray microtomography to determine the three-dimensional shape of the crystal within its surrounding liquid and sample holder.

## Visible light silhouettes

The key aim behind this method is to provide a routine system to build three-dimensional models of the crystal-buffer-loop system by exploiting a standard on-axis sample visualisation system that incorporates a high-quality on-axis camera system for sample alignment. As part of this

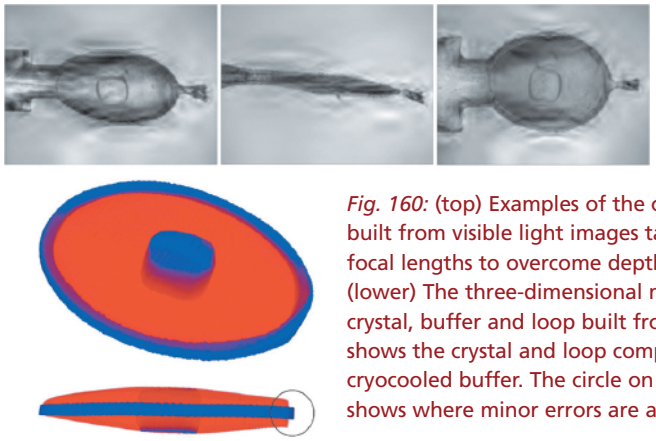

*Fig. 160:* (top) Examples of the composite images built from visible light images taken at different focal lengths to overcome depth-of-field issues; (lower) The three-dimensional model of the insulin crystal, buffer and loop built from the images. Blue shows the crystal and loop components, and red the cryocooled buffer. The circle on the lower image shows where minor errors are apparent in the model.

**Principal publications and authors**

R.M.F. Leal (a,b,c), S.C.M. Teixeira (b,c), V. Rey (a), V.T. Forsyth (b,c) and E.P. Mitchell (a,c); *J. Appl. Cryst.* **41**, 729-737 (2008);
S. Brockhauser (d), M. Di Michiel (a), J.E. McGeehan (d), A.A. McCarthy (d) and R.B.G. Ravelli (d,e); *J. Appl. Cryst.* **41**, 1057-1066 (2008).

*(a) ESRF*
*(b) ILL (France)*
*(c) EPSAM and ISTM, Keele University (UK)*
*(d) EMBL, Grenoble Outstation (France)*
*(e) Leiden University Medical Center (LUMC) (The Netherlands)*

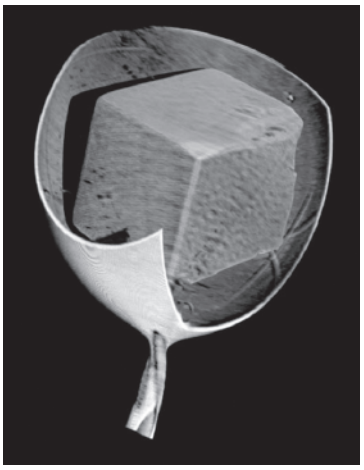

*Fig. 161:* Full three-dimensional reconstruction of a vitrified lysozyme crystal and surrounding cryocooled buffer from X-ray tomography.

development, a software suite (called "3DAC") was developed specifically to reconstruct the 3D model and calculate absorption correction factors using the 2D images from the camera.
A feasibility study was carried out on an insulin crystal from which diffraction data were collected at low energy (6 keV). A high quality three-dimensional model was constructed using just 18 visible-light images at different rotation angles of the sample (**Figure 160**) with the loop, buffer and crystal silhouettes determined using a mixture of automatic and manual procedures. Absorption corrections were determined based on simulated beam paths through the 3D model that consisted of the three separate loop, buffer and crystal components. The corrections were applied to each reflection (whether partially or fully recorded) before merging.

A comparison of the reduced data resulting from the standard empirical approach to scaling MX data and application of the absorption corrections calculated as above showed a distinct and significant improvement in the data when our corrections were applied. Metrics such as the $R_{merge}$, signal:noise ratio and peak heights in phased anomalous difference maps all improved when data having a redundancy of less than approximately three was used. For example, in the best cases, average peak heights corresponding to sulphur positions in the phased anomalous map improved by 10% to 60% depending upon the redundancy of the data (from higher to lower redundancy). The exact effect observed depended on the wedge of diffraction data used, *i.e.* the orientation of the crystal-loop system. However, the best data were consistently obtained with application of the quantitative absorption correction.

## X-ray microtomography

In X-ray tomography, a 3D reconstruction of the sample is obtained after collecting parallel-beam X-ray images at a series of rotation angles. At higher energies (> 5 keV), macromolecular samples typically show very little absorption contrast between the vitrified crystal and its surrounding liquid. Fortunately, one can exploit phase contrast which results in a sample to detector distance-dependent enhancement of the edges between crystal, liquor and sample support.

We have successfully applied the technique of X-ray microtomography to obtain 3D reconstructions of a variety of protein and DNA crystals (**Figure 161**). The great advantage of the technique is that a true "X-ray" view of the crystal is obtained, showing details such as cracks, crystal splitting and satellites, bent crystals and other imperfections. The reconstruction algorithms benefit from existing methods such as those used in electron tomography.

X-ray microtomography leads to superior views of the macromolecular sample and its support compared to visible-light methods, however, it does require a special imaging setup.
The X-ray beam has to fully bathe the sample, and a carefully aligned X-ray imaging detector is needed. We have demonstrated that such a setup, which is default on imaging beamlines, can also be successfully installed and used on a macromolecular crystallography beamline. The doses needed to obtain X-ray tomographic data could stay within a few percent of the Henderson limit, especially if one does not require sub-micrometre resolution. This would make the technique amenable for absorption correction as well as for crystal alignment.

In conclusion, both studies have shown the feasibility of producing and using three-dimensional models of macromolecular crystals and their supporting buffer and loop to improve diffraction data quality. Each method has its own pros and cons, but give complementary information. The tomography method gives stunning models, accurate down to the tiniest details but requires a specific, purpose-built installation. The visible-light method uses standard beamline equipment but produces a model showing only the overall bulk of the crystal, buffer and loop. The methods should provide a clear advantage in situations where data acquisition is limited by crystal lifetime and should

form an essential component of sample characterisation on future beamlines, as part of the overall complete characterisation of the macromolecular crystal. Three-dimensional shape information can also have a practical impact on the design of data collection strategies for X-ray diffraction experiments and for neutron studies. Further work is now concentrating on expanding the number of test cases and comparing the absorption corrections obtained from the two modelling approaches. Given the increasing interest in radiation damage and the study of ever more sensitive macromolecular systems, the time is now right to revive the implementation of fully non-empirical absorption corrections through easy-to-use (even automatic) methodologies.

**Reference**
[1] G. Albrecht, *Rev. Sci. Instrum.*, **10**, 221–222 (1939).

# New technical developments at the ESRF Macromolecular Crystallography Group beamlines

**Authors**
A. Round (a), P. Pernot (b) and G. Leonard (b), on behalf of the ESRF/EMBL Joint Structural Biology Group (JSBG)
*(a) EMBL Grenoble Outstation*
*(b) ESRF*

## ID14-3: A New BioSAXS beamline

In January 2008 work began on the conversion of **ID14-3** from a beamline dedicated to single-wavelength macromolecular crystallography experiments to one dedicated to small-angle X-ray scattering from solutions of biological macromolecules (BioSAXS).

The new facility is intended to complement already existing SAXS facilities at the ESRF that are highly oversubscribed for a wide variety of experiments in the fields of biology, chemistry, materials science, etc. With rapidly-growing interest in BioSAXS from the ESRF's MX User Community, beam-time on the existing resources was set to become even more sought after. Creating a dedicated BioSAXS facility will alleviate the high rate of over-subscription, improve the throughput of such experiments by removing the need for the station to be optimised for every new user group, and result in more beam-time on the ESRF's existing SAXS end-stations being available for experiments in other fields. An additional benefit of building this new facility at the ESRF is the creation of a collaboration with the already established small-angle neutron scattering (SANS) facility at the ILL. Our intention is to allow users, via a single proposal, to access both facilities for appropriate experiments. This will allow the complementary information provided by neutron scattering (*i.e.* contrast variation) and X-ray scattering to be obtained in a single visit to the Grenoble site.

The conversion of ID14-3 has been undertaken in stages. The first of these allowed testing of the proposed design and proof-of-principle experiments before the major renovation of the experimental hutch was undertaken. New beam conditioning hardware and redesigned attenuators have been installed upstream of the original ID14-3 focusing optics in order to minimise parasitic scattering.
To this end a "mini" hutch (the first of its type at the ESRF) has been built in the ID14 mezzanine (**Figure 162**) and houses new beam defining slits, the experimental shutter and beam monitoring devices. The experimental hutch has also been refitted and now


*Fig. 162:* a) The ID14-3 "mini" hutch installed under the mezzanine of ID14; b) the newly refurbished ID14-3 BioSAXS experimental hutch.

contains a 4 m long marble table which supports the new experimental equipment. Two pairs of guard slits are mounted prior to the sample exposure unit (quartz capillary tube mounted in vacuum). An evacuated flight tube with variable length (0.5 to 2.5 m) and a fully-motorised beam-stop sits between the sample environment and a (Vantec-2000) 2D gas filled-detector (**Figure 162**). The commissioning phase of the new BioSAXS facility is now complete and, following positive feedback from a small number of collaborating users during October 2008, the first official experiments took place in November 2008.

The ultimate aim of the conversion of ID14-3 to a dedicated BioSAXS resource is to offer a facility with automatic sample loading/unloading, data collection, processing (conversion of a 2-D image to a normalised 1D X-ray scattering profile, **Figure 163**) and analysis. This will (rapidly) provide users with standard data concerning the size (radius of gyration, maximum dimension and volume) and molecular weight of samples and allow on-the-fly *ab initio* shape reconstruction in order to provide feedback enabling data collection strategies to be optimised. Automation of sample loading will be incorporated on the beamline in the coming months using a device being constructed in a collaboration between the EMBL (Grenoble and Hamburg outstations) and the ESRF. Automated data analysis will be implemented following the model of the SAXS facility at X-33, EMBL Hamburg). Future plans extend to allowing remote access to the new facility. This will be based on the system currently in use on the ESRF's MX end-stations, which is described below.

## Remote access to the ESRF's MX facilities

Modern Structural Biology calls for short but frequent access to synchrotron radiation based macromolecular crystallography facilities (maximum length of experimental session ~6 shifts). For many of the ESRF's external users (both academic and industrial) travel to/from Grenoble, as well as being stressful and tiring, often takes up more time than the experiment itself. Remote access to the ESRF's MX beamlines would mean much less travelling for users. For this, and a number of other reasons, we have developed remote data collection protocols, broadly reflecting the needs of our external users. The modes of remote access currently offered are as follows:

**1. Data collection service**: Here, instructions concerning the data that users would like to be collected from their samples ('diffraction plans') are submitted beforehand via the laboratory information management system (LIMS) ISPyB **[1]** (http: //ispyb.esrf.fr/). ESRF staff then operate the beamlines and take the majority of the decisions concerning data collection. External users can follow progress in real-time using ISPyB and are able to intervene with supplementary instructions should they wish to. This type of remote access is highly labour intensive for in-house staff and so offered only to industrial customers via the well-established MXpress service (see http://www.esrf.fr/Industry).

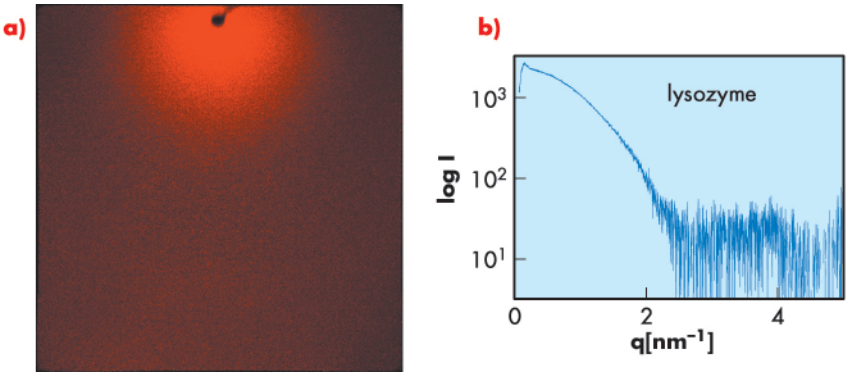


*Fig. 163:* Lysozyme SAXS data collected at ID14-3: **a)** 2-dimensional detector image and **b)** the resulting 1-dimensional X-ray scattering profile.

**2. Full remote control:** In this mode external users can also avoid travelling to Grenoble by sending samples to the ESRF via a courier company. On the day of the experimental session, the samples are loaded into the robotic sample changers, available on all our MX beamlines, by ESRF staff. The external users connect to the beamline control computer and, after having been given control by the experiment Local Contact, control the beamline from the home laboratory in the same manner as if they were using the beamline locally. ESRF beamline staff remain on call to help in case of problems.

**3. 'Hybrid' control**: In this mode, only a few of the users from an external group travel to the ESRF for a scheduled experimental session. Those remaining in the home laboratory can collect data on the samples that they have contributed to the session via remote control of the beamline. In this mode of remote access, sample changer loading and other ancillary tasks are performed by those users who have travelled to Grenoble.

For the hybrid and full remote control modes, reliable external access to the beamline control computers is essential. For this we use NoMachine/NX software (http://www.nomachine.com). This allows access to an ESRF firewall computer from which remote users can then access and login to the relevant beamline control computer. The MxCuBE Graphical User Interface (GUI) **[2]** and beamline control applications can then be started. These applications are displayed and manipulated in real-time on the user's local workstation.

To allow secure remote access to the MX beamlines we developed a master/slave version of MxCuBE (**Figure 164**). Master instances of the GUI are accessed by beamline staff to set up the beamline and to hand over control to a slave instance of the GUI running from a remote location. The master instance of MxCuBE allows beamline staff to follow the experiment and take back control or intervene when necessary. Slave instances of MxCuBE have a limited scope and in particular, cannot take control from any other instance of the beamline GUI.

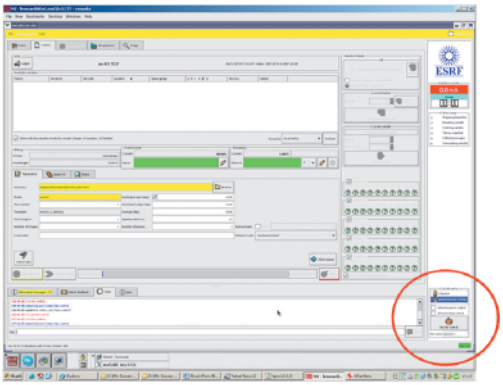

*Fig. 164:* A remote instance of the MxCuBE beamline control GUI. The brick allowing transfer of control and an overview of all other mxCuBE instances running at the beamline is circled.

*Fig. 165:* J. Turkenburg (right) and S. Hart collecting data on ID14-2 from their office at the University of York.

However, it is possible for slave instances to view all other instances of MxCuBE running on a particular beamline, to transfer control or to communicate with them via a 'chat' tab.

Following initial tests with the help of groups from the University of York (**Figure 165**) and the University of Marseilles, hybrid and full remote control access modes were made generally available to external users of the MX beamlines in March 2008. Currently, ~25% of academic and 30% of industrial experimental sessions involve one of these two modes of remote access. We expect these figures to increase rapidly and that remote access will soon become the principal gateway to the ESRF's MX beamlines for our larger user groups.

**References**

[1] A. Beteva, S.M. McSweeney, *et al.*, *Acta Cryst.* **D62**, 1162 (2006).

[2] G. Leonard, J. McCarthy, D. Nurizzo, X. Thibault, *Synchrotron Radiation News* **20**, 18 (2007).

# Accelerator and X-ray Source

## Introduction

Throughout 2008, the Accelerator and Source Division has continued its efforts to ensure reliable operation as well as preparing for the forthcoming upgrade. A number of developments have been carried out, the most important of these are described hereafter.

## Beam parameters of the storage ring

**Table 2** presents a summary of the characteristics of the storage ring's electron beam.

**Table 3** gives the main optic functions, electron beam sizes and divergences at various source points. For insertion device source points, the beta functions, dispersion, sizes and divergences are calculated in the middle of the straight section.

Two representative source points for each type of bending magnet (even or odd number) have been selected, corresponding to observation angles of 3 and 9 mrad from the exit. The bending magnets are such that the magnetic field is 0.4 T and 0.85 T at the tangent point where the radiation is extracted at 3 and 9 mrad angles, respectively. Electron beam profiles are Gaussian and the size and divergence are presented in terms of rms quantities. The associated full width half maximum sizes and divergences are 2.35 times higher. Horizontal electron beam sizes and divergences are given for the uniform filling modes

*Table 2:* Principal characteristics of the electron beam.

| | | |
|---|---|---|
| Energy | [GeV] | 6.03 |
| Maximum current | [mA] | 200 |
| Horizontal emittance | [nm] | 4 |
| Vertical emittance (minimum achieved) | [nm] | 0.025 |
| Revolution frequency | [kHz] | 355 |
| Number of bunches | | 1 to 992 |
| Time between bunches | [ns] | 2.82 to 2816 |

| | | Even ID (ID02, ID06...) | Odd ID (ID01, ID03...) | Even BM (BM02, 4,...) 3 mrad | Even BM (BM02, 4,...) 9 mrad | Odd BM (BM01, 3,...) 3 mrad | Odd BM (BM01, 3,...) 9 mrad |
|---|---|---|---|---|---|---|---|
| Magnetid Field | [T] | Variable | Variable | 0.4 | 0.85 | 0.4 | 0.85 |
| Horiz. beta functions | [m] | 37.5 | 0.3 | 1.3 | 0.9 | 2.1 | 1.6 |
| Horiz. dispersion | [m] | 0.144 | 0.033 | 0.059 | 0.042 | 0.088 | 0.073 |
| Horiz. rms e- beam size | [µm] | 415 | 51 | 95 | 75 | 131 | 112 |
| Horiz. rms e- divergence | [µrad] | 10.3 | 108 | 115 | 111 | 102 | 97.4 |
| Vert. beta functions | [m] | 3.0 | 3.0 | 41.2 | 41.7 | 31.6 | 31.7 |
| Vert. rms e- beam size | [µm] | 8.6 | 8.6 | 32 | 32 | 28 | 28 |
| Vert. rms e- divergence | [µrad] | 2.9 | 2.9 | 1.3 | 1.3 | 0.9 | 0.9 |

*Table 3:* Beta functions, dispersion, rms beam size and divergence for the various source points.

| Filling pattern | | Uniform | 7/8+1 | Hybrid | 16-bunch | 4-bunch |
|---|---|---|---|---|---|---|
| Number of bunches | | 992 | 870 | 24x8+1 | 16 | 4 |
| Maximum current | [mA] | 200 | 200 | 200 | 90 | 40 |
| Lifetime | [h] | 75 | 65 | 30 | 16 | 9 |
| Rms energy spread | [%] | 0.11 | 0.11 | 0.11 | 0.12 | 0.16 |
| Rms bunch length | [ps] | 20 | 20 | 25 | 48 | 55 |

*Table 4:* Current, lifetime, bunch length and energy spread for a selection of filling modes.

and apply to almost all filling patterns except for the single bunch, for which a slightly larger size and divergence is attained because of the increased energy spread of the electron beam. Vertical electron beam sizes and divergences apply to the uniform, 2 x 1/3 and hybrid filling modes only. To increase the lifetime of the stored beam, the vertical beam sizes and divergences are increased by about 50% in the 16 and 4 bunch filling patterns.

The lifetime, bunch length and energy spread mainly depend on the filling pattern. These are given in **Table 4** for a few representative patterns. Note that in both the 16-bunch and 4-bunch filling patterns, the energy spread and bunch length decay with the current (the value indicated in the table corresponds to the maximum current). The bunch lengths are given for the usual radio frequency accelerating voltage of 9 MV (8 MV for 16-bunch and 4-bunch).

# Summary of accelerator operation

In 2008, 685 shifts (5480 hours) of beam were initially scheduled. Of these 5480 hours, 5335 were effectively delivered (including 52 hours of refill). This represents a beam availability of 98.3%, which is in line with recent years. Dead time due to failures accounts for the remaining 1.7%. The number of failures is lower compared to the previous year, thus leading to an all time record mean time between failures of 64.5 hours. This performance was achieved despite the difficulties encountered with the radio frequency cavities and also despite the fact that electrical mains drops occurring between January and June 2008 were not intercepted because the HQPS system was non

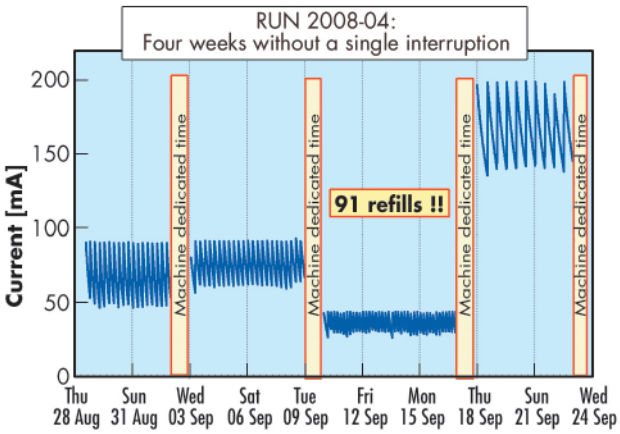


*Fig. 166:* Twenty-three days without a single failure. This is the longest delivery period without beam loss of all time.

| RUN NUMBER | TOTAL 2007 | 2008-01 | 2008-02 | 2008-03 | 2008-04 | 2008-05 | TOTAL 2008 |
|---|---|---|---|---|---|---|---|
| Start | | 15/01/08 | 04/04/08 | 06/06/08 | 22/08/08 | 24/10/08 | |
| End | | 26/03/08 | 28/05/08 | 30/07/08 | 08/10/08 | 15/12/08 | |
| Total number of shifts | **845** | 213 | 162 | 162 | 141 | 156 | **834** |
| Number of USM shifts | **681.96** | 165 | 130 | 132 | 113.9 | 144.1 | **685** |
| Beam available for users (h) | **5291.4** | 1292.5 | 1003 | 1021.2 | 895 | 1123.1 | **5334.7** |
| Availability | **97.82%** | **98.81%** | **97.59%** | **97.5%** | **99.46%** | **98.24%** | **98.32%** |
| Dead time for failures | **2.2%** | 1.2% | 2.4% | 2.5% | 0.54% | 1.8% | **1.7%** |
| Dead time for refills | **0.83%** | 0.9% | 1.2% | 0.8% | 1.2% | 0.8% | **0.97%** |
| Average intensity (mA) | **138.4** | 131 | 144 | 183 | 117 | 137 | **142.3** |
| Number of failures | **96** | 20 | 17 | 21 | 6 | 21 | **85** |
| Mean time between failures (h) | **56.8** | 66 | 61.2 | 50.3 | 151.8 | 54.9 | **64.5** |
| Mean duration of a failure (h) | **1.24** | 0.8 | 1.5 | 1.3 | 0.8 | 1 | **1.09** |

*Table 5:* Storage ring operation in 2008.

functional (see below). Nineteen long delivery periods (*i.e.* more than 100 hours) without a single interruption took place in 2008. In September, the beam was delivered for 23 days without a single failure and interrupted only by the scheduled machine dedicated days. **Figure 166** highlights these four weeks of delivery which is the longest delivery period ever recorded without a single failure.

**Table 5** presents an overview of storage ring operation in 2008.

## Filling patterns

The filling mode labelled "7/8 + 1" is becoming the standard multibunch mode. Developed in 2006-2007, this mode is a worthwhile compromise offering the benefit of a long lifetime multibunch mode while allowing time structure studies with the single bunch. In 2008, delivery in this mode increased to 44%, compared to 24% in 2007. Use of the uniform filling mode has dropped to 13% of the delivery time in 2008, compared to 31% in 2007. The tendency was to replace uniform filling with the "7/8 + 1" mode. Delivery in the other modes remained stable compared to 2007 (**Figure 167**). During run 2 of 2008, a vacuum problem on the storage ring radio frequency cavity 5 resulted in one week of delivery in 7/8+1 mode instead of the initially scheduled 16 bunch mode.

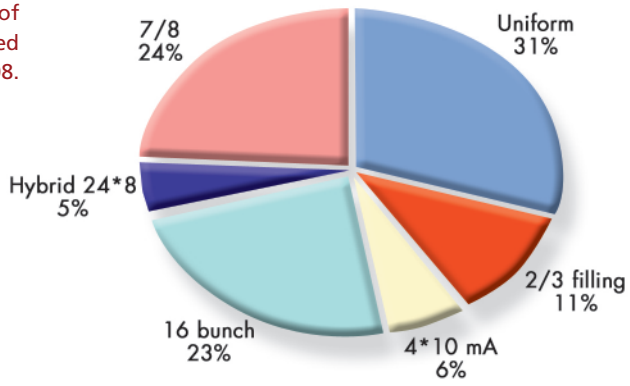


*Fig. 167:* Distribution of filling modes scheduled for 2008.

## A new high-quality power supply

The Grenoble area electricity supply has a dense aerial network providing customers with electricity. Lengthy power interruptions are rare thanks to the 10 interconnected high voltage aerial transport lines (225 kV and 400 kV). Unfortunately the aerial transport lines located in the mountainous areas are exposed to lightning during storms, which results in voltage and frequency drops of the mains. The statistics over the last 10 years show that 300 lightning strikes per year occur on the high voltage lines surrounding the ESRF. This is four times more frequent than the average for France. Eighty of these events result in a mains drop large enough to trigger an electron beam dump in the storage ring. The biggest drops may induce transients that can damage the electronics boards or leave them in an abnormal state requiring a manual reset.

The sensitivity of the various subsystems driving the accelerators has been observed since commissioning in 1992. At that time, a major storm could result in beam interruptions of several hours, one even resulted in 5 days without beam. To protect against mains drops, a high-quality power supply (HQPS) system was put into operation in 1995. It consisted of 10 rotating electro-mechanical storage systems each coupled to a 800 kW diesel engine via a clutch. The system was operated without problems for seven years. The diesel engines were also run to produce electrical power for the accelerator systems during the 22 so-called EJP days in winter when the cost of electricity is very high. In 2002, a major failure of several of the diesel engines occurred, caused by premature ageing of the bearings supporting the crankshaft. The origin of the problem could not be clearly identified and, although the

system continued operation until 2007, it had to be stopped frequently to carry out interventions. The numerous failures provoked premature ageing of a number of components. Therefore, it was decided to replace the HQPS system with a new system without diesel engines, only involves rotating energy accumulators. The new system started operation in July 2008. While several glitches were observed initially, it has protected the accelerator very efficiently, allowing 4 weeks of uninterrupted USM operation in August and September. Due to the absence of diesel engines, the system cannot maintain the full power of 7.8 MW (storage ring with 200 mA and injector in operation) for the accelerator systems for more than 3 seconds. Fortunately, such long interruptions of the mains power are quite rare. During a long power cut, the system is nevertheless designed to switch off the power to the radio frequency system and to the magnets but to maintain power to the critical systems such as computer, vacuum and control, using a single 1 MW diesel engine. This allows a fast restart of the accelerator systems when the power comes back on.

The system is manufactured by the Belgian company KST. It consists of 14 rotating units each providing 800 kVA. A pair of such machines can be seen in the photograph shown in **Figure 168**. In the centre are alternators rotating at 1500 rpm while the accumulators are located at each extremity, they rotate at a nominal speed of 3000 rpm and are magnetically coupled to the alternator rotating axis via windings. During charging time a special winding couples to the accumulator and converts electrical power to stored energy in the accumulator.

*Fig. 168:* A pair of rotating units.

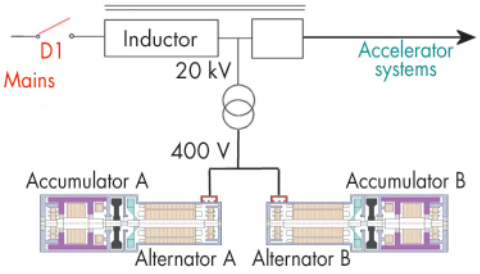


*Fig. 169:* Electrical connection of a pair of rotating machines to the 20 kV electrical grid. The rotating units are operated at 400 V and connected to the 20 kV distribution via a transformer. Seven such pairs of rotating machines operate in parallel with their own transformer and inductor.

**Figure 169** presents a schematic of the connection of a pair of rotating machines to the mains and the accelerator system. When a drop occurs on the mains, the system reacts in one of two different ways. If the missing energy involved in the drop is low enough (very large majority of cases), it operates as a network conditioner and maintains a constant supply of voltage and frequency to the accelerator systems. In the case of large amplitude and/or large duration drops (rare events), the system isolates itself from the mains by opening the 20 kV circuit breaker labeled D1 in **Figure 169**. When isolated, the rotating power stored in the accumulator is transformed into electrical power by the alternator. The accelerator system can run for a few seconds. The system monitors the mains on a permanent basis and tries to reconnect (by closing the D1 circuit breaker) if the mains are back to normal.

## Operation of a cryogenic in-vacuum undulator

A cryogenic permanent magnet undulator (CPMU) offers increased peak field for a given magnetic gap and period allowing the extension of the high brilliance undulator radiation to higher photon energies beyond that available from an in-vacuum undulator. To make the most of the advantages of a CPMU, the magnetic material must be selected with a

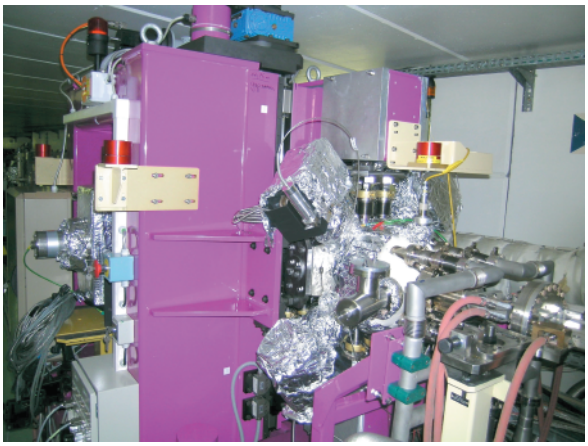

*Fig. 170:* The CPMU Installed in the ID6 straight section.

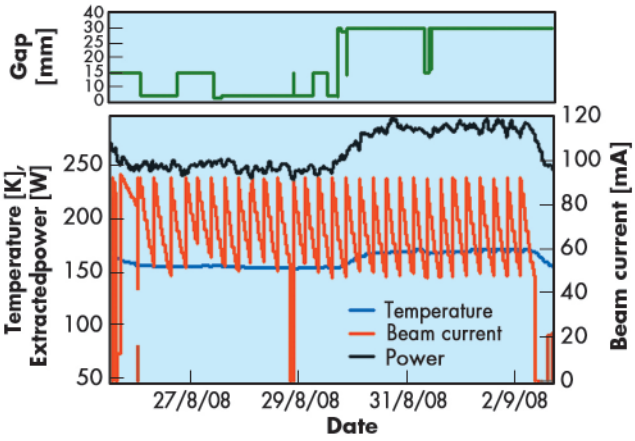


*Fig. 171:* Average temperature of the CPMU (blue) and power extracted by the cryogenic loop (black) versus time in the 16 bunch mode. The undulator gap is shown in the upper curve (green).

maximum remanence and thus a low coercivity. All in-vacuum undulators in operation at the ESRF are baked above 100°C after installation on the ring in order to minimise the Bremstrahlung sent to the beamline. Unfortunately, optimisation of a CPMU results in the selection of low coercivity magnetic material which prevents such baking. To minimise the risk, an initial CMPU prototype was developed which made use of magnetic material that can be baked, at the expense of a reduced field performance. In January 2008, the prototype CPMU was installed in the ID6 straight section (See **Figure 170**). This undulator has a period of 18 mm and a magnetic length of 2 m. During 2007, the undulator was carefully measured with a specially designed magnetic measuring bench operated in-vacuum with the magnetic assembly at cryogenic temperature **[1]**. The measurements confirmed the predicted temperature of 150 K which corresponds to the maximum field. Cryogenic cooling is based on a liquid nitrogen closed loop, identical to the system used in many ESRF beamlines for the cooling of cryogenic monochromators. The installed device is connected to a cryo-pump system located in the technical gallery with a cryogenic line of 50 m.

Temperature measurements on the undulator rely on 20 thermocouples distributed along the magnetic assembly. The power extracted by the cryogenic loop is derived from the measurements of the differential pressure and temperature of the liquid nitrogen between the input and output of the cryogenic pump. **Figure 171** shows the average temperature of the undulator (blue) and power extracted by the cryogenic loop (black) in 16 bunch mode. The upper curve (green) corresponds to the gap of the undulator. It reveals the strong dependence of the magnet temperature as a function of the undulator gap. Both temperature and extracted power are at their maximum for a gap which is fully opened (30 mm). This feature has been observed with other types of filling patterns. It is rather unexpected and it is suspected that this originates from higher-order modes (HOM) of the radio frequency field resonating in the undulator tank. **Table 6** presents the average temperature of the undulator and power extracted by the cryogenic loop for various filling modes and gap settings. High beam induced power of 105 W is observed with a filling pattern corresponding to the filling pattern of the hybrid mode.

| Filling mode | Gap [mm] | Undulator temperature [K] | Total cryogenic power [W] | Power from beam [W] |
|---|---|---|---|---|
| 16 bunch | 30 | 165 | 285 | 75 |
| 16 bunch | 7 | 154 | 247 | 37 |
| 7/8 & uniform | 6 | 151 | 240 | 30 |
| Hybrid | 15 | 177 | 315 | 105 |
| No beam | N/A | 140 | 210 | 0 |

*Table 6:* Measured average temperature of the magnetic assembly and power extracted by the cryogenic loop in different filling modes and with various undulator gaps. The last column presents the net power deposited by the beam.

The measured cryogenic power of 210 W without beam originates from conduction and radiation losses inside the undulator vessel (150 W) plus the losses in the cryogenic line (60 W).

The average observed temperature of the undulator with beam varies from 151 K to 177 K depending on the filling pattern. This corresponds to a change of peak magnetic field smaller than 0.4% [2]. A feature of major importance is the variation of temperature along the 2 metre-long magnet assemblies. This effect was carefully studied during the magnetic measurements. A temperature gradient has an impact on the phase error in a similar manner to a gap variation along the structure (tapering). It has been observed that to reach a phase error of 2.5 degrees rms, a longitudinal temperature gradient smaller than 2 K/m must be obtained. Note that the phase error originating from a longitudinal temperature gradient can be compensated for by a mechanical gap tapering. Initial observations showed a gradient of 7 K/m in the hybrid filling mode. Such a large gradient was the consequence of poor thermal contact between the cooling pipes and the copper blocks located at the entrance of the undulator (see **Figure 172**). The temperature gradient was later reduced to 2 K/m following the installation of a flexible thermal connection during the summer shutdown.

Cooling from 300 to 150 deg K without beam has had an effect on the vacuum. It reduced the pressure by about one order of magnitude to a few $10^{-10}$ mbar. The pressure nevertheless increases with beam current to around $10^{-8}$ mbar at 200 mA of ring current, which is not significantly different to a room temperature in-vacuum undulator. The combination of a large mass of magnets and support pieces at 150 K with a low cryogenic power loss results in a long thermal time constant of 12.5 hours. As a result the cryo-pump driving the liquid nitrogen in the undulator can be switched off for a few hours and then switched on again. The temperatures fluctuates slowly but the system restores its equilibrium without any further interventions.

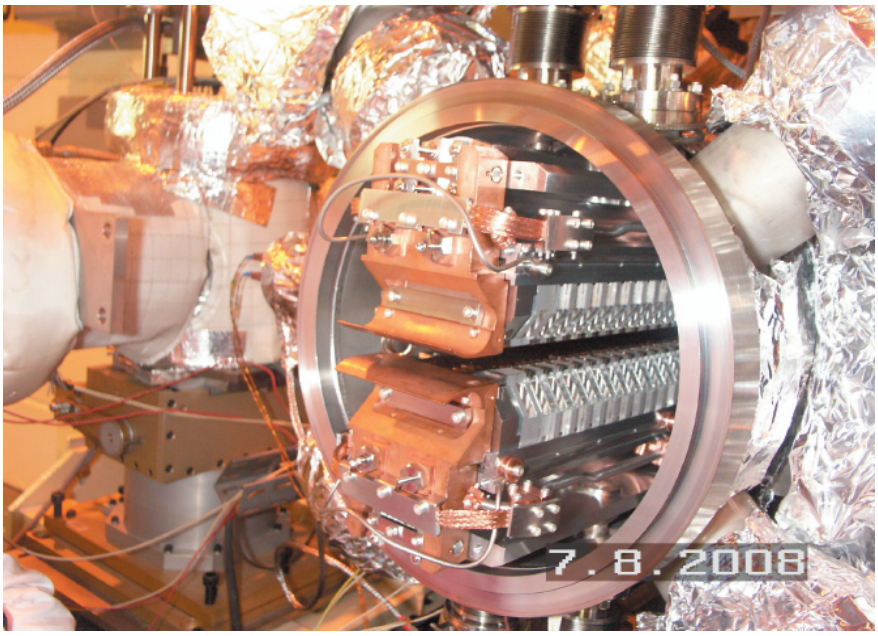


*Fig. 172:* Entrance of the CPMU. The installation of a flexible thermal connection between the cooling tubes and the end copper blocks at the entrance of the undulator has reduced the temperature gradient by a factor of 3.5.

The conclusion of a full year of operation with beam is that the routine use of a CPMU in an ESRF beamline is compatible with the constraints imposed by storage ring operation. While further investigations will be carried out on the existing prototype, a new CPMU will be built in 2009 using higher remanence NdFeB material. The design includes a number of improvements.

**References**
[1] J.Chavanne *et al.*, EPAC'08, June 08, p. 2243, http://accelconf.web.cern.ch/AccelConf/e08/papers/wepc105.pdf
[2] C. Kitegi, PhD Thesis, University Joseph Fourier, 2008.

# Facts and Figures

## Members and associate countries

(as of January 2009)


**Members' share in contribution to the annual budget:**

| | |
|---|---|
| 27.5% | France |
| 25.5% | Germany |
| 15% | Italy |
| 14% | United Kingdom |
| 4% | Spain |
| 4% | Switzerland |
| 6% | Benesync (Belgium, The Netherlands) |
| 4% | Nordsync (Denmark, Finland, Norway, Sweden) |

**Additional contributions**

(percentages refer to Members' total contribution):

| | |
|---|---|
| 1% | Portugal |
| 1% | Israel |
| 1% | Austria |
| 1% | Poland |
| 0.55% | Czech Republic |
| 0.25% | Hungary |
| 0.25% | Slovakia |

## The beamlines

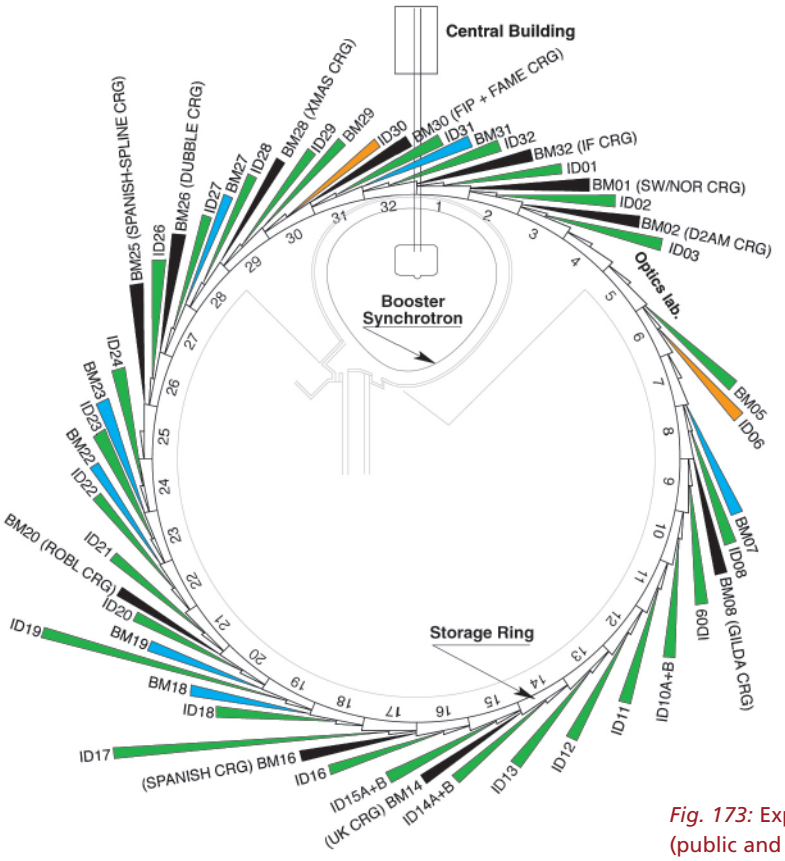


Details of the public ESRF beamlines as well as those operated by Collaborating Research Groups (CRG) are given in **Tables 7** and **8**. **Figure 173** shows the location of the beamlines in the experimental hall.

The transformation of ID06 into a multi-purpose instrumentation development beamline continues. The MX crystallography station at ID14-3 has been transformed into a bio-SAXS end-station dedicated to protein solution scattering experiments. ID14-3 started user operation in November. The GRAAL CRG beamline BM07 stopped operation in November and will be dismantled.

*Public beamlines*

*Instrumentation test and development beamlines*

*CRG beamlines*

*Free bending magnet ports*

*Fig. 173:* Experimental hall showing location of the beamlines (public and CRG beamlines).

| SOURCE POSITION | NUMBER OF INDEPENDENT END-STATIONS | BEAMLINE NAME | STATUS |
|---|---|---|---|
| ID01 | 1 | Anomalous scattering | Operational since 07/97 |
| ID02 | 1 | High brilliance | Operational since 09/94 |
| ID03 | 1 | Surface diffraction | Operational since 09/94 |
| ID06 | 1 | ESRF instrumentation and techniques test beamline | Under commissioning |
| ID08 | 1 | Dragon | Operational since 02/00 |
| ID09 | 1 | White beam | Operational since 09/94 |
| ID10A | 1 | Troika I + III | Operational since 09/94 |
| ID10B | 1 | Troika II | Operational since 04/98 |
| ID11 | 1 | Materials science | Operational since 09/94 |
| ID12 | 1 | Circular polarisation | Operational since 01/95 |
| ID13 | 1 | Microfocus | Operational since 09/94 |
| ID14A | 2 | Protein crystallography EH 1 | Operational since 07/99 |
| | | Protein crystallography EH 2 | Operational since 12/97 |
| ID14B | 2 | Protein solution small-angle scattering EH 3 | Operational since 12/98 |
| | | Protein crystallography EH 4 | Operational since 07/99 |
| ID15A | 1 | High energy diffraction | Operational since 09/94 |
| ID15B | 1 | High energy inelastic scattering | Operational since 09/94 |
| ID16 | 1 | Inelastic scattering I | Operational since 09/95 |
| ID17 | 1 | Medical | Operational since 05/97 |
| ID18 | 1 | Nuclear scattering | Operational since 01/96 |
| ID19 | 1 | Topography and tomography | Operational since 06/96 |
| ID20 | 1 | Magnetic scattering | Operational since 05/96 |
| ID21 | 1 | X-ray microscopy | Operational since 12/97 |
| ID22 | 1 | Microfluorescence | Operational since 12/97 |
| ID23 | 2 | Macromolecular crystallography MAD | Operational since 06/04 |
| | | Macromolecular crystallography microfocus | Operational since 09/05 |
| ID24 | 1 | Dispersive EXAFS | Operational since 02/96 |
| ID26 | 1 | X-ray absorption and emission | Operational since 11/97 |
| ID27 | 1 | High pressure | Operational since 02/05 |
| ID28 | 1 | Inelastic scattering II | Operational since 12/98 |
| ID29 | 1 | Multiwavelength anomalous diffraction | Operational since 01/00 |
| ID30 | 1 | Machine division beamline | Operational since 09/07 |
| ID31 | 1 | Powder diffraction | Operational since 05/96 |
| ID32 | 1 | X-ray standing wave and surface diffraction | Operational since 11/95 |
| BM05 | 1 | Optics - Open Bending Magnet | Operational since 09/95 |
| BM29 | 1 | X-ray absorption spectroscopy | Operational since 12/95 |

*Table 7:* List of the ESRF public beamlines.

| SOURCE POSITION | NUMBER OF INDEPENDENT END-STATIONS | BEAMLINE NAME | FIELD OF RESEARCH | STATUS |
|---|---|---|---|---|
| BM01 | 2 | Swiss-Norwegian BL | X-ray absorption & diffraction | Operational since 01/95 |
| BM02 | 1 | D2AM (French) | Materials science | Operational since 09/94 |
| BM08 | 1 | Gilda (Italian) | X-ray absorption & diffraction | Operational since 09/94 |
| BM14 | 1 | UK CRG | Macromolecular crystallography (MAD) | Operational since 01/01 |
| BM16 | 1 | SPANISH CRG | Structural biology (MAD, SAX) | Operational since 01/03 |
| BM20 | 1 | ROBL (German) | Radiochemistry & ion beam physics | Operational since 09/98 |
| BM25 | 2 | SPLINE (Spanish) | X-ray absorption & diffraction | Operational since 04/05 |
| BM26 | 2 | DUBBLE (Dutch/Belgian) | Small-angle scattering & interface diffraction<br>Protein crystallography + EXAFS | Operational since 12/98<br>Operational since 06/01 |
| BM28 | 1 | XMAS (British) | Magnetic scattering | Operational since 04/98 |
| BM30 | 2 | FIP (French)<br>FAME (French) | Protein crystallography<br>EXAFS | Operational since 02/99<br>Operational since 08/02 |
| BM32 | 1 | IF (French) | Interfaces | Operational since 09/94 |

*Table 8:* List of the Collaborating Research Group beamlines.

# User operation

As we enter into the 15th year of successful operation of the facility for scientific Users, we look back on the year 2008, which once again saw the full complement of 31 public beamlines, together with 11 additional beamlines operated by Collaborating Research Groups (CRGs), available for experiments by visiting research teams. **Figure 174** shows the continuing increase in number of applications for beamtime since 2002 confirming that, although the main beamline construction effort was complete by 1999 and despite the fact that more synchrotrons are now available to European scientists, there is ever-increasing demand for use of the ESRF beamlines and the number of applications for beamtime continues to rise steadily, breaking the 2000 barrier for the first time during 2008.

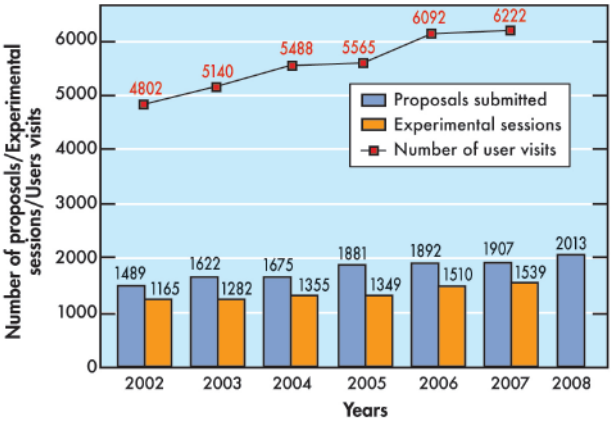


*Fig. 174:* Numbers of applications for beamtime, experimental sessions and user visits, 2002 to 2008. N.B. Final numbers of experiments and user visits for 2008 were not available at the time of going to press.

*Table 9:* Number of shifts of beamtime requested and allocated for user experiments, year 2008.

| Scientific field | Total shifts requested | Total shifts allocated |
|---|---|---|
| Chemistry | 3 104 | 1 257 |
| Hard condensed matter: | | |
| • Electronic and magnetic prop. | 5 355 | 2 031 |
| • Crystals and ordered structures | 4 230 | 1 800 |
| • Disordered systems | 1 693 | 699 |
| Applied materials and engineering | 3 164 | 1 546 |
| Environmental and cultural heritage matters | 2 330 | 699 |
| Macromolecular crystallography | 3 507 | 2 381 |
| Medicine | 1 109 | 507 |
| Methods and instrumentation | 678 | 364 |
| Soft condensed matter | 2 909 | 1 287 |
| Surfaces and interfaces | 3 026 | 1 335 |
| **Totals** | **31 105** | **13 906** |

*Fig. 175:* Shifts scheduled for experiments, March to July 2008, by scientific area.

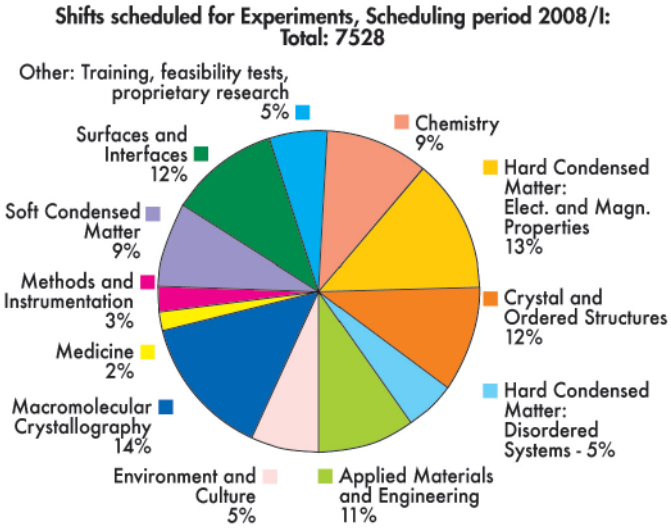


Proposals for experiments are selected and beamtime allocations are made through peer review. Review Committees of specialists, for the most part from European countries and Israel, have been set up in the following scientific areas:

- chemistry
- hard condensed matter: electronic and magnetic properties
- hard condensed matter: crystals and ordered systems
- hard condensed matter: disordered systems and liquids
- applied materials and engineering
- environmental and cultural heritage matters
- macromolecular crystallography
- medicine
- methods and instrumentation
- soft condensed matter
- surfaces and interfaces.

The Review Committees met twice during the year, around six weeks after the deadlines for submission of proposals (1 March and 1 September). They reviewed a record number of 2013 applications for beamtime, and selected 903 (44.9%), which were then scheduled for experiments.

Features of this period:

- increasing numbers of proposals submitted for research into diseases for an ageing society such as neurogenerative diseases (Alzheimer's, Parkinson's) and osteoporosis, and for radiobiology for therapy programs (Microbeam Radiation Therapy, Stereotactic Synchroton Radiation Therapy).
- in the area of Soft Condensed

Matter, around half of all proposals submitted were concerned with biomaterials.

Requests for beamtime, which is scheduled in shifts of 8 hours, totalled 31 105 shifts or 248 840 hours in 2008, of which 13 906 shifts or 111 248 hours (44.7%) were allocated. The distribution of shifts requested and allocated, by scientific area, is shown in **Table 9**.

The breakdown of shifts scheduled for experiments by scientific area in the first half of 2008 is shown in **Figure 175.** This period saw yet another record broken with the number of user visits going beyond the 3000 barrier for a single scheduling period: 3088 visits by scientists to the ESRF under the user programme, to carry out 741 experiments. **Figure 174** shows the rapid rise in the number of user visits since 2002, the higher numbers in recent years reflecting the increased level of automation on many beamlines, resulting in shorter and therefore more frequent experiments across almost all scientific areas but particularly for experiments carried out by the macromolecular crystallography BAG teams.

Overall, the number of users in each experimental team averaged 4 persons as in 2007, but the average stay decreased to 3 days compared with 4 days in 2007, confirming that experiments have tended to become shorter thanks to many factors including higher automation and increased flux from state-of-the-art optics. The year 2008 also saw the implementation of remote access experiments for macromolecular crystallography, whereby users may run their experiments on the ESRF MX beamlines using a control station in their home laboratories. From July to December 2008, of the 1366 users who performed public experiments on the MX beamlines, nearly 200 did so remotely from their home laboratories. User responses to questionnaires show that the ESRF continues to maintain its excellent reputation concerning the assistance given by scientists and support staff on beamlines, and travel and administrative arrangements, in addition to the quality both of the beam and of the experimental stations. Facilities on site, such as preparation laboratories, the Guesthouse and a canteen open 7 days a week, also make an important contribution to the quality of user support.

# Administration and finance

**Expenditure and income 2007**

| Expenditure | kEuro | kEuro | Income | kEuro |
|---|---|---|---|---|
| Accelerator and Source | | | 2007 Members' contributions | 69 742.7 |
| Personnel | | 4 909.2 | Funds carried forward from 2006 | 13.0 |
| Recurrent | | 1 849.8 | | |
| *Operating costs* | *1 590.8* | | Other income | |
| *Other recurrent costs* | *259.0* | | Scientific Associates | 4 275.5 |
| Capital | | 4 324.1 | Sale of beam time | 2 724.5 |
| *Accelerator and Source Developments* | *4 324.1* | | Compensatory funds | 210.0 |
| | | | Scientific collaboration and Special projects | 3 237.7 |
| Beamlines, experiments and in-house research | | | | |
| Personnel | | 24 303.0 | | |
| Recurrent | | 6 743.8 | | |
| *Operating costs* | *3 692.2* | | | |
| *Other Recurrent costs* | *3 051.6* | | | |
| Capital | | 7 546.3 | | |
| *Beamline developments* | *4 029.9* | | | |
| *Beamline refurbishment* | *3 516.4* | | | |
| Technical and administrative supports | | | | |
| Personnel | | 16 651.7 | | |
| Recurrent | | 10 811.2 | | |
| Capital | | 3 064.3 | | |
| Unexpended committed funds | | | | |
| Funds carried forward to 2008 | | 0 | | |
| **Total** | | **80 203.4** | **Total** | **80 203.4** |

## Revised expenditure and income budget for 2008

| Expenditure | | kEuro | Income | kEuro |
|---|---|---|---|---|
| Accelerator and Source | | | 2008 Members' contributions | 70 712 |
| Personnel | | 5 435 | Funds carried forward from 2007 | 0 |
| Recurrent | | 2 040 | | |
| *Operating costs* | *1 633* | | Other income | |
| *Other recurrent costs* | *407* | | Scientific Associates | 4 265 |
| Capital | | 4 932 | Sale of beam time | 2 640 |
| *Accelerator and Source developments* | *4 932* | | Compensatory funds | 92 |
| | | | Scientific collaboration and Special projects | 9 155 |
| Beamlines, experiments and in-house research | | | | |
| Personnel | | 25 380 | | |
| Recurrent | | 7 240 | | |
| *Operating costs* | *4 190* | | | |
| *Other Recurrent costs* | *3 050* | | | |
| Capital | | 7 480 | | |
| *Beamline developments* | *4 360* | | | |
| *Beamline refurbishment* | *3 120* | | | |
| Technical and administrative supports | | | | |
| Personnel | | 17 845 | | |
| Recurrent | | 10 895 | | |
| Capital | | 4 897 | | |
| Industrial and commercial activity | | | | |
| Personnel | | 500 | | |
| Recurrent | | 220 | | |
| Personnel costs provision | | | | |
| **Total** | | **86 864** | **Total** | **86 864** |

## Expenditure 2007 by nature of expenditure

| | kEuro |
|---|---|
| PERSONNEL | |
| ESRF staff | 43 876.6 |
| External temporary staff | 96.4 |
| Other personnel costs | 1 890.9 |
| RECURRENT | |
| Consumables | 7 664.2 |
| Services | 9 295.8 |
| Other recurrent costs | 2 444.7 |
| CAPITAL | |
| Buildings, infrastructure | 1 312.8 |
| Lab. and Workshops | 346.9 |
| Accelerator and Source incl. ID's and Fes | 4 324.1 |
| Beamlines, Experiments | 7 546.3 |
| Computing Infrastructure | 1 136.8 |
| Other Capital costs | 267.9 |
| Unexpended committed funds | |
| Funds carried forward to 2007 | 0 |
| **Total** | **80 203.4** |

## Revised budget for 2008 by nature of expenditure

| | kEuro |
|---|---|
| PERSONNEL | |
| ESRF staff | 47 320 |
| External temporary staff | 85 |
| Other personnel costs | 1 965 |
| RECURRENT | |
| Consumables | 7 665 |
| Services | 10 270 |
| Other recurrent costs | 2 460 |
| CAPITAL | |
| Buildings, infrastructure | 2 422 |
| Lab. and Workshops | 400 |
| Accelerator and Source incl. ID's and Fes | 4 822 |
| Beamlines, Experiments | 7 270 |
| Computing Infrastructure | 1 970 |
| Other Capital costs | 215 |
| **Total** | **86 864** |

## Financial resources in 2006, 2007, 2008 and 2009, by major programme

(current prices in MEuro for the respective years)

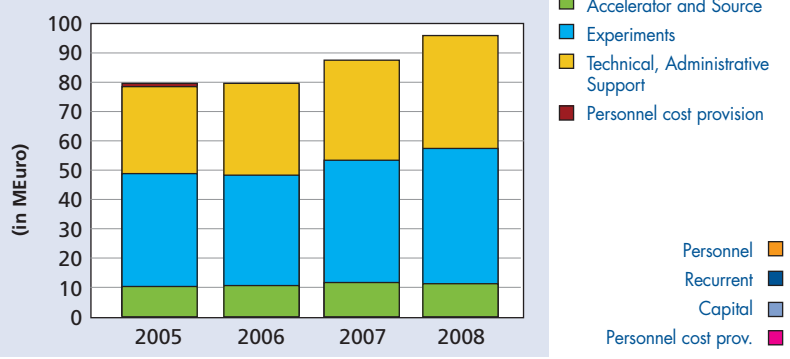


## Financial resources in 2006, 2007, 2008 and 2009, by nature of expenditure

(current prices in MEuro for the respective years)

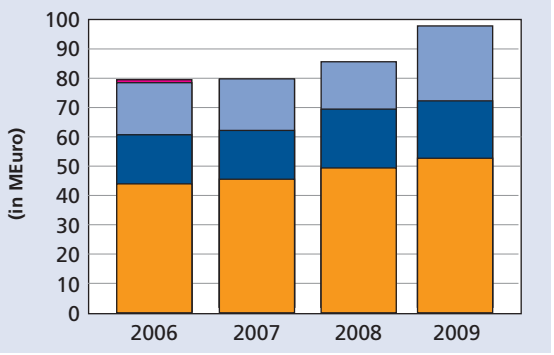

## 2008 manpower *(posts filled on 31/12/2008)*

| | Scientists, Engineers, Senior Administrators | Technicians and Administrative Staff | PhD students | Total |
|---|---|---|---|---|
| ***Staff on regular positions*** | | | | |
| Accelerator and Source | 28 | 38.4 | | 66.4 |
| Beamlines, instruments and experiments* | 212 | 65.2 | 18.5 | 295.7 |
| General technical services | 49.6 | 69.9 | | 119.4 |
| Directorate, administration and central services | 32.5 | 51.9 | | 84.4 |
| *Sub-total* | *322* | *225.4* | *18.5* | *565.9* |
| ***Other positions*** | | | | |
| Short term contracts | 4 | 7 | | 11 |
| Staff under "contrats de qualification" (apprentices) | | 23 | | 23 |
| European Union grants | 12 | 2 | 1 | 15 |
| Temporary workers | | | | |
| **Total** | **338** | **257.4** | **19.5** | **614.9** |
| Absences of staff (equivalent full time posts) | | | | 22.7 |
| *Total with absences* | | | | *592.2* |
| *Scientific collaborators and consultants* | *11* | | | *11* |
| *External funded research fellows* | *7* | | *18* | *25* |

** Including scientific staff on time limited contract.*

# Organisation chart of the ESRF

## (as of January 2009)

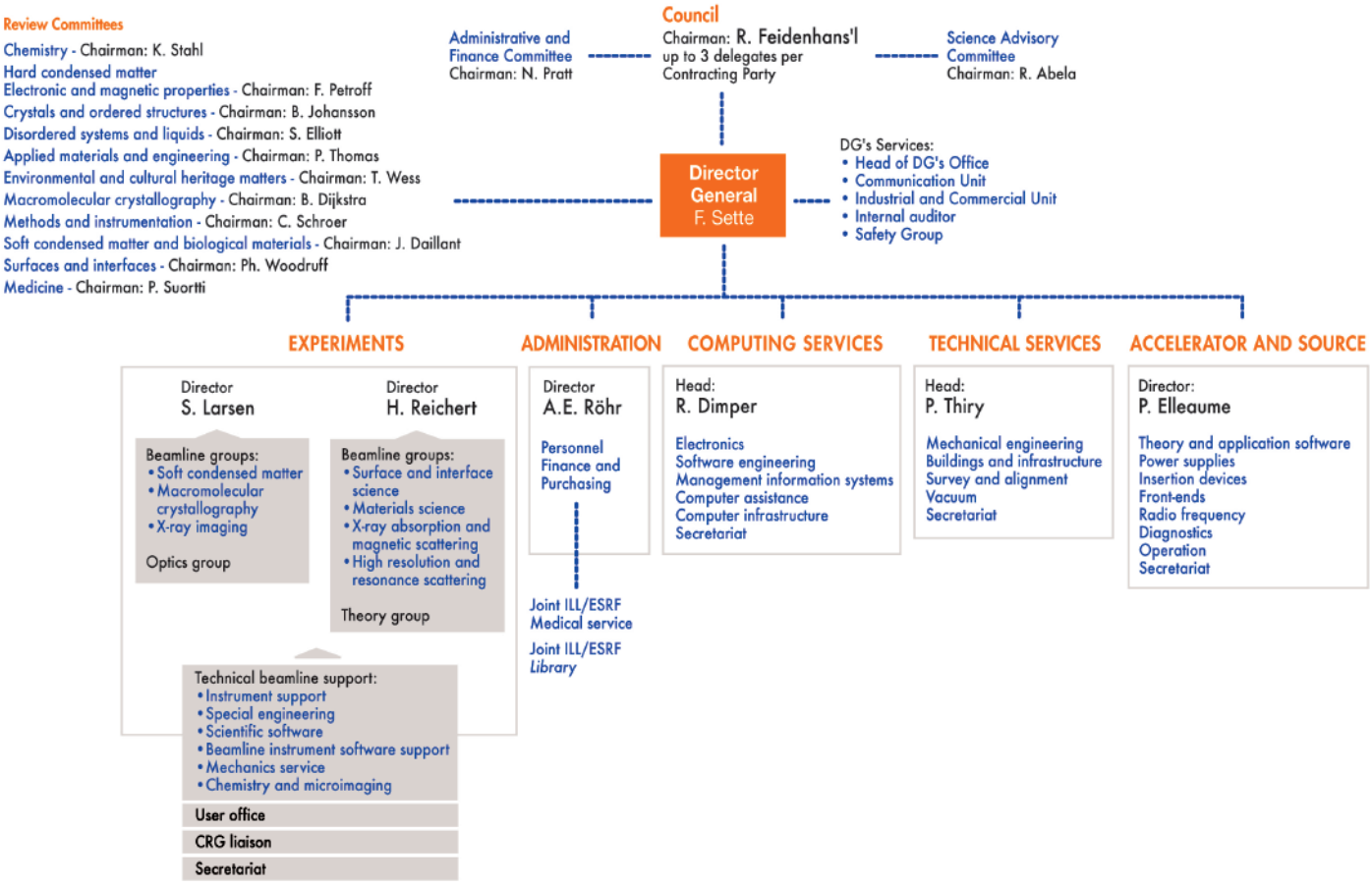

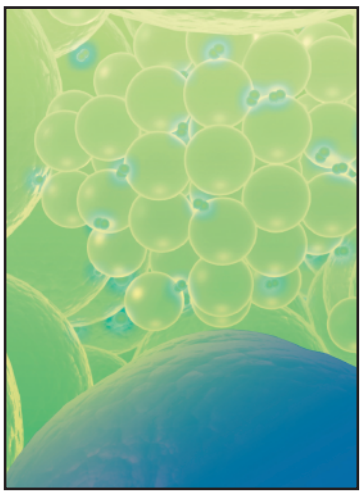

Cover image

How do palladium nanoclusters behave in hydrogen? Di Vece and co-authors observed hydrogen-induced Ostwald ripening, the growth of larger palladium nanoclusters at the expense of the smaller ones. This is a schematic impression of the palladium nanoclusters with interstitial hydrogen between the palladium atoms, which become free to move due to the interstitial hydrogen (see p24). Image courtesy M. Di Vece (K.U. Leuven) and J. Husson.

**We gratefully acknowledge the help of:**

C. Argoud, J. Baruchel, S. Blanchon, B. Boulanger, J-F. Bouteille, N.B. Brookes, J. Chavanne, M. Collignon, F. Comin, E. Dancer, P. Elleaume, A. Fitch, C. Habfast, L. Hardy, E. Jean-Baptiste, A. Kaprolat, M. Krisch, S. Larsen, G. Leonard, J. McCarthy, E. Mitchell, T. Narayanan, H. Reichert, M. Rodriguez Castellano, R. Rüffer, F. Sette, W.G. Stirling, C. Stuck, S. McSweeney, J. Zegenhagen, and all the users and staff who have contributed to this edition of the Highlights.

Editor
G. Admans
Layout
Pixel Project
Printing
Imprimerie du Pont de Claix



Communication Unit
ESRF
BP220 • 38043 Grenoble • France
Tel. +33 (0)4 76 88 20 56 • Fax. +33 (0)4 76 88 25 42
http://www.esrf.eu